THEORY AND APPLICATIONS OF TRANSPORT IN POROUS MEDIA

Geomechanics and Fluidodynamics

With Applications to Reservoir Engineering

Victor N. Nikolaevskiy

GEOMECHANICS AND FLUIDODYNAMICS

Theory and Applications of Transport in Porous Media

Series Editor:
Jacob Bear, *Technion – Israel Institute of Technology, Haifa, Israel*

Volume 8

The titles published in this series are listed at the end of this volume.

Geomechanics and Fluidodynamics

With Applications to Reservoir Engineering

by

Victor N. Nikolaevskiy

Moscow State Oil and Gas Academy,
and Laboratory on Applied Geomechanics,
United Institute of Physics of the Earth,
Russian Academy of Sciences,
Moscow, Russia

SPRINGER-SCIENCE+BUSINESS MEDIA, B.V.

A C.I.P. Catalogue record for this book is available from the Library of Congress.

ISBN 978-90-481-4638-3 ISBN 978-94-015-8709-9 (eBook)
DOI 10.1007/978-94-015-8709-9

Printed on acid-free paper

Originally published by Kluwer Academic Publishers in 1996
Softcover reprint of the hardcover 1st edition 1996

Table of Contents

CHAPTER 3. HYDRODYNAMICS OF RESERVOIRS

CHAPTER 4. COMPLICATED PHENOMENA IN RESERVOIRS

PREFACE.

Geomechanics is the basic science for many engineering fields, including oil and gas recovery, mining, civil engineering, water supply, etc., as well as for many environmental sciences, including earthquake prediction, ecology, landscape dynamics, and explosion works. Historically, the major concepts of geomechanics were founded on the methods of the elasticity theory and the static equilibrium of joints with solid friction. Underground hydrodynamics was developed quite separately and included only simple, conventional ideas of elastic pore-space deformation.

Today, the situation is drastically different. Tremendous achievements in numerical computer technique have eliminated many of the routine difficulties of problem solution with respect to selected mathematical models. As the result, major efforts now are applied to sophisticated experimental studies and to new applications of generalized continuum theories. Of course, traditional rheological schemes have been adjusted to be into account the real properties of such geomaterials as soils, rocks and ice. The main changes have been connected with the kinematics of the internal structure of geomaterials that influences their strength and that can play unusual roles in dynamic processes. The theoretical considerations are in good agreement with experimental observations in situ because of precise measuring devices, impact of modern physics concepts and large-scale monitoring.

This book consists of two lecture courses given by the author to graduate and post-graduate students of the Gubkin Oil and Gas Academy in Moscow. The first course consists of lectures on underground hydrodynamics which I now give and which were initiated long ago by my teacher, Professor Isaak A. Charny. The second course reflects recent studies conducted by the laboratory on Applied Geomechanics in the United Institute of Earth Physics. In addition, I address modern advances in geophysics connected with continuum mechanics and my experience in Civil Engineering and in the Russian National Program on Underground Explosions. The goal of such a course is to unite separate investigations into a common science, to introduce students to this science, and to open wider doors for future work.

Attendance at scientific seminars and my lectures at such in foreign organizations as Brown University (Providence, Rhode Island, USA), The Royal Institute of Technology in Stockholm, Universities in Milan, Minneappolis, Bonn, Stuttgart and Karlsruhe, and participation in many joint research projects in my country, have aided me in selecting themes and in understanding recent scientific interests.

This monograph focuses on adequate mathematical models of the deformation and failure of geomaterials and corresponding experiments. Borehole stability and water, gas and oil reservoir states are studied with respect to changes caused by dilatancy, anisotropy, fluid flow and tectonic stress action. Gas-condensate flows are proposed as the most intriguing part of underground physico-chemical hydrodynamics. Study of the rupture zone of contained explosions is interconnected with the study of evolution of radiated waves, including nonlinear effects. Nonlinear resonances, which play essential roles in the vibro-stimulation of oil production from water-flooded seams, are discussed,

and the effects of oil-water saturation on seismic waves are given with respect to the Frenkel-Biot theory and usage of the effective stress concept.

With regard to rock strength and state at depth, the Earth's crustal faults and water circulation are studied. Their distributions are determined by tectonic plate dynamics, including the local mobility of the upper brittle crust. Earthquakes mechanics and precursor phenomena, as well as deep gas and fluid migration and accumulation, are subjected to periodic changes and are discussed in the framework of space-time dynamics. All considered problems have applications to reservoir engineering.

I am grateful to my colleagues Drs. K. Basniev, E. Detournay (University of Minnesota), I. Garagash, G.Gudehus (University of Karlsruhe), S. Kapustiansky, K. Kirchgassner (Stuttgart), A. Maksimov, G. Martinelli (Bologna) and R. Nova (Milan) for stimulating discussions and support and to Dr.S.Grafutko, Kathy Sikora and Mrs. S. Pomytkina for providing help in realizing this publication.

CHAPTER 1

DEFORMATION AND FRACTURE OF GEOMATERIALS

1.1. Principles of continuum mechanics

1.1.1. AVERAGING PROCEDURE

Real geomaterials are extremely nonhomogeneous. They are composed of many pieces (grains) of crystalline matter cemented into a soft or rigid matrix with pores and cracks often filled with fluids and gases. Describing such a medium is complicated but it can be simplified if the motions or flow patterns of the geomaterials have length scales, L, that are much larger than the characteristic sizes, d, of individual grains. For continuum mechanics, use is made of an intermediate scale, λ, such that [152]

$$L >> \lambda >> d \tag{1.1}$$

In this case, the coordinate system X_1, X_2, X_3 exists such that the elementary volume of the considered medium

$$\Delta V = \Delta X_1 \Delta X_2 \Delta X_3, \qquad \Delta X_i = O(\lambda) \tag{1.2}$$

can be treated as a continuum element filled with uniform material whose properties coincide with corresponding ones at the microlevel but which are averaged over volume ΔV.

For example, the average density is determined by:

$$<\rho> = \frac{1}{\Delta V} \int_{\Delta V} \rho \, dx_1 dx_2 dx_3 \tag{1.3}$$

where ρ is equal to the density of the grain or fluid material or equal to zero if the corresponding micropoint, x_1, x_2, x_3, belongs to an empty void.

The right-hand side of inequalities (1.1) corresponds to the assumption that the volume includes the whole ensemble of grains and voids. As a consequence, result (1.3) coincides with the statistical averaging:

$$\tilde{\rho} = \int_{\Delta\chi} \rho(x_i, \chi) \, d\chi \, , \quad \int_{\Delta\chi} d\chi = 1 \tag{1.4}$$

where $\Delta\chi$ is the ensemble of realizations, and χ is the random parameter. The independence of (1.4) on the choice of the coordinate inside ΔV is known as a property of stationarity in probability theory or as a property of uniformity in continuum terminology.

The averaged value $<\rho>$ corresponds to the mass-center of volume ΔV, which the also is interpreted as macropoint X_1, X_2, X_3. The field $<\rho>$ is assumed to be smooth at the scale L - that is, the Taylor expansion

$$<\rho>(X_i + \Delta X_i) = <\rho>(X_i) + \frac{\partial <\rho>_i}{\partial X_i}\Delta X_i + \ldots \tag{1.5}$$

which is violated only at the singular surfaces of the discontinuity. The corresponding representation of the microfield is valid only at the scale d:

$$\rho(x_i + \Delta x_i) = \rho(x_i) + \frac{\partial \rho}{\partial x_i} d x_i + \ldots \tag{1.6}$$

At the microlevel, there are a number of discontinuity surfaces which correspond to a number of grain contacts. Therefore, continuum description at the microlevel also needs an averaging procedure to introduce additional mean microvariables as functions of macrocoordinates.

The left-hand side of nonequality (1.1) means that it is possible to treat the increments as differentials and that corresponding differential equations of continuum mechanics can be treated as true balance equations in space and time.

1.1.2. DYNAMIC BALANCES

The first balance concerns mass:

$$\frac{\partial \rho}{\partial t} + \frac{\partial \rho v_j}{\partial X_j} = 0 \tag{1.7}$$

where ρ is now the average density, and the symbol of space averaging is omitted. The following averaging procedure was used for mass flux ρv_i:

$$<\rho v_j>_j = \frac{1}{\Delta S_j} \int_{\Delta S_j} \rho(x_i, t) v_j(x_i, t) dx_i dx_k \tag{1.8}$$

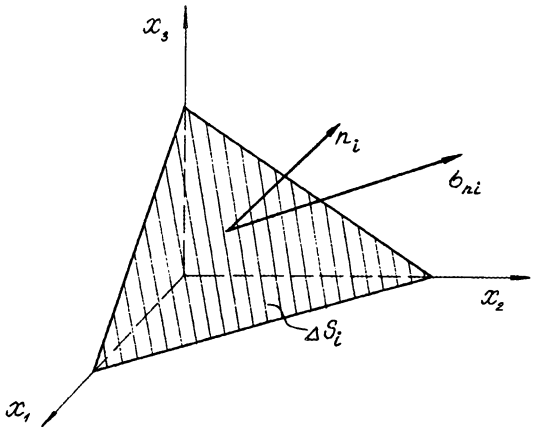

Figure 1.1. Stress-tensor component σ_{ni} acting at oriented cross-section ΔS_i with normal n_i

The integration over surfaces $\Delta S_j = \Delta X_i \Delta X_k$, bounding the volume ΔV, is necessary for all fluxes. This results in the determination of the mass velocity:

$$< v_j >_j = \frac{< \rho v_j >_j}{< \rho >} \tag{1.9}$$

since the flux rate over oriented cross-section $\Delta S_i = n_i \Delta S$ is valid. Here, n_i is a normal to ΔS_i (Figure 1.1) .

The oriented cross-section concept is important. It can be imagined that some part of the considered continuum is absent, but its action must be replaced by some proper set of fluxes at its bounding - oriented cross-sections.

The second balance is completed for the momentum (impulse) - that is,

$$\frac{\partial \rho v_i}{\partial t} + \frac{\partial \rho v_i v_j}{\partial X_j} = \frac{\partial \sigma_{ij}}{\partial X_j} + F_i \tag{1.10}$$

Here, F_i is the body-distributed force, and mass-flux ρv_i is averaged according to rule (1.3); however it is interpreted here as a momentum contained in volume ΔV Momentum fluxes as well as stresses are averaged over bounding cross-sections according to procedure (1.8). It means a definite nonsymmetry of the following type:

$$< \rho v_i v_j >_j \neq < \rho v_j v_i >_i$$
$$< \sigma_{ij} >_j \neq < \sigma_{ji} >_i \tag{1.11}$$

although $\sigma_{ij} \equiv \sigma_{ji}$ and $\rho v_i v_j \equiv \rho v_j v_i$

So, in a medium with microstructure (granular, polycrystalline), the averaged stress tensor is not symmetrical, generally speaking - that is, it has both symmetric and asymmetric parts:

$$\sigma_{ij} = \sigma_{ij}^s + \sigma_{ij}^a \tag{1.12}$$

The symmetric part has a main coordinate system in which the tensor σ_{ij}^s has a diagonal form, with $\sigma_{11} = \sigma_1$; $\sigma_{22} = \sigma_2$; $\sigma_{33} = \sigma_3$ as the main stress values:

$$\sigma_{ij}^s = \begin{pmatrix} \sigma_1 & 0 & 0 \\ 0 & \sigma_2 & 0 \\ 0 & 0 & \sigma_3 \end{pmatrix}$$

and which there are three scalars:

$$I_1 = \sigma_{ij}\delta_{ij} = -3p, \quad I_2 = \sigma_{ij}\sigma_{ij}, \quad I_3 = \sigma_{ij}\sigma_{jk}\sigma_{ki}$$

that are invariant to changes of the coordinate system. Here p is a pressure, δ_{ij} is the unit tensor, and summation is done over repeating indices.

The stress, σ_{ij}^s, is connected with the symmetric kinematic strain tensor e_{ij}, or with the strain-rate tensors, De_{ij}/Dt. Part of σ_{ij}^a has to be connected with the antisymmetric kinematic tensor, which is $\varepsilon_{ijk}\omega_k$, where ω_k is a rotational axial vector, or $\varepsilon_{ijk} D\omega_k/Dt$, where $D\omega_k/Dt$ is a rotational rate vector, and ε_{ijk} is the alternating tensor. Because internal stresses have to be independent on planar or rotational motion of the coordinate system X_i, the rotation vector must only be used relative to the mean rotation of the medium. Therefore, the account of the antisymmetric part of a stress tensor is connected to the introduction of the averaged microrotation $\Phi_i + \omega_i$, which is kinematically independent on mean rotation $\Phi_i = (1/2)\,\varepsilon_{ijk}\,\partial u_j/\partial x_k$, where u_j is a displacement component. As the result, ω_k or $D\omega_k/Dt$ can be interpreted as a spin component of rotation or rate of rotation.

Dynamically, such a motion is controlled by the balance of moment of momentum. The balance of its internal part has the form:

$$\frac{\partial \rho J_{ij}\left(\Phi_j+\omega_j\right)}{\partial t}+\left(\frac{\partial}{\partial X_j}\right)\rho J_{ik}\left(\Phi_k+\omega_k\right)v_j = \frac{\partial \mathcal{M}_{ij}}{\partial X_j}+\varepsilon_{ijk}\sigma_{jk} \qquad (1.13)$$

Its derivation can be found in texts on generalized continuum mechanics (see, for example, [220]).

Here, ρJ_{ij} is a specific moment of inertia of a microparticle (grain), and $\mathcal{M}_{ij}$ is a coupled stress. Equation (1.13) also possesses the body-distributed force couples, $\varepsilon_{ijk}\sigma_{jk}$, generated by the asymmetry of conventional stresses. It can be seen, that this particular case of negligible microstructure effects is characterized by the condition of tangential-stress equality:

$$\sigma_{ij} = \sigma_{ji} \qquad (1.14)$$

For an interpretation of couple stresses, we will examine the forces acting at an arbitrary planar cross-section of a medium (Figure 1.2).

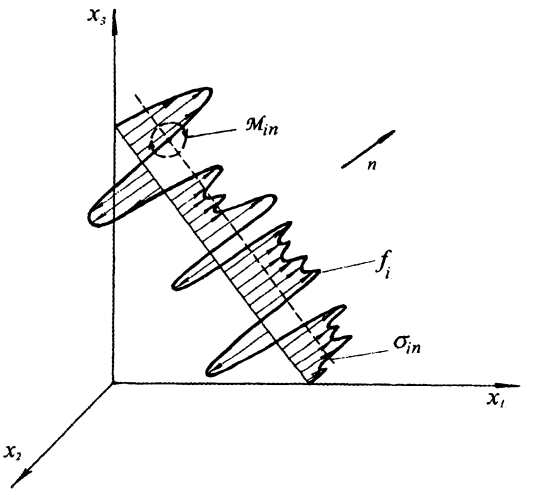

Figure 1.2. Local microtraction f_i, the averaged value σ_{in} (broken line) and the microcouples $\mathcal{M}_{in}$ at the cross-section.

The value of the averaged force is calculated by the following multiplication:

$$< f_i > = \sigma_{ij} n_j \equiv \sigma_{in} \qquad (1.15)$$

where σ_{ij} corresponds to a mean value of a microforce distribution f_i which is non-uniform due to the real nonhomogeneous microstructure of the considered media.

Therefore, we can introduce the second moment of averaging, which is characterized by microcouple distribution and which is equal to couple-stress $\mathcal{M}_{ij}$ mentioned above:

$$\mathcal{M}_{ij} = < f_i^* \zeta_j >_j \tag{1.16}$$

Here, f_i^* is the force pulsation (relative to $< f_i >$), and ζ_j is the polar-vector (relative to the mass-center of ΔV). So, $\mathcal{M}_{ij}$ is generated by the nonuniformity of the microfields and must be used in the formulation of adequate boundary conditions that take into account, for example, asperity effects and wear phenomena.

1.1.3. KINEMATICS AND GOVERNING LAWS

The kinematic variables are created by displacement fields. Again, we have to assume the existence of the Taylor expansion for mean displacements in the vicinity of a mass-center of the elementary volume ΔV:

$$\begin{aligned} u_i(X_j + \Delta X_j) &= u_i(X_j) + \frac{\partial u_i}{\partial X_j} \Delta X_j + \ldots \\ &= u_i(X_j) + e_{ij} \Delta X_j + \frac{1}{2} \varepsilon_{ijk} \Phi_k \Delta X_j \end{aligned} \tag{1.17}$$

Here, the deformation tensor

$$e_{ij} = \frac{1}{2} \left(\frac{\partial u_i}{\partial X_j} + \frac{\partial u_j}{\partial X_i} \right) \tag{1.18}$$

is determined as a symmetric part of the distortion tensor $\partial u_i / \partial X_j$.

The mean rotation, Φ_k, is determined as an asymmetric part of the distortion tensor - that is,

$$\frac{1}{2} \varepsilon_{ijk} \Phi_k = \frac{1}{2} \left(\frac{\partial u_i}{\partial X_j} - \frac{\partial u_i}{\partial X_i} \right) \tag{1.19}$$

In asymmetric Cosserat's mechanics, the microrotation has a non-trivial spin component, ω_k; therefore, consideration of equation (1.13) is necessary. If $\omega_k \equiv 0$, than equation (1.13) is a simple consequence of the momentum balance (1.10). In the case of elastic rheology, constitutive laws, which connect stresses and strains, have the following form:

$$\sigma_{ij}^s = E_{ijkl} e_{kl} \tag{1.20}$$

$$\sigma_{ij}^{a} = \varepsilon_{ijk}\gamma_{kl}\omega_{l} \tag{1.21}$$

$$\mathcal{M}_{ij} = A_{ijlm}\frac{\partial \Phi_{l}}{\partial X_{m}} \tag{1.22}$$

where E_{ijkl} is the elastic modulus tensor, γ_{kl} is the elastic coupling tensor, and A_{ijkl} is a tensor of elastic gradient coefficients. In isotropic cases, these tensors are simplified - for example,

$$E_{ijkl} = \left(K - \frac{2}{3}G\right)\delta_{ij}\delta_{kl} + 2G\,\delta_{ik}\delta_{jl} \tag{1.23}$$

$$\gamma_{kl} = \gamma\,\delta_{kl} \tag{1.24}$$

where K is the volume modulus, and G is the shear modulus (rigidity). You can see that the mass balance (1.7) and the elastic law (1.23) determine the density changes:

$$\rho - \rho_{o} = \frac{p - p_{o}}{K} \tag{1.25}$$

For fluids, the connection in (1.25) is introduced independently and is known as the equation of state. In general, it can be nonlinear and include a temperature.

According to theories of hypo-elasticity [220], the connections in (1.20) and (1.21) are valid only for increments $\Delta\sigma_{ij}$, Δe_{kl}, etc. In these more general theories, the coefficients $K, G,$ etc. are functions of the instant state; thus, the laws (1.20), (1.21) and (1.22), must be formulated in rate form

$$\frac{D\sigma_{ij}^{s}}{Dt} = E_{ijkl}\frac{De_{kl}}{Dt}$$

$$\frac{D\sigma_{ij}^{a}}{Dt} = \varepsilon_{ijk}\gamma_{kl}\frac{D\omega_{l}}{Dt} \tag{1.26}$$

where the Oldroyd derivative is used [152]. For an arbitrary tensor ψ_{ij}, the Oldroyd derivative is :

$$\frac{D\psi_{ij}}{Dt} = \frac{\partial\psi_{ij}}{\partial t} + v_{k}\frac{\partial\psi_{ij}}{\partial X_{j}} - \psi_{ik}\omega_{kj} - \psi_{jk}\omega_{ki} + \psi_{ik}\varepsilon_{kj} + \psi_{jk}\varepsilon_{ki} \tag{1.27}$$

In the elastic laws (1.26), the displacement velocity field

$$v_i = \frac{\partial u_i}{\partial t} + v_j \frac{\partial u_i}{\partial X_j} \tag{1.28}$$

is used for determination of the strain-rate tensor

$$\frac{De_{ij}}{Dt} = \frac{1}{2}\left(\frac{\partial v_i}{\partial X_j} + \frac{\partial v_j}{\partial X_i}\right) \tag{1.29}$$

Only in the case of the Oldroyd derivative (1.26), the constitutive laws automatically fulfill any space-time representations; also, the determination (1.29) of the strain rate does not contradict the Almansi formula [220]:

$$e_{ij} = \frac{1}{2}\left(\frac{\partial u_i}{\partial X_j} + \frac{\partial u_j}{\partial X_i} + \frac{\partial u_i}{\partial X_k}\frac{\partial u_j}{\partial X_k}\right) \tag{1.30}$$

which is basic to the nonlinear theories of elasticity and a proper generalization of equation (1.18).

The constitutive law of viscous media

$$\sigma_{ij} = \mu_{ijkl}\frac{De_{kl}}{Dt} \tag{1.31}$$

reflects Newton's idea that stresses are proportional to strain rates. Of course, in conventional theories, σ_{ij} is assumed to be symmetric and it results in permeability of indexes i and j in law (1.31).

1.1.4. BOUNDARY AND DISCONTINUITY CONDITIONS

The formulated balance equations - (1.7), (1.10) and (1.13) - together with the corresponding constitutive laws, represent a mathematical model for a barotropic type of motion which is not needed in a thermal flux study. The differential balances have to be considered with proper boundary conditions, which can be formulated for forces $\sigma_{in} = \sigma_{ij}n_j$ at a cross-section or for displacements u_i either at the surfaces bounding the medium or moving in it. The discontinuities which were generated by material differences - or by special types of motion can be interpreted as a more general case of boundaries.

Consider the general case. The discontinuity moving with velocity U_j separates two parts, $<<+>>$ and $<<->>$, of the fields, and the material crosses the discontinuity. Then, the following balances are formulated at the discontinuity:

$$\rho^{-}\left(v_j^{-}-U_j\right)n_j = \rho^{+}\left(v_j^{+}-U_j\right)n_j \tag{1.32}$$

$$\rho^{-}v_j^{-}\left(v_j^{-}-U_j\right)n_j - \sigma_{ij}^{-}n_j = \rho^{+}v_i^{+}\left(v_j^{+}-U_j\right)n_j - \sigma_{ij}^{+}n_j \tag{1.33}$$

where n_j is the unit normal vector to the discontinuity surface. These balances can be rewritten as normal flux-equalities at moving discontinuities (shocks) with the velocity $U \equiv U_n$:

$$\rho^{-}\left(v_n^{-}-U\right) = \rho^{+}\left(v_n^{+}-U\right) \tag{1.34}$$

$$\rho^{-}v_n^{-}\left(v_n^{-}-U\right)-\sigma_{nn}^{-} = \rho^{+}v^{+}\left(v_n^{+}-U\right)-\sigma_{nn}^{+} \tag{1.35}$$

The variant of (1.34) and (1.35) for weak shocks ($v_n^{-} << v_n^{+} << U$) is known as acoustic approximation:

$$\sigma_{nn}^{-} - \sigma_{nn}^{+} = \rho^{+}v^{+}U \tag{1.36}$$

In a case of fluid dynamics ($\sigma_{ij} \equiv -p\,\delta_{ij}$), it has the form

$$p^{+}-p^{-} \equiv [p] = \rho^{+}v^{+}U \tag{1.37}$$

where the square-bracket symbol denote for the pressure jump.

Only the impulse balance has to be formulated for tangential fluxes

$$\rho^{-}v_\tau^{-}\left(v_n^{-}-U\right) - \sigma_{\tau n}^{-} = \rho^{+}v_\tau^{+}\left(v_n^{+}-U\right) - \sigma_{\tau n}^{+} \tag{1.38}$$

and it coincides with equality of tangential forces

$$\sigma_{\tau n}^{-} = \sigma_{\tau n}^{+} \tag{1.39}$$

if the mass flux through the discontinuity is absent

$$v_n = U \tag{1.40}$$

Condition (1.40) corresponds to the process of replacement of one material by another if $U \neq 0$. In this case, values ρ^{-} and ρ^{+} may not be interconnected at all.

1.2. Thermodynamics and rheology of geomaterials

1.2.1. ENERGY CONSIDERATIONS

If density ρ is sensitive to temperature, the study of thermal states and fluxes is necessary. The corresponding balance of total energies for the elementary volume ΔV - that is, for the differential volume $dx_1 dx_2 dx_3$, has the following[1] form:

$$\frac{\partial}{\partial t}\rho\left(\varepsilon+\frac{v_i v_i}{2}\right)+\frac{\partial}{\partial x_j}\rho\left(\varepsilon+\frac{v_i v_i}{2}\right)v_j = \\ = \frac{\partial \sigma_{ij} v_i}{\partial x_j} + F_i v_i - \frac{\partial q_j}{\partial x_j} + Q \tag{1.41}$$

where ε is the internal energy, Q is internal heat source, and q_j is the thermal flux. Multiplication of impulse balance (1.10) by the displacement velocity gives the balance of the kinetic energy, $\rho v_i v_i / 2$ - that is,

$$\frac{1}{2}\left(\frac{\partial}{\partial t}\rho v_i v_i + \frac{\partial}{\partial x_j}\rho v_i v_i v_j\right) = v_i\frac{\partial \sigma_{ij}}{\partial x_j} + F_i v_i \tag{1.42}$$

The difference of (1.41) and (1.42) gives us the balance of internal energy inside differential volume:

$$\rho\frac{d\varepsilon}{dt} = \sigma_{ij} e_{ij} - \frac{\partial q_j}{\partial x_j} + Q \tag{1.43}$$

$d/dt = \partial/\partial t + v_j(\partial/\partial x_j)$ is a substational derivative which was used earlier for the determination of displacement velocity (1.27). The mass balance (1.7), the definition of strain rate (1.28) and the suggestion of stress-tensor symmetry were used for this expression (1.43) of the first law of thermodynamics.

The second law of thermodynamics introduces the entropy, s, of the medium

---

[1] Further in this book usual symbol x_i is used instead of X_i because the microcoordinate system will not be studied.

$$\rho T\, dS = dW + \left(Q - \frac{\partial q_i}{\partial x_i}\right) dt \tag{1.44}$$

Here, T is the temperature, and $dW \geq 0$ is the irreversible part of internal work. There are two possibilities for identifying dW - that is, the total strain can be treated as the sum of elastic and plastic (irreversible) components:

$$d\,e_{ij} = d\,e_{ij}^{e} + d\,e_{ij}^{p} \tag{1.45}$$

However, the analogous decomposition can be done also for stresses:

$$\sigma_{ij} = \sigma_{ij}^{e} + \sigma_{ij}^{p} \tag{1.46}$$

The traditional rheologic modeling given in Figures 1.3 and 1.4 underlines the difference between (1.45) and (1.46). The expression for dW has two corresponding forms:

$$dW = \sigma_{ij}\, d\,e_{ij}^{p} \tag{1.47}$$

$$dW = \sigma_{ij}^{p}\, d\,e_{ij} \tag{1.48}$$

which give two representations for the entropy increment:

$$\rho T\, ds = \sigma_{ij}\, d\,e_{ij}^{\ p} + \left(Q - \frac{\partial q_i}{\partial x_i}\right) dt \tag{1.49}$$

$$\rho T\, ds = \sigma_{ij}^{p}\, d\,e_{ij} + \left(Q - \frac{\partial q_i}{\partial x_i}\right) dt \tag{1.50}$$

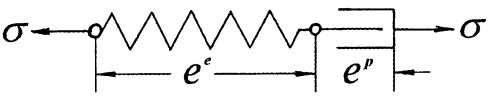

Figure 1.3. Rheological scheme with summation of elastic and plastic strains.

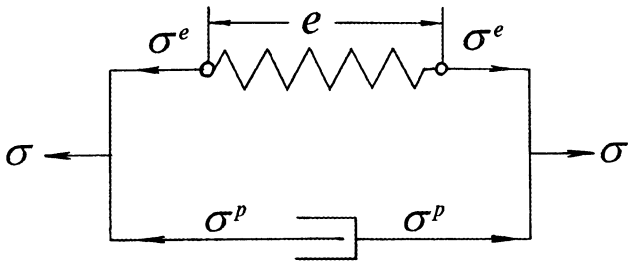

Figure 1.4. Reological scheme with summation of elastic and stresses.

The following combination of the thermodynamic laws - (1.43) and (1.49) - is known as the Gibbs equation:

$$d\varepsilon = \frac{1}{\rho}\sigma_{ij}\, d\, e^{e}_{ij} + T\, ds \tag{1.51}$$

which shows arguments of the internal energy, $\varepsilon = \varepsilon\,(s, e^{e}_{ij})$, as a thermodynamic function in case (1.47) and Figure 1.3.

The free energy, f, can be used instead of the internal energy:

$$df = d\varepsilon - T\, ds - s\, dT \tag{1.52}$$

It is controlled by

$$df = \frac{1}{\rho}\,\sigma_{ij}\, d\, e^{e}_{ij} + s\, dT \tag{1.53}$$

which means that the free energy has measurable arguments - that is, elastic strains and temperature.

The rheology, corresponding to Figure 1.4 and form (1.48), leads to Gibbs equation of the following type

$$d\varepsilon = \frac{1}{\rho}\sigma^{e}_{ij}\, d\, e_{ij} + T\, ds \tag{1.54}$$

and requires the use of the thermodynamical potential, $h = f - (1/\rho)\,\sigma^{e}_{ij} e_{ij}$ - that is

$$dh = \frac{1}{\rho} e_{ij}\, d\sigma^e_{ij} + s\, dT \tag{1.55}$$

Returning to the more conventional rheology (1.51), the quadratic form for the free energy [63]

$$f = \frac{1}{2\rho_o} E_{ijkl}\, e^e_{ij}\, e^e_{kl} - Kz_e(T - T_o)\, e_{ij}\, \delta_{ij} - \frac{C_{hT}}{2} \frac{(T - T_o)^2}{T_o} \tag{1.56}$$

gives the thermo-elastic linear constitutive law

$$\sigma_{ij} = E_{ijkl}\, e^e_{kl} + Kz_e(T - T_0)\, \delta_{ij} \tag{1.57}$$

in accordance with the following sequences of equation (1.53)

$$\frac{1}{\rho}\sigma_{ij} = \frac{\partial f}{\partial e^e_{ij}}, \qquad s = Kz_e e^e_{ij}\delta_{ij} + C_{hT}\frac{(T - T_o)}{T_o} \tag{1.58}$$

Here, z_e is the thermo-dilatation coefficient, C_{hT} is the specific heat capacity (at $T = T_o$), and the tensor E_{ijkl} is expressed by (1.23) for the isotropic case. Using the thermodynamic potential, $h = h(\sigma^e_{ij}, T)$, gives elastic relations analogous to (1.57) but with replacement of e^e_{ij} and σ_{ij} by e_{ij} and σ^e_{ij}, respectively. Thus, (1.57) is a generalization of the elastic law (1.20) and (1.23).

1.2.2. ENTROPY PRODUCTION AND VISCOELASTICITY

Let us now study the opportunities given by the second law - (1.49), (1.50) - of thermodynamics which manifest the entropy growth. Entropy production Π is determined by the following expression:

$$\rho T \Pi \equiv \rho T \frac{ds}{dt} - Q - T\frac{\partial}{\partial x_i}\left(\frac{q_i}{T}\right) = -\frac{dW}{dt} - \frac{q_i}{T}\frac{\partial T}{\partial x_i} \equiv \Sigma X_n I_n \tag{1.59}$$

Here, X_n, I_n are the symbols of thermodynamic forces and fluxes. According to the Onsager theory, linear kinetic relations between X_n and I_n exist as the first approximation [77]. In the case considered here, (1.47) and (1.48) mean, respectively,

$$\frac{De^p_{ij}}{Dt} = B_{ijkl}\sigma_{kl} \tag{1.60}$$

$$e_{ij} = C_{ijkl}\,\sigma^{p}_{kl} \tag{1.61}$$

and rheologic interactions of heat flows and viscous forces are absent because of their different tensor dimensions (the P. Curie principle):

$$q_k = -\kappa\frac{\partial T}{\partial x_i}\,, \qquad \kappa = \frac{A}{T} \tag{1.62}$$

However, the viscosity-coefficient tensor, μ_{ijkl}, of geomaterials is sensitive to temperature. In an isotopic case,

$$\mu_{ijkl} = B_{ijkl}^{-1} = \left(\zeta - \frac{1}{3}\mu\right)\delta_{ij}\,\delta_{kl} + \mu\,\delta_{ik}\,\delta_{jl} \tag{1.63}$$

where μ is the usual shear viscosity, and ζ is the volume viscosity essential for porous geomaterials. For example, concrete possesses $\mu = 10^3\ Pa\cdot s$, limestone $\mu = 10^7\ Pa\cdot s$, salt possesses $\mu = 10^{12}\ Pa\cdot s$ and $\zeta = 10^{12}\ Pa\cdot s$ for asphalt [175].

The temperature dependence of rock viscosity is usually [87] represented by

$$\frac{De_{ij}}{Dt} = B_o \exp\left(-\frac{Q^*}{RT}\right)\left(\frac{\sigma_{ij}}{\sqrt{I_2}}\right)^n \tag{1.64}$$

where Q^* is the activization energy, R is the universal gas constant, $n \geq 1$, and I_2 is the second invariant of the stress tensor. This means that the thermal effects are nonlinear. This effect is essential for intact materials at Earth's depths.

Now, let us formulate constitutive laws for elasto-viscous media, limiting ourselves by introducing by shear properties. Because $\sigma = Ge^e$ and $\sigma = \mu\, De^p / Dt$, the summation according to Figure 1.3 and (1.45) gives the Maxwell rheology [93]:

$$\sigma + \theta\frac{D\sigma}{Dt} = \mu\frac{De}{Dt} \tag{1.65}$$

where $\theta = \mu / G$ is the relaxation time.

In accordance with Figure 1.4 and (1.46), the summation will give us the Voight rheology:

$$\sigma = Ge + \mu\frac{De}{Dt} \tag{1.66}$$

The conventional generalized model is the combination of (1.65) and (1.66):

$$\sigma + \theta\frac{D\sigma}{Dt} = Ge + \mu\frac{De}{Dt} \tag{1.67}$$

This model (1.67) was recommended for describing the elasto-viscous properties of clays and weak soils. However, some dynamic properties discovered in recent experiments [224,231] correspond to a more complicated model, which includes higher time-derivatives.

We can formulate these derivatives for the stress tensor and the strain tensor, including the deviatoric parts, $\tilde{\sigma}_{ij}$ and $\tilde{e}_{ij}$:

$$\sigma_{ij} = -p\,\delta_{ij} + \tilde{\sigma}_{ij} \quad , \qquad e_{ij} = e\,\delta_{ij} + \tilde{e}_{ij} \tag{1.68}$$

in the following forms

$$-p - \sum_{q=1}^{n} a_q \frac{D^q p}{Dt^q} = Ke + \sum_{q=1}^{m} b_q \frac{D^q e}{Dt^q} \tag{1.69}$$

$$\tilde{\sigma}_{ij} + \sum_{q=1}^{n} a_q \frac{D^q \tilde{\sigma}_{ij}}{Dt^q} = 2G\,\tilde{e}_{ij} + \sum_{q=1}^{m} b_q \frac{D^q \tilde{e}_{ij}}{Dt^q} \tag{1.70}$$

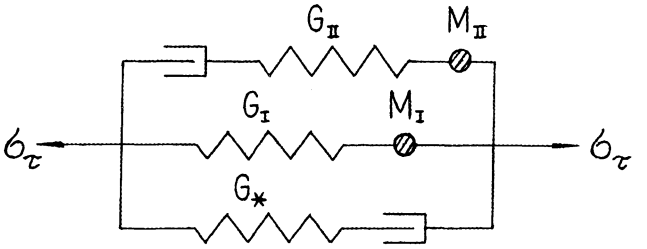

Figure 1.5. Generalized reological model including internal length-scale effect

It can be seen [152] that the case in which n = 3 and m = 5 corresponds to Figure 1.5 - that is, to a combination of the Voight-Maxwell rheology together with introduction two internal concentrated masses, M, with the dimension $[M]=[\rho][L^2]$. Because the impulse itself includes the density, ρ, Figure 1.5 introduces the internal length scale such that

$$d^2 = M/\rho \tag{1.71}$$

This means that the rheology - (1.68) and (1.69) - corresponds to the fragmented media.

1.2.3. THERMODYNAMICS OF SHOCKS

A thermodynamic approach is also necessary for finding energy changes at discontinuities. The corresponding balance

$$\rho^{-}\left(\varepsilon^{-}+\frac{v_i^{-}v_i^{-}}{2}\right)\left(v_j^{-}-U_j\right)n_j \;-\; \sigma_{ij}^{-}v_i^{-}n_j = \tag{1.72}$$

$$= \rho^{+}\left(\varepsilon^{+}+\frac{v_i^{+}v_i^{+}}{2}\right)\left(v_j^{+}-U_j\right)n_j \;-\; \sigma_{ij}^{-}v_i^{+}n_j$$

has to be added to the mass (1.32) and impulse (1.33) balances.

The specific volume, $V = 1/\rho$, of the material, instead of density, is often used for moving shocks. Then the state equation necessary for studies of shock condition can be formulated [232] as

$$\varepsilon = \varepsilon^{o}(V) + \frac{V}{\Gamma(V)}(p-p_0) \tag{1.73}$$

where $\varepsilon^0, p^0 = -\partial\varepsilon^0/\partial V$ are the "cold" energy and pressure (at 0^0K), and $\Gamma = \Gamma_0(V/V_0)$ is the Gruneisen coefficient. The data for parameters Γ_0, V_0 and for the function $\varepsilon^0(V)$ are readily available for many materials in texts on physics.

In practice, the characteristic condition for very strong underground shocks is measured in the form of dependence of shock-front velocity, U, on the mass velocity, v, behind the shock:

$$U = U_0 + Bv \tag{1.74}$$

Breaks of this linear form are treated as phase transitions at the proper pressure levels. Another accepted form of shock adiabate (1.74) is known as the Hugoniot adiabat:

$$p_H = p_H(V_H) \;, \qquad \varepsilon_H(V_H) = \frac{1}{2}p_H(V_0-V_H) \tag{1.75}$$

and is often used to describe shocks in gas dynamics.

The first relation (1.75) can be measured experimentally - as well as (1.74). The second one is a consequence of the balance (1.72) together with (1.33) and (1.34).

The negligible role of the stress deviator is argued in such cases by extremely high pressures under intense shock conditions. However, this hydrodynamic description is not sufficient for minor stress levels. Moreover, if the equation of state can be formulated only in a rate form, the shock depends on motion out of shock and is essential for intense explosions in dilating geomaterials.

1.3. Dilatant elasto-plasticity of geomaterials

1.3.1. FRICTION AND DILATANCY CONCEPTS

The irreversible deformation of geomaterials is generated by microslips and microcracks of the polycrystalline and granular strata structure. Every elementary act of deformation is connected with the overcoming of bonds or solid friction as governed by the Coulomb law [44]

$$|R| = N\, tg\varphi_c + chs \tag{1.76}$$

where R is the tangential force, N is the normal force acting at the slip contact, φ_c is the contact friction angle, and chs is the cohesion.

Implicitly, it is suggested that the limit condition (1.76) valid in reality at a number of grain contacts corresponds to the bulk limit state formulated for stress invariants in a form of the yield continuum condition:

$$\Phi_\sigma \equiv |\sigma_\tau| - \alpha\, p - Y = 0 \tag{1.77}$$

Here, pressure p and shear stress intensity σ_τ are involved, and Y is the yield value, α is the internal-friction coefficient. If the yield condition is valid, irreversible (plastic) deformation takes place.

According to rule (1.60), irreversible strain-rate must be determined by the nonassociative flow rule [144]

$$\frac{De_{ij}^{\,p}}{Dt} = -\,(p+H)\,\delta_{ij}\frac{D\xi}{Dt} + (\sigma_{ij} + p\,\delta_{ij})\,\frac{D\lambda}{Dt} \tag{1.78}$$

which contains two unknown scalar functions: $D\xi/Dt$ and $D\lambda/Dt$. These scalar functions have to equal zero if the condition (1.77) is not satisfied; then, the deformation process is pure elastic.

If the limit condition (1.77) is fulfilled, it must be considered together with the balance equations and, therefore, will determine one of the mentioned scalars. So, one more condition is necessary to determine the second scalar function. This condition has to reflect the kinematic connection of volume and shear increment strains (Figure 1.6) typical of granular materials, found qualitatively by O. Reynolds in 1885 and named by him as the dilatancy. Quantitatively, it has to have a connection between invariants of the irreversible strain-rate tensor [143]:

$$\Phi_\varepsilon = \frac{De_{ij}^{\,p}}{Dt}\delta_{ij} - \Lambda\left|\frac{D\gamma^p}{Dt}\right| = 0 \tag{1.79}$$

where Λ is the dilatancy rate (coefficient), and γ^p is the plastic shear intensity.

On the microscale level, the dilatant behavior can be explained by the repacking of discs from a dense to loose state, with the distance between their centers being constant (Figure 1.6). This is a sufficient explanation for soils and polycrystalline rocks with weak bonds.

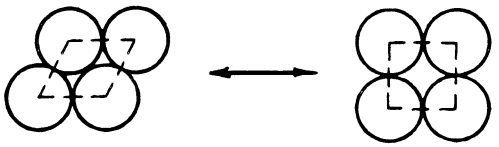

Figure 1.6. Dilatancy can be explained as repacking of discs in contacts according to O.Reynolds(1885).

In the case of fracturing with the same length scale as the mineral grain diameter, the dilatancy process is illustrated by growth of tensile cracks under the usual shear (Figure1.7).

Phenomenologically, the dilatant process is described by the dilatancy rule (1.79) with $\Lambda \geq 0$. The case $\Lambda < 0$ corresponds to plastic enhancement of pore collapse.

The exclusion of $D\xi / Dt$ from (1.78) with the help of the dilatancy condition (1.79) permits the use of only one additional unknown scalar function, $D\lambda / Dt$.

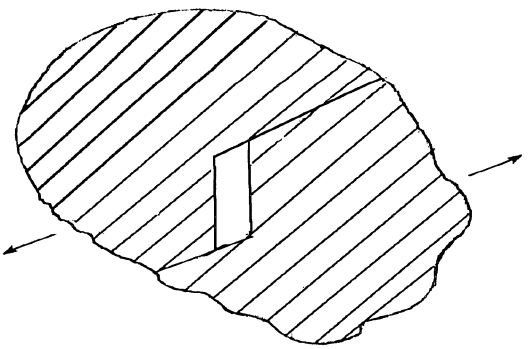

Figure 1.7. Crack dilating during shear [209].

1.3.2. PLASTIC FLOW RULES

The idealized case of equality of the coefficients α and Λ corresponds to the so-called associative rule [56]:

$$\frac{De_{ij}^{\ p}}{Dt} = \frac{\partial \Phi_\sigma}{\partial \sigma_{ij}} \frac{D\lambda}{Dt} \tag{1.80}$$

Which was found to be valid for metal plasticity, where $\alpha = \Lambda = 0$ [140]. However, experiments have shown that $\alpha > \Lambda$ for all known geomaterials (sands, rocks, polycrystalline ice). Correspondingly, the plastic potential $\Psi(\sigma_{ij})$ such that

$$\frac{De_{ij}^{\ p}}{Dt} = \frac{\partial \Psi}{\partial \sigma_{ij}} \frac{D\lambda}{Dt} \tag{1.81}$$

cannot coincide with the yield function Φ_σ [144].

The yield surface typical for geomaterials is represented (Figure 1.8) in the plane of the stress invariants σ_τ, p as a number of straight lines. Every solid line corresponds to the instant limit condition (1.77); broken lines correspond to plastic isopotential surfaces

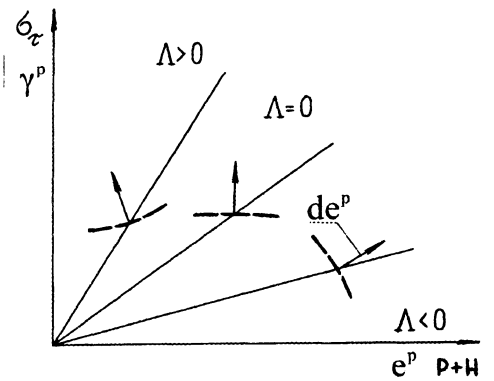

Figure 1.8. Representation of yield surfaces with plastic strain increments (arrows).

$$\Psi = \sigma_\tau^2 - 2\,\alpha\Lambda\,(p+H)^2 = \sigma_\tau^0(p_0+H)(\alpha-\Lambda) \tag{1.82}$$

and vectors correspond to plastic strain increments. The process of geomaterial plastic compaction ($\Lambda < 0$) leads to pore closure, to internal friction, α, and cohesion coefficient, H, growth. Correspondingly, the solid line moves up to the so-called critical

state ($\Lambda = 0$). The plastic-loosening process ($\Lambda > 0$) creates new pores and diminishes internal friction and cohesion [152].

It is necessary, therefore, to treat plastic states as being instant and depending on the additional hardening (softening) parameter χ: $\alpha = (\chi)$, $Y = Y(\chi)$. The plastic active process with hardening is determined correspondingly by the following conditions:

$$\Phi_\sigma(p, \sigma_\tau, \chi) = 0 \quad , \qquad d'\Phi_\sigma = \frac{\partial \Phi_\sigma}{\partial p} dp + \frac{\partial \Phi_\sigma}{\partial \sigma_\tau} d\sigma_\tau > 0 \tag{1.83}$$

In the case of softening, there are two conditions:

$$\Phi_\sigma(p, \sigma_\tau, \chi) = 0, \qquad d'\Phi_\sigma = \frac{\partial \Phi_\sigma}{\partial p} dp + \frac{\partial \Phi_\sigma}{\partial \sigma_\tau} d\sigma_\tau < 0 \tag{1.84}$$

Neutral loading is determined by

$$\Phi_\sigma(p, \sigma_\tau, \chi) = 0 \quad , \qquad d'\Phi_\sigma = 0 \quad , \qquad d\lambda = 0 \tag{1.85}$$

and the unloading process is determined by

$$\Phi_\sigma < 0 \quad , \qquad d\lambda = 0 \tag{1.86}$$

Becouse plastic-volume deformation (Figures 1.9 and 1.10)

$$e_{ij}^{\ p} \delta_{ij} = e^p = \chi \tag{1.87}$$

is a measurable value of the irreversible change of porosity, the hardening parameter χ can be identified with it. Another possibility is to use the plastic shear strain

$$\chi = \gamma^p$$

which is equivalent approximately to (1.87) because of the dilatancy condition (1.79). However, the value γ^p is much more difficult to measure than e^p.

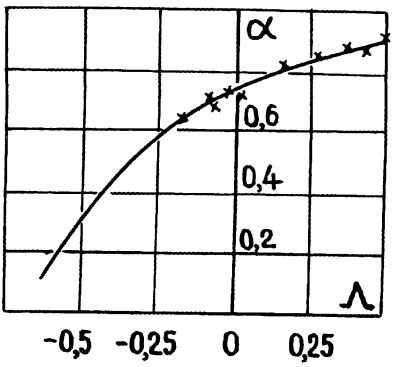

Figure 1.9. Solid friction, α, and dilatancy, Λ, coefficients for river quartz sands as functions of the same state parameter.

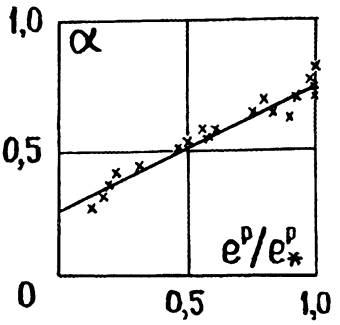

Figure 1.10. Usage of plastic volume deformation (irreversible porosity increments) as hardening parameter, χ.

Conditions (1.82) through (1.85) contain the following increment

$$d'\Phi \equiv (\partial\Phi_\sigma / \partial\chi)d\chi \tag{1.88}$$

and reflect the yield surface changes with plastic deformation.

The constitutive law (1.78) is the incremental flow rule, and it cannot be integrated separately from the equilibrium equations - that is, the constitutive law of plasticity is nonholonomic [144]. Only in the case of proportional loading (to any single parameter)

at all boundaries (for example, $\sigma_{ij} n_j = f_i(t)$) the corresponding state equation may be found, but it will be not the same one for other variants of boundary conditions.

The total strains, e_{ij}, are determined by rule (1.45), where the elastic components are governed by Hooke's law - (1.20) and (1.22). In isotropic cases one has:

$$d\sigma_{ij} = \left(K - \frac{2}{3} G \right) \delta_{ij} de^e + 2G de^e_{ij} \tag{1.89}$$

1.3.3. EXPERIMENTAL DILATANCY OF ROCKS

Let us examine, the typical process of triaxial deformation of limestone sample, represented in Figure 1.11. In this type of testing, the axial stress, σ_1, and confining pressure, $p_* = -\sigma_3$, can be changed independently. You can see that initial hydrostatic loading ($\sigma_1 = \sigma_3 = -p_*$) diminishes pore space and, thus, volume strains are negative. The further loading is nonproportional because the axial force, σ_1, increases, although the confining pressure, p_*, is kept constant. This type of loading is characteristic for stress anisotropy and enhances pore collapse.

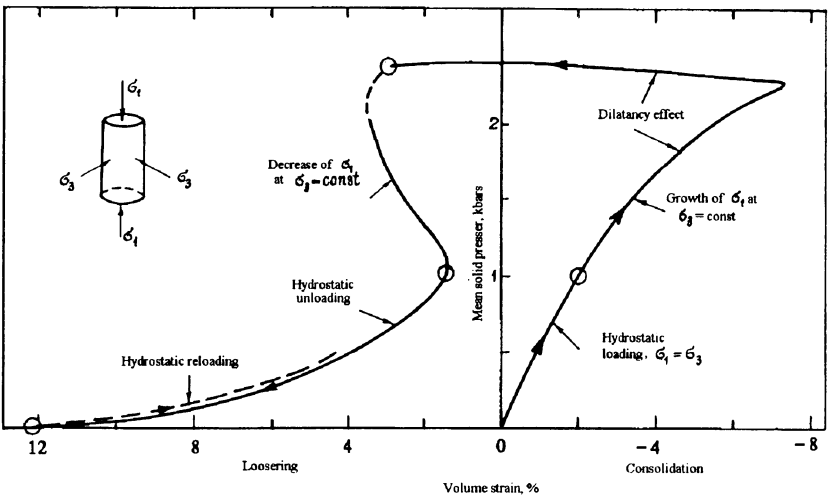

Figure 1.11. Limestone triaxial testing performed by Terra-Tek Corporation, Salt Lake City (Courtesy of S. J. Green).

When the pore volume reaches a certain level, an important change takes place - that is, compaction is replaced by loosening because of dilatancy process. Diminishing the axial stress component σ_1 means the cessation of further plastic deformation, although elastic deformation continues in accordance with the unloading process. In the first stage of the unloading $\sigma_3 = const$; however at the second stage, $\sigma_1 = \sigma_2$, and both are diminishing. The elastic nature of the corresponding stresses are proven by the coincidence of the unloading and reloading paths (broken line).

The complexity of Figure 1.11 means that each loading process of a dilatant material must be characterized by two stress parameters: p and σ_τ.

In Figure 1.12, the dilatancy of granite is presented as a function of a shear stress inensivity, σ_τ for the constant pressure level.

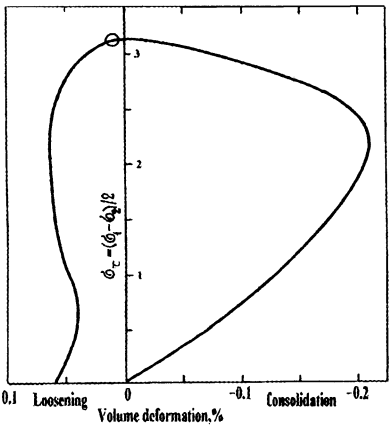

Figure 1.12. Triaxial test of granite Westerly performed by Terra-Tek Corporation, Salt Lake City (Courtesy of S. J. Green).

1.3.4. PLANE PLASTICITY

For planar problems, the yield condition (1.77) has the following form:

$$\frac{1}{2}\sqrt{(\sigma_{xx}-\sigma_{yy})^2+4\sigma_{xy}^2}+\frac{\sigma_{xx}+\sigma_{yy}}{2}\sin\varphi = H\sin\varphi \tag{1.90}$$

which uses the angle φ of internal bulk friction. Here, $\alpha = \sin\varphi$, $Y = H\sin\varphi$, and

$$p = -\frac{\sigma_{xx} + \sigma_{yy}}{2} \quad , \qquad \sigma_\tau = \frac{1}{2}\sqrt{(\sigma_{xx} - \sigma_{yy}) + 4\sigma_{xy}^2} \tag{1.91}$$

Using the Cartesian coordinates x, y, turned at angle ψ relative to the direction of the main stress components,

$$tg\psi = \frac{2\sigma_{xy}}{\sigma_{xx} - \sigma_{yy}} \tag{1.92}$$

the stress state can be expressed only in terms of pressure and the angle ψ [140]

$$\begin{aligned} \sigma_{xx} &= H - (p + H)(1 - \sin\varphi\cos 2\psi) \\ \sigma_{yy} &= H - (p + H)(1 + \sin\varphi\cos 2\psi) \\ \sigma_{xy} &= (p + H)\sin\varphi\sin 2\psi \end{aligned} \tag{1.93}$$

and the limit condition (1.90) will be satisfied.

For planar problems, the dilatancy connection (1.79) can be transformed to

$$d\,e_{xx}^{\,p} + d\,e_{yy}^{\,p} = \sin\nu\sqrt{(d\,e_{xx}^{\,p} - d\,e_{yx}^{\,p})^2 + 4(d\,e_{xy}^{\,p})^2} \tag{1.94}$$

where ν is the dilatancy angle. The condition of the collinearity of the stress and the strain increment tensor must also be used

$$\frac{De_{xy}^{\,p}}{Dt} = \left(\frac{De_{xx}^{p}}{Dt} - \frac{De_{yy}^{p}}{Dt}\right) tg\psi \tag{1.95}$$

where the angle ψ of relation (1.95) is the same one as in relation (1.92).

If we consider the idealized case when the elastic part of strains are negligible

$$\frac{D\,e_{ij}}{Dt} \equiv \frac{D\,e_{ij}^{p}}{Dt} = \frac{1}{2}\left(\frac{\partial v_i}{\partial x_j} + \frac{\partial v_j}{\partial x_i}\right) \tag{1.96}$$

then,

$$tg\psi = \frac{2\sigma_{xy}}{\sigma_{xx} - \sigma_{yy}} = \left(\frac{\partial v_x}{\partial x} + \frac{\partial v_y}{\partial y}\right) \Big/ \left(\frac{\partial v_x}{\partial x} - \frac{\partial v_y}{\partial y}\right) \tag{1.97}$$

and total changes of density ρ can be interpreted as increments of the hardening parameter χ. Therefore, the mass balance equations (1.7) have to be added to the equilibrium equations (1.10). They have the following form for planar problems

$$\frac{d\rho}{dt} + \rho\left(\frac{\partial v_x}{\partial x} + \frac{\partial v_y}{\partial y}\right) = 0 \tag{1.98}$$

$$\frac{\partial \sigma_{xx}}{\partial x} + \frac{\partial \sigma_{xy}}{\partial y} = 0 \tag{1.99}$$

$$\frac{\partial \sigma_{yx}}{\partial x} + \frac{\partial \sigma_{yy}}{\partial y} = 0 \tag{1.100}$$

where the stress symmetry is assumed for simplicity - that is $\sigma_{xy} \equiv \sigma_{yx}$.

If representation (1.93) is used, the equilibrium equations follow [152]

$$\begin{aligned}(1 - \sin\varphi\cos 2\psi)\frac{\partial p}{\partial x} + \sin\varphi\sin 2\psi\frac{\partial p}{\partial y} + \\ \left\{-\cos 2\psi\frac{\partial \psi}{\partial x} + \sin 2\psi\frac{\partial \rho}{\partial y}\right\}\frac{\partial}{\partial \rho}\{(p+H)\sin\varphi\} - \\ 2(p+H)\sin\varphi\left\{\sin 2\psi\frac{\partial \psi}{\partial x} + \cos 2\psi\frac{\partial \psi}{\partial y}\right\} = 0,\end{aligned} \tag{1.101}$$

$$\begin{aligned}\sin\varphi\sin 2\psi\frac{\partial p}{\partial x} + (1 + \sin\varphi\cos 2\psi)\frac{\partial p}{\partial y} - \\ \left\{\sin 2\psi\frac{\partial \rho}{\partial x} - \cos 2\psi\frac{\partial \rho}{\partial y}\right\}\frac{\partial}{\partial \rho}\{(p+H)\sin\varphi\} + \\ 2(p+H)\sin\varphi\left\{\cos 2\psi\frac{\partial \psi}{\partial x} - \sin 2\psi\frac{\partial \psi}{\partial y}\right\} = 0,\end{aligned} \tag{1.102}$$

where the unknown variables are ψ, p and ρ. If the hardening effect is not essential,

$$(\partial / \partial\rho)\{(p+H)\sin\varphi\} = 0,$$

and the equilibrium equations can be solved independently of the kinematic equations. The corresponding works are known as the limit statics [205] of geomaterials. However, in the most practical cases, the boundary conditions are formulated for

displacements. In addition, the hardening effect is extremely important for dilating geomaterials.

Let us formulate effective kinematic equations. The dilatancy condition (1.94) can be rewritten as:

$$\frac{\partial v_x}{\partial x}+\frac{\partial v_y}{\partial y}=\sin\nu\sqrt{\left(\frac{\partial v_x}{\partial x}-\frac{\partial v_y}{\partial y}\right)^2+\left(\frac{\partial v_x}{\partial y}+\frac{\partial v_y}{\partial x}\right)^2} \tag{1.103}$$

Using the angle ψ as one of unknown variables can transform collinearity (1.97) and dilatancy (1.103) conditions to field equations for displacement velocities:

$$(\cos 2\psi-\sin\nu)\frac{\partial v_x}{\partial x}+(\cos 2\psi+\sin\nu)\frac{\partial v_y}{\partial y}=0 \tag{1.104}$$

$$\sin 2\psi\frac{\partial v_x}{\partial x}+\sin\nu\frac{\partial v_x}{\partial y}+\sin\nu\frac{\partial v_y}{\partial x}+\sin 2\psi\frac{\partial v_y}{\partial y}=0 \tag{1.105}$$

These equations are linear if ψ is known from equilibrium equations (1.101), (1.102).

1.3.5. SLIP SURFACE CONDITIONS

The main problem of the theory is to find slip surfaces which are created due to localization of plastic shear into thin bands. The localization process was studied by J. Rudnicki and J. Rice [186], who identified it with the bifurcation of deformation inside a plane band. Besides the dilatant elastoplastic pressure-sensitive model [144] was supposed to be valid inside the band [186] and it was assumed also that there is no stress-strain changes outside the band. However, it is only valid initially because, in reality, slip-surface appearance changes the stress distribution. For example, the bulk plasticity can disappear totally after a slip surface is created.

According to Coulomb, the limit condition (1.76) can be formulated for the slip surface

$$|\sigma_{\tau n}|=\sigma_{nn}\,tg\,\varphi_s+chs_s \tag{1.106}$$

and has to be valid for the case of a tangential relative motion of edges <<+>> and <<->>, which are in contact at the slip surface. Here φ_s is the solid friction angle along the slip surface, and the cohesion, chs_s, is the asperity strength. Moreover, it is not at all necessary to have plastic states (1.77) inside the edges.

The continuity condition for forces at the slip plane are:

$$[\sigma_{nn}]\equiv\sigma_{nn}^{+}-\sigma_{nn}^{-}=0 \tag{1.107}$$

$$[\sigma_m] \equiv \sigma_m^+ - \sigma_m^- = 0 \tag{1.108}$$

Implicitily, the slip along the Coulomb surface means the possibility of tangential velocity discontinuity:

$$[v_\tau] \equiv v_\tau^+ - v_\tau^- \neq 0 \tag{1.109}$$

Let us now consider the case of plastic fields with symmetrical stress tensors but different internal frictions in parts adjoining the slip surface. Introduction of expression (1.93) into force balances (1.107) and (1.108) gives the following two relations:

$$(p^+ + H)(1 + \sin\varphi^+ \cos 2\psi^+) = (p^- + H)(1 + \sin\varphi^- \cos 2\psi^-) \tag{1.110}$$

$$(p^+ + H)\sin\varphi^+ \sin 2\psi^- = (p^- + H)\sin\varphi^- \sin 2\psi^- \tag{1.111}$$

These can be reduced to the connection between inclination angles ψ^+ and ψ^- of the slip surface to the main compression:

$$\sin\varphi^+ \sin 2\psi^+ - \sin\varphi^- \sin 2\psi^- + \sin\varphi^+ \sin\varphi^- \sin 2(\psi^+ - \psi^-) = 0 \tag{1.112}$$

We need to remember that, in a plastic field, the tangential jump of displacement velocity (1.109) could be realized only, [158], along the characteristics of the velocity field due to linear-type equations (1.104) and (1.105). The velocity characteristics are inclined to the main compression at the angle:

$$\psi^- = \frac{\pi}{4} - \frac{\nu^-}{2} \tag{1.113}$$

In the simplest case of the constant bulk solid friction angle φ and dilatancy angle ν outside of the slip surface,

$$\varphi = \varphi^+ = \varphi^-, \tag{1.114}$$

$$\nu = \nu^+ = \nu^- \tag{1.115}$$

the relation (1.112) has the form:

$$\cos(\psi^+ - \psi^-) = \cos(\psi^- - \psi^+)\sin\varphi \tag{1.116}$$

and the following expression can be found

$$\psi^{+} = \pm\left(\frac{\pi}{4} - \theta\right) + k\pi \tag{1.117}$$

where

$$\theta = arctg\,\frac{\sin\varphi - tg(\nu/2)}{1 - tg(\nu/2)} \tag{1.118}$$

Moreover, the normal ($\sigma^{+}_{nn} = \sigma^{-}_{nn}$) and the tangential ($\sigma^{+}_{\tau n} = \sigma^{-}_{\tau n}$) force components at the slip surface

$$\sigma^{+}_{nn} = H - (p^{+} + H)(1 + \sin\varphi\sin\nu) \tag{1.119}$$

$$\sigma^{+}_{\tau n} = (p^{+} + H)\sin\varphi\cos\nu \tag{1.120}$$

will satisfy the Coulomb limit condition (1.106) if [46,158]

$$tg\varphi_s = \frac{\sin\varphi\cos\nu}{1 - \sin\varphi\sin\nu} \tag{1.121}$$

$$chs_s = H\,tg\varphi_s \tag{1.122}$$

Thus, (1.121) is equivalent to the following expression [120]:

$$\sin\varphi_s = \cos(\varphi_s - \nu)\sin\varphi \tag{1.123}$$

The real slip occurs along the Coulomb surface with the surface solid friction angle φ_s which is smaller than the bulk value φ; therefore, the bearing capacity of a body decreases due to slip-surface appearance (Figure 1.13).

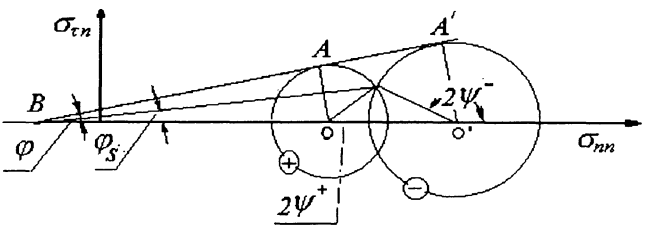

Figure 1.13. Stress conditions at slip surface as the Morh circles intersection.

The stress conditions at the slip surface are, shown in Figure 1.13 as a crossing of two Mohr circles (see Section 1.4); bulk, φ, and surface, φ_s, solid friction angles are also

shown. Bulk plastic states inside both edges in contact are shown here by the circle touching line BA with the solid friction angle φ.

1.3.6. DILATANCY INSIDE THE LOCALIZATION BAND

Mathematically, slip surfaces are thin zones, of high-gradient change. Let us suppose that the same equations of dilatant plasticity (1.93), (1.103) are valid inside these zones [202] and that the axis x_1 is tangential to the band, and the axis x_2 is in a normal direction to it. Because the band is narrow and the shear is intensive, the prevailing velocity gradients across the band,

$$\frac{\partial v_2}{\partial x_2}, \frac{\partial v_1}{\partial x_2} \quad >> \quad \frac{\partial v_2}{\partial x_1}, \frac{\partial v_1}{\partial x_1}$$

In this case, the dilatancy condition (1.103) reduces to the ordinary equation

$$\frac{d v_2}{d x_2} = \sin \nu \sqrt{\left(\frac{d v_2}{d x_2}\right)^2 + \left(\frac{d v_1}{d x_2}\right)^2} \tag{1.124}$$

which determines the proportionality of velocity-component increments:

$$dv_2 / dv_1 = tg\nu \tag{1.125}$$

The integration of equation (1.125) across the thickness of the shear band gives the following result if the dilatancy angle is constant:

$$[v_2] = [v_1]\, tg\nu \tag{1.126}$$

So, the jump of tangential velocity

$$[v_1] = v_1(+h) - v_1(-h)$$

which is nonequal to zero at the slip surface, has to be accompained by the jump of its normal component

$$[v_2] = v_2(+h) - v_2(-h)$$

where $2h$ is the band thickness. The shear band can increase or decrease its thickness during slip, depending on the sign of dilatancy. As a result, there is a tendency to diminish internal friction inside the band or, in other words, the effective Coulomb friction at the slip surface.

1.4. Particle rotation effects in granulated materials

1.4.1. THE MOHR CIRCLE FOR ASYMMETRIC STRESSES

Let us consider the equilibrium of triangle ABC with sides AB and BC corresponding to coordinate lines $x = const$, $y = const$ (Figure 1.14).

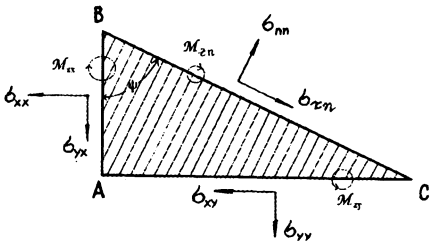

Figure 1.14. Stress equilibrium taking into account asymmetry, $\sigma_{yx} \neq \sigma_{xy}$, and couple stresses, $\mathcal{M}_{zx}$, $\mathcal{M}_{zy}$, $\mathcal{M}_{zn}$.

If the side lengths of triangle ABC are also taken into account, two balance equations can be written for the x and y - components of force [140]:

$$\sigma_{nn}\cos\psi + \sigma_{tn}\sin\psi = \sigma_{xx}\cos\psi + \sigma_{xy}\sin\psi \tag{1.127}$$

$$\sigma_{nn}\sin\psi - \sigma_{tn}\cos\psi = \sigma_{xx}\sin\psi + \sigma_{yx}\cos\psi \tag{1.128}$$

These equations can be transformed to:

$$\sigma_{nn} = \frac{\sigma_{xx} - \sigma_{yy}}{2} + \frac{\sigma_{yy} - \sigma_{xx}}{2}\cos 2\psi + \frac{\sigma_{xy} + \sigma_{yx}}{2}\sin 2\psi \tag{1.129}$$

$$\sigma_{tn} = \frac{\sigma_{yy} - \sigma_{xx}}{2}\sin 2\psi + \frac{\sigma_{xy} - \sigma_{yx}}{2} - \frac{\sigma_{xy} - \sigma_{yx}}{2}\cos 2\psi \tag{1.130}$$

If the angle ψ is excluded, then the quadratic algebraic equation can be found:

$$\left(\sigma_{nn} - \frac{\sigma_{xx} + \sigma_{yy}}{2}\right)^2 + \left(\sigma_{tn} - \frac{\sigma_{xy} - \sigma_{yx}}{2}\right)^2 = \left(\frac{\sigma_{yy} - \sigma_{xx}}{2}\right)^2 + \left(\frac{\sigma_{xy} + \sigma_{yx}}{2}\right)^2 \tag{1.131}$$

which generalizes Mohr's geomaterial interpretation [140]. We can see here, pressure $p^{-} = -(\sigma_{xx} + \sigma_{yy}) / 2$ for planar problems and, instead of the second invariant, (1.91) the asymmetrical generalization:

$$\sigma_\tau = \sqrt{\left(\frac{\sigma_{yy} - \sigma_{xx}}{2}\right)^2 + \left(\frac{\sigma_{xy} + \sigma_{yx}}{2}\right)^2} \tag{1.132}$$

So, it is possible to rewrite relation (1.131) as follows:

$$(\sigma_{nn} - a_\sigma)^2 + (\sigma_{\tau n} - b_a)^2 = R_\sigma^2 \tag{1.133}$$

where:

$$a_\sigma = p = -\frac{\sigma_{xx} + \sigma_{yy}}{2} \quad , \quad b_\sigma = \sigma^a = \frac{\sigma_{xy} - \sigma_{yx}}{2} \quad , \quad R_\sigma = \sigma_\tau \tag{1.134}$$

The stress conditions at any cross-section of the solid body belong to the circle presented in Figure 1.15.

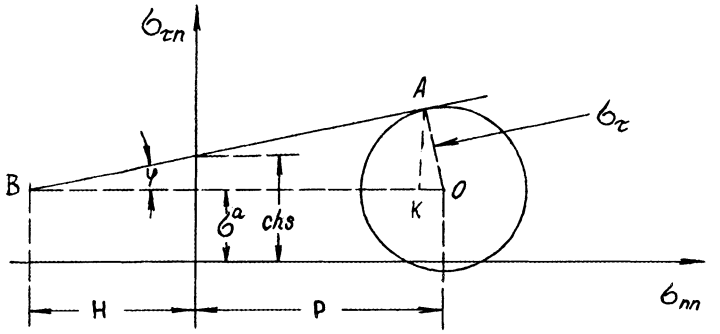

Figure 1.15. The Mohr stress circle moves upward in the asymmetric case [193].

In the case of stress symmetry, $\sigma^a = 0$, the center O is at the axis σ_{nn} ; the bulk yield condition (1.90), formulated earlier as a linear relation between invariants of stress-tensor, can now be interpreted as a limit relation between the radius and the center coordinates of the Mohr circle.

The limit line *BA* can be introduced as the yield condition (in Figure 1.15) for asymmetrical stress tensor; hence, the limit condition (1.90) will be generalized to

$$|\sigma_\tau| - p \sin\varphi + |\sigma_a| \cos\varphi - chs \cos\varphi = 0 \tag{1.135}$$

Stresses at the cross-section, corresponding to point A, are limited by the Coulomb condition

$$|\sigma_{\tau}| + \sigma_{nn} tg\varphi = chs \tag{1.136}$$

where $H\ tg\varphi = chs - \sigma_a$.

However, if $\sigma_{xy} \neq \sigma_{yx}$ the triangle ABC (in Figure 1.14) can rotate as a whole and must be prevented by the couple-stresses, $\mathcal{M}_{ij}$, distributed over its sides.

The corresponding moment-of-momentum balance must now be introduced

$$\Delta_{zn} \equiv \mathcal{M}_{zn} - \mathcal{M}_{zy} \cos\psi - \mathcal{M}_{zx} \sin\psi = \frac{h}{\sqrt{2}}(\sigma_{yx} - \sigma_{xy}) \sin 2\psi \tag{1.137}$$

Here, Δ_{zn} is the disbalance of the couple-stresses, which equalize the asymmetry of conventional stresses. Because the balance equations - (1.127), (1.128) and (1.137) - are formulated for the vicinity of the point A, the characteristic size h of triangle ABC has to be infinitely small, but not smaller than the microstructure scale d (for example, the mineral grain diameter) which is implicitly included in the couple-stresses $\mathcal{M}_{zn}$. If $h << d$, the intact solid material inside grains is considered; here, it is supposed to be devoid of microstructure. The symmetric mechanics is also valid if d / h is negligible - that is, if the granular microstructure is absent ($h = d$).

1.4.2. STRESS-SPACE CURVE

As you can see, the balance equations - (1.127), (1.128) and (1.137) - determine a space curve (Figure 1.16) in the coordinate system σ_{nn}, σ_{τ}, $\mathcal{M}_{zn}$, which is a generalization of the Mohr plane for a nonsymmetric case. This curve depend on a single parameter ψ and has a radius-vector [72]

$$\vec{r} = (a_\sigma \cos 2\psi - c_\sigma \sin 2\psi)\,\vec{i} + (a_\sigma \sin 2\psi - c_\sigma \cos 2\psi)\,\vec{j} + b_\sigma \sqrt{2} \sin 2\psi \vec{k} \tag{1.138}$$

where the notations (1.134) are used together with

$$c_\sigma = (\sigma_{xy} + \sigma_{yx})/2 \tag{1.139}$$

and $\vec{i}$, $\vec{j}$, $\vec{k}$ are the unit axial vectors of the space.

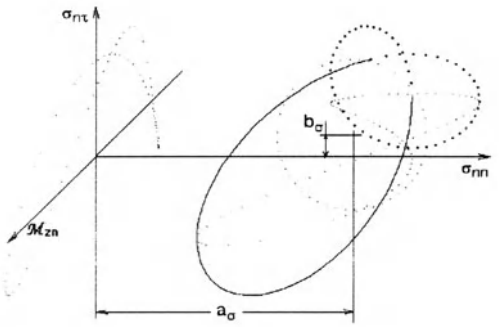

Figure 1.16. Space curve representing the stress state in the case of nontrivial moment-of-momentum.

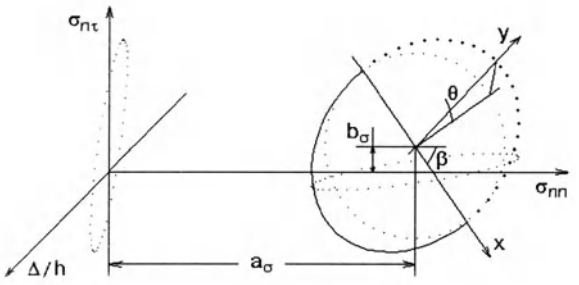

Figure 1.17. The elliptic cross-section of the cylinder characterizing the stress-state inside geomaterials.

The derivative of $\vec{r}$ with respect to ψ

$$\frac{\partial \vec{r}}{\partial \psi} = 2\left(-a_\sigma \sin 2\psi + c_\sigma \cos 2\psi\right)\vec{i} + 2\left(a_\sigma \cos 2\psi + c_\sigma \sin 2\psi\right)\vec{j} + 2\, b_\sigma \sqrt{2} \cos 2\psi \vec{k} \tag{1.140}$$

determines the vector tangential to the curve (1.138). Vectorial multiplication of (1.138) and (1.140) determines the normal to the plane created by $\vec{r}$ and $d\vec{r} / d\psi$. As can be seen, this normal is independent of the angle ψ:

$$\vec{n}_r = \vec{r} \times (\partial \vec{r} / \partial \psi) = -b_\sigma c_\sigma \vec{i} - a_\sigma b_\sigma \vec{j} + \left(a_\sigma^2 + b_\sigma^2\right)\vec{k} \tag{1.141}$$

Consequently, as (Figure 1.17) shows, the curve (1.138) lies in the plane oriented orthogonal to the normal (1.141); the plane equation is:

$$b_\sigma \sqrt{2}(c_\sigma \sigma_{nn} + a_\sigma \sigma_{\tau n}) - (a_\sigma^2 + b_\sigma^2)(\Delta_{zn} / h) = a_\sigma b_\sigma (b_\sigma + c_\sigma)\sqrt{2} \qquad (1.142)$$

So, the space curve (1.138) is really the plane curve and, moreover, the ellipse:

$$\frac{x^2}{I^2} + \frac{y^2}{D^2} = 1 \qquad (1.143)$$

Here,

$$x = (\sigma_{nn} - a_\sigma)\cos\beta + (\sigma_{n\tau} - b_a)\sin\beta\cos\theta + \frac{\Delta_{zn}}{h}\sin\beta\cos\theta,$$

$$y = -(\sigma_{nn} - a_\sigma)\sin\beta + (\sigma_{n\tau} - b_\sigma)\cos\beta\cos\theta + \frac{\Delta_{zn}}{h}\cos\beta\sin\theta, \qquad (1.144)$$

$$I^2 = J_2 + \frac{1}{4}(\sigma_{yx} - \sigma_{xy})^2 \quad , \quad D^2 = J_2$$

and the Euler angles β and θ are used:

$$\beta = arctg\frac{\sigma_{\tau n} - b_\sigma}{\sigma_{nn} - a_\sigma} \quad , \quad \theta = arctg\, b_\sigma\sqrt{\frac{2}{J_2}} \qquad (1.145)$$

This ellipse has invariants

$$\frac{1}{I^2} + \frac{1}{D^2} \quad , \quad \frac{1}{(ID)^2} \qquad (1.146)$$

or, equivalently, their ratio and the ellipse eccentricity:

$$I^2 + D^2 \quad , \quad \frac{\sigma_{yx} - \sigma_{xy}}{I\sqrt{2}} \qquad (1.147)$$

The ellipse is inclined at the angle θ to the horizontal plane $\Delta_{zn} = 0$, where its projection is the Mohr circle (1.131).

1.4.3. DILATANT KINEMATICS WITH ROTATION

To study the internal kinematic properties of granulated material, it is necessary to use the difference between the mean velocity field, v_i and the rigid rotation, $\Phi_{ij} = \varepsilon_{ijk}(\Omega_k + \omega_k)$, of particles in the vicinity of the same point A. Here, Ω_k is the rotational velocity of mean displacement field, ω_k is the spin (microrotation) component, and Φ_k is the total rotational velocity. This gives the following expression

for the relative velocity of two particles, A and A', which are separated by the distance, h:

$$\Delta v_i = (\partial v_i / \partial x_j) h n_j - \Phi_{ij} h n_j + O(h^2)$$

$$= \frac{1}{2}(\partial v_i / \partial x_j + \partial v_j / \partial x_i) h n_j - \varepsilon_{ijk} h n_j \omega_k + O(h^2) \tag{1.148}$$

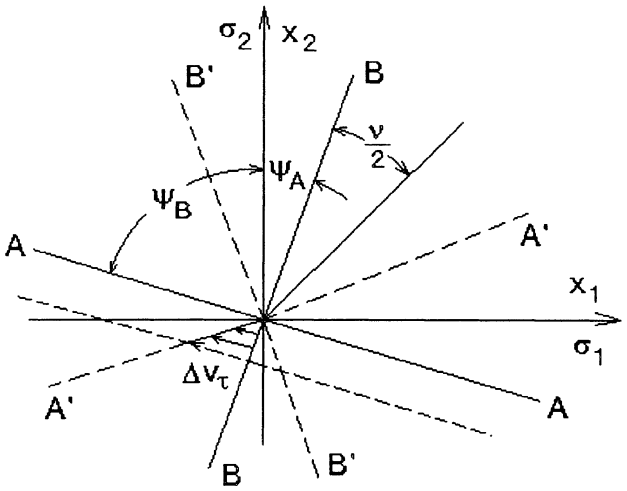

Figure 1.18. Velocity characteristics BB, B'B' and shear without dilatancy along orthogonal lines AA, A'A'.

Further multiplication of (1.148) by normal n_i determines the elongation rate, Δv_n, of the distance, h, and multiplication by unit vector l_i, such that $n_i l_i = 0$, determines the tangential velocity component, Δv_τ, of the particle relative displacement. Using the angle ψ between the normal and the coordinate x_2 (see Figure 1.18),

$$n_1 = \sin\psi \quad , \quad n_2 = \cos\psi \quad , \tag{1.149}$$

$$l_1 = -\cos\psi \quad , \quad l_2 = \sin\psi \tag{1.150}$$

we can get the following two expressions:

$$\frac{\Delta v_n}{h} = \frac{1}{2}\frac{\partial v_i}{\partial x_i} + \frac{1}{2}\left(\frac{\partial v_y}{\partial y} - \frac{\partial v_x}{\partial x}\right)\cos 2\psi + \frac{1}{2}\left(\frac{\partial v_x}{\partial y} + \frac{\partial v_y}{\partial x}\right)\sin 2\psi \tag{1.151}$$

$$\frac{\Delta v_\tau}{h} = \frac{\omega}{2} + \frac{1}{2}\left(\frac{\partial v_y}{\partial y} - \frac{\partial v_x}{\partial x}\right)\sin 2\psi - \frac{1}{2}\left(\frac{\partial v_x}{\partial y} + \frac{\partial v_y}{\partial x}\right)\cos 2\psi \qquad (1.152)$$

where $\omega = \omega_z$ is the nonzero spin velocity. According to these expressions, Δv_n and Δv_τ belong to the circle

$$(\Delta v_n - h\, a_\varepsilon)^2 + (\Delta v_\tau - h\, b_\varepsilon)^2 = h^2 R_\varepsilon^2 \qquad (1.153)$$

where

$$R_\varepsilon = \frac{1}{2}\sqrt{\left(\frac{\partial v_y}{\partial y} - \frac{\partial v_x}{\partial x}\right)^2 - \left(\frac{\partial v_y}{\partial x} + \frac{\partial v_x}{\partial y}\right)^2} = \frac{D\gamma}{Dt}$$

$$a_\varepsilon = \frac{1}{2}\left(\frac{\partial v_x}{\partial x} + \frac{\partial v_y}{\partial y}\right) = \frac{De}{Dt}, \qquad b_\varepsilon = \omega, \qquad (1.154)$$

The dilatancy condition (1.94), that has not accounted for the grain rotation effect, can be rewritten as:

$$a_\varepsilon = R_\varepsilon \sin \nu \qquad (1.155)$$

meaning that the relative velocity circle (1.153) crosses the axis $\Delta v_n = 0$ while the rotation velocity is determining the circle displacement along the vertical line in the plane of Figure 1.19.

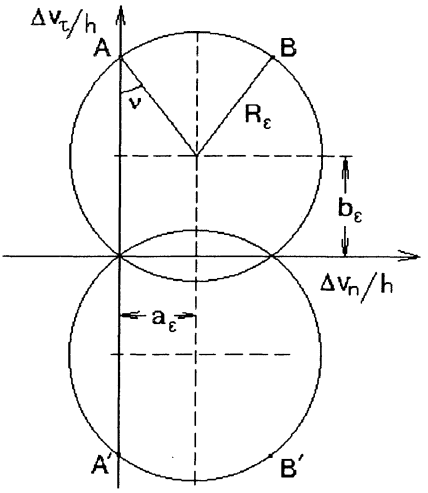

Figure 1.19. Relative velocity circles crossing the Δv_τ axis due to the dilatancy condition.

It also means that there is a line, AA, in the vicinity along which pure tangential relative motion of particles in contact is possible. Line AA must be orthogonal to the velocity characteristic BB (Figure 1.18). This tangential motion may be interpreted as initial slip.

However, the line AA cannot be a real discontinuity as the velocity characteristic BB that connects the relative motion of the adjointed smooth plastic or rigid velocities fields.

Moreover, according to Figure 1.19, the relative motion along BB is connected necessarily with thickening of the band along BB. We can get the result (1.126) if $b_\varepsilon = \Omega$. So, the conventional (symmetric) mechanics is sufficient to find slip-surfaces. Inside slip bands the deformation needs irreversible changes of microstructure. So, the microplasticity has to be studied more carefully.

1.4.4. LIMIT CONDITION FOR ASYMMETRIC PLASTICITY

One needs a more general theory for continuum description of plastic states inside a transition zone corresponding to the slip line..

Such a theory includes asymmetrical parameters in the limit condition for slip, as, for example, is done in equation (1.135), while the Coulomb condition (1.136) is the same one. However, the friction angle φ will be a function of the rotation angle ϕ such that

$$\omega = d\phi / dt \tag{1.156}$$

Correspondingly, the dilatancy rate Λ will be the function of the same angle ϕ. Then condition (1.94) will be rewritten as

$$\frac{De}{Dt} = \frac{D\Lambda|\gamma|}{Dt} = \Lambda\frac{D|\gamma|}{Dt} + |\gamma|\omega\frac{d\Lambda}{d\phi} \tag{1.157}$$

The planar case will be described by the generalized dilatancy law:

$$\frac{De}{Dt} = |\frac{D\gamma}{Dt}|\sin\nu + \omega\sin\theta_* \tag{1.158}$$

This means that volume changes can be created by the grain's internal rotation effect. Here, θ_* is the new angle parameter.

However, three additional limit conditions are needed, two of which correspond to the solid friction effects of rotation, torque, and to microdilatancy limitation of higher gradient kinematics. In other words, the rheological connections between σ_a and ω and between $\mathcal{M}_{zn}$ and $\partial\Phi_i / \partial x_j$ must be determined and the limitation for gradient coefficients in (1.22) be found.

1.4.5. EXPERIMENTAL DAMAGE IN THE PLANE SAMPLES

Prof. J. F. Labuz (University of Minnesota) found some experimental evidence of initial damage along line *AA* by acoustical emission methods during biaxial testing of plane rock samples (Figures 1.20 and 1.21). Initial damage has a form of the diffusion (random) cloud in the vicinity of initially round notch. Then the damage is concentrated roughly along line *AA*.

However, finite rupture takes place along another line which is closer to the main compression (vertical) axis.

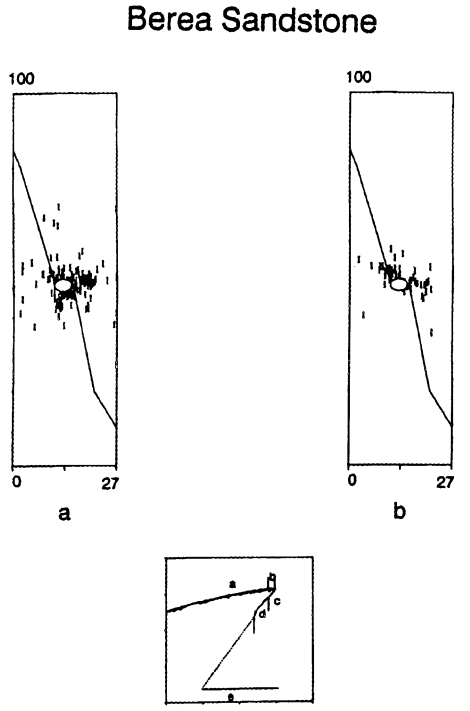

Figure 1.20. During initial stages of deformation the internal damage is concentrated along lines orthogonal to velocity characteristics. (Courtesy of J.F.Labuz.)

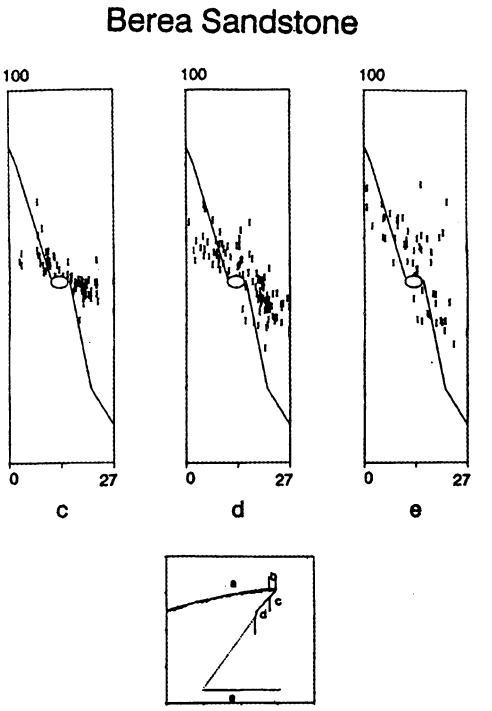

Figure 1.21. Finally, the damage is removed to the rupture lines along the velocity characteristics. (Courtesy of J.F.Labuz.)

One can speculate that there is no room for necessary microstructure changes along line *AA* because the corresponding band cannot be thicker. Necessary microstructure changes inside the shear bands - that is, grain rotation, decreasing the cohesion and the friction, needs the lateral thickening due to the dilatancy, and this is possible only along the velocity characteristic *BB*.

1.5. Brittle fracturing of rocks

1.5.1. GLOBAL THERMODYNAMICS OF FRACTURING

Geomaterial at contacts have different properties than the same geomaterial inside the body of rock or soil masses, as manifested by the specific friction conditions at slip surfaces. The localization process has shown that the contacts, joints and cracks, which can be treated as singular surfaces or mathematical discontinuities, have thin but finite thickness in reality.

As a result, we can introduce the internal energy, ε_s, for geomaterial at the surface which is non-equal to its bulk value, $\varepsilon\left(\sigma_{ij}, T\right)$, determined by equation (1.51) for the elementary volume, ΔV, of the body. The fracturing process is usually identified with the loss or changes of the bearing capacity of the rock masses. Correspondingly, the thermodynamical analysis has to be performed for a whole body.

Let us introduce a symbolic total load P and a total displacement Δ, together with the total internal energy $\mathcal{E}$ and heat flux Q [177]. Then the first law of thermodynamics is formulated as

$$Pd\Delta + Qdt = d\mathcal{E} \tag{1.157}$$

The entropy production, S, is controlled by heat flux, Q, and internal dissipation, Π - that is,

$$T\Pi dt + Qdt = TdS \tag{1.158}$$

where T is the mean body temperature. Introduction of free energy

$$F = \mathcal{E} - TS \tag{1.159}$$

permits the internal dissipation as a difference of total load work and free energy increment

$$T_0\Pi = P\Delta - (d\mathcal{E} - T_0 S) = P\Delta - dF \tag{1.160}$$

if the isothermal case ($T = T_0$) is considered.

The free energy, F, can also be expressed as the sum of elastic bulk energy of the body $W_b\ (P, l)$ and the surface energy at the crack that is proportional to its length, l, - that is,

$$F = W_b\ (P, l) + 2\theta\gamma_0 l \tag{1.161}$$

Here, the specific energy, γ_0, equals the difference between surface energy, ε_s, and bulk energy, ε, and corresponds to the unit length of a crack (Section 1.5.4).

1.5.2. CRITERION OF ELASTO - BRITTLE FRACTURE

Usually, the nondissipative case ($\Pi = 0$) is considered, for which we can find the connections between admissible variations of body strain, $\delta\Delta$, and crack length, δl:

$$P\delta\Delta - \delta F = \left(-\frac{\partial W_b}{\partial l} - 2\gamma_0\right)\delta l + \left(-\frac{\partial W_b}{\partial \Delta} + P\right)\delta\Delta = 0 \qquad (1.162)$$

According to equality (1.162), the crack can grow if changes of elastic bulk energy corresponding to its unit-length increment are equalized by increasing the specific energy of new surfaces:

$$-\frac{\partial W_b}{\partial l} = 2\gamma_0 > 0 \qquad (1.163)$$

Only in this case, will any disturbance lead to crack growth. The secondary sequence of the equality (1.162) is the elastic constitutive relation for the whole body: $P = \partial W_b / \partial \Delta$.

The fracture critical condition (1.163) was suggested by A.Griffith (1922) and is the basis of conventional fracture theory. The irreversible work, γ_*, spent for an unit of new surface can be included into the specific surface energy if corresponding dissipation is not dependent on crack length, in which case, the effective surface energy, γ, is the sum:

$$\gamma = \gamma_0 + \gamma_* \qquad (1.164)$$

1.5.3. FRACTURE GROWTH IN DISSIPATING STRATA

A more sophisticated condition is formulated for plastic or viscous effects in geomaterials when $\Pi \neq 0$ and the dissipation is dependent on crack scale. For such a case, let us suppose that the dissipation function, Ψ, includes: (1) the bulk dissipation rate, $Z_b(P, l)$, for a body with a crack; (2) the part of the work, $2\gamma_* \dot{l}$, which is spent irreversibly to create new crack surfaces; and (3) additional dissipation inside the thin layer, $2\xi l$, due to differences between the surface and bulk viscosity of geomaterials. Then, the following definition [145] is used:

$$T_0\Psi = Z_b(P,l) + 2\gamma_* \dot{l} + 2\xi l \qquad (1.165)$$

According to the Onsager principle [77], the critical condition of fracture with dissipation is formulated as

$$\delta(\Pi - \Psi) = 0 \tag{1.166}$$

This means that changes of the entropy production, Π, and the dissipation rate, Ψ, must be equal.

Variations of Π and Ψ are determined by the two following equalities:

$$\delta\Pi = \Delta\delta P - \delta F = \Delta\delta P - \frac{\partial}{\partial P}\left(\frac{\partial W_b}{\partial t}\right)\delta P - \frac{\partial}{\partial l}\left(\frac{\partial W_b}{\partial t}\right)\delta l \tag{1.167}$$

$$\delta\Psi = \delta Z_b + 2\xi\delta l = \frac{\partial Z_b}{\partial P}\delta P + \frac{\partial Z_b}{\partial l}\delta l + 2\xi\delta l \tag{1.168}$$

Then the generalized fracture critical condition [145] of the crack growth without changes of stresses ($\delta P = 0$) is

$$-\frac{\partial}{\partial l}\left(Z_b + \frac{\partial W_b}{\partial t}\right) = 2\xi + 2i\frac{\partial\gamma}{\partial l} \tag{1.169}$$

Let us consider elastoviscous geomaterial. In this case, superfluous elastic energy, W_b, and rate of dissipation, Z_b, are proportional to the area of stress concentration - that is, to l^2. Then we have:

$$W_b = -B_1\frac{P^2}{2E}l^2 + C_1 \quad , \qquad Z_b = B_2\frac{P^2}{2\mu}l^2 + C_2 \tag{1.170}$$

where B_1, B_2 are numerical coefficients, E is the elastic modules, μ is the viscosity and C_1, C_2 are constants independent of crack length l. Substitution of the expressions (1.170) into (1.169) gives the differential equation

$$B_1\frac{P^2}{E}\frac{dl}{dt} - B_2\frac{P^2}{\mu}l + 2\xi = 0 \tag{1.171}$$

relative to crack length.

The dissipation rate, ξ, corresponds to the unit length of cracks and is assumed to depend only upon crack velocity, dl / dt. For viscous dissipation, there is reason to suggest that

$$\xi = \frac{1}{2} B_3 \left(\frac{dl}{dt} \right)^2 \tag{1.172}$$

Thus, equation (1.171) determines the crack velocity dl / dt as a function of its instant size l :

$$B_3 \left(\frac{dl}{dt} \right)^2 + B_1 \frac{P^2}{E} \left(\frac{dl}{dt} \right) - B_2 \frac{P^2}{\mu} l = 0 \tag{1.173}$$

1.5.4. CRACK - TIP AUTONOMICS

There is another simple approach to crack-growth study. Consider a growing crack and use the system of coordinates x_1, x_2, which moves with the velocity U_i of the crack-tip. Usually, it is assumed that fracturing is independent near the crack-tip and that fields of stresses and strain (or strain-rate) are stationary inside the contour $\Gamma = \Gamma_i + \Gamma_{0i} + \Gamma_{i0} + \Gamma_0$ around the tip (Figure 1.22).

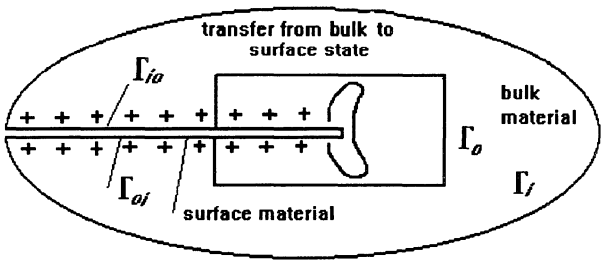

Figure 1.22. The control volume moving with the crack tip illustrates the change of geomaterial from the bulk to the surface state.

The energy fluxes in and out of this contour need be equalized - that is,

$$J = \int_{\Gamma} \left\{ \rho \left(\varepsilon + \frac{v_i v_i}{2} \right) (U_i - v_i) + \sigma_{kj} v_k - q_j \right\} n_j \, d\Gamma = 0 \tag{1.174}$$

If the fluxes at the crack edges are absent, then the fluxes at Γ_l and Γ_0 are equal to each other. Because we have to discriminate bulk internal energy ε_b and the surface energy ε_s of the body, the corresponding contour integral for Γ_0 has the surplus part

$$\int_{\Gamma_0} \rho\,(\varepsilon_s - \varepsilon_b)(U_i - v_i)\,d\gamma = \lim_{d\to 0} 2[\varepsilon]\rho\dot{l}d = 2\gamma_0\dot{l} \tag{1.175}$$

The energy difference, $[\varepsilon]$, for the masses, $2\rho d$, adjacent to new surfaces determines the Griffith surface energy , γ_0 . We can also see that, here, $U_i - v_i = \dot{l}$. Accounting for dissipation [145]

$$D \sim \left(\dot{e}_{ij}^{\,p}\dot{e}_{ij}^{\,p}\right)^n \sim \frac{1}{d^{2n}}\left(\dot{l}\right)^{2n} \quad , \quad \dot{e}_{ij} \sim \frac{\dot{l}}{d} \tag{1.176}$$

localized inside contour Γ_0 with the area $A_0 \sim d^2$ permits addition of the dissipate term

$$2\gamma_*\dot{l} = 2\,d^{2-2n}(\dot{l})^{2n-1}\dot{l} \tag{1.177}$$

to the right-hand side of (1.175). For example, for plastic dissipation, $n = 1/2$, - that is, $\gamma_* = \gamma_*(T)$. However, in the case of viscous dissipation, $n = 1$ and

$$\gamma_* = \eta_*\dot{l} \tag{1.178}$$

where η_* is the viscous resistance.

For further details it is necessary to also use the contour integral for heat fluxes. The difference of the contour integrals for total energy and for heat fluxes gives us the possibility of using the free energy $f(\sigma_{ij}, T)$, which is conventionally used as the elastic potential. This operation leads to the well-known J-integral [94,152] which is valid in the isothermal case:

$$J = \int_{\Gamma_0}\left\{\rho\left(f_v + \frac{v_k v_k}{2}\right)dX_2 - \sigma_{kj}\frac{\partial u_k}{\partial X_1}\right\}n_j\,d\Gamma = 2(\gamma_0 + \gamma_*) = 2\gamma \tag{1.179}$$

The non-zero right-hand side term is motivated by the transition from the general specific free energy f value [63] to its bulk equivalent, f_b. In the adiabatic case, the constant γ (or γ_0 and η_*) has to be different.

Viscous geomaterials may be fractured also with the stationary stress distribution in the vicinity of the crack tip, but this condition corresponds to stationary of strain-rate fields. Therefore, the following equation must be integrated over the contour Γ:

$$\frac{d}{dt}\left\{\rho\frac{d\varepsilon}{dt} - \sigma_{ij}\frac{\partial v_i}{\partial x_j} + \frac{\partial q_j}{\partial x_j}\right\} = 0 \tag{1.180}$$

The preliminary differentiation of the heat balance equation over time is also necessary. In the isothermal case, the result is

$$N = \int_{\Gamma_i}\left(\frac{\partial f}{\partial t} + 2Z_b\right)dx_2 - \sigma_{mj}\frac{\partial v_m}{\partial x_1}n_j\,d\Gamma = 2\xi + 2\frac{\partial\gamma}{\partial l}\dot{l} \tag{1.181}$$

If the velocity field can be separated into viscous and elastic parts,

$$v_i = v_i^{\,p} + v_i^{\,e} \tag{1.182}$$

then the integral (1.181) can be represented as

$$N = -\frac{\partial Z_b}{\partial l} + \frac{\partial W_b}{\partial l}\dot{l} = 2\xi + 2\frac{\partial\gamma}{\partial l}\dot{l} \tag{1.183}$$

which coincides with the criterion (1.179).

1.5.5. MATERIAL TOUGHNESS CONCEPT

The additive condition (1.182) opens the possibility of using some viscous solutions. For example, the plate under tension [145] is characterized by

$$\frac{\partial Z_b}{\partial l} = -(\kappa+1)^{-1}\frac{K^2}{8\mu} \tag{1.184}$$

$$G = -\frac{\partial W_b}{\partial l} = (\kappa+1)^{-1}\frac{K^2}{4E}(1+\nu) \tag{1.185}$$

where K is the coefficient of stress concentration, κ is the coefficient of strain condition (that is, $\kappa = 3-4\nu$ for plane strain and $\kappa = (3-4)/(1+\nu)$ for the plane-stress state), and ν is the Poisson's coefficient [94]. The introduction of (1.184) and (1.185) into criterion (1.183) leads to the differential equation

$$\frac{K^2}{\mu} - \dot{l}\frac{2(1+\nu)}{E}\frac{\partial K^2}{\partial l} = 16(1+\kappa)\left(\xi + \frac{\partial\gamma}{\partial l}\dot{l}\right) \tag{1.186}$$

The solution of (1.186) determines the values K_c of crack growth in viscoelastic plate. For the pure elastic case,

$$K_c^2 = \frac{1+\kappa}{1+\nu} 8E\gamma \tag{1.187}$$

For the viscous case,

$$K_c^2 = 16(1+\kappa)\xi\mu \tag{1.188}$$

On the other hand, the concentration coefficient, K, can be represented as a function of stresses applied to the body. For example, for the plate with a crack,

$$K = P\sqrt{\pi (l/2)} \tag{1.189}$$

The measurement of P at the initial moment of crack growth allows the possibility of determining the critical values, K_c (or *toughness*), of materials experimentally. If $K_c = const$, equality (1.189) is valid and the fracturing is elasto-brittle.

The data for $K_c(I)$, corresponding to fracturing under tension are given in the Table 1.1. The variability of K_c for the same geomaterials is connected with its nonhomogeneity and the influence of crack-growth velocity.

TABLE 1.1. Critical stress concentration values for geomaterials.

Geomaterial	$K_c(I)$	Geomaterial	$K_c(I)$
Coal	0.27	Anhydrite	0.62-0.89
Alevrolite	0.53	Mergel	0.71-0.89
Sandstone	0.36-1.42	Metasomatite	1.24-1.42
Granite	0.567	Basalt	0.62-1.60
Fused quartz	0.640	Diorite	0.89-1.77
Shale	0.55-0.93	Gabbrodiabase	1.50-1.77
Dry alevrolite	0.73	Porphyrite	1.24-1.77
Saturated one	0.74	Dolerite	1.60-2.13
Dolomite	0.71	Amphibole	1.60-1.95
Marble	0.36-1.06	Porphyritic basalt	2.04-2.49
Limestone	0.36-1.24		

If the experiment shows the proportionality of K_c to crack velocity, we have the case of pure viscous fracturing and expression (1.188) is valid. The following suggestion is reasonable for the specific viscous dissipation:

$$\xi \sim (\dot{l})^2 \quad , \quad K_c \sim \dot{l} \tag{1.190}$$

The viscous type of fracturing is observed for a long observation interval and is typical for the creep growth of the Earth crustal fault. As can be seen, lower creep-fracture velocity needs a lower stress concentration.

Critical values of the stress-concentration factor for other modes of fracturing are parameters independent of $K_c(I)$. So, for sandstone with fine grains, $K_c(I) = 1.47 MPa\sqrt{m}$, but its shear toughness, $K_c(II)$ is $4.75 MPa\sqrt{m}$.

The critical factors are functions of the confining pressure. For limestone's, that $K_c(I) = 0.93\ (MNm\sqrt{m})$ if $p \leq 20\ MPa$, but

$$K_c(I) = \{0.93 + 0.07(p - 20\ MPa)\}\ (MNm\sqrt{m})$$

if $p \geq 20\ MPa$. This effect is connected with the pressure-dependent plastic dissipation or solid friction at the crack tip.

1.5.6. TRIAXIAL RUPTURE TESTING

The general dependence of rock strength on pressure and temperature is illustrated by Figure 6.1, where data of triaxial tests are gathered. Because it is possible to study the residual damage and fracture types in rock, their rupture data are known in more detail than in the case of granular media.

At the moment of rupture, the force applied to testing machine is diminished sharply. The magnitude of this diminishing is known as a stress drop. If the stress drop is not equal to zero, the failure is brittle in the macroscale; if it is absent, the macrofailure is ductile, although the microdamage can be yet brittle. Therefore, this brittle-ductile transition [34] does not coincide with the same transition estimated by the presence or absence of brittle cracks in the finite states of samples (Figure 6.1).

Sometimes instant stress drop is interpreted as a blast type of rupture, but this is not adequate because the energy released at the moment of rupture depends not only on the stress drop but also on the path increments of the loading disk. These path increments are limited by deformation of the machine itself. If the deformation is small, the process of unloading can be smooth. It is also be influenced by the form of the sample.

The quantitative values of the bearing capacity of the sample at the rupture moment is interpreted as the strength of the geomaterial. Sometimes it does not correspond to the peak value of the bearing capacity because of the delay of the localization of the internal crack into be macrofracture. By wave sounding, by cutting, or by acoustic emission, it was found that cracks begin to appear at a limit of elasticity much lower than the surface strength. Acoustic emissions will reappear only after stress reaches the upper level of the previous loading (the Kaiser effect) [104]. Because of the unavoidable opening of cracks or pores in most geomaterials due to their polycrystalline microstructure, this limit

can be also called the dilatancy limit. The quantitative description of such complicated brittle features are given in the Table 1.2.

TABLE 1.2. Main strength parameters of some geomaterials.

Geomaterial (at room temperature)	Young's modulus $E\ 10^5\ MPa$	Poissonn coefficient ν	Compression strength $MPa\ (\sigma_3 = 0)$	Extension strength $MPa\ (\sigma_3 = 0)$
Granite	0.5-0.9	0.21-0.28	210	9-13
Gabbro	1.0	0.34	200	22
Basalt	1.0	0.28	290	16
Marble	1.1	0.28	250	15-20
Limestone	0.2-0.9	0.23-0.20	30-180	2.1-10
Sandstone	0.02-0.7	0.3-0.4	10-42	0.3-1.1
Chalk	0.05-0.7	0.4	15-19	0.5-0.9
Concrete	0.17	0.3	30	2.5
Coal	0.4	5-7	1.9-2.4	
Quartzite	0.1-0.3	250	14	

According to some experimental measurements, dynamic and static strengths are different at strain rates, characteristic of explosions, laser and electronic pulses, etc. [148]. However, this difference is explained by the limit velocity for fracture growth (see, Section 5.1). The effect was also mentioned [100] for individual cracks and influences dilatant changes of internal rock and soil voidness (Figure 1.23). Slippage along existing crack edges has the same limit-velocity [29].

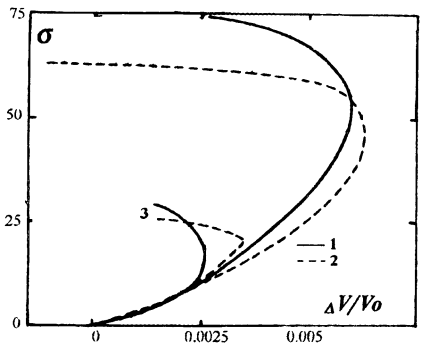

Figure 1.23. Dynamic (1) and static (2) dilatant curves under confining conditions and without confining pressure (3). Here, $[\sigma] = 1000$ *pounds / sq.inch* [41].

CHAPTER 2

MECHANICS OF A SATURATED GEOSTRATUM

2.1. Interpenetrating continua

2.1.1. DYNAMICS OF SATURATED POROUS MEDIA

Porous media saturated with gases or fluids can be described by the method of continuum mechanics if the sizes of all elements of microstructure such as pores and cracks - that is, if fluid channels in a solid matrix, fluid drops and gas bubbles are much less than the average scale of space, which is equal to the linear dimension of an elementary (differential) volume of the medium. It is also assumed that every differential volume has a complete statistical ensemble of micro-elements and the macroscale of the considered object (problem) is much more than dimensions of the elementary volume [156].

From another perspective, a porous saturated medium is a mixture of two phases - that is, of a solid deformable matrix and a fluid. Such a medium is modeled by a mixture of two (interpenetrating) continua which are presented in the same macropoint simultaneously. A very close continuum model has been in development for a gas multicomponent mixture since the works of Maxwell and Stefan [220], but a saturated porous medium is a multi-phase mixture. The difference consists largely in the existence of phase boundaries at the microlevel. Correspondingly, the averaging procedure (Section 1.1) includes integration over these boundary surfaces, with the result being the momentum balances in a nondivergent form due to phase interaction terms (as will be shown). The method of space averaging will be illustrated by its application to problems of dispersion in filter flows (Section 3.5); here however the formal continuum approach is used.

Two sets of averaged balance equation can be formulated directly, including interaction terms. Let us begin with mass balances [156]

$$\frac{\partial}{\partial t}(1 - m)\,\rho^{(s)} + \frac{\partial}{\partial x_i}(1 - m)\,\rho^{(s)} v_i^{(s)} = 0 \tag{2.1}$$

$$\frac{\partial}{\partial t} m\,\rho^{(f)} + \frac{\partial}{\partial x_i} m\,\rho^{(f)} v_i^{(f)} = 0 \tag{2.2}$$

where m is a porosity and indices s and f are symbols of solid and fluid phases respectively. If phase transition takes place (from a solid to a fluid state, for example,

due to melting), then the right-hand sides of equations (2.1) and (2.2) are not equal zero, although their sum must be equal zero because of the law of matter conservation.

The next step concerns the formulation of momentum balances. Let us begin with the total momentum balance, because it does not yet include unknown forces of interaction:

$$\frac{\partial}{\partial t}\left\{(1-m)\,\rho^{(s)} v_i^{(s)} + m\,\rho^{(f)} v_i^{(f)}\right\} + \frac{\partial}{\partial x_j}\left\{(1-m)\,\rho^{(s)} v_j^{(s)} v_i^{(s)} + m\,\rho^{(f)} v_i^{(f)}\right\} = \\ = \frac{\partial \Gamma_{ij}}{\partial x_j} + \left\{(1-m)\,\rho^{(s)} + m\,\rho^{(f)}\right\} g_i \tag{2.3}$$

Here, g_i is the gravity acceleration and Γ_{ij} are the total stresses applied to the arbitrary cross-section of the medium (Figure 2.1):

$$\Gamma_{ij} = (1-m)\,\sigma_{ij} - mp\,\delta_{ij} \tag{2.4}$$

In addition, σ_{ij} is the true stress in the solid matrix, and p is the pore pressure. The distribution (2.4) accounts for the phase areas at the arbitrary cross-section of the porous saturated medium.

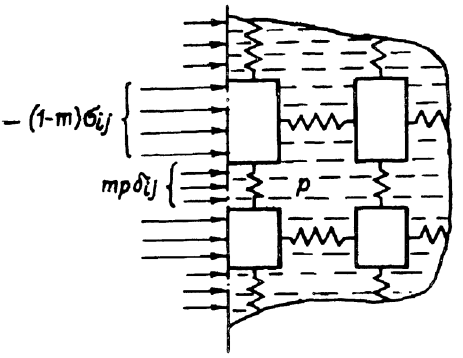

Figure 2.1. Scheme of stress distribution in a porous saturated medium [156].

The momentum balance for fluid phase can be written in the following form:

$$\frac{\partial}{\partial t}\rho_{(f)} m v_i^{(f)} + \frac{\partial}{\partial x_j}\rho_2^{(f)} m v_j^{(f)} v_i = -\frac{\partial mp}{\partial x_i} + \Psi_i + \rho^{(f)} m\, g_i \tag{2.5}$$

where Ψ_j is the interaction force. It can be determined on the base of experience as:

$$\Psi_j = p\frac{\partial m}{\partial X_j} + R_j \tag{2.6}$$

because only in this case is the driving force within the fluid-saturated reservoir the gradient of pore pressure, p. As a result [156],

$$\frac{\partial}{\partial t} m \rho^{(f)} v_i^{(f)} + \frac{\partial}{\partial x_j} m \rho^{(f)} v_i^{(f)} v_j^{(f)} = - m\frac{\partial p}{\partial x_i} + R_i + m\rho^{(f)} g_i \tag{2.7}$$

Expression (2.6) as well as balance (2.7) also include viscous resistance, R_i, to the relative fluid flow.

The case, for which $\Psi_i = R_i$, corresponds to multicomponent models typical of gas mixtures where, according to the Dalton law, the driving force is proportional to the gradient of concentration (the latter being equivalent to the porosity). You can see now that the variant (2.6) is correct, because the flow is absent in a nonhomogeneous medium when $p = const$ but not when $mp = const$.

The difference of equations (2.3) and (2.5) gives us the momentum balance for the solid matrix:

$$\begin{aligned} &\frac{\partial}{\partial t}(1-m)\rho^{(s)} v_i(s) + \frac{\partial}{\partial x_j}(1-m)\rho^{(s)} v_i^{(s)} v_j^{(s)} \\ &= \frac{\partial}{\partial x_j}\sigma_{ij}^{ef} - (1-m)\frac{\partial p}{\partial x_j} - R_i + (1-m)\rho^{(s)} g_i \end{aligned} \tag{2.8}$$

Here, the effective stresses are introduced (see [47]):

$$\sigma_{ij}^{ef} = (1-m)(\sigma_{ij} + p\,\delta_{ij}) = \Gamma_{ij} + p\,\delta_{ij} \tag{2.9}$$

that correspond to the difference of the total stress at a cross-section and the pore pressure.

The second term on the right-hand side of equation (2.8) shows that the pressure gradients corresponding to filter flow acts at the solid matrix exactly as the gravity forces. However, it also shows the nondivergency of the dynamic nonlinear equations (2.7) and (2.8) and is explained by the reaction of the solid walls porous channel to fluid microflows. It leads to the conclusion that the Bernoulli equation is valid along a microstream line.

2.1.2. THERMODYNAMICS OF POROUS SATURATED MEDIA

The energy balances for solid and fluid phases can be written in the following form

$$(1-m)\rho^{(s)}\frac{d_s}{dt}\left(\varepsilon^{(s)}+\frac{v_i^{(s)}v_i^{(s)}}{2}\right)=\frac{\partial}{\partial x_j}\{(1-m)\sigma_{ij}v_i^{(s)}\}+(1-m)\rho^{(s)}g_i v_i^{(s)} + (1-m)Q^{(s)}-\frac{\partial q_j^{(s)}}{\partial x_j}+\frac{\partial W^{(sf)}}{\partial t}, \tag{2.10}$$

$$m\rho^{(f)}\frac{d_f}{dt}\left(\varepsilon^{(f)}+\frac{v_i^{(f)}v_i^{(f)}}{2}\right)=-\frac{\partial}{\partial x_j}(mp\,v_j^{(f)})+m\rho^{(f)}g_i v_i^{(f)} + mQ^{(f)}-\frac{\partial q_j^{(f)}}{\partial x_j}+\frac{\partial W^{(fs)}}{\partial t} \tag{2.11}$$

where the mass balances - (2.1) and (2.2) - are taken into account, $\varepsilon^{(s)}$, $\varepsilon^{(f)}$ are the phase internal energies, $Q^{(s)}$, $Q^{(f)}$ are the body-distributed heat sources and $q_i^{(s)}$, $q_i^{(f)}$ are the phase heat fluxes. The interface work rates are then introduced; in general, their sum is not equal to zero [156] - that is,

$$\frac{\partial W^{(sf)}}{\partial t} \neq -\frac{\partial W^{(fs)}}{\partial t} \tag{2.12}$$

This inequality is due to the heat produced by this type of work [152]. The special "phase" derivatives used in (2.10) and (2.11) are:

$$\frac{d_s}{dt}=\frac{\partial}{\partial t}+v_j^{(s)}\frac{\partial}{\partial x_j} \quad , \quad \frac{d_f}{dt}=\frac{\partial}{\partial t}+v_j^{(f)}\frac{\partial}{\partial x_j} \tag{2.13}$$

The equations of kinetic energy result from multiplication of the momentum balances by the corresponding phase velocities:

$$(1-m)\rho^{(s)}\frac{d_s}{dt}v_i^{(s)}\frac{v_i^{(s)}}{2} = \frac{\partial}{\partial x_j}\left\{(1-m)\sigma_{ij}v_i^{(s)}\right\}-(1-m)\sigma_{ij}\frac{\partial}{\partial x_j}v_j^{(s)} + (1-m)\rho^{(s)}g_i v_i^{(s)}-\Psi_i v_i^{(s)} \tag{2.14}$$

$$m\rho^{(f)}\frac{d_f}{dt}v_i^{(f)}\frac{v_i^{(f)}}{2} = \frac{\partial}{\partial x_j}mp\,v_j^{(f)} + mp\frac{\partial v_i^{(f)}}{\partial x_i} + m\rho^{(f)}g_i v_i^{(f)} + \Psi_i v_i^{(f)} \tag{2.15}$$

The differences equations (2.10) and (2.11) and (2.14) and (2.15) give the corresponding heat balances for phases, which include the effective stresses and pore pressure working on the corresponding rates of matrix deformation and specific volumes $V_{(s)} = 1/\rho^{(s)}$, $V_{(f)} = 1/\rho^{(f)}$ - that is,

$$(1-m)\rho^{(s)}\left\{\frac{d_s\varepsilon^{(s)}}{dt} + p\frac{d_s V^{(s)}}{dt}\right\} = \sigma_{ij}^{ef}\frac{d_s e_{ij}^{(s)}}{dt} + (1-m)Q^{(s)} - \frac{\partial q_i^{(s)}}{\partial x_i}, \tag{2.16}$$

$$m\rho^{(f)}\left\{\frac{d_f\varepsilon^{(f)}}{dt} + p\frac{d_f V^{(f)}}{dt}\right\} = mQ^{(f)} - \frac{\partial q_i^{f}}{\partial x_i} \tag{2.17}$$

Of course, this corresponds to the choice of interface energy exchange (2.12) that could be found.

The next step in our thermodynamic study is the introduction of phase entropies $s^{(s)}$, $s^{(f)}$:

$$(1-m)\rho^{(s)}T^{(s)}\frac{d_s s^{(s)}}{dt} = (1-m)Q^{(s)} - \frac{\partial q_i^{(s)}}{\partial x_i} + \sigma_{ij}^{ef}\frac{d_s e_{ij}^{p}}{dt} \tag{2.18}$$

$$m\rho^{(f)}T^{(f)}\frac{d_f s^{(f)}}{dt} = mQ^{(f)} - \frac{\partial q_i^{(f)}}{\partial x_i} + R_i(v_i^{(f)} - v_i^{(s)}) \tag{2.19}$$

where $T^{(s)}$, $T^{(f)}$ are the phase temperatures and e_{ij}^{p} is the irreversible part of the matrix strain.

Thus, there are mechanical sources of heat produced by plastic or viscous works in the solid phase (due to deformation of the matrix) and by viscous dissipation in the fluid phase (due to filter flows).

The exclusion of heat fluxes gives the Gibbs equations, which reveal the thermodynamic variables acting in the porous saturated media:

$$(1-m)\rho^{(s)}d_s\varepsilon^{(s)} - \sigma_{ij}^{ef}d_s e_{ij}^{e} + (1-m)\rho^{(s)}p\,d_s V^{(s)} = (1-m)\rho^{(s)}T^{(s)}d_s s^{(s)} \tag{2.20}$$

$$\rho^{(f)} d_f \varepsilon^{(f)} + \rho^{(f)} p\, d_f V^{(f)} = \rho^{(f)} T^{(f)} d_f s^{(f)} \tag{2.21}$$

where $e_{ij}^{e} = e_{ij}^{(s)} - e_{ij}^{p}$ is the elastic part of the matrix strain $e_{ij}^{(s)}$.

Correspondingly, equations (2.20) and (2.21) can be rewritten using the free energy concept:

$$(1-m)\rho^{(s)} d_s f^{(s)} = \sigma_{ij}^{ef} d_s e_{ij}^{e} - (1-m)\rho^{(s)} p\, d_s V^{(s)} + (1-m)\rho^{(s)} s^{(s)} d T^{(s)} \tag{2.22}$$

$$\rho^{(f)} d_f f^{(f)} = -\rho^{(f)} p\, d_f V^{(f)} + m\rho^{(f)} s^{(f)} dT^{(f)} \tag{2.23}$$

This means that the state equations for the solid matrix have the general forms:

$$\sigma_{ij}^{ef} = \left(\frac{\partial f^{(s)}}{\partial e_{ij}^{e}}\right)_{\rho^{(s)},T^{(s)}} \qquad p = -\frac{V^{(s)}}{(1-m)}\left(\frac{\partial f^{(s)}}{\partial V^{(s)}}\right)_{e_{ij}^{e},T^{(s)}}$$

$$s^{(s)} = \frac{V^{(s)}}{(1-m)}\left(\frac{\partial f^{(s)}}{\partial T^{(s)}}\right)_{e_{ij}^{e},\rho^{(s)}} \tag{2.24}$$

In the linear case, they are equivalent to the following poro-thermo-elastic law [156]:

$$\sigma_{ij}^{ef} = (K - \frac{2}{3}G) e^{e} \delta_{ij} + 2G\, e_{ij}^{e} - \alpha^{(s)} K T^{(s)} \delta_{ij} + \beta^{(1)} Kp\, \delta_{ij} \tag{2.25}$$

where the elastic coefficients K, G of the porous matrix, the compressibility $\beta^{(s)}$ and the coefficient of thermal expansion $\alpha^{(s)}$ correspond to the equation of state of the solid intact phase:

$$\rho^{(s)} / \rho_0^{(s)} = 1 - \frac{1}{3}\beta^{(s)} \sigma_{ij} \delta_{ij} - \alpha^{(s)} T^{(s)} \tag{2.26}$$

The corresponding state equation for a fluid saturating porous space corresponds to the thermodynamic parameters of the Gibbs equation (223) - that is,

$$\rho^{(f)} = \rho^{(f)}(p, T) \tag{2.27}$$

The linear variant of (2.27) can be written as

$$\rho^{(f)} / \rho_o^{(f)} = 1 + \beta^{(f)} p - \alpha^{(f)} T^{(f)} \tag{2.28}$$

2.1.3. ENTROPY PRODUCTION AND KINETIC RELATIONS

For a proper account of entropy production, we have to use the fixed space elementary volume through which both phases move. It allows the possibility of finding out the phase interaction which also leads to entropy growth in the system being considered. So, the entropy production, Σ, is determined by the following equations:

$$\frac{\partial}{\partial t}\{(1-m)\rho^{(s)}s^{(s)}+m\rho^{(f)}s^{(f)}\}+\frac{\partial}{\partial x_j}\{(1-m)\rho^{(s)}s^{(s)}v_j^{(s)}+m\rho^{(f)}s^{(f)}v_j^{(f)}\} = \frac{\partial}{\partial x_j}\left\{\frac{q_j^{(s)}}{T^{(s)}}+\frac{q^{(f)}}{T^{(f)}}\right\}+\Sigma \tag{2.29}$$

$$\Sigma = -\left(\frac{1}{T^{(s)}}\right)^2 q_j^{(s)}\frac{\partial T^{(s)}}{\partial x_j}-\left(\frac{1}{T^{(f)}}\right)^2 q_j^{(f)}\frac{\partial T^{(f)}}{\partial x_j}+ +\frac{R_i}{T^{(f)}}(v_i^{(f)}-v_i^{(s)})+Q\left(\frac{1}{T^{(s)}}-\frac{1}{T^{(f)}}\right) \tag{2.30}$$

Here, we assume that internal heat sources are connected only with the phase heat exchange: $Q^{(s)}(1-m)=-Q=Q$.

In the case of local stationary, the Onsager rule can be used to formulate proper rheological laws. The proportionality between the thermodynamic forces and fluxes, from which the products are composed in expression (2.30), is valid [152]:

$$R_i = r_{ij}(v_j^{(f)}-v_j^{(s)})+\frac{L_{ij}^{(q)}}{T^{(f)}}\frac{\partial T^{(f)}}{\partial x_j} \quad , \tag{2.31}$$

$$r = \frac{L_{ij}}{T^{(f)}} \quad , \tag{2.32}$$

$$Q = \kappa_q(T^{(f)}-T^{(s)}) \quad , \tag{2.33}$$

$$\kappa_q = \frac{L}{T^{(f)}T^{(s)}} \quad , \tag{2.34}$$

$$q_i^{(s)} = -D_{ij}^{(s)}\frac{\partial T^{(s)}}{\partial x_j} \quad , \tag{2.35}$$

$$D_{ij}^{(s)} = \frac{L_{ij}^{(s)}}{T^{(s)}T^{(s)}} \quad , \tag{2.36}$$

$$q_i^{(f)} = - D_{ij}^{(f)} \frac{\partial T^{(f)}}{\partial x_j} \quad , \tag{2.37}$$

$$D_{ij}^{(f)} = \frac{L_{ij}^{(f)}}{T^{(f)}T^{(f)}} \quad . \tag{2.38}$$

Here, the symbols L correspond to kinetic coefficients [152] and P. Curie's principle of tensor symmetry is used. The kinetic relations (2.31) through (2.38) complete the system of dynamic equations for saturated porous media.

2.1.4. CONDITIONS AT BOUNDARIES AND MOVING DISCONTINUITIES

Mathematical problems also include boundary conditions, which can have kinematic or static origin. For example, if there is no flux of matter at the impermeable boundary, the adequate condition is

$$m\rho^{(f)}(v_i^{(f)} - U_i) + (1 - m)\rho^{(s)}(v_i^{(s)} - U_i) = 0 \tag{2.39}$$

where U_i is the velocity of the boundary itself. The simplest variant of (2.39) corresponds to the immovable boundary ($U_i \equiv 0$) and to the immovable porous matrix ($v_i^{(s)} \equiv 0$). Then (2.39) gives the condition $v_i^{(f)} = 0$.

The induced movement of the boundary is formulated as

$$v_i^{(s)} = U_i \tag{2.40}$$

The fluid velocity, $v_i^{(f)}$, is determined by other conditions.

At the shock surface, condition (2.39) is replaced by the mass balance for a discontinuity:

$$[m\rho^{(f)}(v_i^{(f)} - U_i) + (1 - m)\rho^{(s)}(v_i^{(s)} - U_i)] = 0 \tag{2.41}$$

where the square brackets are the differences of the values at the sides <<+>> and <<->> of the considered jump.

The boundary can be treated as a special type of discontinuity and balance (2.41), which includes the conditions (2.39) and (2.40) as particular cases, can be considered.

The boundary parameter values have to be given at outer side <<->> of the medium. These values are denoted by the star symbol.

With regard to traction conditions, the load can be applied to the matrix and the pore fluid (Figure 2.2) - that is,

$$\Gamma_{ij}(-0)n_j \equiv \Gamma^*_{ij}n_j = \left(\sigma_{ij}^{ef}(+0) - p(+0)\,\delta_{ij}\right)n_j \tag{2.42}$$

where n_j is the normal to the boundary and the left-hand side of condition (2.42) corresponds to the given boundary value. This condition must be added to the mass balance condition (2.39).

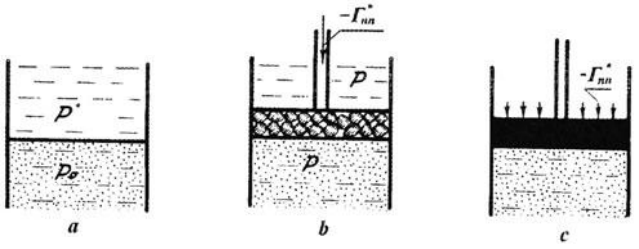

Figure 2.2. Three types of loading must be accounted for (a) - fluid piston; (b) - permeable piston; (c) - intact piston [156].

However, the load can only be applied to the porous matrix, in which case the effective traction is given by

$$\Gamma_{ij}(-0)\,n_j \equiv \Gamma^*_{ij}\,n_j = \sigma^{ef}_{ij}(+0)\,n_j \tag{2.43}$$

and the pore pressure is continuous and can be found from the problem solution:

$$[p] = p^* - p(+0) = 0 \tag{2.44}$$

When the load is applied only to the fluid, the pore pressure is

$$p^* = p(-0) \tag{2.45}$$

and will be a jump if $p(+0) = p_0$, where p_0 is the initial value.

In the case of shock fronts, the inertial forces must be added to the tractions - that is, the momentum fluxes should be equal at both jump sides:

$$[m\rho^{(f)}v_i^{(f)}(v_j^{f}-U_j)+(1-m)\rho^{(s)}v_i^{(s)}(v_j^{(s)}-U_j)- \\ -(1-m)\sigma_{ij}v_j^{(s)}-mpv_i^{(f)}] = 0 \tag{2.46}$$

Conditions (2.41) and (2.46) are sufficient for barotropic case when the temperature changes are not essential at the jump. The total energy balance at the jump has the form

$$[m\rho^{(f)}\frac{v_i^{(f)}v_i^{(f)}}{2}(v_j^{(f)}-U_j)+(1-m)\rho^{(s)}\frac{v_i^{(s)}v_i^{(s)}}{2}(v_j^{s}-U_j)+ \\ +m\rho^{(f)}\varepsilon^{(f)}+(1-m)\rho^{(s)}\varepsilon^{(s)}-(1-m)\sigma_{ij}^{(s)}v_i^{(s)}+mpv_i^{(f)}] = 0 \tag{2.47}$$

Remember that the total momentum and energy balances (2.47) are not sufficient to determinate shock adiabats in saturated porous media. The momentum and energy distribution over phases must be added, resulting in the unsolved problem of phase interaction inside the shock structure [152]. However, the phenomenological dynamic equations considered here may not be valid; the determination of Ψ_i and $dW^{(fs)}/dt$ values, as well as the Onsager kinetic relations, must be re-estimated for the structure.

The energetic condition for the gas outflow from porous media under high pressure appears to be necessary because of the sudden expansion of gas after passing the boundary. It has to be formulated as isoentropical condition:

$$[m\rho(v_i^{(f)}-v_i^{(s)})s] = 0 \tag{2.48}$$

if $m(+0) << m(-0)$.

The shear forces acting at the surface of porous media must be proportional to the gradient of tangential velocity, v_τ, in the flow adjacent to the porous boundary. However, in the case of a permeable wall, the usual nonslip condition at the intact wall

$$v_\tau = 0 \tag{2.49}$$

will change to the Beavers-Joseph condition [16]

$$v_\tau - \frac{\sqrt{k}}{B}\frac{\partial v_\tau}{\partial n} = (v_\tau^{(f)}-v_\tau^{(s)})m \tag{2.50}$$

The right-hand term corresponds to the fluid-flow relative velocity inside the porous space. The second left-hand term is determined by the outside fluid and includes the new empirical parameter B of a porous medium besides its permeability k.

2.2. Microstructure and permeability

2.2.1. ANISOTROPY OF FILTER RESISTIVITY

The force interaction between phases depends mainly on the relative velocity

$$R_i = r_{ij}(v_j^{(f)} - v_j^{(f)}) \tag{2.51}$$

and includes the symmetrical resistance tensor r_{ij}. Its components are functions of the fluid viscosity, the internal length (grain) size, d, the porosity, m, and the vector-director, ν_i, determing the anisotropy.

Accordingly the resistance tensor must be the following of vector combination

$$r_{ij} = r_0 \delta_{ij} + r_* \nu_i \nu_j \tag{2.52}$$

where scalar coefficients, r_0 , r_*, are functions of other scalar arguments mentioned above.

The dimensional analysis shows [11, 80] that

$$r_{ij} = \frac{\mu m^2}{d^2}(\chi_0 \delta_{ij} + \chi_* \nu_i \nu_j) \tag{2.53}$$

Here χ_0, χ_* are the anisotropy coefficients of a porous medium and the fluid viscosity μ is given evidently.

The vector-director ν_i is induced as a generalized continuum variable [220] which describes the microstructure properties, that is, the distribution of fluid channels or grains and their packing in a porous matrix. It is a dynamical variable and is governed by the balance of moment of momentum (1.13):

$$\frac{d_s}{dt}\rho J_{ij}\Phi_j = \frac{\partial \mathcal{M}_{ij}}{\partial x_j} - \varepsilon_{ijk}\sigma^{ef}_{jk} - \mathcal{N}_i \tag{2.54}$$

where J_{ij} is the specific inertia tensor, Φ_j is the total rotational velocity, $\mathcal{M}_{ij}$ are the couple stress, ε_{ijk} is the alternation tensor

$$\varepsilon_{ijk} = -\varepsilon_{jik}\,, \quad \varepsilon_{123} = 1\,, \quad \ldots, \quad \varepsilon_{113} = 0\,, \quad \ldots \tag{2.55}$$

and, consequently, the effective stress tensor, σ^{ef}_{ij}, must include antisymmetrical part. Here the bulk moment of momentum $\mathcal{N}_i$, acting at the porous matrix and created by a fluid filter flow is also introduced. The inertia tensor has dimension of d^5 but it has to be

divided by the grain volume d^3 to find its specific value. Therefore, J_{ij} has the same order as permeability of a porous medium [11]

$$J_{ij} \sim d^2 \sim k \tag{2.56}$$

This means that there is a strong link between microstructure dynamics and permeability changes.

We can also consider the moment of momentum balance for the fluid phase, but here, we limit ourselves to the introduction of the moment of interface forces $\mathcal{N}_i$.

The local angular momentum can be expressed by the vector-director rate [11]:

$$\rho J_{ij} \Phi_j = j \varepsilon_{ijk} v_j \frac{dv_k}{dt} \tag{2.57}$$

and dynamic variables as β_{ij} , ψ_i , G_i can be introduced such that:

$$\mathcal{M}_{ij} = \varepsilon_{ikl} v_k \beta_{lj} \quad , \quad \mathcal{N}_i = \varepsilon_{ijk} n_j G_k \, ,$$

$$\varepsilon_{ikl} n_k \psi_l = \varepsilon_{ikl} \left(\frac{\partial n_k}{\partial x_j} \beta_{lj} - \sigma^{ef}_{kl} \right) \tag{2.58}$$

Equation (2.54) can now be expressed as

$$j \frac{d^2 v_j}{dt^2} = \frac{\partial \beta_{jk}}{\partial x_k} + \psi_j + G_j \tag{2.59}$$

The density of the bulk moment of momentum is assumed to be proportional to relative phase velocity [11] :

$$G_j = \kappa^{(\omega)}_{ij} (v_i^{(f)} - v_i^{(s)}) \tag{2.60}$$

This means that individual grains can rotate under fluid flow and diminish the viscous resistance of the medium. In the linear theory, the coefficient $\kappa^{(\omega)}_{ij}$ is supposed to be independent on the vector-director v_i.

Of course, this rotation is limited by grain contacts with the neighboring grains; therefore, the free energy of the solid matrix depends on the gradient of the vector-director, and the elastic laws for the porous matrix are changed accordingly:

$$\sigma_{ij}^{ef} = \left(K - \frac{2}{3}G\right)e_{kk}\,\delta_{ij} + 2G\,e_{ij} + K\beta p\,\delta_{ij} + a_1\left(\frac{\partial v_k}{\partial x_k}\delta_{ij} - e_{ik}\frac{\partial v_j}{\partial x_k}\right) \tag{2.61}$$

$$- a_2\frac{\partial v_k}{\partial x_k}\frac{\partial v_i}{\partial x_j} - a_3\frac{\partial v_k}{\partial x_i}\frac{\partial v_k}{\partial x_j} - a_4\frac{\partial v_k}{\partial x_i}\frac{\partial v_j}{\partial x_k}$$

$$\beta_{ij} = b_1\frac{\partial v_k}{\partial x_k}\delta_{ij} + b_2\frac{\partial v_i}{\partial x_j} + b_3\frac{\partial v_j}{\partial x_i} + d_1 e_{kk}\,\delta_{ij} \quad , \quad \psi_i = -av_i \tag{2.62}$$

where the temperature effects mentioned above are omitted. Introduction of (2.61) and (2.62) into the balances of momentum and moment of momentum describe the effect of induced anisotropy in porous media.

2.2.2. THE DARCY LAW AND ITS DEVIATIONS

The constitutive law (2.51) corresponds to Darcy's experiment when the porous matrix is immovable. Because inertial forces are negligible, the fluid flow equation (2.7) has the following form:

$$-\frac{\partial p}{\partial x_i} + \rho^{(f)} g_i = \frac{1}{m} r_{ij} v_j^{(f)} \tag{2.63}$$

This equation can be rewritten conventionally as [169]

$$w_i = m v_i^{(f)} = -\frac{k_{ij}}{\mu}\frac{\partial}{\partial x_j}(p + \delta_k \gamma_i x_k) \tag{2.64}$$

where $\gamma_i = \rho^{(f)} g_i$ is the specific weight of the fluid, and k_{ij} is the permeability tensor:

$$k_{ij} = \mu\left(\frac{r_{ij}}{m^2}\right)^{-1} \tag{2.65}$$

Introduction of the permeability corresponds to using of the filter velocity, w_i, as well as the fluid viscosity, μ. The filter velocity concept is very convenient, because it is measured as the flow rate through a unit area of the cross-section of the porous medium without having to measure the porosity m. Another measurable quantity is the pressure, p (or the head, h), at the flow cross-section.

One-dimensional vertical flow is considered in the Darcy experiment and results in the proportionality of the filter velocity and the head gradient

$$w = -c_f \frac{\partial h}{\partial x} \quad , \quad h = \frac{p}{\gamma} + z \tag{2.66}$$

where the filter coefficient c_f is used:

$$c_f = -\frac{k\gamma}{\mu} = -\frac{kg}{\nu} \tag{2.67}$$

The dimension of c_f is L / T and the isotropy of permeability is assumed to be valid:

$$k_{ij} = k\delta_{ij} \quad , \quad k = \mu \frac{m^2}{r} \quad , \quad r_{ij} = r\delta_{ij} \tag{2.68}$$

It can also be seen that the characteristic (hydraulic) length, l_*, of the internal microstructure

$$l_* = \sqrt{k / m} \tag{2.69}$$

corresponds to the true mean velocity, $v_j^{(0)}$ The latter determines the deviations of Darcy's law (2.66) or the equivalent deviations of Onsager's rule (2.31).

The inertial losses can violate Darcy's law (2.64). If so,

$$R_i = r_{ij}(v_j^{(s)} - v_j^{(f)}) + r_{ij}^*(v_j^{(s)} - v_j^{(f)})|v_j^{(s)} - v_j^{(f)}| \tag{2.70}$$

The velocity, $v_j^{(s)}$, is kept in Darcy's law if the reservoir matrix motion is required to account for. The corresponding Reynolds number has the form [156]

$$Re = \frac{\rho v l_*}{\mu} = \frac{\rho |v^{(s)} - v^{(f)}|}{\mu} \sqrt{\frac{k}{m}} \tag{2.71}$$

and rule (2.70) can be rewritten as

$$R_i = \Phi(Re)\mu \frac{m}{k}(v^{(s)} - v^{(f)}) \tag{2.72}$$

The function $\Phi(Re)$ is given in Figure 2.3 and in Table 2.1 for some typical porous media.

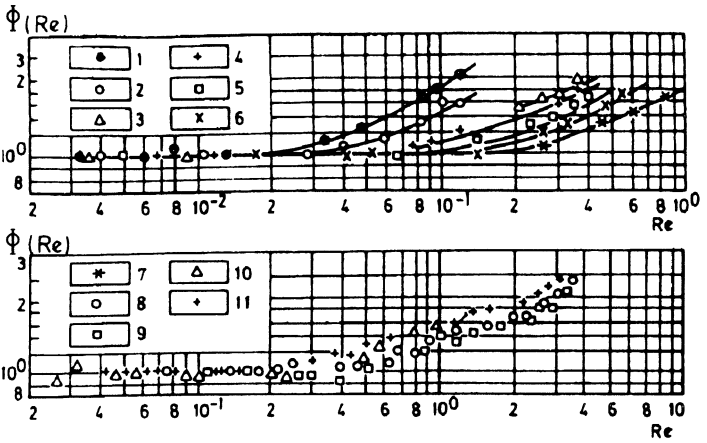

Figure 2.2. Deviation of Darcy's law due to inertial losses [156]: sandstones (1-6) and sphere packing (7-11).

As you can see, the Chezy-Krasnopolsky law for "turbulent" flows through porous media is asymptotically valid

$$w_j|w_j| = -\frac{m}{b}\frac{k_{ij}}{\mu}\frac{\partial}{\partial x_j}(p + \delta_{jl}\gamma_l x_j) \tag{2.73}$$

where b is the "turbulent" parameter of the medium.

Another source of the Darcy law deviations are connected with violation of continuum limits (for example, in the case of ultrasound wave propagation), because their lengths have the same order as porous channels - in other words, as a microstructure element. In such cases, formula (2.72) can be replaced by:

$$R_i = \frac{\mu m^2}{k} F(\kappa)(v_i^{(s)} - v_i^{(f)}) \tag{2.74}$$

where Biot's correction is introduced [20]

$$F(\kappa) = 1 + \frac{z_*^2}{15} + \frac{z_*^4}{525} \quad , \quad |z_*| < 0.624 \quad , \quad z_* = i\sqrt{\kappa}$$
$$\kappa = S\sqrt{\omega / \omega_c} \quad , \quad \omega_c = m\eta / (\rho^f k) \quad , \quad S = 5 - 12 \tag{2.75}$$

Here, ω is the wave frequency, and S is the parameter of pore shape. The product $i\omega$ appears because of differentiation in respect to time, and expression (2.75) is replaced by the following operator [37]:

$$F_\omega\left\{\frac{\partial}{\partial t}\right\} = 1 - a\frac{\partial}{\partial t} + b\frac{\partial^2}{\partial t^2} \tag{2.76}$$

where parameters a , b can be expressed by the quantities in (2.75).

Interphase heat flux is proportional to temperature difference according to the Onsager rule:

$$Q = \kappa_q(T^{(f)} - T^{(s)}) \tag{2.77}$$

where the coefficient of heat interphase exchange, κ_q, can be estimated in the following manner:

$$\kappa_q = \frac{m}{k}\sqrt{D^{(s)}D^{(f)}}\left(F_0 + F_q\left\{\frac{\partial}{\partial t}\right\}\right) \tag{2.78}$$

Again, the operator, F_q, is used to account for non-stationarity of microstreams and F_0 is a constant. Of importance here is that the coefficient, κ_q, is inverse - proportional to the medium permeability, k [152].

The permeability of an anisotropic medium can be expressed as a combination of the vector-director [80]:

$$k_{ij} = k_0\,\delta_{ij} + (k_v - k_0)\,v_i\,v_j \tag{2.79}$$

If vector v_i can change its orientation, then the case of induced anisotropy results, see (2.52). The scalar coefficients of the resistance tensor (2.53) can now be expressed as

$$\chi_0 = \frac{1}{k_0} \quad , \quad \chi_* = \frac{k_0 - k_v}{k_0 k_v} \tag{2.80}$$

2.2.3. PERMEABILITY AND POROSITY

The permeability, k, is proportional to some power of porosity m, and as it follows from the direct measurement of porous samples during the deformation process [156],

$$\frac{k}{k_0} = \left(\frac{m}{m_0}\right)^n \tag{2.81}$$

The case for which $n = 3$ corresponds [233] to representation of porous space as a ensemble of flat channels. The case for which $n = 10$ corresponds to a real sandstone.

The mass balances - (2.1) and (2.2) - show us the dependence of porosity, m, on thermodynamic forces. Consider the linear variant of (2.1)

$$-\rho_0^{(s)} \frac{\partial m}{\partial t} + (1 - m_0) \frac{d\rho^{(s)}}{d\sigma} \frac{\partial \sigma}{\partial t} + (1 - m) \rho_0^{(s)} \frac{\partial v_j^{(s)}}{\partial x_i} = 0 \qquad (2.82)$$

which can be rewritten as

$$dm = \frac{(1 - m_0)}{\rho_0^{(s)}} \left(\frac{d\rho^{(s)}}{d\sigma} \right) d\sigma + (1 - m_0) de_{ij}\, \delta_{ij} \qquad (2.83)$$

This shows that the porosity depends mainly on the volume deformation of porous media as well as on the pore pressure, p, since the true stress, σ, can be expressed as

$$\sigma = -p + (1 - m)\, \sigma^{ef} \qquad (2.84)$$

and, further, as a linear combination of pore pressure, p, and matrix strain, $e = e_{ij}\, \delta_{ij}$.

TABLE 2.1. Diameter, porosity and permeability of samples in Figure 2.2

No	d, cm	m, %	k, 10^{-8} cm^2	No	d, cm	m, %	k, 10^{-5} cm^2
1	0.01	19.7	0.182	7	0.016	22.1	3.3
2	0.0065	19.2	0.130	8	0.246	40.5	2.7
3	0.025	11.9	1.13	9	0.319	38.9	4.1
4	0.014	15.9	0.35	10	0.246	39.4	2.5
5	0.017	26.9	2.5	11	0.319	38.5	3.64
6	0.014	13.6	0.355				

2.3. Dynamic poro-elasticity

2.3.1. LINEAR WAVE DYNAMICS

The linearized system of the dynamic equations for porous saturated media is based on the state equation for both phases. For the solid matrix,

$$\frac{\rho^{(s)}}{\rho_0^{(s)}} = 1 - \frac{1}{3}\beta^{(s)}\sigma_{ij}\delta_{ij} - \alpha^{(s)}T^{(s)} \tag{2.86}$$

because the true stress, σ_{ij}, determines the pressure inside the solid material which is equal to $\sigma = (-1/3)\sigma_{ij}\delta_{ij}$ and which is connected with pore pressure, p, and effective stresses, according to (2.84).

The equation of state for the fluid phase has the same form:

$$\frac{\rho^{(f)}}{\rho_0^{(f)}} = 1 - \beta^{(f)}p - \alpha^{(f)}T^{(f)} \tag{2.87}$$

The constitutive law connecting the strain and effective stress in the solid matrix [156]

$$\sigma_{ij}^{ef} = (K - \frac{2}{3}G)e\,\delta_{ij} + 2G\,e_{ij} + \beta^{(s)}Kp\,\delta_{ij} - \alpha^{(s)}KT^{(s)}\delta_{ij} \tag{2.88}$$

is analogous to the thermoelasticity law but includes pore-pressure effect. Equations (2.86) through (2.88) allow us to rewrite the mass balances - (2.1) and (2.2) - as follows:

$$\frac{\partial m}{\partial t} - \beta^{(s)}(1-m_0)\frac{\partial p}{\partial t} - \frac{1}{3}\beta^{(s)}\frac{\partial \sigma_{ij}^{ef}}{2t}\delta_{ij} - \\ -(1-m_0)\frac{\partial v_i^{(s)}}{\partial x_i} + \alpha^{(s)}(1-m_0)\frac{\partial T^{(s)}}{\partial t} = 0 \tag{2.89}$$

$$\frac{\partial m}{\partial t} + \beta^{(f)}m_0\frac{\partial p}{\partial t} + m_0\frac{\partial v_i^{(f)}}{\partial x_i} + \alpha^{(f)}m_0\frac{\partial T^{(f)}}{\partial t} = 0 \tag{2.90}$$

According to the Gibbs equations - (2.20) and (2.21) - the porosity, m, is not the parameter of state. It plays the role of volume concentration and can be excluded from mass balances (2.89) and (2.90).

The linear form of the momentum balances can be written as

$$(1-m)(\rho^{(s)}\frac{\partial v_i^{(s)}}{\partial t} - \rho^{(f)}\frac{\partial v_i^{(f)}}{\partial t}) = \frac{\partial \sigma_{ij}^{ef}}{\partial x_j} + \frac{\mu}{k}(v_i^{(f)} - v_i^{(s)}) \tag{2.91}$$

$$\rho^{(f)}\frac{\partial v_i^{(f)}}{\partial t} = -\frac{\partial p}{\partial x_i} - \frac{\mu}{k} m(v_i^{(f)} - v_i^{(s)}) \tag{2.92}$$

Equation (2.91) includes the fluid acceleration force, which is not the Biot effect of the adjoined fluid mass but a sequence of effective stress introduction. Equation (2.92) corresponds to simple addition of the fluid inertial force to the filter equation traditional for flows in porous media if $w_i = mv_i^{(f)}$ is taken into account.

Heat transfer equations are necessary, for example, to describe the dynamics of oil-saturated strata if gases are dissolved:

$$(1-m_0)C_{up}^{(s)}\frac{\partial T^{(s)}}{\partial t} = (1-m_0)D_s\nabla^2 T^{(s)} + \\ + (1-m_0)z_e^{(s)}T_0\frac{\partial \sigma}{\partial t} - \kappa_q(T^{(s)} - T^{(f)}) \tag{2.93}$$

$$m_0 C_{hp}^{(f)}\frac{\partial T^{(f)}}{\partial t} = m_0 D_f \nabla^2 T^{(f)} + m_0 z_e^{(f)} T_0 \frac{\partial p}{\partial t} \tag{2.94}$$

where $\sigma = -(1/3)\sigma_{ij}\sigma_{ij}$ is the true solid "pressure".

Let us now introduce the scalar, Φ, and vector, Ψ_k, wave potentials for both phase velocities such that

$$v_i = \frac{\partial \Phi}{\partial x_i} + \varepsilon_{ijk}\frac{\partial \Psi_k}{\partial x_j} \tag{2.95}$$

Shear waves (S-waves) propagate through a porous medium in accordance with the following equation [150]:

$$\Theta_\rho \frac{\partial}{\partial t}\left(\frac{\partial^2 \Psi_k}{\partial t^2} - c_{s\infty}^2 \nabla^2 \Psi_k\right) + \left(\frac{\partial^2 \Psi_k}{\partial t^2} - c_{s0}^2 \nabla^2 \Psi_k\right) = 0 \tag{2.96}$$

that includes the two wave velocities

$$c_{S\infty}^2 = \frac{G}{(1-m)\rho_0^{(s)}} \quad , \quad c_{S0}^2 = \frac{G}{\rho_0} \tag{2.97}$$

which are determined only by rigidity of the matrix.

Equation (2.97) has the typical form for relaxation dynamics with characteristic time

$$\Theta_\rho = \frac{k}{\mu} \frac{\rho_0^{(s)} \rho_0^{(f)}}{m_0(1 - m_0)\rho_0} \tag{2.98}$$

and which depends on the permeability and inertial properties of the medium.

The wave velocities (2.97) show that the "frozen" state corresponds to motion of the matrix alone because the effective density is determined only by the solid phase, see (2.97). In the "equilibrium" state, both phases are involved in motion, and the effective density is changed to the mean value of saturated porous media:

$$\rho_0 = (1 - m_0)\rho_0^{(s)} + m_0 \rho_0^{(f)} \tag{2.99}$$

So, the initial impulse is distributed only over the solid matrix because shear stresses are absent in the fluid phase. However, the viscous fluid is involved in shear-wave motion due to the interphase force proportional to permeability.

The longitudinal waves (P-waves) propagate according to the following equation [75]:

$$\frac{\partial}{\partial t}\left(\frac{\partial^2 \Phi}{\partial t^2} - c^2 \frac{\partial^2 \Phi}{\partial x^2}\right) + \Theta_\rho \left(\frac{\partial^2}{\partial t^2} - c_+^2 \frac{\partial^2}{\partial x^2}\right)\left(\frac{\partial^2 \Phi}{\partial t^2} - c_-^2 \frac{\partial^2 \Phi}{\partial x^2}\right) = 0 \tag{2.100}$$

where temperature effects are omitted, the coefficients are:

$$c^2 = \frac{1}{\rho_0}\left(K + \frac{4}{3}G + a_3 + a_2 + 2a_1\right), \quad 2c_\pm^2 = c_1^2 + c_2^2 \pm \sqrt{(c_1^2 - c_2^2)^2 + 4c_{12}^2 c_{21}^2}$$

$$c_1^2 = \frac{1}{m_0 \rho_0^{(s)}}\left(K + \frac{4}{3}G + a_3\right) \quad , \quad c_2^2 = \frac{a_2}{(1 - m_0)\rho_0^{(f)}}$$

$$c_{12}^2 = \frac{a_1}{m_0 \rho_0^{(s)}} \quad , \quad c_{21}^2 = \frac{a_1}{(1 - m_0)\rho_0^{(f)}} \tag{2.101}$$

$$a_1 = \frac{m_0(1 - m_0 - \beta^{(s)} K)}{\beta} \quad , \quad a_2 = \frac{m_0^2}{\beta}$$

$$a_3 = \frac{(1 - \beta)^2 - M_0^2 - 2m_0(1 - m_0 - \beta^{(s)} K)}{\beta} \quad , \quad a_4 = \frac{m_0^2 \mu}{k}$$

and the mean compressibility of a porous medium is used:

$$\beta = (1 - m_0)\beta^{(s)} + m_0 \beta^{(f)} \tag{2.102}$$

You can see that P-waves are described by more complicated dynamic equations of a higher order than usual wave equations because there are two types of possible particle motion and two corresponding wave modes. In addition, the phase compressibilities are limited by porous matrix rigidity.

2.3.2. WAVE DYNAMICS OF SOFT STRATA

In the case of soft rocks, the small parameter appears [156]

$$\beta^{(s)} K << 1 \tag{2.103}$$

and the method of expansion in a series can be used. Then, the initial system - (2.89) through (2.92) - in the isothermal case splits into two systems corresponding to the two wave modes mentioned previously. For the first mode,

$$\begin{aligned}
&\beta \frac{\partial p}{\partial t} + (1 - m_0) \frac{\partial v_i^{(s)}}{\partial x_i} + m_0 \frac{\partial v_i^{(f)}}{\partial x_i} = 0 \\
&\rho_0^{(s)} \frac{\partial v_i^{(s)}}{\partial t} + \frac{\partial p}{\partial x_i} + \frac{m_0^2}{1 - m_0} \frac{\mu}{k} (v_i^{(s)} - v_i^{(f)}) = 0 \\
&\rho_0^{(f)} \frac{\partial v_i^{(f)}}{\partial t} + \frac{\partial p}{\partial x_i} - m_0 \frac{\mu}{k} (v_i^{(s)} - v_i^{(f)}) = 0
\end{aligned} \tag{2.104}$$

That is, at the first mode motion the soft porous media are equivalent dynamically to fluid with suspended solid grains. The system (2.104) can be deduced to the form:

$$\Theta_\rho \frac{\partial}{\partial t} \left(\frac{\partial^2 p}{\partial t^2} - c_{P\infty}^2 \nabla^2 p \right) + \left(\frac{\partial^2 p}{\partial t^2} - c_{P0}^2 \nabla^2 p \right) = 0 \tag{2.105}$$

where "frozen" and "equilibrium" wave velocities are used:

$$c_{P\infty}^2 = \frac{1}{\rho_\infty \beta} \quad , \quad \frac{1}{\rho_\infty} = \frac{1 - m_0}{\rho_0^{(s)}} + \frac{m_0}{\rho_0^{(f)}} \quad , \quad c_{P0}^2 = \frac{1}{\rho_0 \beta} \tag{2.106}$$

Let transform the system (2.104) to the equivalent system

$$\rho_0 \frac{\partial U_i^*}{\partial t} + \frac{\partial p}{\partial x_i} = 0 \quad , \quad \beta \frac{\partial p}{\partial t} + \frac{\partial V_i^*}{\partial x_i} = 0 \quad ,$$

$$\frac{\partial V_i^*}{\partial t} - \frac{\rho_0}{\rho_\infty} \frac{\partial U_i^*}{\partial t} = \frac{U_i^* - V_i^*}{\Theta_\rho} \tag{2.107}$$

for interpretation of these wave velocities. Here, the mean mass and volume velocities are introduced [156]

$$\rho_0 U_i^* = (1 - m_0)\, \rho_0^{(s)} v_i^{(s)} + m_0\, \rho_0^{(f)} u_i^{(f)}$$

$$V_i^* = (1 - m_0)\, v_i^{(s)} + m_0\, v_i^{(f)} \tag{2.108}$$

You can now see directly that in "frozen" state

$$\rho_0 U_i^* = \rho_\infty V_i^* \qquad (t_p / \Theta_\rho \to 0)$$

which means that

$$\rho_0^{(s)} v_i^{(s)} = \rho_0^{(f)} v_i^{(f)} \tag{2.109}$$

The "equilibrium" state is characterized by

$$U_i^* = V_i^* \qquad (t_p / \Theta_\rho \to \infty)$$

which means that

$$v_i^{(s)} = v_i^{(f)} \tag{2.110}$$

Here, t_p is a characteristic time in the dynamic process under consideration, and the relaxation time, Θ_ρ, is determined by (2.98). So, the "frozen" wave velocity corresponds to the equal pulse distribution over two phases (2.109). The interphase force is proportional to difference of phase velocities, and therefore the "equilibrium" state corresponds to condition (2.110). The wave velocities (2.106) do not depend on the rigidity of the pore matrix but only on phase compressibilites.

Both phases move in one direction in the P-wave of the first mode. The second mode is characterized by phase motions in the opposite directions.

For soft media, the corresponding system of equations has the form

$$
\begin{aligned}
&(1-m_0)\frac{\partial v_i^{(s)}}{\partial x_i}+m_0\frac{\partial v_i^{(f)}}{\partial x_i}=0\\
&(1-m_0)\rho_0^{(s)}\frac{\partial v_i^{(s)}}{\partial t}=\frac{\partial \sigma_{ij}^{(ef)}}{\partial x_j}-(1-m_0)\frac{\partial p}{\partial x_i}-\frac{m_0^2\mu}{k}(v_i^{(s)}-v_i^{(f)})\\
&m_0\rho^{(f)}\frac{\partial v_i^{(f)}}{\partial t}=-m_0\frac{\partial p}{\partial x_i}+\frac{m_0^2\mu}{k}(v_i^{(s)}-v_i^{(f)})\\
&\sigma_{ij}^{ef}=(K-\frac{2}{3}G)e\,\delta_{ij}+2G\,e_{ij}
\end{aligned}
\qquad (2.111)
$$

You can see that phase compressibilities are absent here. System (2.111) is the basic system for conventional soil mechanics if inertial forces are negligible. The dynamic variant (2.111) includes P-waves of the second mode and the S-waves considered above.

Thus,

$$
\frac{\partial^2\Phi}{\partial t^2}-c_*^2\nabla^2\Phi+\frac{\mu(1-m_0)}{km_0}\frac{\partial\Phi}{\partial t}=0 \qquad (2.112)
$$

for P-waves. Here, the corresponding wave velocity is determined by the following expression:

$$
c_*^2=\frac{1}{\rho_*}\left(K+\frac{4}{3}G\right) \qquad (2.113)
$$

which is determined by the elastic modulus of the porous matrix and by the following effective density:

$$
\rho_*=\frac{(1-m_0)}{m_0}\frac{\rho_0^{(s)}\rho_0^{(f)}}{\rho_\infty}=\frac{1-m_0}{m_0}\rho_0^{(s)}\rho_0^{(f)}\left(\frac{(1-m_0)}{\rho_0^{(s)}}+\frac{m_0}{\rho_0^{(f)}}\right) \qquad (2.114)
$$

The important case of negligible density of fluid phase $\rho^{(f)}\to 0$ ("dry" porous media) is characterized by the effective density

$$
\rho_*=(1-m_0)\rho_0^{(s)} \qquad (2.115)
$$

which is equal to real-matrix density. This means that, in the limit case, the P-waves of the second mode coincide with the usual seismic waves, but the waves of the first modes disappear because $p\to 0$ simultaneously with $\rho^{(f)}\to 0$. However, in the case of media saturated with fluids, the waves (2.112) can be seen only at very short distances because of their intense dissipation (see the third term of equation (2.112)).

2.3.3. WEAK NONLINEAR WAVES

Now let us consider a more complicated case of non-linear waves, accounting for high-frequency deviations - (2.74)-(2.75) - from Darcy's law. We use the balance equations (2.1), (2.2), (2.7) and (2.8) for one-dimensional motion with regard to nonlinear convective terms. The following two dynamic equations must be considered

$$\frac{\partial}{\partial t}\left\{(1-m)\left(\rho^{(s)}\frac{\partial v^{(s)}}{\partial t}+v^{(s)}\frac{\partial \rho^{(s)}}{\partial t}+\rho^{(s)}v^{(s)}\frac{\partial v^{(s)}}{\partial x}\right)\right\}+ \\ +m\left(\rho^{(f)}\frac{\partial v^{(f)}}{\partial t}+v^{(f)}\frac{\partial \rho^{(f)}}{\partial t}+\rho^{(f)}v^{(f)}\frac{\partial v^{(f)}}{\partial x}\right)=\frac{\partial^2}{\partial x^2}\left(a_1 v^{(s)}+a_2 v^{(f)}\right) \tag{2.116}$$

$$\frac{\partial}{\partial t}\left(\rho^{(f)}\frac{\partial v^{(f)}}{\partial t}+\rho^{(f)}v^{(f)}\frac{\partial v^{(f)}}{\partial x}+v^{(f)}\frac{\partial \rho^{(f)}}{\partial x}\right)- \\ -\frac{\mu m^2}{k}\left(1-a\frac{\partial}{\partial t}+b\frac{\partial^2}{\partial t^2}\right)\frac{\partial}{\partial t}(v^{(s)}-v^{(f)})=0 \tag{2.117}$$

In order to get the evolution equation for such waves, the moving coordinate system must be used:

$$\xi=\eta^{\alpha}(x-ct) \quad , \quad \tau=\eta^{\beta}t \tag{2.118}$$

where $\eta << 1$ is a small parameter used simultaneously for representation of dynamic variables in the form of series:

$$\begin{aligned}\rho^{(s)}&=\rho_0^{(s)}+\eta\rho_1^{(s)}+\eta^2\rho_2^{(s)}+\ldots\\ \rho^{(f)}&=\rho_0^{(f)}+\eta\rho_1^{(f)}+\eta^2\rho_2^{(f)}+\ldots\\ v^{(s)}&=\eta v_1^{(s)}+\eta^2 v_2^{(s)}+\ldots\\ v^{(f)}&=\eta v_1^{(f)}+\eta^2 v_2^{(f)}+\ldots\end{aligned} \tag{2.119}$$

The difference of phase velocity can to be estimated by the same parameter, η [37],

$$\zeta = v_1^{(s)}-v_1^{(f)} = O(\eta^{\gamma}) \tag{2.120}$$

because, from the previous linear analysis, we know that this difference has to have the same order for the first mode of P-waves. So, we can assume that $\gamma \geq 1$ and the first approximation of equations (2.116) and (2.117), where the interphase force is omitted, gives us

$$(a_1 - (1 - m_0)\rho_0^{(s)} c^2)\frac{\partial^2 v_1^{(s)}}{\partial \xi^2} = (m\rho_0^{(f)} c^2 - a_2)\frac{\partial^2 v_1^{(f)}}{\partial \xi^2}$$
$$a_3 \frac{\partial^2 v_1^{(s)}}{\partial \xi^2} = (\rho_0^{(f)} c^2 - a_4)\frac{\partial^2 v_1^{(f)}}{\partial \xi^2} \qquad (2.121)$$

The condition of comparability of these equations determines the wave velocity for the first mode:

$$c_I^2 = \{N_I \pm (N_I^2 - 4R_I Q_I)^{1/2}\} / (2R_I) \qquad (2.122)$$

where

$$N_I = \rho_0^{(f)}(a_1 - ma_3) + (1 - m)\rho_0^{(s)} a_4$$
$$R_I = (1 - m_0)\rho_0^{(s)}\rho_0^{(f)} \quad , \quad Q_I = a_1 a_4 - a_2 a_3$$

The second approximation gives us the evolution equation:

$$\frac{\partial \zeta}{\partial \tau} + (\sigma_* - \nu_* + \mu_* \zeta)\frac{\partial \zeta}{\partial \xi} - \delta\zeta = \phi \frac{\partial^2 \zeta}{\partial \xi^2} \qquad (2.123)$$

where constants $\sigma, \nu_*, \mu_*, \delta, \phi$ can be expressed in terms of $a, b, a_1, \ldots$. Here, $\mu_* \to 0$ if $m \to 0$ or $m \to 1$; $\delta = O(\mu_* m / k)$; $\nu_* = 0$; and $\phi = 0$ if the operator $F = 1$. The transitions to the usual scales of time and distance were completed.

The evolution equation has a sink ($\delta > 0$) of energy due to interphase force action and the Burgers term, which is on the right-hand side of (2.123) and which disappears along with the Darcy's law deviations when $b \to 0$, $\phi \to 0$.

The waves of the second mode are determined by the condition [37]

$$\zeta_I = v_1^{(s)} - v_1^{(f)} = O(1) \qquad (2.124)$$

The wave velocity is determined by the same expression (2.122) but with other values of constants. The corresponding evolution equation

$$\frac{\partial \zeta}{\partial \tau} + (\sigma_{**} + \mu_{**}\zeta)\frac{\partial \zeta}{\partial \xi} = \nu_{**}\frac{\partial^2 \zeta}{\partial \xi^2} - \nu_{***}\frac{\partial^2 \zeta}{\partial \xi \partial \tau} \qquad (2.125)$$

has the form of the Burgers equation with the additional term on the right-hand side. Again the second-order terms are connected with the Darcy's law deviations: $\nu_{**}, \nu_{***} = O(a)$ - see (2.76). So, for the Darcy law validity, both P-waves are evaluated according to the nonlinear equation for simple waves. As was shown recently [119], equation (2.125) would include the third derivatives with respect to ξ if the gradient viscous forces were accounted for in the dynamic equations of interpenetrating continua

2.4. Pore pressure and induced deformation of saturated strata

2.4.1. DEFORMATION OF STRATA

Let us consider the dynamic deformation process in a saturated porous stratum. According to this theory, essential strains of the porous matrix are created by P-waves of the second type and by S-waves when volume changes are developed simultaneously with fluid drainage. This can be seen from the different one-dimensional dynamic action on a soft saturated porous medium (Figure 2.4.).

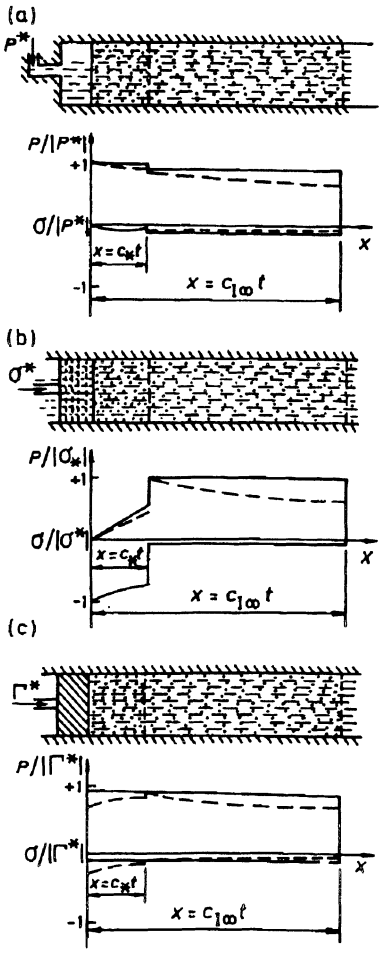

Figure 2.4. Scheme of stress waves of two modes in a saturated soft medium [156].

If fluid can leave the medium (case a) through a permeable piston, pore pressure and effective stress are essentially diminished. Therefore, poro-elastic deformation is also essential behind the second P-wave front with wave velocity c_*.

The first P-wave changes initial conditions for pore pressure from the value p_0 to p_*. Practically, p_* has the order of total applied load (σ_* , p_* or Γ_* depending on the type of loading). Because of this, the condition of zero strain ahead of the second P-wave front is more convenient for soft-saturated media and is used in practical soil mechanics.

Moreover, because of the high filter damping of the wave motion, equation (2.112) changes practically from the "telegraph" type to the Fourier type:

$$\frac{\partial p}{\partial t} = \kappa \nabla^2 p \quad , \quad \kappa = \frac{m_0}{(1 - m_0)} \frac{k}{\mu} (K + 4 / 3G) \tag{2.126}$$

where the pore pressure can be used instead of the scalar wave potential, Φ.

The problem, illustrated by case a in Figure 2.4, corresponds to "cooling" of a porous space "heated" by the first P-wave. The solution of (2.126) has the form [152, 156]

$$p(\zeta) = -\frac{2\sigma_*^{ef}}{\sqrt{\pi}} \int_0^{\zeta} e^{-z^2} dz \quad ,$$

$$\zeta = x/\sqrt{4\kappa t} \quad , \quad p(x, 0) = -\sigma_*^{ef} \quad , \tag{2.127}$$

$$\sigma^{ef}(0, t) = \sigma_*^{ef} \quad , \quad p(0, t) = 0$$

and is known as the one-dimensional plane process of filter consolidation. The displacement of the "piston"

$$u(0, t) = -\frac{\sigma_*^{ef}}{\sqrt{K + (4G / 3)}} \sqrt{\frac{k}{\pi \mu t}} \tag{2.128}$$

is developed in time and corresponds to the settlement of a foundation on a saturated soil.

The more general case of planar or three-dimensional slow (quasistatic) motion corresponds to linear system (2.111) but without inertial forces:

$$\frac{\partial m}{\partial t} + m_0 \frac{\partial v_i^{(f)}}{\partial x_i} = 0 \quad , \quad -\frac{\partial m}{\partial t} + (1 - m_0)\frac{\partial v_i^{(s)}}{\partial x_i} = 0$$

$$\frac{\partial \sigma_{ij}^{ef}}{\partial x_j} - (1 - m_0)\frac{\partial p}{\partial x_i} - \frac{m_0^2 \mu}{k}(v_i^{(s)} - v_i^{(f)}) = 0 \qquad (2.129)$$

$$\frac{\partial p}{\partial x_i} = -\frac{m_0 \mu}{k}(v_i^{(s)} - v_i^{(f)})$$

$$\sigma_{ij}^{ef} = (K - \frac{2}{3}G)\,\delta_{ij}\,e_{kl}\,\delta_{kl} + 2G\,e_{ij}$$

The following Biot form is used for this system for planar problems of stress-strain states in saturated soils or for the upper part of sedimentary rocks [156]:

$$G\nabla^2 u_1^{(s)} + (K + G/3)(\partial e/\partial x_2) - (\partial p/\partial x_2) = 0$$

$$G\nabla^2 u_2^{(s)} + (K + G/3)(\partial e/\partial x_2) - (\partial p/\partial x_2) = 0 \qquad (2.130)$$

$$\frac{\partial e}{\partial t} = \kappa \nabla^2 e \quad , \quad \kappa = \frac{k_0}{\mu_0 (K + 4G/3)}$$

if the displacement components $u_1^{(s)}$, $u_2^{(s)}$ are used and the physically reasonable initial condition of strain absence in the initial moment is

$$e(t, x_1, x_2) = 0 \quad , \quad t = 0 \qquad (2.131)$$

Equations (2.129) describe the process of pore-pressure "diffusion", including the biharmonic operator [156]:

$$\frac{\partial}{\partial t}\nabla^2 p = \kappa \nabla^4 p \qquad (2.132)$$

The operator ∇^4 is common for elasticity theory. The difference between equation (2.126) and (2.132) is explained by including both the shear and volume strains of the solid matrix in the second. Only in one-dimensional planar problems and in some plane-strain ($e_{3i} = 0$) and plane-stress ($\sigma_{3i}^{ef} = 0$) problems equations (2.126) and (2.132) are equivalent.

McNamee and Gibson [125] suggested an effective approach for studying the system (2.130). They introduced two potentials, S and Φ, such that

$$u_1^{(s)} = -\frac{\partial \Phi}{\partial x_1} + x_2 \frac{\partial S}{\partial x_2}$$
$$u_2^{(s)} = -\frac{\partial \Phi}{\partial x_2} + x_2 \frac{\partial S}{\partial x_2} - S \tag{2.133}$$

and, correspondingly,

$$e = \nabla^2 \Phi$$
$$p = (K + \frac{4}{3}G)\nabla^2 \Phi - 2G\frac{\partial S}{\partial x_2} \tag{2.134}$$

These potentials satisfy the following two equations which can be solved separately by integral transformation:

$$\frac{\partial}{\partial t}\nabla^2 \Phi = \kappa \nabla^4 \Phi \tag{2.135}$$

$$\nabla^2 S = 0 \tag{2.136}$$

2.4.2. DEFORMATION OF A LAYER

Reservoirs are usually modeled as thin porous layers in a highly stratified rock mass. Consider a small element of such a layer under uniaxial vertical load $\Gamma_{33} = \Gamma^*$, created by the weight of overcovering strata. Displacements of the porous matrix are also uniaxial ($z = x_3$):

$$u = u_1^{(s)} \quad , \quad u_1^{(s)} = u_2^{(s)} = 0 \tag{2.137}$$

If there is no drainage, then the condition for the fluid phase is

$$v_i^{(s)} = v_i^{(f)} \tag{2.138}$$

In the isothermal case, the mass balances (2.89) and (2.90) give the following differential connection:

$$\beta \frac{\partial p}{\partial t} - \frac{1}{3}\beta^{(s)} \frac{\partial \sigma^{ef}}{\partial t} + \frac{\partial^2 u}{\partial z \partial t} = 0 \tag{2.139}$$

Because

$$e = e_{33} = \partial u / \partial z \tag{2.140}$$

equation (2.136) can be represented in the form

$$\beta p - \frac{1}{3}\beta^{(s)} \sigma^{ef} + e = 0 \tag{2.141}$$

Additionally, we have the two following sequences of Hooke's law

$$\sigma_{33}^{ef} = (K + \frac{4}{3}G)e + K\beta^{(s)} p \tag{2.142}$$

$$\frac{1}{3}\sigma^{ef} = Ke + K\beta^{(s)} p \tag{2.143}$$

Excluding the strain, e, and the mean effective stress, σ^{ef}, gives the following connection between phase stresses:

$$(1 - K\beta^{(s)})\, \sigma_{33}^{ef} = -\{(K + \frac{4}{3}G)\beta + K\beta^{(s)}(\frac{4}{3}G\beta^{(s)} + 1)\}\, p \tag{2.144}$$

which allows determination of the distribution of total load

$$\Gamma^* = \sigma_{33}^{ef} - p \tag{2.145}$$

over phases for undrained conditions [152, 156]

$$\sigma_{33}^{ef} = (1 - n_{und})\, \Gamma^* \quad , \quad p = -n_{und}\, \Gamma^*$$

$$n_{und} = \frac{1 - K\beta^{(s)}}{1 + (K + \frac{4}{3}G)\beta - 2K\beta^{(s)}(1 + \frac{2}{3}G\beta^{(s)})} \tag{2.146}$$

In Table 2.2, the numerical value of the distribution parameter n_{und} is given for different compression modulus ratios $K\beta^{(s)}$, which show the consolidation levels of the porous matrix.

TABLE 2.2. Load distribution over phases.

$K\beta^{(s)}$	$<<0.1$	0.1	0.2	0.3	0.4	0.5
n_{und}	1.00	0.75	0.57	0.44	0.33	0.25
n_{dr}	1.00	0.9	0.8	0.7	0.6	0.5

The following additional data taken for this calculation are valid if Poisson's coefficient equals $\nu = 0{,}2$ and $\beta / \beta^{(s)} = 2.5$.

$$\beta(K + \frac{4}{3}G) = 5K\beta^{(s)} \quad , \quad 2G/3 = (1/2)K\beta^{(s)}$$

The ideal drainage condition means that fluid can escape from the layer element during loading so that the initial pressure, p_0, is kept constant. Then, Hooke's law (2.88) gives

$$e_{33} = \frac{\sigma_{33}^{ef} - K\beta^{(s)} p_0}{K + 4G/3} = -\frac{p^{ef}}{K + 4G/3} \tag{2.147}$$

that is, the uniaxial strain of the layer element is proportional to the effective pressure, p^{ef}, which is the part of the applied load:

$$p^{ef} = -\Gamma^* - n_{dr} p_0 \quad , \quad n_{dr} = 1 - K\beta^{(s)} \tag{2.148}$$

The correction coefficient, n_{dr}, is also given in Table 2.2.

Both considered situations can be modeled by special tests with rock samples in uniaxial cells (analogous to Figure 2.1, case c) when pore pressure is being measured under undrained conditions according to deformation law (2.148). During the testing of sandstone under drainage, it was found that $n_{dr} = 0.85$, which means that $K\beta^{(s)} = 0.15$ in this case.

In the case of soft soil $K\beta^{(s)} << 1$. Then, according to the Fillunger-Terzaghi concept [47, 216], normal strains are proportional to effective stresses. The generalized Hooke law (2.88) determines the connection of strains with both the effective stresses and the pore pressure. However, the advantage of the effective stress, σ_{ij}^{ef}, is explained by its being a difference (2.145) of two other measurable variables : applied total stress, Γ_{ij}, and pore pressure, p. Moreover, the failure criteria of saturated layers are formulated in terms of effective stress (Section 2.5) rather than the true stress, σ_{ij}.

2.4.3. PIEZOCONDUCTIVITY OF SATURATED FORMATIONS

As discussed previously, the load distribution inside a porous medium, including pore pressure, depends on fluid motion relative to the matrix. Therefore, deformation of the saturated layer is determined by the filter flow inside it, and these two processes are interconnected.

There is a simplifying hypothesis for analysis of seam deformation. In it, the main axis of the strain-stress state is vertical (two others are in the seam plane.), the matrix deformation, e_{ij}, is not equal to zero only along this axis ($i = j = 3$), and it is in accordance with the following estimations:

$$e_z = e_{33} = \partial u_3 / \partial x_3 \quad >> \quad \partial u_1 / \partial x_1 \, , \; \partial u_2 / \partial x_2 \tag{2.149}$$

Hooke's law (2.88) can be used here in the form

$$e_z = \frac{\sigma_z^{ef} - \beta^{(s)} Kp}{K + (4G/3)} \quad , \quad \sigma_{ij}^{ef} \delta_{ij} = 3K e_z + \beta^{(s)} Kp \tag{2.150}$$

and the total mass balance can be written as

$$\beta \frac{\partial p}{\partial t} - \frac{1}{3} \frac{\partial \sigma_{ij}^{ef}}{\partial t} \delta_{ij} + (1 - m_0) \frac{\partial v_i^{(s)}}{\partial x_i} + m_0 \frac{\partial v_i^{(f)}}{\partial x_i} = 0 \tag{2.151}$$

Their combination, together with Darcy's law, gives the equation of pore and effective pressure distribution in the saturated seam:

$$a \frac{\partial p}{\partial t} + b \frac{\partial \sigma_z^{ef}}{\partial t} = \frac{\partial}{\partial x_i} \left(\frac{k}{\mu} \frac{\partial p}{\partial x_i} \right)$$

$$a = \beta - \beta^{(s)} \beta^{(s)} K - \frac{(1 - m_0)(1 - \beta^{(s)} K)}{K + (4G/3)} \tag{2.152}$$

$$b = \frac{1 - m_0 - \beta^{(s)} K}{K + (4G/3)}$$

where $i \, , \, j = 1 \, , \, 2$ and displacements of the solid matrix in the layer plane are assumed to be negligible [152, 156].

At the impermeable upper and lower boundaries of the layer, the following condition is valid:

$$\sigma_z^{ef} - p = \Gamma_z \tag{2.153}$$

but there are two variants for total load determination. According to the first,

$$\Gamma_z = const \quad , \quad \partial p/\partial t = \partial \sigma_z / \partial t \tag{2.154}$$

and the well-known Fourier equation follows

$$\frac{\partial p}{\partial t} = \kappa \frac{\partial^2 p}{\partial x_i \partial x_i} \tag{2.155}$$

with the coefficient of piezoconductivity [156]

$$\kappa = \left(\beta - \beta^{(s)} \beta^{(s)} K - \frac{m_0 \beta^{(s)} K}{K + (4G/3)} \right) \frac{k}{\mu} \tag{2.156}$$

According to the second variant, the total stress is determined by the elastic solution for surrounding strata. Such a solution has to connect the pore pressure changes inside the reservoir with settlement of ground surface above the reservoir. Because the boundary condition (2.153) includes two variables, it is necessary to add one more condition - for example, one concerning the boundary displacement:

$$u_z = n_z \sigma_z^{ef} \quad , \quad n_z = h / E \tag{2.157}$$

where h is the layer thickness, and E is the Young modulus. Consider the plane case and model the upper strata as an infinite elastic plate with effective rigidity, $E_* H^3$, under the lithostatic pressure , $\Gamma = \gamma H$, determined by its own thickness, H (that is, by the depth, H, of the reservoir). Then the strata equilibrium is governed by the equation [156]

$$E_* H^3 \frac{\partial^4 u_z}{\partial x^4} = \Gamma + \sigma^{ef} - p \tag{2.158}$$

and higher-order derivatives appear in the nonlocal piezoconductivity equation:

$$\frac{a}{a+b} \frac{E_* h H^3}{E_l} \frac{\partial^5 p}{\partial x^4 \partial t} + \frac{\partial p}{\partial t} = \kappa \left(\frac{\partial^2 p}{\partial x^2} - \frac{E_* h H^3}{E_l} \frac{\partial^6 p}{\partial x^6} \right) \tag{2.159}$$

$$\kappa = \left(\frac{k}{\mu} \right) (a+b)^{-1}$$

The vertical displacements, u_z (that is, the ground settlement), can be calculated for pore pressure changes found from equation (2.159):

$$u_z = -\frac{h}{2}\int_{-\infty}^{\infty}\frac{p(\xi,t)}{E}exp\left(-\frac{x-\xi}{H\sqrt{2}}\sqrt{\frac{HE}{hE_*}}\right)sin\left(-\frac{x-\xi}{H\sqrt{2}}\sqrt{\frac{HE}{hE_*}}+\frac{\pi}{4}\right)d\xi \tag{2.160}$$

$$\approx -\frac{h}{2\sqrt{2}}\int_{-\infty}^{\infty}\frac{p(\xi,t)}{E}exp\left(-\frac{\pi(x-\xi)^2}{8H^2}\sqrt{\frac{HE}{hE_*}}\right)d\xi$$

Of course, more detailed calculation, found numerically or analytically in combination with the equation (2.152), includes the full elastic solution for the upper overloading strata. In the case of axial symmetry, the piezoconductivity equation following from (2.152) will have the integro-differential form [152]

$$\frac{\partial p}{\partial t}+bK_*\int_0^{\infty}\frac{h\xi^2 J_0(\xi r)}{d-\xi h}\left\{\frac{\partial}{\partial r}\int_0^{\infty} y\,J_0(\xi y)p(y,t)dy\right\}d\xi = \frac{\kappa}{r}\frac{\partial}{\partial r}\left(r\frac{\partial p}{\partial r}\right) \tag{2.161}$$

where K_* is an effective volume modulus, J_0 is the Bessel function, and

$$d = \frac{n_z}{G}\frac{K+(4G/3)}{K+(G/3)}$$

Equation (2.161) is valid for deep and thin layers determined by the nonequality

$$H >> h \tag{2.162}$$

Some calculations have shown that simultaneous changes of pore pressure and effective stress can cause local extreme values of pore pressure inside saturated strata. This is the Mandel-Crayer effect, which is explained by deformation of porous space [152]; it is impossible for the simple piezoconductivity equation of the Fourier type as (2.155). This could open an approach to the liquifaction phenomena.

2.5. Hydrofailure and hydrofracturing of rocks

2.5.1. IRREVERSIBLE DEFORMATION OF SATURATED STRATA

The theoretical study of nonelasticity and fracture of saturated geomaterials is based on the effective stress principle. This means that all critical states of a porous matrix, as a conglomerate, are controlled by the effective stresses [216].

For example, the plastic state of geomaterials appears if the following limit condition is fulfilled [152]:

$$\sigma_\tau + \alpha\sigma^{ef} - Y = 0 \tag{2.163}$$

Then, the corresponding constitutive law for plastic is

$$\frac{De_{ij}^p}{Dt} = \left\{\sigma_{ij}^{ef} + \frac{2}{3}\Lambda Y\,\delta_{ij} - \left(1 + \frac{2}{3}\Lambda\alpha\right)\sigma_{ij}^{ef}\delta_{ij}\right\}\frac{d\lambda}{dt} \tag{2.164}$$

and the elastic parts of strain-rates are valid:

$$\frac{D\sigma_{ij}^{ef}}{Dt} = (K - \frac{2}{3}G)\frac{De^e}{dt}\delta_{ij} + 2G\frac{de_{ij}^e}{dt} - \beta^{(s)}K\frac{dp}{dt} \tag{2.165}$$

As usual, they are combined by the simple summation into total deformation

$$\frac{De_{ij}}{Dt} = \frac{De_{ij}^e}{Dt} + \frac{De_{ij}^p}{Dt} \tag{2.166}$$

and a new scalar parameter, $d\lambda\ /\ dt$, is unknown a priori. This scalar must be found by solving equations (2.89), (2.90), (2.91) and (2.92), together with (2.163) through (2.166). Generally speaking, it is proper to solve problems in displacement velocity form and to obtain the displacements themselves after integration.

Although, formally, condition (2.163) is analogous to the one for dry porous geomaterial, there is the difference in the weakening of geomasses due to pore pressure increase. This effect is very essential and can be seen from another form of (2.163) - that is,

$$\sigma_\tau + \alpha(\Gamma - p) - Y = 0 \tag{2.167}$$

The elastic modules, K, G, and dilatancy rate, Λ, are assumed to be the same as in the dry states of the medium. However, there are some experimental data which show a definite diminishing of K and G due to fluid presence at particle contacts in soils.

Typical deformation curves for saturated Berea sandstone during triaxial tests are given in Figure 2.5 (according to J.Handin, see [8]). You can see that stress-strain

curves are different if the pore pressure is a parameter, but they coincide if effective confining pressure plays such a role.

According to the same data, there are two upper limits for shear stress. The first one corresponds to the peak value of curves and can be easy seen at low confining pressure. It can be interpreted as the strength of matrix internal bounds. The second one can be interpreted as the strength of saturated sandstone and corresponds to plastic matrix flow (unlimited deformation). The same experiments [8] show that if one used the effective stress concept, the second one corresponded to the Coulomb line (2.163) with friction angle $\chi = 29^o$ and cohesion $\approx$ 20 *MPa*. The disappearance of "peak" strength at high confining pressure may be understood as the transition to plastic flow without the preliminary brittle crushing of matrix contact bounds.

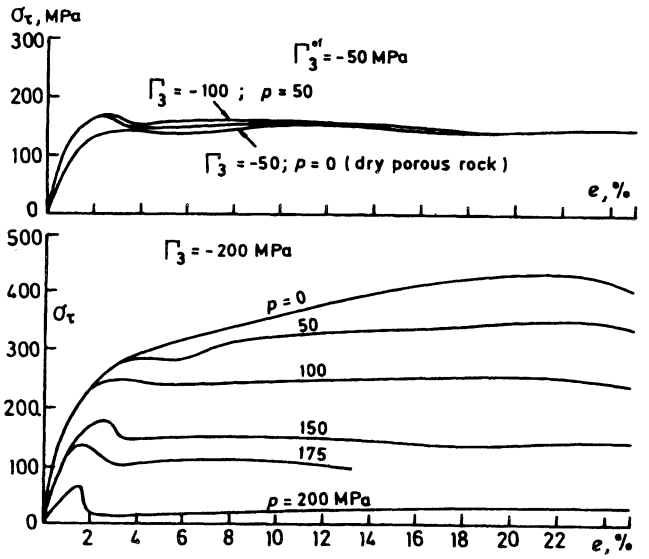

Figure 2.5. Handin's data shows that the effective stress governs the strength of a porous sandstone.

In Figure 2.6, the effect of sand-grain rupture is shown at pressures above *70 bars*, according to [86]. You can see that it creates a kink of yield surface (2.167) corresponding to the change of friction angle values. The same phenomenon is observed in tuffs (Figure 2.7) and can be explained by the rupture of bonds and the change of internal strength mechanisms.

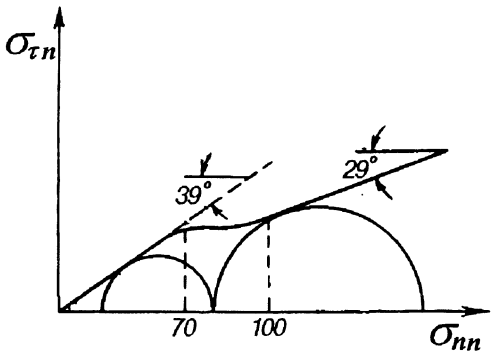

Figure 2.6. Crushing of grains causes diminishing of internal friction angle [86]

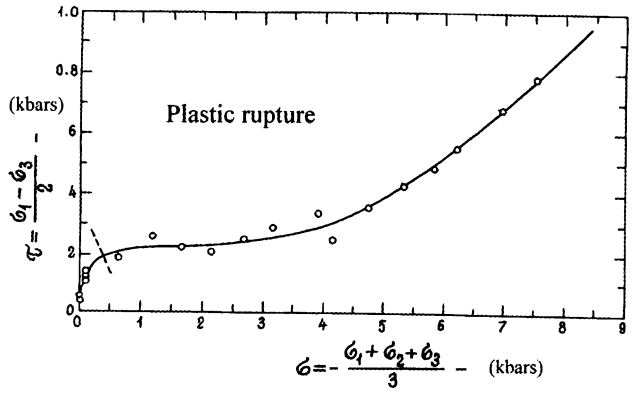

Figure 2.7. Yield surface of tuffs (Courtesy of R.N.Schock).

In accordance with the effective stress concept, the viscoelastic porous matrix saturated with fluid is governed by the following stress-strain connection [35]:

$$\sigma_{ij}^{ef} = (K - \frac{2}{3}G)e\,\delta_{ij} + G\,e_{ij} + \beta^{(s)}\,Kp\,\delta_{ij} + \tag{2.168}$$

$$+\mu\left(\frac{\partial v_i^{(s)}}{\partial x_j} + \frac{\partial v_j^{(s)}}{\partial x_i} - \frac{2}{3}\frac{\partial v_k^{(s)}}{\partial x_k}\delta_{ij}\right) + \zeta\frac{\partial v_k^{(s)}}{\partial x_k}\delta_{ij}$$

where μ , ζ are shear and volume viscosity's of the matrix, respectively. This constitutive law can be used to study clay stratum deformation or rock creep.

2.5.2. PLASTICITY OF A WELL VICINITY

Consider the problem of plastic zone creation around an uncased well due to pumping fluids from the stratum (a problem studied by the author and T.K. Ramazanov). The axisymmetrical equilibrium equations for total stresses in saturated media can be written as

$$\frac{1}{r}\frac{\partial}{\partial r}(r\,\sigma_{rr}^{ef}) - \frac{\sigma_{\theta\theta}^{ef}}{r} + \frac{\partial \sigma_{rz}^{ef}}{\partial z} - \frac{\partial p}{\partial r} = 0$$

$$\frac{1}{r}\frac{\partial}{\partial z}(r\,\sigma_{zz}^{ef}) + \frac{1}{r}\frac{\partial}{\partial r}(r\,\sigma_{rz}^{ef}) - \frac{\partial p}{\partial z} - (1-m)(\rho^{(s)} - \rho^{(f)}) = 0 \tag{2.169}$$

where σ_{rr}^{ef} , $\sigma_{\theta\theta}^{ef}$, σ_{zz}^{ef} and σ_{rz}^{ef} are the radial, hoop, axial and shear effective stresses, respectively.

We can now use the Westergaard stress functions f and F for total stress Γ_{ij} such that

$$\sigma_{rr}^{ef} = (\rho^{(s)} - \rho^{(f)})z + \frac{1}{r}\frac{\partial^2 F}{\partial z^2} + \frac{f}{r} + p$$

$$\sigma_{\theta\theta}^{ef} = (\rho^{(s)} - \rho^{(f)})z + \frac{\partial f}{\partial r} + p \tag{2.170}$$

$$\sigma_{zz}^{ef} = (\rho^{(s)} - \rho^{(f)})z + \frac{1}{r}\frac{\partial^2 F}{\partial r^2} + p$$

$$\sigma_{rz}^{ef} = -\frac{1}{r}\frac{\partial^2 F}{\partial r \partial z}$$

For this stress solution, the compatibility equations are used, which utilize the condition that six strains, e_{ij} , are generated by only three displacement functions, u_j, in the elastic zone. The analysis shows that

$$f = C_1 r + \frac{A(z)}{r} \quad , \quad \frac{\partial^2 F}{\partial z^2} \approx 0$$

Correspondingly, the effective stresses are

$$\sigma_{rr}^{ef} = (\rho^{(s)} - \rho^{(f)})z - \frac{A(z)}{r^2} + C_1 - p$$
$$\sigma_{\theta\theta}^{ef} = (\rho^{(s)} - \rho^{(f)})z + \frac{A(z)}{r^2} + C_1 - p \tag{2.171}$$

If the saturated stratum is sealed by the impermeable layer of thickness, H, and density, ρ, then the parameter C_1 can be determined:

$$\sigma_{rr}^{ef} = \rho H + (\rho^{(s)} - \rho^{(f)})(z - H) - \frac{A(z)}{r^2} + p$$
$$\sigma_{\theta\theta}^{ef} = \rho H - (\rho^{(s)} - \rho^{(f)})(z - H) + \frac{A(z)}{r^2} + p \tag{2.172}$$

Assume that the plastic state takes place in a form of plane flow inside the ring zone $r_w \le r \le b(z)$, where r_w is the well radius, and $b(z)$ is the elastoplastic boundary. It is suggested that the disturbances of axial normal stresses in this zone are negligible. So, the limit condition (2.163) can be rewritten as

$$\sigma_{\theta\theta}^{ef} - (N+1)\sigma_{rr}^{ef} = q \tag{2.173}$$

The introduction of (2.169) into (2.173) permits us to find the stress function, f, for the plastic zone and determine the stresses there:

$$\sigma_{rr}^{ef} = C_1 r^N - \frac{q}{N} + r^N \int \frac{\partial p}{\partial r}\frac{dr}{r^N}$$
$$\sigma_{\theta\theta}^{ef} = (N+1)C_1 r^N - \frac{q}{N} + (N+1)\int \frac{\partial p}{\partial r}\frac{dr}{r^N} \tag{2.174}$$

The constant C, unknown function $A(z)$ and elastoplastic boundary $b(z)$ are evaluated from the following boundary conditions. The first is the equality of total radial stresses at the uncased well surface to pore pressure - that is,

$$\sigma_{rr}^{ef} = 0 \quad , \quad r = r_\omega \tag{2.175}$$

The second condition means equality of the radial stresses at the elastoplastic boundaries:

$$[\sigma_{rr}^{ef}] = 0 \quad , \quad r = b(z) \tag{2.176}$$

The third condition means the continuity of the solid displacement velocity at the same boundary:

$$[v_r^{(s)}] = 0 \quad , \quad r = b(z) \tag{2.177}$$

Sometimes the equality of hoop stress components is used instead of (2.177):

$$[\sigma_{\theta\theta}^{ef}] = 0 \tag{2.178}$$

Physically, this means that the same limit condition is used as a criterion for geomaterial failure and for plastic flow in a failure state inside the zone of plasticity. In other words, condition (2.173) is used at both the <<+>> and <<->> sides of the boundary $r = b(z)$. This is a particular case.

The evaluation of fluid flow can be done on the basis of the simple dilatancy condition

$$\frac{\partial v^{(s)}}{\partial r} + \frac{v^{(s)}}{r} = \Lambda_*\left(\frac{\partial v^{(s)}}{\partial r} - \frac{v^{(s)}}{r}\right)\theta_\gamma \tag{2.179}$$

the momentum balance for fluid flow (equivalent to the following form of Darcy's law)

$$\frac{k}{\mu}\frac{\partial p}{\partial r} = -m(v^{(f)} - v^{(s)}) \tag{2.180}$$

and the mass balances

$$\frac{\partial}{\partial t}\rho^{(s)}(1-m) + \frac{1}{r}\frac{\partial}{\partial r}(r\,\rho_1^{(s)}(1-m)\,v^{(s)}) = 0 \tag{2.181}$$

$$\frac{\partial}{\partial t}\rho^{(f)}m + \frac{1}{r}\frac{\partial}{\partial r}(r\,\rho^{(f)}m\,v^{(f)}) = 0 \tag{2.182}$$

Here, Λ_* is the dilatancy rate for this type of flow geometry:

$$\Theta_\gamma = sign\,(\partial v / \partial r - v / r) = sign\,(\sigma_{rr}^{ef} - \sigma_{\theta\theta}^{ef}).$$

The integration of (2.179) gives the first dilatational connection inside the plastic zone $r < b$

$$v^{(s)} = \frac{C_2(t)}{r^n} \quad , \quad n = \frac{1 + \Lambda_*\Theta_\gamma}{1 - \Lambda_*\Theta_\gamma} \tag{2.183}$$

Then, the porosity distribution follows from (2.181)

$$m = 1-(1-m_0)r^{n-1}\{r^{1+n}-(1-n)W\}^{\frac{1-n}{1+n}} \tag{2.184}$$

if $\rho^{(s)} = const$ and $m = m_0$ at $t = 0$. Here,

$$W = \int_0^t C_2(t)dt \quad , \quad C_2(t) = -\frac{Q^{(s)}}{2\pi h r_w} r_w^n < 0 \tag{2.185}$$

and the "sand production", $Q^{(s)}$, is determined by the solid particle velocity at the well surface:

$$Q^{(s)} = -2\pi r_w v^{(s)}(r_w)(1-m_w) \tag{2.186}$$

Using the porosity (2.184) in the fluid equations - (2.180) and (2.182) - permits us to find

$$-\frac{k}{\mu}\frac{\partial p}{\partial r} = \frac{C_2(t)}{r^n} + \frac{B(t)}{r}$$

$$B(t) = \frac{Q^{(f)} - Q^{(s)}}{2\pi h} \tag{2.187}$$

where $Q^{(f)}$ is the well's fluid production. Further, it is possible to find the stress distribution in the vicinity of the well due to sand production. The output productions $Q^{(f)}$ and $Q^{(s)}$ can be measured or calculated, for example, on the basis of assumptions on far pore pressure and total (lithostatic) stress constancy.

This sand production is connected with reservoir failure and has a catastrophic character. Additional minor damage of the reservoir is connected with the transportation of fine particles inside the fluid or gas flow to the well. Creation of fluid channels inside a weak porous matrix also takes place in reality [200].

2.5.3. HYDROFRACTURE OF SEAMS

The elastic stresses around a well can lead to the hydrofracturing of rocks that may be used to increase well productivity [59, 233]. Consider the following solution, which corresponds to the nonequal horizontal pressures $P_1 = -\Gamma_1$ and $P_2 = -\Gamma_2$, which are assumed to be smaller than the vertical pressure. The problem is planar:

$$\sigma_{rr} = -\frac{1}{2}(P_1+P_2)\left(1-\frac{r_w^2}{r^2}\right) - \frac{1}{2}(P_1-P_2)\left(1+3\frac{r_w^4}{r^4}-4\frac{r_w^2}{r^2}\right)\cos 2\theta \tag{2.188}$$

$$\sigma_{\theta\theta} = -\frac{1}{2}(P_1 + P_2)\left(1 + \frac{r_w^2}{r^2}\right) + \frac{1}{2}(P_1 + P_2)\left(1 + 3\frac{r_w^4}{r^4}\right)\cos 2\theta \qquad (2.189)$$

$$\sigma_{r\theta} = +\frac{1}{2}(P_1 + P_2)\left(1 - 3\frac{r_w^4}{r^4} + 2\frac{r_w^2}{r^2}\right)\sin 2\theta \qquad (2.190)$$

According to these expressions, the lowest compression stress exists at the well radius at the angles $\theta = 0\ ,\ \pi / 2$:

$$\sigma_{\theta\theta} = -(3P_2 - P_1) \quad , \quad P_2 > P_1 \qquad (2.191)$$

So, if a small crack of rock exists at this point, it is necessary to overcome not only the lithostatic pressure (2.191) but also the tensile strength, σ_t [197], which is resistant to fracture process (Section 1.5.5).

Practically, crack growth can be reached by the hydrofracturing (that explain the entrance of fluid into defects in the porous layer, which has a form of radial microcracking). The pressure of injected fluid must be equal the total resistance mentioned above:

$$p_{\mu hf} = (3P_2 - P_1 - p_0) + \sigma_t \qquad (2.192)$$

Here, it is assumed that, in accordance with the effective stress concept, pore pressure existing in the reservoir, p_0, at $r = r_w$ diminishes lithostatic forces. The tensile strength, σ_t, is essentially smaller for a porous matrix than for intact rocks.

If injected fluid enters into pore space, the real fracturing develops inside the matrix and the effective stress, created by lithostatic forces, is diminished according to the expression (2.146). Then,

$$p_{\mu hf} = \frac{1}{n_{und}}(3P_2 - P_1 - p) + \sigma_t \qquad (2.193)$$

and n_{und} is chosen for fast fracturing when the injected fluid has no practically possibility for drainage. If the process is very slow, drainage conditions are fulfilled and the bigger coefficient, n_{dr}, is introduced into (2.193) instead of n_{und}. This means that then breakdown-fracture pressure is lower in the case of a low-viscosity fluid and a low rate of injection. So, the vertical fracture appears. Because the horizontal lithostatic pressure grows faster with depth then the vertical lithostatic pressure, the horizontal hydrofracturing occurs more often at deep reservoirs.

Well pressure can be measured during the injection process. The typical curve and its interpretation are given in Figure 2.8 according to [59], where more useful details and technological methods are described.

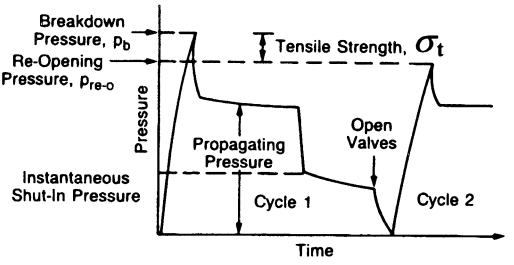

Figure 2.8. Borehole pressure as a function of time during a cycle hydrofracturing (Courtesy of M.J.Economides)

Additional fracture propagation is connected with the pressure drop inside the narrow channel in which width w is unknown. There are two approximations for this estimation. The first accounts for the rigidity of elastic matrix:

$$w = a\frac{p - p_0}{E}x_f \tag{2.194}$$

where x_f is the normalized distance from the crack tip, and a is the numerical constant.

The second approximation is based on the elastic displacement in the direction orthogonal to the crack:

$$w = \frac{p - p_0}{E}\frac{h}{2} \tag{2.195}$$

Here, h is the thickness of the layer. Introducing one of these expressions into the fluid balance inside the crack results in the nonlinear Fourier equation [59]:

$$\frac{\partial w}{\partial t} = \frac{E}{h\mu}\frac{\partial}{\partial x}\left(w^3\frac{\partial w}{\partial x}\right) \tag{2.196}$$

The second necessary boundary condition must be formulated for the fluid mass injected into the crack, where the permeability of the crack is proportional to w^3 and fluid percolation from the crack is ignored. The initial and boundary conditions are:

$$w(x, t = 0) = 0 \quad ; \quad w(x, t) = 0 \quad , \quad x \geq x_f \tag{2.197}$$

Recall that equation (2.196) determines the finite zone of the nontrivial solution $w(x, t) > 0$ as the nonlinear diffusion equation (see, Section 3.1).

The tensile strength is negligible comparative to the lithostatic forces, which must be in equilibrium with the fluid pressure distribution in the crack vicinity - that is,

$$\frac{2}{\pi} \int_0^{x_f} \frac{p(x)\, dx}{\sqrt{x_f^2 - x^2}} = \Gamma^* \approx P_1, P_2 \tag{2.198}$$

according to the Barenblatt analysis (see [59, 233]). Here, Γ^* is the mean compression stress, and the stress concentration is taken into account. Singularities at a crack tip have to be studied carefully [48].

The sand is injected together with the fracturing fluid to keep the crack in an open state after the pressure decline.

The diminishing values P_1, P_2, in comparison with such averaged estimations as $P \approx \gamma H$, indicates that there is some global geological reason for the local unloading of a porous matrix can be explained by further geomechanical studies. As seen in Figure 2.9, hydrofracturing pressures are higher at the vicinities of the fault and are also dependent on geological structure.

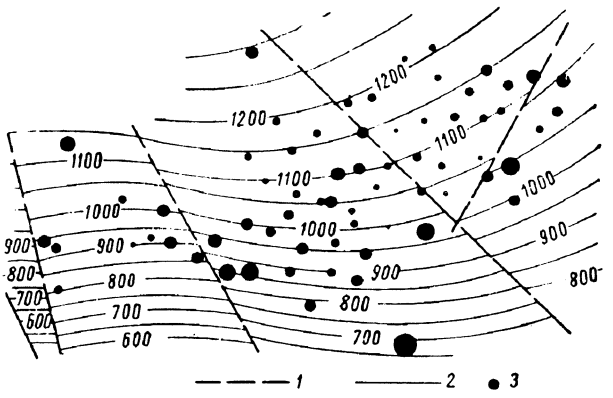

Figure 2.9. The map of fracture pressure excess above hydrostatic pressure for Umbaki oil reservoir in Azerbaijan (1 = tectonic fault, 2 = depth, 3 = relative excess), according to the author diploma thesis (1957).

CHAPTER 3

HYDRODYNAMICS OF RESERVOIRS

3.1. Basic nonstationary flows of a homogeneous fluid

3.1.1. HYDRAULIC THEORY OF GROUNDWATER FLOW

According to the conventional approach, reservoir pore pressure and well productivity are determined by more simple mathematical models than those discussed above.

In the case of water flows in soils above rigid and impermeable basements (Figure 3.1), the mass balance (2.2) is averaged over the cross-section and Darcy's law (2.66) is used with the assumption that the porous matrix is immovable. Thus,

$$m\frac{\partial h}{\partial t} + \frac{\partial h w_i}{\partial x_i} = 0 \tag{3.1}$$

because ρ , $m = const$, water content h coincides with the cross-sectional flow area, and

$$w_i = -c_f \frac{\partial h}{\partial x_j} \quad , \qquad c_f = \frac{k\rho^{(f)} g}{\mu} \tag{3.2}$$

where h also plays the role of a filter head assumed to be uniform in a cross-section of flow. The combination of (3.1) and (3.2) gives the Boussinesq equation

$$\frac{\partial h}{\partial t} = \frac{c_f}{m}\frac{\partial}{\partial x_j}\left(h\frac{\partial h}{\partial x_j}\right) \tag{3.3}$$

Here, c_f is the filter coefficient (2.67) whose dimension coincides with the filter velocity dimension and i , $j = 1$, 2. The main sequence of its nonlinearity possibly has moving fronts with sharp changes of unknown variables, while the linear variant of equation (3.3), which is the nonlinear Fourier equation [169], permits smooth solutions only for $t > 0$.

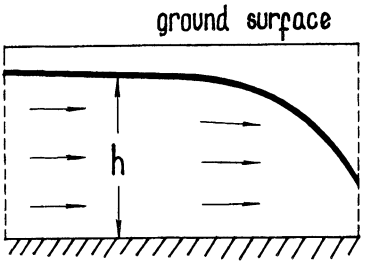

Figure 3.1. The hydraulic theory of groundwater flow is based on assumption that head is constant in a cross-section.

In the case of infiltration or water inflow from the deeper reservoirs through the half-permeable basement, sources will appear in the mass balance (3.1) and subsequently on the right-hand side of the resulting equation (3.3) for the hydraulic theory of groundwater flow.

Equation (3.3) is nonlinear and can be solved by an asymptotic [169] or numerical method. An example is given in Figure 3.2 where the following variables are used:

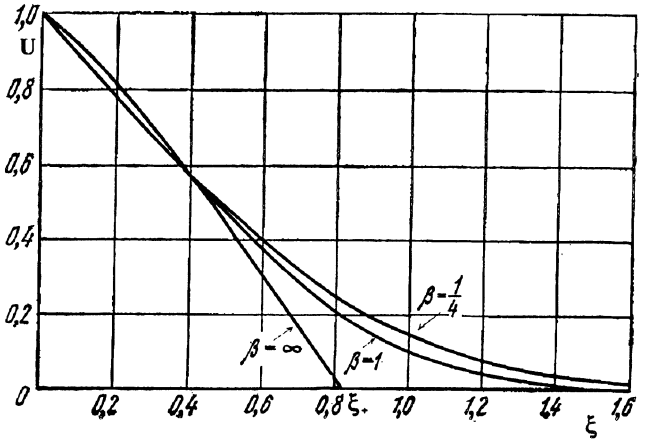

Figure 3.2. Groundwater planar flow (with water front if $\beta=\infty$) into a porous barrier.

$$U = \frac{h - H_2}{\Delta H} \quad , \qquad \xi = \frac{x}{\sqrt{2c_f t}} \tag{3.4}$$

with β as a parameter

$$\beta = \frac{\Delta H}{H_2} \quad , \qquad \Delta H = H_2 - H_1 \tag{3.5}$$

of the nonstationary groundwater flow with the following boundary conditions:

$$h(x, 0) = h(\infty, t) = H_2 \quad , \qquad h(0, t) = H_1 \tag{3.6}$$

You can see the principal peculiarity of the nonlinear equation (3.3). In the case of a zero initial condition ($H_2 = 0$ or $\beta = \infty$), there is a value ξ_+ which corresponds to the front of water presence moving with finite [169] velocity

$$\frac{dx}{dt} = \xi_+ \sqrt{\frac{c_f}{2mt}} \tag{3.7}$$

At this front, the conditions

$$h(\xi_+) = 0 \quad , \qquad [dh / d\xi] \neq 0 \tag{3.8}$$

of the second-order discontinuity is valid. In the case of any nonzero initial water head, $H_2 \neq 0$ in the porous barrier, the initial discontinuity, $\Delta h\,(0, 0) = \Delta H_2$, will disappear instantly and only a smooth solution will be valid everywhere - that is,

$$[dh / d\xi] = 0 \quad , \qquad x\,, t > 0 \tag{3.9}$$

3.1.2. ELASTIC REGIME OF FILTER FLOW

Head-filter flows are characterized by the total sealing of cross-sections by rigid impermeable walls. The pore space is filled completely with moving fluid, pore pressure is not directly connected to fluid presence, and fluid and pore space compressibilities are accounted for. The corresponding set of equations has the following form:

$$\frac{\partial m \rho^{(f)}}{\partial t} + \frac{\partial \rho^{(f)} w_i}{\partial x_i} = 0$$

$$w_i = -\frac{k_{ij}}{\mu} \frac{\partial}{\partial x_j}\left(p + \rho^{(f)} g\, \delta_{i3} x_3\right) \tag{3.10}$$

where $i, j = 1, 2, 3$, x_3 is the vertical coordinate, and the matrix displacement is neglected - compare with (2.129). Fluid compressibility can be taken in linear form (2.87) for water (or oil) with coefficients independent of pore pressure. For gases, relation (2.87) changes to

$$\rho^{(g)} = \frac{p}{RTZ} \tag{3.11}$$

Here, R is the universal gas constant, T is the absolute temperature, and Z is the supercompressibility coefficient which accounts for the real deviation from the perfect gas equation of state. However, the state equation (3.11) is usually utilized in another form:

$$\rho^{(g)} = \rho_0^{(g)} \frac{p}{p_0} \tag{3.12}$$

where $\rho_0^{(g)}$, p_0 are values corresponding to the reference state (at normal conditions when $p_0 = 1\ bar = 0.1\ MPa$, and $T_0 = +20^{\circ}C$).

Here, the deformation of pore space is accounted for by the porosity changes with pore pressure:

$$\frac{m(p)}{m_0} = 1 + a_m(p - p_0) \tag{3.13}$$

Connection (3.13) uses the assumption [156]

$$\Gamma_{ij} = \sigma_{ij}^{ef} - p = const \quad , \qquad i = j \tag{3.14}$$

because it allows the use of the true constitutive law (2.88), the consequence (2.89) of the mass balance of the solid material, and to avoid more complicated analyses (Section 2.4).

The simplest linear form of the piezoconductivity equation is valid for planar head flows in layers with constant temperature and permeability, k:

$$\frac{\partial p}{\partial t} = \kappa \nabla^2 p \quad , \qquad \kappa = \frac{k}{\mu_0 \beta m_0} \tag{3.15}$$

which follows from equations (3.10), (2.87), (3.13) and (3.14). Here, $\beta = a_m + a_\rho$ is the effective compressibility of the layer, and κ is the piezoconductivity [196]. If the layer is inclined, then the gravity effect has to be included [14, 195]:

$$\frac{\partial p}{\partial t} = \kappa\left(\nabla^2 p + g\,\rho_0^{(f)} \nabla^2 z\right) \tag{3.16}$$

where $z(x_1, x_2)$ is the height of the seam middle plane above the reference horizontal.

Nonlinear piezoconductivity corresponds to essential changes of porous space when [156]

$$\frac{m}{m_0} = e^{-a_m(p-p_0)} \quad , \qquad \frac{k}{k_0} = e^{-a_k(p-p_0)} \tag{3.17}$$

and the analogous exponential connections can be used for fluid density and viscosity as well as for seam thickness

$$\frac{\rho^f}{\rho_0^f} = e^{-a_\rho(p-p_0)} \quad , \qquad \frac{\mu}{\mu_0} = e^{-a_\mu(p-p_0)} \quad , \qquad \frac{h}{h_0} = e^{-a_h(p-p_0)} \tag{3.18}$$

Their introduction into the system (3.10) gives the nonlinear equation [156]

$$\frac{\partial \varphi}{\partial t} = \kappa \nabla^2 \varphi^\gamma \quad , \quad \varphi = e^{-\beta(p-p_0)}$$

$$\gamma = \frac{\alpha}{\beta} \quad , \quad \kappa = \frac{k_0}{\mu_0 m_0 \alpha} \tag{3.19}$$

$$\alpha = a_k + a_\rho + a_h - a_\mu \quad , \quad \beta = a_m + a_\rho + a_h$$

and Darcy's law (3.11) has now the form

$$W_i \equiv h w_i = -\frac{k_0 h_0}{\mu_0 \alpha} \frac{\partial \varphi}{\partial x_j}$$

The ideal gas-filter flows are governed by the Leibenson equation, which follows from (3.10) and (3.11) if the porous space is not deformable:

$$\frac{\partial p}{\partial t} = \kappa \nabla^2 p^2 \quad , \qquad \kappa = \frac{k}{2\mu m} \tag{3.20}$$

In the more general case, equations (3.19) and (3.20) can be represented by the nonlinear form [156]

$$f(\Phi)\frac{\partial \Phi}{\partial t} = \nabla^2 \Phi \tag{3.21}$$

where the Leibenson function is used [152] because the substitution (3.18) changes pressure, p, by Φ in every function:

$$\Phi = \int \frac{k(p)\,\rho(p)\,h(p)}{\mu(p)}\,dp$$

and

$$f(\Phi) = \frac{d(m\rho h)}{d\Phi}$$

3.1.3. NONSTEADY FLOWS IN RESERVOIRS

Nonstationary fluid flows are extremely simple for layers with constant thickness because the corresponding basic solutions are self-similar. Consider plane flow with following initial and boundary conditions and governed by the equation (3.19):

$$\varphi(x, 0) = 1\,, \quad \varphi(\infty, t) = 1\,, \quad \varphi(0, t) = \varphi_0 \tag{3.22}$$

The transition to the variable

$$\xi = \frac{x}{\sqrt{2\kappa t}} \tag{3.23}$$

where x is the coordinate along the layer, reduces (3.19) to the ordinary differential equation

$$\frac{d^2\varphi^\gamma}{d\xi^2} + \xi\frac{d\varphi}{d\xi} = 0 \tag{3.24}$$

and three conditions (3.22) properly correspond to the following two conditions:

$$\varphi(\xi = \infty) = 1\,, \qquad \varphi(0, t) = \varphi_0 \tag{3.25}$$

The nonlinear ordinary equation (3.24) was solved numerically, and the results are shown in Figure 3.3 for different values of the parameter γ. The solutions do not deviate essentially from linear variant $(\gamma = 1)$ of the equation (3.14). This means that the linear equation

$$\frac{\partial\Phi}{\partial t} = \kappa\frac{\partial^2\Phi}{\partial x^2}\,, \qquad \Phi = \varphi^\gamma \tag{3.26}$$

is a sufficient approximation for all nonlinear types of pore-pressure changes in infinite reservoirs.

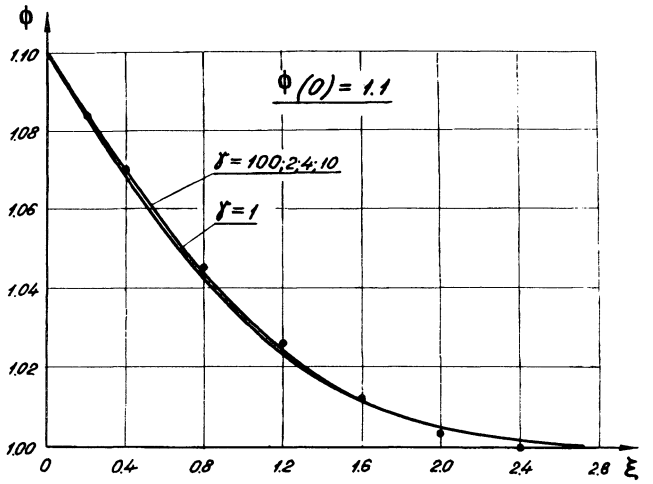

Figure 3.3. Nonlinear (points) and linearized calculations for planar underground flows in a infinite reservoir [156].

The axisymmetric filter self-similar flows are governed by equation (3.19) in the form

$$\frac{\partial \varphi}{\partial t} = \frac{\kappa}{r}\frac{\partial}{\partial r}\left(r\frac{\partial \varphi^{\gamma}}{\partial r}\right) \tag{3.27}$$

for the following initial and boundary conditions

$$\varphi(r,0) = 1\,;\ r\frac{\partial \varphi^{\gamma}}{\partial r} = -\frac{Q\mu_0\alpha}{2\pi h_0 k_0 \rho_0} = Q^{*},\ r \to 0\,;\ \varphi(\infty,t) = 1 \tag{3.28}$$

Here, Q is the constant well production rate. The variable

$$\xi = \frac{r}{\sqrt{2\kappa t}} \tag{3.29}$$

permits the reduction of (3.27) to the ordinary differential equation

$$\frac{d^2\varphi^\gamma}{d\xi^2} + \frac{1}{\xi}\frac{d\varphi^\gamma}{d\xi} + \xi\frac{d\varphi}{d\xi} = 0 \qquad (3.30)$$

Again the three conditions of (3.28) are transformed into the following two conditions:

$$\xi\frac{d\varphi}{d\xi} = -\frac{Q\mu_0\alpha}{2\pi h_0 k_0 \rho_0} = Q^* \quad , \qquad \varphi(\xi=\infty) = 1 \qquad (3.31)$$

The numerical solutions are given in Figure 3.4 for different values of well production. These data conform to the requirements for using the linear equation (3.26) for the Leibenson function as the approximation of nonlinear piezoconductivity in infinite reservoirs.

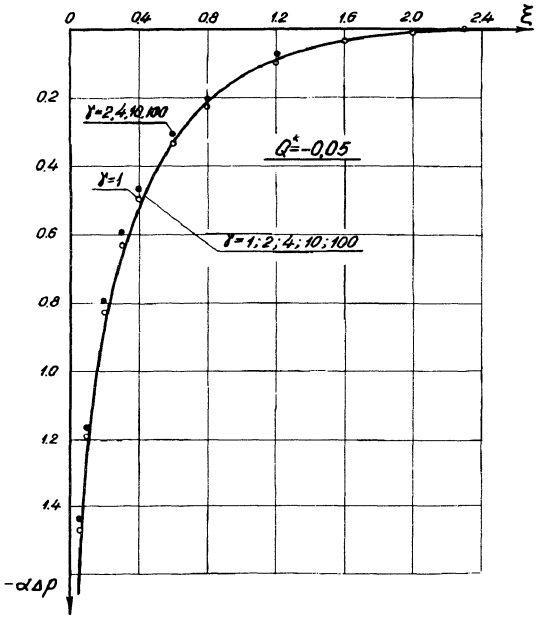

Figure 3.4. Nonlinear (points) and linearized calculations for pumping from a planar infinite reservoir.

The considered solutions have shown that the depression or pressure increase is limited by the boundary $\xi = \xi_+ \approx 2$, - that is, by the moving front

$$x_+(t) \approx \sqrt{8\kappa t} \qquad (3.32)$$

or, in the axisymmetric case,

$$r_+(t) \approx \sqrt{8\kappa t} \tag{3.33}$$

When the front reaches the outer boundary of the reservoir, $R = const$, the self-similar solution becomes invalid. The numerical solutions of the gas filter equation (3.20) are illustrated in Figure 3.5 for the impermeable condition at the outer boundary:

$$w_r = 0 \quad , \qquad r / R = 1 \tag{3.34}$$

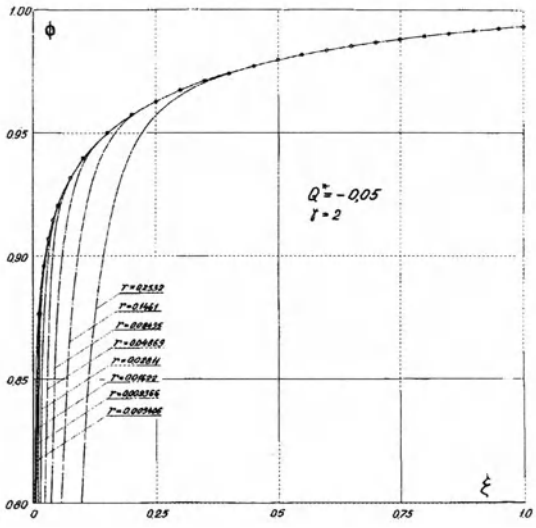

Figure 3.5. Finite reservoir radius effects on pore-pressure distribution at longer times.

As can be seen, the self-similar solution is valid not everywhere, and the deviations suggest that dependance is separate upon time and radial distance, r / R, which is given here in the form ξ and r / R. Of course, the deviations begin earlier for the bigger production rate, Q^*. The curve $r / R = 1$ would correspond to a pore-pressure decline at the reservoir boundary. The interval of self-similar solution validity can be defined as the first stage of a nonstationary flow. Then, the second stage corresponds to the time intervals of the deviations from self-similarity.

3.1.4. PORE PRESSURE BUILD-UP PROCESS

Pressure changes at the well after instant closure are important. The analytical solution of linear equation (3.25) is used to interpretate the field measurements. The pore pressure is searched for in the form of a nonstationary disturbance

$$\frac{Q\mu}{2\pi kh}\Phi_*(r,t) = \Phi(r,t) - \Phi_0(r) \tag{3.35}$$

of an initial distribution, $\Phi_0(r)$, for which the following limitation is necessary

$$r\frac{\partial\Phi_0}{\partial r} = \frac{Q\mu}{2\pi kh} \quad (r \to 0) \tag{3.36}$$

Then equation (3.26) with initial and boundary conditions

$$\Phi_*(r,t) = \Phi_*(\infty,t) = 0 \quad , \qquad r\frac{\partial\Phi_*}{\partial r} = -1 \quad (r \to 0) \tag{3.37}$$

must be solved. Problem (3.37) is also self-similar but, now, the linear variant of equation (3.30)

$$\frac{du}{d\xi} + \left(\xi + \frac{1}{\xi}\right)u = 0 \quad , \qquad u = \frac{d\Phi}{d\xi} \tag{3.38}$$

can be integrated:

$$u = \frac{d\Phi_*}{d\xi} = \frac{C}{\xi}exp\left(-\xi^2\right) \tag{3.39}$$

where C is the constant determined by condition (3.37). The second integration gives

$$\Phi_*(r,t) = \frac{1}{2}Ei\left(-\frac{r^2}{4\kappa t}\right) \tag{3.40}$$

where Ei is the well-known exponential integral function

$$-Ei\left(-\xi^2\right) = \int_{\xi^2}^{\infty}\frac{e^{-x}}{x}dx \approx ln\,\xi^2 - 0.5772 \tag{3.41}$$

You can see now that

$$\Delta\Phi = \Phi(r_w, t) - \Phi_0(r_R) \approx 0.1832 \frac{Q\mu}{kh} \lg \frac{2.246\,\kappa t}{r_w^2} \approx$$

$$\approx 0.1832 \frac{Q\mu}{kh}\left(\lg \frac{2.246\kappa}{r_w} + \lg t\right) \tag{3.42}$$

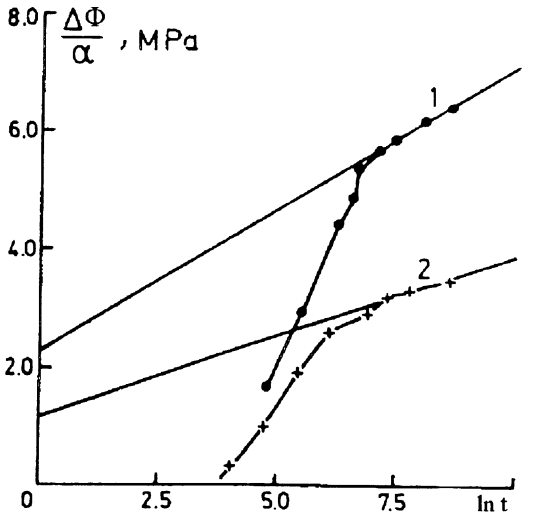

Figure 3.6. Two build-up curves measured at fissured reservoirs with pressure-sensitive pore volumes.

where condition (3.37) at $r \to 0$ and the actual well scale ($r_w / r \approx 0$) permits use of the result (3.40) at the well surface ($r = r_w$).

Therefore, the half-logarithmic system of coordinates is used (Figure 3.6) for interpretation of measurements of pressure build-up curves in the well after closure [172, 211]. Deviations from the straight line in the plane $\Delta\Phi$, $\lg t$ or Δp, $\lg t$ are initiated by different sources of additional visco-elastic pressure relaxation and will be discussed later. The straight line shown in Figure 3.6 gives us two parameter combinations which are used for the reservoir technology design:

$$A = i \lg \frac{2.246\,\kappa}{r_i^2}, \qquad i = 0.1832 \frac{Q\mu}{kh} \tag{3.43}$$

3.2. Stationary flows and well spacing

3.2.1. STATIONARY WELL PRODUCTIVITY

Pore-pressure fields in the vicinity of the infinite drainage gallery

$$p(x) = p_* + \frac{Q\,\mu_0}{h_0\,b\,k_0\,\rho_0}(x - x_*) \quad , \qquad x < x_+ \tag{3.44}$$

and of the well

$$p(r) = p_w + \frac{Q\,\mu_0}{2\pi\,k_0\,h_0\,\rho_0}\,ln\left(\frac{r}{r_w}\right) \quad , \qquad r < r_+ \tag{3.45}$$

can be treated as stationary during the time interval that the front $x_+(t)$ or $r_+(t)$ has moved nonessentially - see (3.32), (3.33). This front can be treated as a feeding contour because it is characterized by conditions for the radial flow case

$$p \approx const = p_R \quad , \qquad r = r_+ \approx const = R \tag{3.46}$$

(or $\Phi \approx const$, see Section 3.1).

Distributions (3.44) and (3.45) can be found to be stationary solutions of the piezoconductivity equation (3.9) when it has a form of the Laplace equation $\nabla^2\Phi = 0$. Correspondingly, one obtains the following formulae for the fluid output of the drainage gallery:

$$Q = \frac{k_0\,bh\,\rho_0}{\mu}\,\frac{p_+ - p_*}{L} \tag{3.47}$$

where b is the width of the plane layer and $x_+ - x_* = L$.

The expression for well production determined by radial pressure field (Figure 3.7) is

$$Q = \frac{2\pi\,k_0\,h_0\,\rho_0}{\mu_0}\,\frac{p_R - p_w}{ln\,(R\,/\,r_w)} \tag{3.48}$$

This formulae corresponds to the straight line in the plane Q, $\Delta p = p_R - p_w$ which is used to estimate well productivity. The deviation from the straight line requires that nonlinear effects be accounted for. They can be described by the Leibenson function Φ, in the expression (3.48), instead of p.

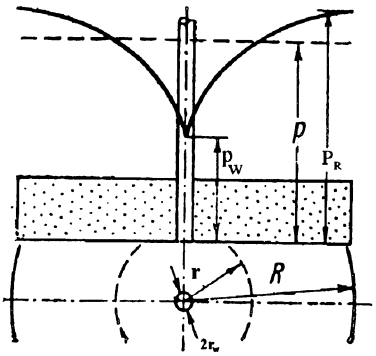

Figure 3.7. Depression curve for an axisymmetric reservoir with a producing well.

For example, the permeability changes controlled by pore pressure are of the following type [156]

$$\Phi = \frac{1}{\alpha} exp\left(-\alpha \Delta p\right) \quad , \qquad \Delta p = p_R - p \tag{3.49}$$

The specific output rate (per unit pressure drop) is the well productivity, K_Q :

$$K_Q = \frac{Q}{\Delta p_w} = \frac{2\pi k_0 h_0 \rho_0}{\mu_0 ln(R / r_w)} \frac{1 - exp(-\alpha \Delta p_w)}{\alpha \Delta p_w} \tag{3.50}$$

Its limit as $\alpha \Delta p_w \to 0$ corresponds to the Dupuit formulae (3.48) when $K_Q = const$.

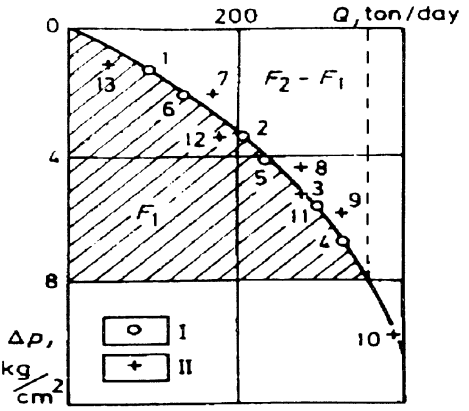

Figure 3.8. Well production curve, with two sets (I , II) of measurements, and its treatment [156].

It is possible to determine parameters K_Q and α by the proper treatment of well production data (Figure 3.8). Integrating equality (3.48) over the interval of Δp_w and if formulae (3.49) is valid, we get the values F_1 and F_2 , as shown in Figure 3.8:

$$F_1 = \int_0^{\Delta p_w} Qd(\Delta p_w) \quad , \qquad F_2 = Q\Delta p_w \tag{3.51}$$

This integration permits us to use the function [121, 124] shown in Figure 3.9:

$$F(\Delta p_w) = \frac{F_1}{F_2} = \frac{1}{1 - exp(-\alpha \Delta p_w)} - \frac{1}{\alpha \Delta p_w} \tag{3.52}$$

Here, the positive values of $\alpha \Delta p_w$ correspond to fluid production from the reservoir and the negative ones correspond to the fluid injections.

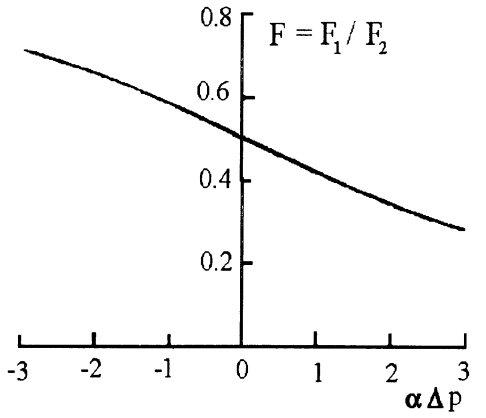

Figure 3.9. Tabulated functions for interpretation of well production data.

The value α can be determined by comparing the graphical results in Figure 3.8 with those in Figure 3.9 and then calculating well productivity by formula (3.50).

The data of Figure 3.8 correspond to the following numerical values:

$$\alpha = \frac{0.186}{MPa} \quad , \qquad K_Q = \frac{84.5}{MPa} \frac{ton}{day} \tag{3.53}$$

It is possible to represent maps of reservoir hydraulic deformability if the parameter α is found for a number of wells. Such an example is given in Figure 3.10, where the circles are proportional to the α-values. As can be seen, its maxima are concentrated at the upper part of the geological structure disturbed by two tectonic faults.

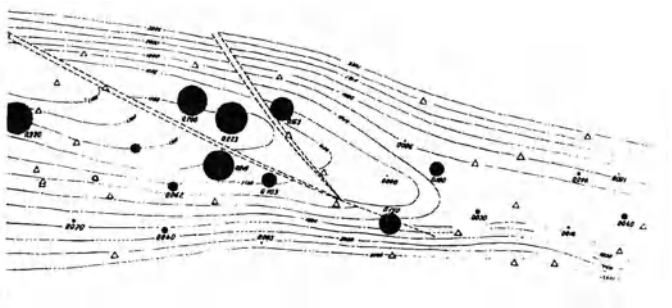

Figure 3.10. Reservoir structure map and the pressure-dependent pore space factor α.

The nonlinear deviations of the Dupuit formulae are typical for gas wells, but not all of them can be accounted for by introduction of the proper Leibenson function ($\Phi = p^2$ for the perfect gas). The reason for this is the "turbulent" filter resistance that appears because of the high production of gas wells, see (2.70). The formula

$$\frac{p_R^{\,2} - p_w^{\,2}}{Q} = a + bQ \tag{3.54}$$

is often used, where Q is the well output rate (usually normalized to the normal conditions). The following data are typical:

$$a = 60 \quad , \quad b = 0.15 \quad \text{at} \quad p = 5\ MPa \quad , \quad Q = 10^5\ m^3/day \tag{3.55}$$

3.2.2. WELL PERFORATION EFFECT

The "turbulent" resistance can be essential because fluid flow drastically changes in the vicinity of the well from radial to spherical. This is so because the well column is perforated and fluid has to flow through a number of small holes. The flow is governed by the equation

$$\frac{1}{r^2}\frac{\partial}{\partial r}\left(r^2\frac{\partial \Phi}{\partial r}\right) = 0 \tag{3.56}$$

inside the sphere with radius $r = r_*$ around every perforation (Figure 3.11). The integration of this equation gives the pressure distribution [14]

$$p = p_* + C\left(\frac{1}{r_*} - \frac{1}{r}\right) \tag{3.57}$$

where the constant, C, can be determined from the expression for filter velocity

$$w = \frac{Q}{2\pi r_w hn\rho_0} = -\frac{k_0}{\mu_0}\frac{C}{r_p^2} \tag{3.58}$$

where n is the number of holes and r_p is the perforation radius. As the result,

$$Q = \frac{2\pi k_0 h_0 \rho_0}{\mu_0}\frac{p_* - p_w}{1-(r_p / r_*)}\left(n\frac{r_w}{r_p}\right) \tag{3.59}$$

where p_* can be found from expression (3.48) with r_* and p_* instead of r_w and p_w, respectively. Numerical calculations have shown that the radius is $r_* \approx (2-3)r_w$. In this way, additional resistance due to perforation effect can be found.

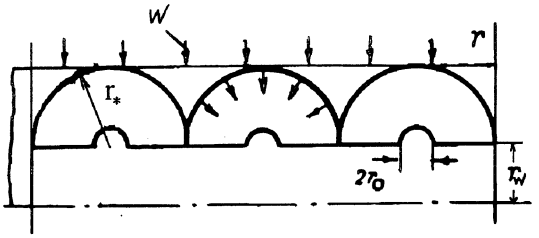

Figure 3.11. Flows in the vicinity of well-perforation holes.

Remember, however, that the perforation procedure includes now usage of cumulative charges that create perforation channels and change permeability drastically in their vicinities [171]. As during explosions (Section 5.1), grain crushing takes place and induced permeability has a nonmonotonous distribution, which has to be accounted for in the case of detailed calculations [152].

3.2.3. INDUCED ANISOTROPY OF PERMEABILITY

Sometimes the coefficient, α, that accounts for changes of permeability induced by pore pressure fields and which is calculated on the basis of well data, appears to be negative. This can be explained by microstructure changes under the filter velocity action. To account for this effect, resistivity (2.53) must be introduced into the system of equations for axisymmetric flow in the well vicinity. Then,

$$\frac{dp}{dr} = -\frac{\mu}{m_0^2}(\chi_0 + \chi_* v_r v_r)\frac{Q}{2\pi r h} \tag{3.60}$$

The rule of grain rotation (2.60)

$$G_r = -\kappa^{(\omega)} w \tag{3.61}$$

must be introduced into the balance of moment of momentum - (2.59) through (2.62) - which will be represented as the following equation for the vector-director and determine induced matrix anisotropy:

$$\frac{d^2 v_r}{dr^2} + \frac{1}{r}\frac{d v_r}{dt} - \left(Z_e^{\,2} + \frac{2}{r^2}\right) v_r = \frac{Z_a Q}{m_0 r} \tag{3.62}$$

where Z_e is the elastic coefficient, corresponding [11,80] to relative grain rotation, and Z_a is the aerodynamic coefficient proportional to $\kappa^{(\omega)}$. You can see that equation (3.62) has the Bessel form.

So, the system of equations (3.60) and (3.62) includes pore pressure and a new unknown variable, v_r which is a measure of induced anisotropy. The case $v_r = 0$ corresponds to isotropy of the porous medium. However, because of the nonlinearity of (3.60), the numerical calculation of the system is preferable. It is also possible to find the solution of (3.62) at the beginning and then use the result in (3.60). The corresponding solution is given in Figure 3.12 in the form of two production curves, A and B (without and with induced anisotropy of a permeability), and the corresponding distribution of vector-director, v_r, its value equal to zero at $r = R$. It is assumed that there is no coupled stress at the well surface. (Grain rotation is free.)

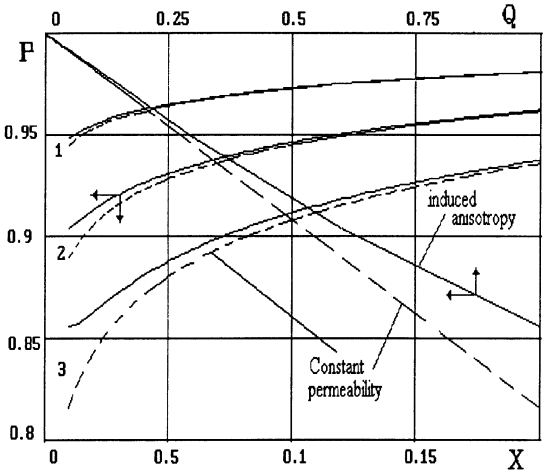

Figure 3.12. Depression curves for the reduced rate $Q_1^* = 0.3$, $Q_2^* = 0.6$, $Q_3^* = 1.0$ and well productivity changes due to induced anisotropy [80].

3.2.4. WELL SPACING AT RESERVOIRS

Well spacing is very important to reservoir development [102] because of the interference effect between acting wells. The method of sinks and sources is usual for the Laplace equation

$$\nabla^2 \Phi = 0 \tag{3.63}$$

because, in large scale, wells can be modeled by point singularities. In planar layer, the potential field around each well (with index "i ") is determined as

$$\Phi_{(i)} = Q_i^* \, ln \, r_w^{(i)} + C_i \tag{3.64}$$

and their cumulative action is the sum

$$\Phi = \sum_i Q_{(i)}^* \, ln \, r_w^{(i)} \tag{3.65}$$

The filter velocity, w_i, is also calculated by the summation procedure [14]

$$w_j = \sum_i w_j^{(i)} \tag{3.66}$$

and, in every point of the layer, the individual velocity vector is oriented to the corresponding sink (source):

$$w_j^{(i)} = \left(\frac{Q_{(i)}^*}{r_w^{(i)}} \right)_j \tag{3.67}$$

The impermeable boundary can be accounted for by mirror introducing additional sinks (sources) with the same intensity as in the corresponding points of reflection. If the sign of Q_i changes during this procedure, then the boundary will be the feeding contour [14].

The effective approximation was developed (by Yu.P.Borisov) for design of filter flows between well rows at the oil reservoir [102]. In large scale, every j-row is modeled by the drainage gallery (Figure 3.13), with cumulative production:

$$Q_j = \frac{2l_j n_j k_0 \rho_0 h}{\mu_0} \frac{\Phi_k - \Phi_j}{L_j} \tag{3.68}$$

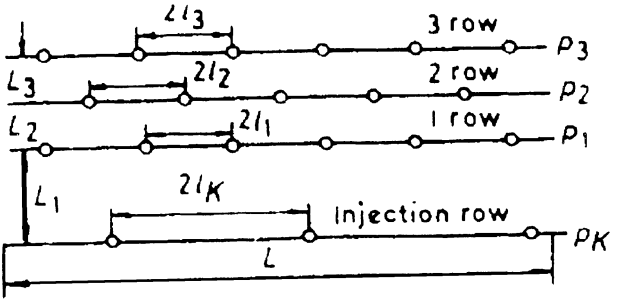

Figure 3.13. Scheme of well systems used for flooding of oil reservoirs [156].

The fluid flow corresponding to every individual well is directed to the linear element of the row equal to $2l_j$. So, it can be treated as length of feeding contour, $2\pi R_j$:

$$R_j = \frac{l_j}{\pi} \tag{3.69}$$

The introduction of this result into the formulae for output production of the well (3.48) results in

$$\frac{Q_j}{n_j} = \frac{2\pi k_0 \rho_0 h}{\mu_0} \frac{\Phi_j - \Phi_w}{ln\left(l_j / \pi r_{wj}\right)} \tag{3.70}$$

The combination of equations (3.68) and (3.70) gives the following result:

$$\frac{Q_j}{n_j} = \frac{2\pi k_0 \rho_0 h}{\mu_0} \frac{\Phi_R - \Phi_{wj}}{(L_j / 2l_j) + ln(l_j / \pi r_{wj})} \tag{3.71}$$

The solution of the Laplace equation, which can be obtained by the sink-source method [102]

$$\frac{Q_j}{n_j} = \frac{2\pi k_0 \rho_0 h}{\mu} \frac{\Phi_R - \Phi_{wj}}{ln\left[2 \sin h(\pi L_j / l_j)\right] + ln(l_j / \pi r_{wj})} \tag{3.72}$$

contains the approximate solution (3.71) as the main part due to the asymptotic formulae

$$ln(2 \sin hx) \approx x \quad , \qquad x << 1 \tag{3.73}$$

where $x = \pi L_j / l_j$. This suggests that expression (3.71) is valid if the distances between rows are much larger than between the wells inside the row.

Recall that horizontal wells play the role of rows of vertical wells very effectively [58] in the case of thin productive layers. "Feeding" contours inside the well system can also be found from the proper approximation of formula developed by the method of sinks and sources. The problem of well interference can be solved very effectively with the use of modern computers.

3.3. Two-phase flows in reservoirs

3.3.1. FLOODING FRONT MODEL

This type of flow is very important for oil and gas reservoirs because of the natural and technological process of displacing one fluid by another. Usually, the displacing agent is water, and the process is called flooding. It can maintain initial pore pressure, reserve and delay gas release from an oil stratum.

The flooding front is a discontinuity. The "piston" displacement concept means that the fluid particle has the same velocities, v^-, v^+, as the front itself U:

$$v^+ = \frac{w^+}{m} = v^- = \frac{w^-}{m} = U = \frac{dx_f}{dt} \tag{3.74}$$

where x_f is the front coordinate. The mass balance (1.32) discussed earlier,

$$\rho^-\left(v^- - U\right) = \rho^+\left(v^+ - U\right) \tag{3.75}$$

determines the independence of densities, ρ^-, ρ^+, ahead and behind the displacement front. Moreover, momentum balance (1.33) means that

$$\sigma_{ij}^- n_j = \sigma_{ij}^+ n_j \tag{3.76}$$

That is, for pore space, we have

$$p^- = p^+ \tag{3.77}$$

Because porous channels have different sizes, total frontal displacement is only useful idealization. In reality, one part of the displacing fluid moves faster than the front, another one moves slower, and the fluid which is being displaced partly remains behind the front.

3.3.2. TWO-PHASE HYDRODYNAMICS

This adequate theory is based on a generalization of Darcy's law, according to which two fluids can be presented simultaneously in the same macropoint but move with different filter velocities [108, 139]:

$$w_i^{(\alpha)} = -\frac{k}{\mu^{(\alpha)}} f^{(\alpha)}\left(\theta^{(\alpha)}\right)\frac{\partial p^{(\alpha)}}{\partial x_i} \tag{3.78}$$

where $\theta^{(\alpha)}$ is the saturation of pore space by fluid phase α

$$\sum_{\alpha} \theta^{(\alpha)} = 1 \tag{3.79}$$

and $p^{(\alpha)}$ and $\mu^{(\alpha)}$ are the phase pressure and the viscosity, respectively.

The basic concept [139] consists of the relative phase permeability $f^{(\alpha)}(\theta^{(\alpha)})$ measured experimentally for rock samples under stationary conditions (typically represented in Figure 3.14 for a two-phase system). The essential feature is the existence of the intervals $\theta^{(\alpha)} < \theta_*^{(\alpha)}$ of the immovable phase α with threshold values $\theta_*^{(\alpha)}$. At small saturation, every phase is represented by individual drops or films separated by another fluid phase in porous space. Therefore, there are no continuous streams in this interval, and it cannot move by its own pressure gradient.

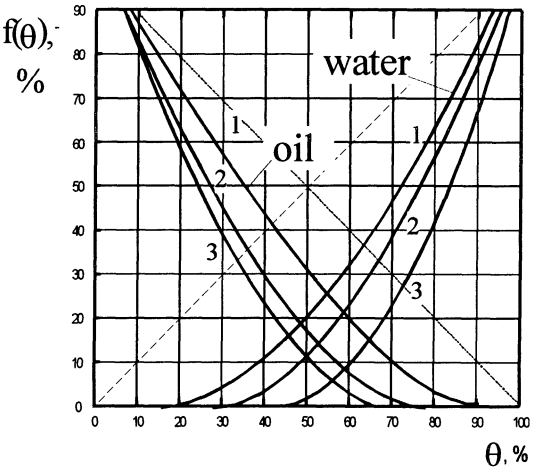

Figure 3.14. Relative phase permeabilities for a water-oil system, changing with its dispersivity [108] (for drop size $D_1 < D_2 < D_3$ and fixed porous space; broken lines correspond to the absolute absence of capillary effects).

However, the drops can be removed by another pressure field and equation (3.78) be further generalized in the following manner:

$$-\frac{\partial p^{(\alpha)}}{\partial x_j} = \sum_{\beta} r_{ij}^{(\alpha\beta)} v_i^{(\beta)} \tag{3.80}$$

where $r_{ij}^{(\alpha\beta)}$ are the phase-resistance coefficients. Usually, calculations are based on the more simple expression (3.78) - that is, $r_{ij}^{(\alpha\beta)}$ are assumed zero if $\alpha \neq \beta$.

The phase pressures are interconnected by the expression [157]

$$p^{(\alpha)} - p^{(\beta)} = p_c^{(\alpha\beta)}(\theta) + \tau_c \frac{d\theta}{dt} \tag{3.81}$$

which corresponds to Onsager's rules (Section 1.2). Here, $p_c^{(\alpha\beta)}(\theta)$ is the capillary pressure, the function of saturation $\theta^{(1)} = \theta$ or $\theta^{(2)} = 1 - \theta$ for the two-phase system (Figure 3.15)

$$p_c^{(\alpha\beta)}(\theta) = \gamma \sqrt{\frac{k}{m}}\, J(\theta) \cos\varphi \tag{3.82}$$

Here, γ is the interface tension , φ is the contact angle of fluids at the solid surface of the porous matrix, and $J(\theta)$ is the Leverett function [14].

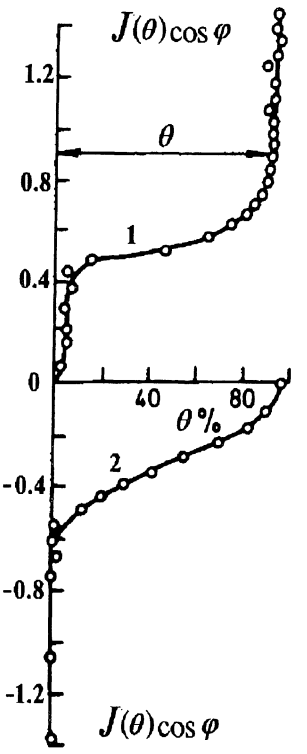

Figure 3.15. Capillary pressure dependence on saturation for (1) wetting and (2) nonwetting phase [156].

The second term of expression (3.81) takes account of delay in phase-local redistribution in porous space with capillary relaxation time, τ_c. In the case of local stationarity, $\tau_c / t \to 0$; correspondingly, the second term on the right-hand side of equation (3.81) can be neglected.

The mass balances must be formulated for every phase separately when components and phases are identical (Section 4.1):

$$\frac{\partial}{\partial t} m \rho^{(\alpha)} \theta^{(\alpha)} + \frac{\partial}{\partial x_j}\left(\rho^{(\alpha)} w_j^{(\alpha)}\right) = 0 \tag{3.83}$$

3.3.3. ONE-DIMENSIONAL PLANAR MIXTURE FLOW

The system of (3.78), (3.81) and (3.83) permits the study of fluid redistribution of masses in an oil (or gas) reservoir that usually contains natural or injected waters. Consider the simple planar one-dimensional water-flooding process in an oil reservoir. In this case,

$$m = const \quad , \quad \rho_1 = const \quad , \quad \rho_2 = const$$

and the system of equations is reduced to:

$$\begin{aligned} m\frac{\partial \theta}{\partial t} &= \frac{\partial}{\partial x}\left(\frac{k}{\mu^{(1)}} f^{(1)}(\theta)\frac{\partial p^{(1)}}{\partial x}\right) \\ m\frac{\partial (1-\theta)}{\partial t} &= \frac{\partial}{\partial x}\left(\frac{k}{\mu^{(2)}} f^{(2)}(\theta)\frac{\partial p^{(2)}}{\partial x}\right) \end{aligned} \tag{3.84}$$

Their sum has the following form [14]:

$$\begin{aligned} &\frac{\partial}{\partial x}\left\{\left(\frac{f^{(1)}(\theta)}{\mu^{(1)}} + \frac{f^{(2)}(\theta)}{\mu^{(2)}}\right)k\frac{\partial p}{\partial x} + \frac{f^{(2)}(\theta)}{\mu^{(2)}} k \frac{dp_c}{d\theta}\frac{\partial \theta}{\partial x}\right\} \\ &\equiv \frac{\partial}{\partial x}\left(w^{(1)} + w^{(2)}\right) = 0 \end{aligned} \tag{3.85}$$

where $\left(p^{(1)} \equiv p\right)$, and integration gives the first integral

$$w^{(1)} + w^{(2)} = w(t) \tag{3.86}$$

If one excludes the pressure gradient

$$-\frac{\partial p}{\partial x}=\left(\frac{w(t)}{k}+\frac{f^{(2)}(\theta)}{\mu^{(2)}}\frac{d\,p_c(\theta)}{d\theta}\frac{\partial\theta}{\partial x}\right)\Big/\left(\frac{f^{(1)}(\theta)}{\mu^{(1)}}+\frac{f^{(2)}(\theta)}{\mu^{(2)}}\right) \tag{3.87}$$

the first equation (3.84) gives the following for water saturation:

$$m\frac{\partial\theta}{\partial t}+\frac{\partial}{\partial x}\left(F(\theta)w(t)+kF(\theta)\frac{f^{(2)}(\theta)}{\mu^{(2)}}\frac{d\,p_c(\theta)}{d\theta}\frac{\partial\theta}{\partial x}\right)=0 \tag{3.88}$$

where $\theta=\theta^{(1)}$ and $F(\theta)$ is flow distribution function (Figure 3.16)

$$F(\theta)=\frac{f^{(1)}(\theta)/\mu^{(1)}}{\left(f^{(1)}(\theta)/\mu^{(1)}\right)+\left(f^{(2)}(\theta)/\mu^{(2)}\right)} \tag{3.89}$$

if capillary pressure is negligible and equation (3.88) has the form of a nonlinear simple wave equation:

$$\frac{\partial\theta}{\partial t}+\frac{w(t)}{m}F'(\theta)\frac{\partial\theta}{\partial x}=0 \tag{3.90}$$

As usual, this equation is compared with the equation for characteristics

$$\frac{d\theta}{dt}\equiv\frac{\partial\theta}{\partial t}+\frac{\partial\theta}{\partial x}\frac{dx}{dt}=0 \tag{3.91}$$

It follows that value $\theta=const$ propagates with the velocity:

$$\frac{dx}{dt}=\frac{w(t)}{m}\frac{dF}{d\theta} \tag{3.92}$$

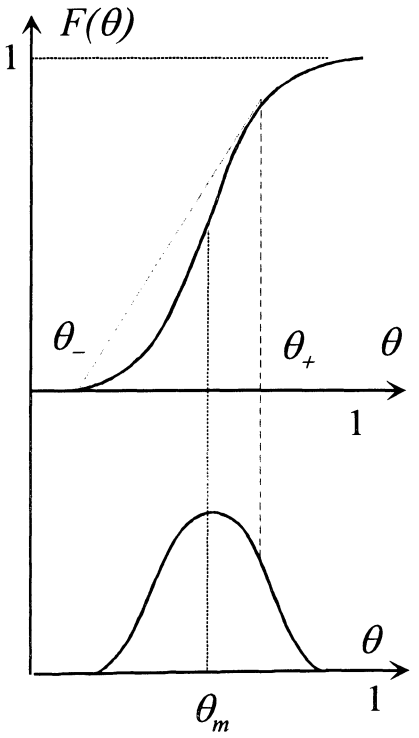

Figure 3.16. Rate distribution function $F(\theta)$ for two-phase flow in porous media (the broken line corresponds to front discontinuity) [14].

3.3.4. FRONTAL SATURATION STRUCTURE

The typical form of curves $F(\theta)$ and $dF / d\theta$ are shown in Figure 3.16. You can see that there are two intervals: one of growing velocity of θ-propagation, and one of its decline. This means that there is value $\theta = \theta_m$ propagates with the highest velocity. Therefore, a jump from some smaller value θ_- to some value θ_+ must be introduced. This discontinuity moves with the velocity, U which can be found from balance (1.31) and written now for the phase masses:

$$\left[w^{(\alpha)} - m\theta^{(\alpha)}U\right] = 0 \tag{3.93}$$

where incompressibility is accounted for. Indeed, one can find (Figure 3.16) that

$$U = \frac{1}{m}\frac{w_+^{(1)} - w_-^{(1)}}{\theta_+ - \theta_-} \tag{3.94}$$

from the first phase balance $(\alpha = 1)$. The second balance will give the same result because of integral (3.86).

This front is stable if

$$U > \frac{dx}{dt} \quad , \quad \theta > \theta_+ \quad ; \quad U < \frac{dx}{dt} \quad , \quad \theta < \theta_- \tag{3.95}$$

and unstable in the opposite cases [17]. Really, higher saturations cannot move ahead of the front, but smaller values of displaced fluid (oil) can be redistributed in this zone. The condition of coincidence of velocities (3.92) and (3.94)

$$dx / dt = U \tag{3.96}$$

will determine the dependence of θ_+ on θ_- - that is,

$$F'(\theta_+) = \frac{F(\theta_+) - F(\theta_-)}{\theta_+ - \theta_-} \tag{3.97}$$

because $w^{(1)} = F(\theta)w$.

Of course, the saturation discontinuity must coincide with the displacement front found from the idealized scheme of one-phase calculation (3.74). The residual oil amount can be found by integration of $\theta^{(2)}$ behind the front.

Capillary effect is studied by adding the space derivative of second order in equation (3.88). This means that the discontinuity must be changed into a thin continuous "stabilized" zone with high gradient of saturation. For proper study, it is possible to find the stationary solution of equation (3.88) in the coordinate system $(\xi = x - Ut)$ moving with the front velocity:

$$-U\frac{d\theta}{d\xi} + \frac{w(t)}{m}\left(\frac{dF}{d\theta}\right)\frac{d\theta}{d\xi} + \frac{k}{m}\frac{d}{d\xi}F(\theta)\frac{f^{(2)}(\theta)}{\mu^{(2)}}\frac{d\,p_c}{d\theta}\frac{d\theta}{d\xi} = 0 \tag{3.98}$$

The boundary conditions must be selected according to the requirement of coinciding with the jump conditions (3.93) for saturation - that is,

$$\theta(-\infty) = \theta_+ \quad , \qquad \theta(+\infty) = \theta_- \tag{3.99}$$

If $d\theta / d\xi \to 0$ at $\xi \to -\infty$, the first integral is:

$$U(\theta_+ - \theta) + \frac{w(t)}{m}\left(F(\theta_+) - F(\theta)\right) = -\frac{k}{m} F(\theta) \frac{f^{(2)}(\theta)}{\mu^{(2)}} \frac{d\, p_c}{d\theta} \frac{d\theta}{d\xi} \qquad (3.100)$$

Further integration of (3.100) determines the saturation distribution inside the stabilized zone as it is shown schematically in Figure 3.17, see also [105].

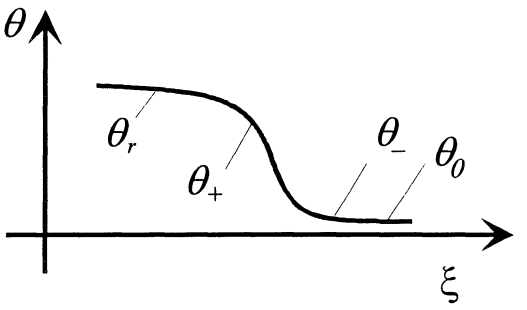

Figure 3.17. Moving stabilized zone is the structure of front discontinuity from θ_- to θ_+ (from θ_0, initial water content, to θ_r, residual state in the scheme of "piston" displacement).

3.3.5. UNIFORM VELOCITY CASES

The opposite case, of absolute negligible capillary effects (at supercritical states, for example), can change even the form of phase permeability curves. It was found experimentally that, in this case, their curvature is diminishing and tends to straight lines (shown in Figure 3.14 by broken lines). Moreover, mass balances (3.83) become identical with simple convection equations if phase densities are constant. The saturation θ will play the role of volume concentration - that is, system (3.84) will have the following form:

$$m\frac{\partial \theta}{\partial t} = \frac{\partial}{\partial x}\left(\frac{k}{\mu}\theta\frac{\partial p}{\partial x}\right) \quad , \quad \frac{\partial w}{\partial x} = 0 \quad , \quad p^{(1)} = p^{(2)} = p$$

$$w_1 = \theta\, w \quad , \quad w = -\frac{k}{\mu}\frac{\partial p}{\partial x} \quad , \quad \mu^{(1)} = \mu^{(2)} \qquad (3.101)$$

Another practical and important variant of simplification is the case of gas microbubbles moving with the same velocity, w_j, as the fluid when their saturation, θ, in the fluid volume does not change. Then the mixture density has the form

$$\rho = A + Bp \quad , \qquad A = \rho^{(1)}(1-\theta) \quad , \qquad B = \left(\rho_0^{(2)} / p_0\right)\theta \tag{3.102}$$

and its substitution into the balance equation (3.83) will give the nonlinear equation, as it had been suggested by L. S. Leibenson (1932) before the phase permeability concept was developed:

$$m\frac{\partial \varphi}{\partial t} = \frac{\partial}{\partial x_j}\left(\frac{k}{\mu B}\frac{\partial \varphi^2}{\partial x_j}\right) \quad , \qquad \varphi = A + Bp \tag{3.103}$$

This declares the increase of potential of fluid underground flow in comparison with usual pressure. Such an effect can be seen in oil reservoir data (measured by A.T.Gorbunov and given in Figure 3.18) as the sudden increase of well productivity at gas-dissolving pressures and the reduction due to gas bubble growth. The latter interval corresponds to the phase permeability ($f^{(\alpha)} < 1$) concept.

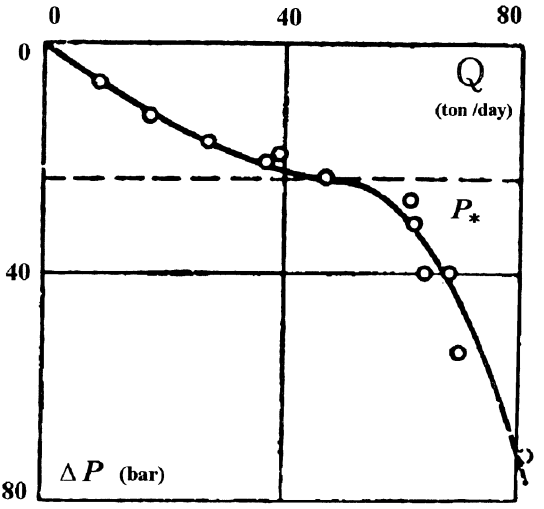

Figure 3.18. Typical well output curve for oil production, where p_* is the pressure of gas release from the dissolved or adsorbed state.

3.4. Flows in fractured reservoirs

3.4.1. STRESS DISTRIBUTION IN A DOUBLE-POROUS SYSTEM

Fractured rock masses can be treated as standard porous media but with high level of anisotropy created by systems of cracks opened by the dilatancy effect - that is, by shear stresses during tectonic activity.

However, if such fracturing takes place in a porous reservoir, the medium with double porosity, $m^{(1)}$ and $m^{(2)}$, appears, the first corresponding to tectonic cracks and the second one to initial pores (Figure 3.19). The mathematical modeling is based on ideas of interpenetrating porous continua [12, 156]. (The alternative is connected with the fractal approach [50]).

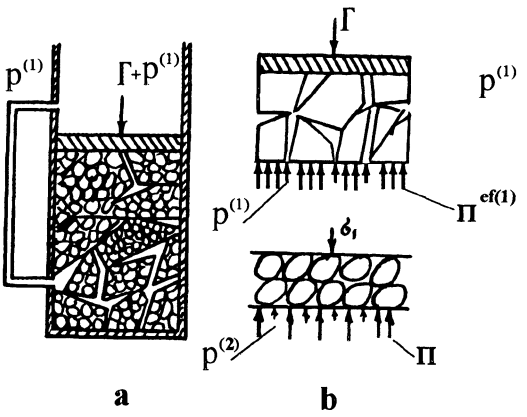

Figure 3.19. Load distribution in the crack-pore system of a medium with a double-porosity.

The total (lithostatic) stresses, Γ_{ij}, created by tectonic processes in such a reservoir are supported by the true stresses, $\Pi_{ij}^{(1)}$, and pore pressure, $p^{(1)}$, acting on a large scale (that is, in the system of blocks and cracks):

$$\Gamma_{ij} = \left(1 - m^{(1)}\right)\Pi_{ij}^{(1)} - m^{(1)} p^{(1)} \delta_{ij} \tag{3.104}$$

The effective stress, $\Pi_{ij}^{ef(1)}$, can be introduced such that [152]

$$\Gamma_{ij} = \Pi_{ij}^{ef(1)} - p^{(1)} \delta_{ij} \tag{3.105}$$

The total stress for the second (porous) system appears to be equal to $\Pi_{ij}^{(1)}$:

$$\Pi_{ij}^{(1)} = \Pi_{ij}^{ef(2)} - p^{(2)}\delta_{ij} \tag{3.106}$$

where $\Pi_{ij}^{ef(2)}$ is the second effective stress. Of course, this local stress distribution leads to definite nonsymmetry of the piezoconductivity in the media with double porosity. So, under constant Γ_{ij}, it is assumed that

$$m^{(1)} = m^{(1)}\left(p^{(1)}\right) \quad , \qquad k^{(1)} = k^{(1)}\left(p^{(1)}\right) \tag{3.107}$$

and that the second system's parameters are functions of both pressures in general:

$$m^{(2)} = m^{(2)}\left(p^{(1)}, p^{(2)}\right) \quad , \qquad k^{(2)} = k^{(2)}\left(p^{(1)}, p^{(2)}\right) \tag{3.108}$$

3.4.2. MASS BALANCES AND EXCHANGE

The prime feature of double-porous media is the mass exchange modeling by body distributed sinks (sources) proportional to the pressure difference [233]:

$$I_m = \frac{\rho}{\chi}\left(p^{(1)} - p^{(2)}\right) \tag{3.109}$$

Here, χ is the dimensionless coefficient which is dependent on the permeability of porous blocks, $k^{(2)}$, and their specific (per unit volume) area ($A \approx l^{-1}$, where l is the fracture length). Therefore,

$$\chi \approx k^{(2)} A^2 \approx \frac{k^{(2)}}{l^2} \tag{3.110}$$

According to this idea, the mass balances are formulated separately for both interpenetrating porous continua:

$$\frac{\partial}{\partial t} m^{(1)} \rho + \frac{\partial}{\partial x_i} \rho w_i^{(1)} + I_m = 0 \tag{3.111}$$

$$\frac{\partial}{\partial t} m^{(2)} \rho + \frac{\partial}{\partial x_i} \rho w_i^{(2)} - I_m = 0 \tag{3.112}$$

altogether with the separate Darcy law formulations ($\alpha = 1, 2$)

$$w_i^{(\alpha)} = -\frac{k^{(\alpha)}}{\mu}\frac{\partial p^{(\alpha)}}{\partial x_i} \tag{3.113}$$

3.4.3. ZONES OF PRESSURE CHANGES

The homogeneous fluid flow is governed by the following combination of equations (3.109) and (3.111) through (3.113) in the form of total mass fluid balance and its balance in the continuum of fractures [156]

$$\begin{gathered}\left(\eta_{(1)} + \eta_{(12)}\right)\frac{\partial p^{(1)}}{\partial t} + \frac{\partial p^{(2)}}{\partial t} = \kappa\left(\eta_{(2)}\nabla^2 p^{(2)} + \nabla^2 p^{(1)}\right) \\ \eta_{(1)}\frac{\partial p^{(1)}}{\partial t} - \frac{p^{(2)} - p^{(1)}}{\tau} = \kappa\nabla^2 p^{(1)}\end{gathered} \tag{3.114}$$

where the two small parameters are introduced

$$\eta_{(1)} = \frac{m_0^{(1)}\beta^{(1)}}{m_0^{(2)}\beta^{(2)}} << 1 \quad , \qquad \eta_{(2)} = \frac{k^{(2)}}{k^{(1)}} << 1 \tag{3.115}$$

So, the effective fluid capacity of the crack system and the fluid permeability of pores are supposed to be relatively small. The relaxation time τ is characterizing the delay due to fluid exchange

$$\tau = \mu m^{(2)}\beta^{(2)} / \chi \tag{3.116}$$

Here, the effective piezoconductivity is utilized:

$$\kappa = k^{(1)} / (m^{(2)}\beta^{(2)}\mu) \tag{3.117}$$

The coefficient $\eta_{(12)}$ reflects the relative compressibility of the porous continuum due to pressure changes in the continuum of fractures; $\eta_{(12)}$ is assumed to be even smaller than $\eta_{(1)}$.

The next step is connected with the dimension analysis of equations (3.114). Introducing such variables [156] as

$$p^{(1)} = p_{(1)} \quad , \qquad p^{(2)} = \eta\, p_{(2)} \quad , \qquad p_{(1)} = \mathrm{O}\left(p_{(2)}\right) \tag{3.118}$$

we can obtain

$$\eta_{(1)}\frac{\partial p_{(1)}}{\partial t} + \eta\frac{\partial p_{(2)}}{\partial t} = \frac{\kappa T}{L^2}\left(\nabla^2 p_{(1)} + \eta_{(2)}\eta\nabla^2 p_{(2)}\right)$$

$$\eta_{(1)}\frac{\partial p_{(1)}}{\partial t} - \frac{\eta p_{(2)} - p_{(1)}}{\tau}T = \frac{\kappa T}{L^2}\nabla^2 p_{(1)} \tag{3.119}$$

So, terms with coefficients $\eta_{(1)}$, $\eta_{(2)} << 1$ can be neglected only if

$$\eta = O(1) \quad , \qquad T = O(\tau) \quad , \qquad L = O(\sqrt{\kappa t}) \tag{3.120}$$

Then the flow is governed by

$$\frac{\partial p^{(2)}}{\partial t} = \kappa\nabla^2 p^{(1)}$$

$$\kappa\nabla^2 p^{(1)} - \frac{p^{(2)} - p^{(1)}}{\tau} = 0 \tag{3.121}$$

Note that the system (3.121) is equivalent to the following equation:

$$\frac{\partial p}{\partial t} = \kappa\tau\frac{\partial}{\partial t}\nabla^2 p + \kappa\nabla^2 p \tag{3.122}$$

where p could be $p^{(1)}$ or $p^{(2)}$. The difference is determined by the choice of initial and boundary conditions.

For small time intervals but essential distances,

$$T_0 = O(\eta_{(1)}\tau) \quad , \qquad L_0 = O\left(\sqrt{k\tau}\right) \tag{3.123}$$

the second equation (3.119) gives the equation of piezoconductivity in the crack system with sinks into porous blocks

$$\frac{\partial p^{(1)}}{\partial t} + \frac{p^{(1)}}{\tau\,\eta_{(1)}} = \frac{\kappa}{\eta_{(1)}}\nabla^2 p^{(1)} \tag{3.124}$$

The asymptotic solution of this equation determines the changes of initial conditions from zero values to the proper ones for equations (3.121). The effective relaxation time, $\tau\,\eta_{(1)}$, is much smaller in (3.124), but the effective piezoconductivity, $\kappa\,/\,\eta_{(1)}$, is much bigger than in (3.121).

For intervals of usual times and small distances:

$$T_* = O(\tau) \quad , \qquad L_* = O\left(\sqrt{\kappa\tau\,\eta_{(2)}}\right) \tag{3.125}$$

system (3.119) gives the following equation for pore pressure changes

$$\eta_{(2)}\kappa\nabla^2 p^{(2)} = \frac{\partial p^{(2)}}{\partial t} + \frac{p^{(2)}}{\tau} \tag{3.126}$$

inside the narrow zone at the boundary of the medium. Here, the effective piezoconductivity, $\eta_{(2)}\kappa$, is diminished, and the sink of the intensity, $p^{(2)}\,/\,\tau$, is compensated by the source for the crack system:

$$\kappa\nabla^2 p^{(1)} + \frac{p^{(2)}}{\tau} = 0 \tag{3.127}$$

Equation (3.127) is the consequence of the same estimation as (3.126). The solutions of (3.126) correspond to changes of boundary condition if the fluid penetrated into the pore space of the medium, not through the crack system.

Let us suppose that the double-porous medium is in contact with another fluid system via its porous space. Integration of equation (3.126) across the narrow zone L_* gives:

$$\eta_{(2)}\kappa\left[\frac{\partial p^{(2)}}{\partial x}\right] = \frac{\partial}{\partial t} < p^{(2)} > + \frac{1}{\tau} < p^{(2)} > \tag{3.128}$$

where $< p >$ is the average value over thickness L_*.

Because of the second condition (3.115) the fluxes can be neglected and the equation can be obtained only for average pressure inside zone L_* :

$$\frac{d}{dt} < p^{(2)} > + \frac{1}{\tau} < p^{(2)} > = 0 \tag{3.129}$$

Integration of this equation determines the decay of this pressure in time

$$< p^{(2)} > = < p^{(2)} >_0 \exp\left(-t\,/\,\tau\right) \tag{3.130}$$

where the initial reservoir pressure, p_0, and the boundary pressure, $p_* = p_-^{(2)}$, can be used for the following identification:

$$p_+^{(2)} - p_* = (p_0 - p_*)\, exp(-t / \tau) \tag{3.131}$$

Here, $p_+^{(2)}$ is the effective boundary value for equation (3.126). Analogous analysis can show that the pressure jump $\left(p_+^{(1)} - p_-^{(2)}\right)$ in the crack system decays instantly. So, the measurement of nonstationary pressure at the well bottom can show principally its contact condition with the reservoir.

The total filter velocity is determined by pressure gradients as follows:

$$w_j = -\frac{k}{\mu}\left(\frac{\partial p^{(1)}}{\partial x_j} + \eta_{(2)}\frac{\partial p^{(2)}}{\partial x_j}\right) \approx -\frac{k}{\mu}\frac{\partial p^{(1)}}{\partial x_j} \approx$$

$$\approx -\frac{k}{\mu}\left(\frac{\partial p^{(2)}}{\partial x_j} + \tau\frac{\partial^2 p^{(2)}}{\partial x_j \partial t}\right) \tag{3.132}$$

where the previous approximation is used.

3.4.4. NONSTATIONARY AXIAL FLOWS IN FISSURED RESERVOIRS

It is possible to show that the following solution of equation (3.114) is valid in the axisymmetric case, modeling the flow to the well in an infinite plane reservoir [156]:

$$\frac{2\pi kh\rho}{Q\mu}\left(p_0 - p^{(1)}\right) = F_1(r,t) + \frac{1}{\tau}\int_0^t F_1(r,z)\, dz - \eta_2^{3/2}\, F_2(r,t)$$

$$\frac{2\pi kh\rho}{Q\mu}\left(p_0 - p^{(2)}\right) = \eta_{(2)}\, F_1(r,t) + \frac{1}{\tau}\int_0^t F_2(r,z)\, dz + \sqrt{\eta_{(2)}}\, F_3(r,t) \tag{3.133}$$

Here, $\eta_{(12)} << \eta_{(1)}$ and

$$F_1(r,t) = \frac{1}{2} e^{-t/\tau} \int_0^e I_0\left(2\frac{t}{\tau}\sqrt{\frac{z(1-z)}{\eta_{(1)}}}\right) exp\left(-\frac{t}{\tau}\frac{z}{\eta_{(1)}} - \frac{r^2}{4\kappa t}\frac{\eta_{(1)}}{z}\right)\frac{dz}{z}$$

$$F_2(r,t) = \frac{t}{r\tau}\sqrt{\kappa t}\ exp\left(-\frac{t}{\tau} - \frac{r^2}{8\,\eta_{(2)}\kappa t}\right) W_{-3/2,0}\left(\frac{r^2}{4\,\eta_{(2)}\kappa t}\right) \tag{3.134}$$

$$F_3(r,t) = \frac{\sqrt{\kappa t}}{r}\ exp\left(-\frac{t}{\tau} - \frac{r^2}{8\,\eta_{(2)}\kappa t}\right) W_{-1/2,0}\left(\frac{r^2}{4\,\eta_{(2)}\kappa t}\right)$$

where $W_{p,q}$ is the Witteker function, I_0 is the modified Bessel function of the first type, and the following conditions are satisfied:

$$p^{(1)} = p^{(2)} = p_0 \quad , \quad t = 0 \quad ; \quad p^{(1)} = p^{(2)} \quad , \quad r = r_w \approx 0$$

$$-r\left(\frac{\partial p^{(1)}}{\partial r} + \eta_{(2)}\frac{\partial p^{(2)}}{\partial r}\right) = \frac{Q\mu}{2\pi k\rho h} \tag{3.135}$$

The approximate solution of equation (3.124), which does not include the parameter $\eta_{(2)}$, can be written as [228]

$$\frac{2\pi k\rho h}{Q\mu}\left(p_0 - p^{(1)}\right) \approx 0.80908 - \frac{1}{2}ln\frac{r}{\sqrt{\kappa t}}$$

$$-\frac{1}{2}Ei\left(-\frac{t\left(1+\eta_{(1)}\right)}{\tau\,\eta_{(1)}}\right) + \frac{1}{2}Ei\left(-\frac{t\left(1+\eta_{(1)}\right)^2}{\tau\,\eta_{(1)}}\right) \tag{3.136}$$

These solutions correspond to nonstationary pressure field in the reservoir if the well begin to act with mass production, Q, and if

$$p_w(t) = p(r_w, t) \quad , \qquad t \geq 0 \tag{3.137}$$

Its instant closure causes pressure to build-up. The measurement of pressure at the well bottom, $p_w(t) = p(r_w, t)$, permits Laplace transformation, $P_w(s)$, according to the rule

$$P_w^{(\alpha)}(x,s) = \int_0^\infty p_w^{(a)}(x,t)\, e^{-st}\, dt \tag{3.138}$$

The function $P_w(s)$ can be identified with pressure transformation, $P_w^{(1)}(s)$ or $P_w^{(2)}(s)$, depending on what combination shown in (3.139) coincides with the straight line in half-logarithmic coordinate system ($C = 0.5772$):

$$s\, P_w^{(1)}(s) = s(1+s\tau)\, P_w^{(2)}(s) = \frac{Q\mu}{2\pi k\rho h}\left(-ln\frac{C}{2} - \frac{1}{2}ln\frac{r_w}{\kappa} + \frac{1}{2}ln\left(\tau + \frac{1}{s}\right)\right) \tag{3.139}$$

In this way, the boundary condition that corresponds to proper hydraulic connection of the well with the reservoir can be identified. As usual, the quantity

$$\frac{Q\mu}{2\pi kh\rho} = \frac{p_w - p_0}{ln\,(R / r_w)} \tag{3.140}$$

is determined from the well-productivity curve (3.50), and τ can be found by the comparison method. The time of relaxation, τ, may be very different (from the first minutes to tens of hours, according to Dr. A. Ban).

3.4.5. NONLINEAR FISSURE-FLOW EFFECTS

In reservoirs with double porosity, the nonlinear effects are essential in the case of gas filter flow or (and) due to permeability changes of the crack system. The first effect is accounted by introduction of the Leibenson function into the mass exchange formulae (3.110) and into the divergence of fluxes. For example, the ideal gas flow is governed by system [234] instead of its linear variant (3.121):

$$\frac{\partial\, p^{(2)}}{\partial t} = \kappa\nabla^2\left(p^{(1)}\right)^2, \qquad \left(p^{(1)}\right)^2 - \left(p^{(2)}\right)^2 = \kappa\nabla^2\left(p^{(1)}\right)^2 \tag{3.141}$$

The same approach was developed to account for permeability changes by introducing the following as the Leibenson function:

$$\Phi(p) = \frac{1}{\alpha}\, exp\left(-\alpha\, p^{(1)}\right) \tag{3.142}$$

The resulting equations can be linearized for further analytical study, with fluxes unchanged and introducing approximate into time derivatives [152].

3.5. Filter-convective diffusion

3.5.1. AVERAGING OF CONCENTRATION FIELDS

The phenomenon of tracer spreading in underground flows is explained by the dispersion of marked particles in numerous pore channels of different sizes [195]. Obviously, the study should begin from the microlevel, where the concentration field C' is governed by the usual molecular diffusion with the coefficient D_m and the convective velocity $v_{i'}$:

$$\frac{\partial C'}{\partial t} = \frac{\partial}{\partial x_i}\left(D_m \frac{\partial C'}{\partial x_i}\right) - \frac{\partial C' v_i'}{\partial x_i} \tag{3.143}$$

Averaging this equation over fluid space ΔV_l of the elementary macrovolume $\Delta V = \Delta X_1 \Delta X_2 \Delta X_3$, the mass balance of the marked particles in this volume results:

$$\frac{\partial}{\partial t}\int_{\Delta V_f} C' dV = \int_{\Delta A_f} D_m \frac{\partial C'}{\partial x_i} n_i \, dA - \int_{\Delta A_f} C' v_i' n_i \, dA + \tag{3.144}$$

$$+ \int_{A_m} D_m \frac{\partial C'}{\partial x_i} n_i \, dA - \int_{A_m} C' v_i' n_i \, dA$$

Here, ΔA_f is the fluid part of the bounding surfaces of the volume, ΔV, and A_m is the surface of solid matrix inside ΔV. So, the first two terms of the right-hand side determine mass fluxes inside and out of ΔV, and the second couple of terms corresponds to adsorption of the particles at solid internal surfaces.

The mean value of concentration can be introduced for the fluid volume:

$$C(X_i, t) = \frac{1}{\Delta V_f}\int_{\Delta V_f} C' \, dV \tag{3.145}$$

Its introduction into integral balance (3.144) gives us the macro-differential equation

$$\frac{\partial C}{\partial t}\frac{\partial a}{\partial t} = \frac{\partial}{\partial X_i}(D_{ij}^{0} + D_{ij})\frac{\partial C}{\partial X_j} - v_i \frac{\partial C}{\partial X_i} \tag{3.146}$$

where the following definitions are used:

$$v_i = \frac{1}{\Delta S_f} \int_{\Delta S_f} v_i \, dS$$

$$D_{ij}^{\,0} \frac{\partial C}{\partial X_j} = \frac{1}{\Delta S_f} \int_{\Delta S_f} D_m \frac{\partial C'}{\partial x_i} n_i \, dS \tag{3.147}$$

$$D_{ij} \frac{\partial C}{\partial X_j} = \frac{1}{\Delta S_f} \int_{\Delta S_f} (C' - C)(v_i' - v_i) dS \equiv \frac{1}{\Delta S} \int_{\Delta S_f} C^* v_i^* \, dS$$

The area ΔA_f is composed of six boundary cross-sections, ΔS_f, determined by normal-vectors n_j of the coordinate axis. Here, $(\partial/\partial x_i) n_i = \partial/\partial x_n$, $D_{ij}^0 = t_{ij} D_m$, t_{ij} is the tortuosity tensor, and the superscript asterisk (*) means the pulsation value. The adsorption process is accounted for by body-distributed sinks (sources) [23]:

$$\frac{\partial a}{\partial t} = \int_{Am} \left(D_m \frac{\partial C'}{\partial x_i} + C' v_i \right) n_i \, dA \tag{3.148}$$

3.5.2. TENSORIAL DIFFUSION COEFFICIENT

Now we shall concentrate on the filter-diffusion coefficient, D_{ij}, which depends on velocity-vector v_i [142] . The isotropic microstructure of the porous medium does not introduce additional vectorial parameters. Multiplying D_{ij} by two arbitrary vectors b_i , d_j. It gives us the scalar quantity

$$D_{ij} b_i d_j = \varphi (b_i d_i , \; b_i v_i , \; d_i v_i) \tag{3.149}$$

which is a function of the shown scalar products. Because there is a linear form on the left-hand side, the function φ depends linearly on the vectors b_i and d_j. This results in following geometric connection

$$D_{ij} = A v_i v_j + B \delta_{ij} \tag{3.150}$$

where the arbitrariness of b_i and d_j is used. The next step is to use the dimension rule:

$$Dim \{D_{ij}\} = L^2 T^{-1} \quad , \qquad Dim \{v_i\} = L T^{-1} \tag{3.151}$$

which means

$$Dim\{D_{ij}\} = L\, v_j \tag{3.152}$$

The proper combination of results - (3.150) and (3.152) - gives the resulting law of the filter-convective diffusion [142]:

$$D_{ij} = Q_{ijkl} \frac{w_k}{|w_k|} \frac{w_l}{m} \tag{3.153}$$

$$Q_{ijkl} = (\lambda_1 - \lambda_2)\, \delta_{ik}\, \delta_{jl} + \lambda_2\, \delta_{ij}\, \delta_{kl} \tag{3.154}$$

where the filter velocity, w_i, is used according to (2.64), and connection (3.153) has a general form but expression (3.154) corresponds to the particular case of an isotropic porous medium...Here λ_1, λ_2 are the internal characteristic lengths.

3.5.3. EXPERIMENTAL DIFFUSION PARAMETERS

If you compare the filter dispersion with the Brownian motion [194], then λ_1 and λ_2 are the "mean free paths" in the longitudinal and lateral directions. The length, λ_i, is proportional to grain diameter or to $\sqrt{k / m}$, where k is the permeability.

These parameters, λ_1, λ_2, may be functions of the Peclet (Pe) and Reynolds (Re) numbers, which have the following relation:

$$Pe = \frac{|v_i| d}{D_m} = \frac{|v_i| d}{\nu} \frac{\nu}{D_m} = Re\ Pr \tag{3.155}$$

where $Pr = (\nu / D_m)$ is the Prandtl number and includes the kinematic viscosity of the fluid, ν. $Pr = 1$ for gases, but $Pr = 10^2 - 10^3$ for liquids.

Therefore, Pe and Re are nonequivalent, and the experiments (Figure 3.20) show that the longitudinal diffusion coefficients for gas and liquid flows coincide if the Reynolds number, Re, is used.

It underlines the hydrodynamic (not molecular) character of the filter dispersion for $Re \geq 10^{-3}$, where the proportionality between D and v is evident. This means that $\lambda = const$. However, for smaller Re -values, the dependence of D or Pe (and of λ on w) was also found.

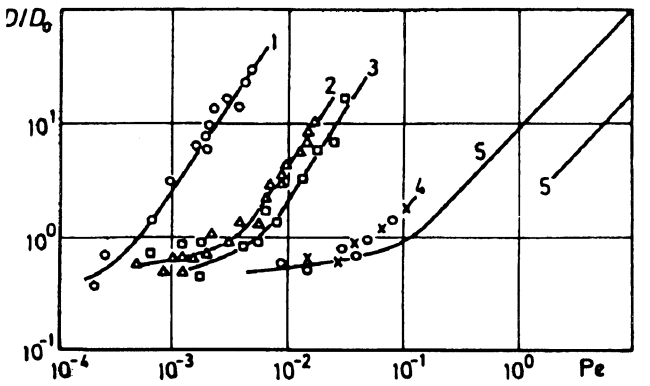

Figure 3.20. Effective diffusion depends on the internal Re number [33].

Darcy's law is violated for $Re \geq \left(10^{-2} \div 10^{-1}\right)$ for the permeability interval [121]

$$0{,}1 \ darcy \ \leq \ k \ \leq \ 1 \ darcy \tag{3.156}$$

Then, again, $\lambda = \lambda(Re)$, but for

$$0{,}1 \ \leq \ Re \ \leq \ 10 \tag{3.157}$$

another interval of invariance of the value $\lambda \approx 0.1\sqrt{k / m}$ appears.

The following experimental results can be cited here for river sands:

$$\lambda_1 = 0.127 \ cm \ , \quad \lambda_2 = 0.0089 \ cm \ , \quad \lambda_1 / \lambda_2 \approx 14.2$$
$$\left(D_1 / \nu\right) = 83 \, Re^{1.2} \ , \quad k = 10^{(-10)} \ m^2 = 100 \ darcy \tag{3.158}$$

and for gravels:

$$\left(D_1 / \nu\right) = 54 \, Re^{1.2} \ , \quad k = 3 \times 10^{-9} \ m^2 = 1000 \ darcy$$
$$\left(D_2 / \nu\right) = 2.95 \, Re^{0.7} \ , \quad D_1 / D_2 \approx 18.3 \tag{3.159}$$

3.5.4. RECOMMENDATION FOR THE PLANAR DISPERSION

For planar flow, it is possible to use "so-called" natural coordinate system $\varphi = const$, $\psi = const$, where

$$v_i = \frac{\partial \varphi}{\partial x_i} \quad , \qquad v_1 = \frac{\partial \psi}{\partial x_2} \quad , \qquad v_2 = -\frac{\partial \psi}{\partial x_1} \tag{3.160}$$

with φ being the potential and ψ being the stream function. Then equations (3.146) and (3.154) get the following form [15, 152]:

$$\frac{\partial C}{\partial t} + \frac{\partial a}{\partial t} = v^2 \frac{\partial}{\partial \varphi}\left((\lambda_1 |v| + D_0) \frac{\partial C}{\partial \varphi} - C \right) + v^2 \frac{\partial}{\partial \psi}\left((\lambda_2 |v| + D_0) \frac{\partial C}{\partial \psi} \right) \tag{3.161}$$

This equation is used for complicated filter flows when the negative components of the diffusion coefficient tensor appear in coordinate systems not determined by filter flow streams.

3.5.5. ADSORPTION AND ECOLOGY PROBLEMS

The adsorption rate is determined by the difference between concentration in the fluid phase and the equilibrium value of absorbed mass [23]:

$$\frac{\partial a}{\partial t} = \beta (C - y) \tag{3.162}$$

The equilibrium value, y, can be determined by the Henry isotherm

$$y = a / \gamma \tag{3.163}$$

where γ is the Henry constant, or by the Langmuir isotherm

$$a = \frac{y}{q + py} \tag{3.164}$$

where q and p are also constants of fluid and the porous medium. All of them are very sensitive to the temperature that permits control of the adsorption process.

The boundary conditions are formulated on the basis of mass balances. At the entrance into the porous medium, the equality of concentration is sufficient

$$C_*(t) \equiv C^+ = C^- \quad , \qquad x = 0 \tag{3.165}$$

where C_* is the concentration in the fluid injected into the reservoir being considered or added to the natural flow at the boundary (3.165).

At the exit from the porous media, the value $C_*(t)$ can be measured but is out of our control. Therefore, the mass balance is used, taking into account the intense diffusion inside the porous medium and its absence outside [28]:

$$w C^+ = w C^- - D(\partial C / \partial n) \tag{3.166}$$

Because $C^+ \equiv C^-$, the Dankwertz exit condition can be obtained:

$$\partial C / \partial n = 0 \tag{3.167}$$

where n is the normal to the exit boundary.

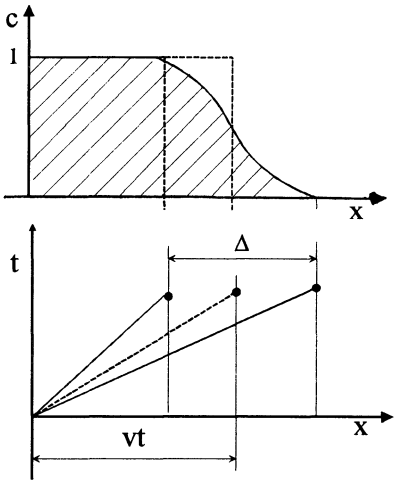

Figure 3.21. Dispersion Δ of neutral additives due to filter-convective diffusion.

Consider the characteristic feature of the filter-convective diffusion. The dispersion zone, Δ, estimated as is usual in diffusion theory (Figure 3.21), gives the following result because of (3.153):

$$\Delta \approx \sqrt{Dt} \approx \sqrt{\lambda L} \tag{3.168}$$

This means that the dispersion, Δ, is independent of convection velocity and time but dependent on the convection distance, L.

The mass transfer - (3.146) and (3.154) - takes into account of the adsorption effect according to the Henry isotherm (3.163), which can be reduced to the simple relaxation equation [157]

$$\Theta_a \frac{\partial}{\partial t}\left(\frac{\partial C}{\partial t} - D\frac{\partial^2 C}{\partial x^2} + v\frac{\partial C}{\partial x}\right) + \left(\frac{\partial C}{\partial t} - \frac{D}{1+\gamma}\frac{\partial^2 C}{\partial x^2} + \frac{v}{1+\gamma}\frac{\partial C}{\partial x}\right) = 0 \qquad (3.169)$$

which is valid for one-dimensional plane flow.

Here, Θ_a is the adsorption relaxation time:

$$\Theta_a = \frac{\gamma}{1+\gamma}\frac{1}{\beta} \qquad (3.170)$$

If $T << \Theta_a$, only the first diffusion operator acts and the usual diffusion process with negligible adsorption takes place. However, if $T >> \Theta_a$, the effective time [157]

$$t^{(\gamma)} = \frac{t}{(1+\gamma)} \qquad (3.171)$$

is used in this equation:

$$\frac{\partial C}{\partial t^{(\gamma)}} = D\frac{\partial^2 C}{\partial x^2} - v\frac{\partial C}{\partial x} \qquad (3.172)$$

Every chemical component of a mixture has its own parameters $\gamma^{(\alpha)}$. Therefore, the adsorption components, spreading with a joint convective velocity but with their own diffusion coefficients, are separated drastically. This process is known as chromatography.

With regard to the role of adsorption and diffusion in ecology, the higher is the concentration C, the more intensive the adsorptive cleaning of fluid flow that takes place in accordance with equation (3.162). So, the diffusion process diminishes the values of C in the flow and hence the adsorption rate. As can be seen, all calculations of mass transfer in filter flows without diffusion give the lower boundary of real penetration of wastes or other dangerous matter. In Figure 3.22, the calculation of the spread of radionuclides is given for *25 min* after the underground nuclear explosion. The danger is lower by order (broken line) if diffusion is not taken into account, in comparison with the real process with diffusion and adsorption [152].

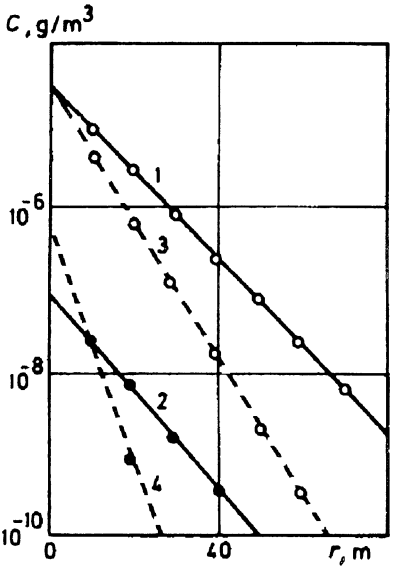

Figure 3.22. Concentration fields of cesium (1,3) and xenon (2,4) with (1,2) and without (3.4) diffusion in the vicinity of a spherical cavity (according to N. A. Kudryashov).

Some efforts were made to account for crack presence in rocks on the basis of probability theory and fractal techniques [50].

CHAPTER 4

COMPLICATED PHENOMENA IN RESERVOIRS

4.1. Miscible and gas-condensate flows

4.1.1. HYDRODYNAMICS OF MISCIBLE FLUIDS

In the case of mixture flows of miscible phases, mass balance has to be formulated for every component in all phases - that is [157]

$$\frac{\partial}{\partial t}\left(\rho^{(\alpha)} C_{(k)}{}^{(\alpha)} m \theta^{(\alpha)}\right) + \frac{\partial}{\partial x_j}\left(\rho^{(\alpha)} C_{(k)}{}^{(\alpha)} w_j{}^{(\alpha)}\right) = \Sigma_\beta N_{(k)}{}^{(\alpha\beta)} \tag{4.1}$$

where the phase symbols (α), (β) correspond to values (1), ... , (J); $(k) = (1)$, ... , (K), is the component index; $C_{(k)}^{(\alpha)}$ is the mass concentration of the component k in the phase α ; $\theta^{(\alpha)}$ is the saturation of the porous space by the phase α and $N_{(k)}{}^{(\alpha\beta)}$ is the mass exchange of the component k between phases; α and β. The number of equations (4.1) is equal to JK.

It is accepted that the generalized Darcy's law can be utilized

$$w_j{}^{(\alpha)} = -\frac{k^{(\alpha)}\left(\theta^{(\alpha)}\right)}{\mu^{(\alpha)}} \nabla_j p^{(\alpha)} \tag{4.2}$$

with usual phase permeability (Section 3.3)

$$k^{(\alpha)} = k\, f^{(\alpha)}\left(\theta^{(\alpha)}\right) \tag{4.3}$$

the same relative phase permeability, $f^{(\alpha)}\left(\theta^{(\alpha)}\right)$, and the phase pressure concept (3.82) as in the case of immiscible phase filter flows. Of course, the interface tension γ is changing due to miscibility,

$$\sum_\alpha \theta^{(\alpha)} = 1$$

and k is the absolute permeability of the medium.

The most interesting case is of gas-condensate flows originated by so-called "retrograde condensation" due to molecular interaction of different types of heavy hydrocarbons if gas pressure p belongs to some interval (Figure 4.1):

$$p_- \leq p \leq p_+ \tag{4.4}$$

where p_- , p_+ are corresponding threshold values. Then one can use only two types of concentrations: $g_{(k)}$ and $l_{(k)}$ in gas $(\alpha = g)$ and liquid $(\beta = l)$ phases,

$$\sum_k^N g_{(k)} = 1 \quad , \qquad \sum_k^N l_{(k)} = 1 \tag{4.5}$$

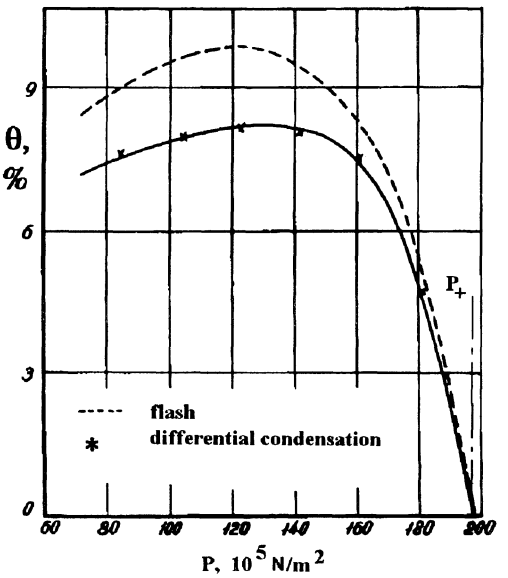

Figure 4.1. Experimental retrograde condensation of a hydrocarbon mixture in a PVT-cell. (Saturation θ is the cell volume (%) occupied by a liquid phase).

The rate of mass exchange between phases must be proportional to the difference of chemical potentials $\chi_{(k)}^{(\alpha)}$ [150, 157]:

$$N_{(k)}^{(\alpha\beta)} = \frac{\chi_{(k)}^{(\alpha)} - \chi_{(k)}^{(\beta)}}{\tau_{(k)}^{(\alpha\beta)}} \tag{4.6}$$

where $\tau_{(k)}^{(\alpha\beta)}$ is the relaxation time.

4.1.2. RULE OF HETEROGENEOUS EQUILIBRIUM

Let us suggest that there is a local thermodynamic equilibrium - that is, instant mass exchange takes place:

$$\chi_{(k)}^{(g)} = \chi_{(k)}^{(l)} \tag{4.7}$$

and that phase pressures and temperatures are equal:

$$p^{(g)} = p^{(l)} \tag{4.8}$$

$$T^{(g)} = T^{(l)} \tag{4.9}$$

The important point here is the determination of independent equilibrium parameters, or so-called chemical degrees-of-freedom, which will be arguments of component concentrations $g_{(k)}$ and l_k. Consider the problem.

The total number of variables is the sum of a number of concentrations, $J(K-1)$, number of saturation, $J-1$, plus two (pressure and temperature):

$$J(K-1)+2+(J-1)=JK+1 \tag{4.10}$$

However, some of these variables are interconnected by the equalities shown in (4.7), with a number equal to $K(J-1)$. Therefore, the number of component mass balances (4.1) has to be equal to total number of components K and including mass contents in both phases:

$$\frac{\partial}{\partial t} m\left(\rho^{(g)}\theta^{(g)} g_{(k)} + \rho^{(l)}\theta^{(l)} l_{(k)}\right) + \frac{\partial}{\partial x_j}\left(\rho^{(g)} g_{(k)} w_j^{(h)} + \rho^{(l)} l_{(k)} w_j^{(l)}\right) = 0 \tag{4.11}$$

So, the number of independent variables corresponding to the effective system (4.11) is equal to the following difference:

$$(JK+1)-K(J-1)=K+1 \tag{4.12}$$

Therefore, one more equation must be added - the heat balance. In the isothermal case, when $T = const$, number (4.12) coincides with the number of equation (4.11).

If the chemical potentials, $\chi_{(k)}^{(\alpha)}$, also depend on the phase saturation, $\theta^{(\alpha)}$, of a porous space, then the number of arguments for $g_{(k)}$ and $l_{(k)}$ would be exactly determined by (4.12), which included a number of saturation. If so, the data of

concentration distribution found by the PVT-cell measurements for the mixture only within a porous medium can be used (to account for capillary forces).

If the influence of phase saturation (in other words, of capillary forces) on the chemical potentials is negligible, then the initial number (4.10) is diminished by the number of independent saturation and is equal to

$$J(K-1)+2 \tag{4.13}$$

Then, the degree-of-freedom, d_f, will be determined by the Gibbs phase rule as the difference of (4.13) and $K(J-1)$:

$$d_f = J(K-1)+2-K(J-1) = K-J+2 \tag{4.14}$$

This means that the component distribution over phases of gas-condensate flows $(J=2)$ in isothermal reservoirs has the value $d_f = K-1$. So, the isothermal case of a gas solution in oil $(K=2)$ is determined by the value $d_f = 1$, showing the gas content in the liquid phase, $l = l(p)$, is the function of a pore pressure as well as its concentration in the gas phase, $g = g(p)$. Therefore, gassy oil is characterized by gas solubility in oil depending on pressure (and on temperature as a reservoir-constant parameter but not as a parameter of flow processes).

The three-component mixture of hydrocarbons is characterized by component distribution in gas and liquid phases which is dependent on pressure and one independent concentration, C_f , according to the Gibbs phase rule (4.14):

$$g_k = g_k(p, C_f) \quad , \qquad l_k = l_k(p, C_f) \quad , \qquad T = const \tag{4.15}$$

The C_f-parameter can be chosen as follows [157,162]

$$C_f = \frac{l_{(2)}}{l_{(2)} + l_{(3)}} \tag{4.16}$$

However, this could be the "convergence" pressure instead of (4.16) as it was used in some textbooks.

4.1.3. PVT-MODELING OF A RESERVOIR

The mass balances (4.11) can be useful for interpretation the measurement data of "flash" and "differential" condensations in PVT-cell. To this aim, equations (4.11) is averaged over space:

$$\frac{d}{dt}V\left\{g_k\rho^{(g)}(1-\Theta)+l_{(r)}\rho^{(l)}\right\}=-g_{(k)}\left(1-\beta_{(k)}\right)Q \qquad (4.17)$$

where V is the cell volume, Q is the average mass gas output, and $\beta_{(k)}$ is gas fraction returned to the cell for special evaporation of the residual liquid condensate. You can see that equation (4.17) can also be used to estimate hydrocarbon masses in the reservoir volume as a whole. As a result, the PVT-cell sometimes plays the role of an experimental volume-averaged model of the reservoir.

During "flash" condensation, volume $V = V(t)$ is a given function of time, but fluxes are absent ($Q = 0$). The differential condensation is characterized by the conditions $V = const$ and $Q = const$. The corresponding calculation is represented in Figure 4.2 which shows an essential difference in the condensate saturation field for illustrating a "methane + butane + decane" mixture [162].

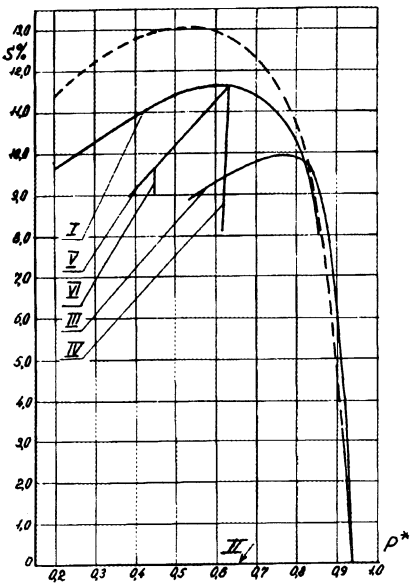

Figure 4.2. Calculations of retrograde condensation with gas cycling (I variant -differential condensation, $\beta_{(k)} = 0$; II - reach gas return, $\beta_{(1)} = 1$; $\beta_{(2)} = \beta_{(3)} = 0$; III,V - $\beta_{(1)} = 0.5$; $\beta_{(2)} = \beta_{(3)} = 0$; IV,VI -$\beta_{(1)} = \beta_{(2)} = \beta_{(3)} = 1$.

However, parameter (4.16) changes with pressure along the universal curve where the gas return into the cell or reservoir is excluded (curves I in Figure 4.3).

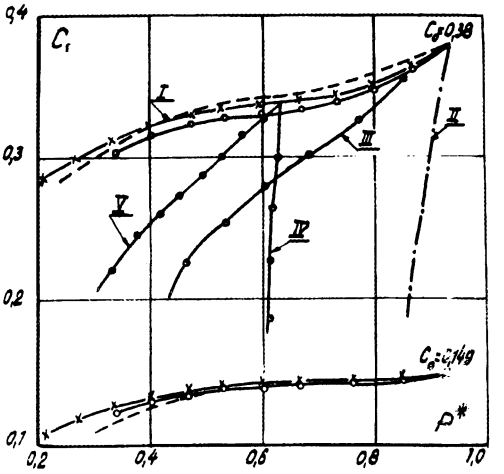

Figure 4.3. Cumulative curves for the Gibbs free concentration, C_f , in gas-condensate flow for two initially different gas mixtures (C_0 = 0.38 ; C_0 = 0.149); $p_* = p / p_+$ [162].

This point was used for some simplified mathematical modeling of gas-condensate flows suggesting that g_k and l_k are functions of pressure only.

4.1.4. GAS-CONDENSATE WELL PRODUCTIVITY

The equations for gas-condensate stationary flows in a reservoir can be rewritten as:

$$\frac{\partial}{\partial x_i}\left(\Gamma\Gamma_k \frac{\partial p}{\partial x_i}\right) = \Gamma_k \frac{\partial}{\partial x_i}\left(\Gamma \frac{\partial p}{\partial x_i}\right) + \Gamma\left(\frac{\partial p}{\partial x_i}\right)\left(\frac{\partial \Gamma_k}{\partial x_i}\right) = 0 \qquad (4.18)$$

where $\Gamma_{(k)}$ is the ratio of the mass flow rate of the corresponding components to the total mass flow:

$$\Gamma_k = \frac{g_{(k)}\mathrm{M} + l_{(k)}}{\mathrm{M}+1} \quad , \qquad \mathrm{M} = \frac{\rho^{(g)} w_i^{(g)}}{\rho^{(l)} w_i^{(l)}} \qquad (4.19)$$

Accounting for the total mass balance:

$$\frac{\partial}{\partial x_i}\left(\Gamma \frac{\partial p}{\partial x_i}\right) = 0,$$

$$\sum \Gamma_k = 1 \quad , \qquad \Gamma = \rho^{(g)} k \frac{f^{(g)}}{\mu^{(g)}} + \rho^{(l)} k \frac{f^{(l)}}{\mu^{(l)}} \tag{4.20}$$

and according to (4.18), the scalar production of the two vector-gradients is equal to zero:

$$(\partial \Gamma_{(k)} / \partial x_i)(\partial p / \partial x_i) = 0 \tag{4.21}$$

If the flow exists, the pressure gradient does not equal to zero and [157]

$$\partial \Gamma_{(k)} / \partial x_i = 0 \quad , \qquad \Gamma_k = const \tag{4.22}$$

along stream lines. The number of such conditions is $K - 1$, and they give the opportunity to determine all variables - that is, θ , $g_{(k)}$, $l_{(k)}$ as functions of pressure, p, only.

Only the total mass balance must considered further. It has the form:

$$\nabla^2 H = 0 \quad , \qquad H = \int \Gamma dp \tag{4.23}$$

and determines the rate of well production as [42]

$$Q_{(k)} = \Gamma_{(k)} \frac{2\pi kh}{ln(R / r_w)} \{H(R) - H(r_w)\} \tag{4.24}$$

However, equation (4.22) is invalid if one of phases is immovable - that is, if M = 0 or M = ∞. Then, $\Gamma_k \equiv l_k$ or $\Gamma_k \equiv g_k$ and conditions (4.22) reduce to the condition of zero pressure gradient that cancels the flow. Therefore, the quasistationary solution [125] was suggested for the case in which concentrations $l_{(k)}$, $g_{(k)}$ are assumed to be dependent only on space coordinates (although saturation can be functions of time and space). This is possible if the permeability of the moving (gas) phase is independent of liquid phase saturation (as is practically so for $\theta^{(l)} \le \theta_*^{(l)}$, where $\theta_*^{(l)}$ is the threshold value). The corresponding calculations illustrate the process of accumulation of liquid phase around gas-condensate wells (Figure 4.4).

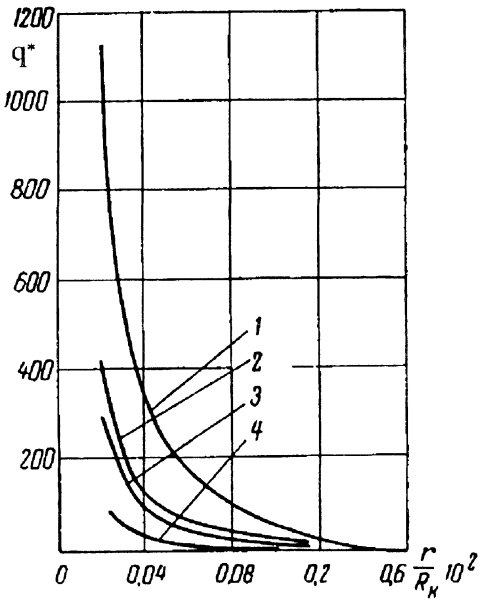

Figure 4.4. Reduced gas flow rate into a productive well that is proportional to saturation rate.

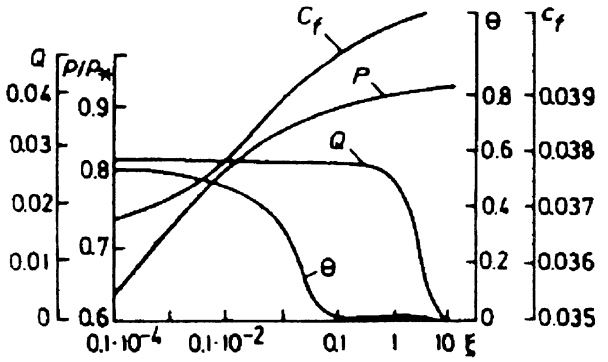

Figure 4.5. Gas-condensate flow parameters for the beginning of constant well production, $\left(\xi = r/\sqrt{t}\right)$.

The C_f changes are also situated practically in the vicinity of the same universal curve seen in Figure 4.3 as well as in the case of nonstationary flow to the well, which begins to act with constant mass production $Q = const$, $t \geq 0$. This flow is a function of one variable: $\xi = r / \sqrt{t}$ (Figure 4.5) [162].

4.1.5. GAS RECIRCULATION PROCESS

Methane returns to the reservoir during the so-called cycling process, when the gas (with some addition of intermediate fractions) diminishes the effect of liquid residual condensation. This process is more complicated than flooding because injected gases penetrate through the displacement front (the latter being moved with the velocity U_i). At this boundary, the mass balances (1.31) account for the transfer in both phases for all components: $(k) = 1, \ldots, K$:

$$\left[g^{(k)}\rho^{(g)}\left(w_i^{(g)} - m(1-\theta)U_i\right) + l^{(k)}\rho^{(l)}\left(w_i^{(l)} - m\theta U_i\right)\right] = 0 \qquad (4.25)$$

Due to negligible inertia forces, the continuity of pressure at this front ($[p] = p^+ - p^- = 0$) is a sequence of the impulse balance.

Because the differential equations - (4.2) and (4.11) - are valid everywhere out of this front, the Boltzman substitution, $\xi = x/\sqrt{t}$, permits determination of one-dimensional self-preserving solutions to describe the gas-cycling process. The corresponding curves are presented in Figure 4.6. The broken line denotes the front movements with time, according to the rule $x = \xi_+\sqrt{t}$ [162].

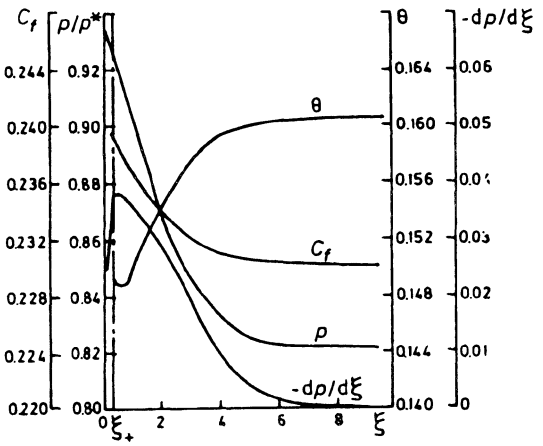

Figure 4.6. Gas-cycling process in a plane, one-dimensional layer $\xi = x / \sqrt{t}$.

4.1.6. OSCILLATIONS IN GAS-CONDENSATE FLOWS

V. Mitlin [99] has found that some gas-condensate filter flows are unstable. Consider the mass-balances given in (4.11) written in the following form:

$$\nabla\left(\Gamma\Gamma_{(k)}\nabla p\right) = m\frac{\partial N z_{(k)}}{\partial t} \tag{4.26}$$

where z_k is the local mass concentration of the component k,

$$z_{(k)} = \frac{\rho^{(g)}}{\rho}\theta^{(g)}g_{(k)} + \frac{\rho^{(l)}}{\rho}\theta^{(l)}l_{(k)} \quad , \qquad \sum_k z_{(k)} = 1 \tag{4.27}$$

and $\rho = \rho^{(l)}\theta^{(l)} + \rho^{(g)}\theta^{(g)}$ is the mean density of the mixture.

Disturbances of gas-condensate flows are described by linear equations

$$\frac{\partial p'}{\partial t} = I\ \nabla^2 p' \tag{4.28}$$

$$\frac{\partial z'_{(k)}}{\partial \tau} = \left(\Gamma_{(k)} - z_{(k)}\right)\frac{k\Gamma}{m\rho}\nabla^2 p' \tag{4.29}$$

and can be represented in the following form:

$$\begin{gathered} z'_{(k)} = z_{(k)} - z^{o}_{(k)} = -z''_{(k)}\,exp(-iqx) \ , \\ p' = p - p^0 = p''\,exp(-iqx) \end{gathered} \tag{4.30}$$

You can see that disturbances with wave number q will grow if $I < 0$, but they will decay if $I > 0$:

$$dp'' / dt = -I\,q^2\,p'' \tag{4.31}$$

So, the criterion of gas-condensate flow instability can be formulated in the following form:

$$I = \frac{k}{m}\Gamma\frac{dp}{d\rho} < 0 \tag{4.32}$$

where the derivative sense is determined by the following rule (mentioned by my student - L. Pausner, 1993), valid for isothermal conditions in accordance with equations (4.26):

$$\left(\left(\frac{\partial\rho}{\partial p}\right)_{z(k)} + \sum_{k=1}^{K-1}\left(\frac{\partial\rho}{\partial z_{(j)}}\right)_{p,z(k\neq j)} \frac{d\,z_{(j)}}{dp}\right)\frac{dp}{d\rho} = 1 \tag{4.33}$$

This derivative may be negative because of the mass concentration changes created by nonequal phase fluxes. The numerical examples [134] are given in Figure 4.7, where disturbances are generated by the calculation mesh.

Instability of gas-condensate well production is sometimes observed in situ, but it can also be explained by the unstable regime of flows in the well column and at its boundary with the stem. Some laboratory studies [134] of gas-condensate flow have also shown instability, but it is unclear if it is connected with bulk flow instability or with boundary effects.

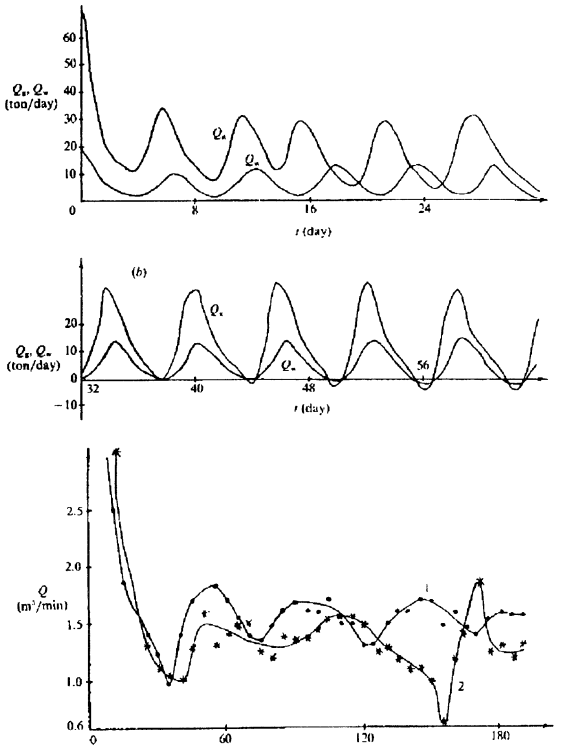

Figure 4.7. Gas-condensate unstable flow: calculations for plane radial flows (a,b) and experiment (c) under plane one-dimensional condition [134].

In all these calculations, the conventional phase permeability curves were used for gas and liquid phases. However, more sophisticated curves would be used to account for the decrease of capillary forces in the vicinity of supercritical thermodynamic states. Asymptotically, these curves have to coincide with the corresponding saturation ($f^{(\alpha)}(\theta^{(\alpha)}) \approx \theta^{(\alpha)}$) see (3.101) and broken lines in Figure 3.14.

4.1.7. MICRO-EMULSION MASS TRANSFER

Another possible type of gas-condensate flow can be realized in the form of micro-emulsion transfer with mean filter velocity, w_i. In this case, the liquid phase is separated into movable and adsorbed parts. A corresponding system of mass balances can be formulated as follows:

$$\frac{\partial m \rho^{(g)} \theta^{(g)}}{\partial t} + \frac{\partial}{\partial x_j}\left(\rho^{(g)} \theta^{(g)} w_i\right) = -\frac{\partial a^{(g)}}{\partial t} \tag{4.34}$$

$$\frac{\partial m \rho^{(l)} \theta^{(l)}}{\partial t} + \frac{\partial}{\partial x_j}\left(\rho^{(l)} \theta^{(l)} w_i\right) = -\frac{\partial a^{(l)}}{\partial t} \tag{4.35}$$

$$\frac{\partial (1-m) \rho^{(s)}}{\partial t} = \frac{\partial a^{(g)}}{\partial t} + \frac{\partial a^{(l)}}{\partial t} \tag{4.36}$$

where w_j is determined by Darcy's law for homogeneous flow, $\rho^{(s)}$ is the solid matrix density, $\theta^{(g)} \equiv \theta$, $\theta^{(l)} = 1 - \theta$, and the isotherms , $i^{(\alpha)}$, of gas phase and microemulsion adsorption have to be measured:

$$a^{(g)} = m\rho^{(g)} i^{(g)}(\theta) \quad , \qquad a^{(l)} = m\rho^{(l)} i^{(l)}(\theta) \tag{4.37}$$

V. Petrenko has discovered the possibility of such a transfer of liquid condensate by the presence of distilled water films created around condensate drops in the gas well production. The system - (4.34) through (4.36) - is interconnected with the approach given in (3.101) which was suggested by A.A. Barmin and D.I. Garagash [13] for water-oil transfer. They have shown that system - (4.34) through (4.37) - can be reduced to the following one-dimensional plane wave equation:

$$\frac{\partial \theta}{\partial t} + Z(\theta)\frac{\partial \theta}{\partial x} = 0 \tag{4.38}$$

$$Z(\theta) = \left(\frac{dA}{d\theta}\right)^{-1} \frac{W(\theta)}{\gamma(\theta) - \theta} \tag{4.39}$$

$$A(\theta) = m\{1 + i^{(g)}(\theta) + i^{(l)}(\theta)\},$$

$$B(\theta) = m\{\theta + i^{(g)}(\theta)\},$$

$$(m_0/m) = 1 + \left(\rho_{(g)}/\rho\right) i^{(g)}(\theta) + \left(\rho_{(l)}/\rho\right) i^{(l)}(\theta)$$

$$W(\theta) = exp\left(\int_0^{\theta} \frac{d\theta}{\gamma(\theta) - \theta}\right) \quad , \qquad \gamma(\theta) = \frac{dB}{dA}$$

You can see the analogy with equations (3.101) and (3.103), presented in Section 3.3 for the cases of nonlinear convective transfer in two-phase flows.

4.1.8. A NOTE ON THE SURFACTANT EFFECT

Some variants of two-phase flow theory were developed to account for chemical changes of water by adding of some surfactants, polymers, etc. This procedure is done for later displacement of crude oil from reservoir matrix. In such a theory the relative phase permeabilities are suggested to the functions of saturation and concentration of additives:

$$f^{(\alpha)} = f^{(\alpha)}(\theta, C) \tag{4.40}$$

This creates many new possibilities for boundary conditions at the front discontinuities as well as for continuous flows [17,61].

However, we have to remember that the proper theory of two-phase flows with surfactant additives will account for transition of oil (water) phases into microemulsion states. This increases a number of balance equations and needs another variant of kinetics.

4.2. Permafrost and gas-hydrate mechanics

4.2.1. PERMAFROST THAWING

The problem of soil freezing was the initial impetus for the Stefan problem of heat transfer with phase transition at the moving boundary. Here we consider the formulation which accounts for processes inside geomaterial pore space under freezing or thawing conditions.

Let the liquid phase (water) occupy a volume $m\theta$ and the solidified phase (ice) a volume $m(1-\theta)$ joined to the solid matrix phase. The thermodynamic condition of phase coexistence is formulated for temperature T which must be equal to the phase-transition temperature:

$$T = T_f(p,l) \tag{4.41}$$

The latter is assumed to be the following function of mass salt concentration l in the water and pressure

$$T_f(p,l) = T_w - A\,l - B\,(p - p_a) \tag{4.42}$$

where T_w is the phase-transition temperature of pure water at atmospheric pressure, p_a, and A, B are the coefficients.

The rate of water filtration, w_i, is governed by the same generalized Darcy law (3.78), although ice is in the immovable phase in the case considered here. Using the mass balances in (4.1) gives the following nonlinear equation [118] for pore pressure:

$$\frac{\partial p}{\partial t} + K_f\left(1 - \frac{\rho_i}{\rho_w}\right)\frac{\partial \theta}{\partial t} = \kappa_f \frac{\partial^2 p}{\partial x_j \partial x_j} + \frac{kK_f}{m\mu_w}\frac{df_w}{d\theta}\frac{\partial \theta}{\partial x_j}\frac{\partial p}{\partial x_j} \tag{4.43}$$

where K_f is the effective compressibility of the medium, ρ_i and ρ_w are the densities of ice and water, and κ_f is the effective coefficient of piezoconductivity.

The energy balance must be formulated in this case and can be written as follows:

$$\rho C_{ht}\frac{\partial T}{\partial t} + mq\frac{\partial \theta}{\partial t} = \frac{\partial}{\partial x_j}\left(\lambda_f \frac{\partial T}{\partial x_j}\right) \tag{4.44}$$

where C_{ht} is the effective heat capacity of the medium, λ_f is the effective thermal conductivity, and q is the heat discharge for the phase transition. Heat convection with a filter flow is assumed to be negligible.

The third necessary equation is the balance of the dissolved substance, the salt, for example:

$$\frac{\partial l\theta}{\partial t} = \frac{\partial}{\partial x_j} D(\theta) \frac{\partial l}{\partial x_j} \tag{4.45}$$

where $D(\theta)$ is the effective diffusion coefficient.

Equation (4.43) corresponds to the distribution of water saturation, including possible discontinuities. Salt concentration, pressure and temperature have to be continuous:

$$[l] = 0, \quad [p] = 0, \quad [T] = 0 \tag{4.46}$$

However, the finite jump of saturation has to be included into the following fluxes at the front of thawing $X(x_i, t)$, which moves with the velocity, $U_i = dX_i / dt$:

$$m[\theta]\left(1 - \frac{\rho_i}{\rho_w}\right) U_i = [w_i]$$

$$m[\theta] l U_i + m\left[D(\theta) \frac{\partial l}{\partial x_i}\right] = 0 \tag{4.47}$$

$$m[\theta] q U_i + \left[\lambda_f \frac{\partial T}{\partial x_i}\right] = 0$$

In the frozen ($\theta = \theta_0$) and thawed ($\theta = 1$) zones, the equations for temperature, concentration and pressure conduction split, although the coefficients are different:

$$\frac{\partial T}{\partial t} = a \frac{\partial^2 T}{\partial x_j \partial x_j} \quad , \quad \frac{\partial l}{\partial t} = D_0 \frac{\partial^2 l}{\partial x_j \partial x_j} \quad , \quad \frac{\partial p}{\partial t} = \kappa \frac{\partial^2 p}{\partial x_j \partial x_j} \tag{4.48}$$

One-dimensional calculation of the problem on the basis of equations (4.48) have shown that in the front vicinity thermodynamic equilibrium is violated [118]. If $a < \kappa$, the violation creates the "supercooling" effect in the frozen zone when the temperature is lower than the phase transition temperature in the frozen zone. The "superheating" effect takes place in the frozen zone if $a > \kappa$, when the temperature is higher than its phase-transition value.

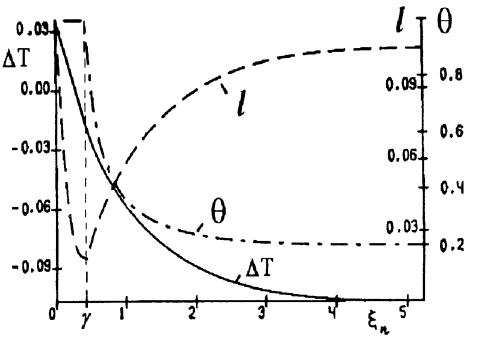

Figure 4.8. Self-similar solution of one-dimensional planar permafrost thawing where ΔT is the normalized deviation from T_w and γ is the thawing front position [118].

Therefore, the model of partial phase transition was developed assuming that continuous transition from the solid to liquid state is valid. In this case, the water saturation is found based on equations (4.43) through (4.45). Some results of numerical calculations for the self-similar solution are given in Figure 4.8, where the zone of continuous thawing is shown and where $X = \gamma\sqrt{t}$.

4.2.2. GAS-HYDRATE SOILS

Phase transitions must also be considered for the gas-hydrates present in some marine soils and in the gas reservoirs in the vicinity of producing wells [91,116]. Gas-hydrate is a solid material composed of natural gas, water or ice, including oil sediments.

During the creation of hydrates, the soil increases its volume from 5% to 12%, and hydrate dissociation leads to decreasing soil volume. If drainage is impossible, the soil can transfer to a unconsolidated state and the essential part of external loading is transmitted to the pore water pressure. In Figure 4.9, the growth of pore pressure is shown for triaxial tests together with shear stress [174]. As can be seen, these curves have roughly the same form because the undrained conditions take place for soft geomaterial and normal effective stress is unchanged. This situation is very unstable.

However, if the soil possesses a very high saturation of gases in the form of small bubbles after hydrate dissociation, then the pore pressure grows proportionally to pore volume decrease (Figure 4.10). The shear stresses are equalized by the normal effective stress.

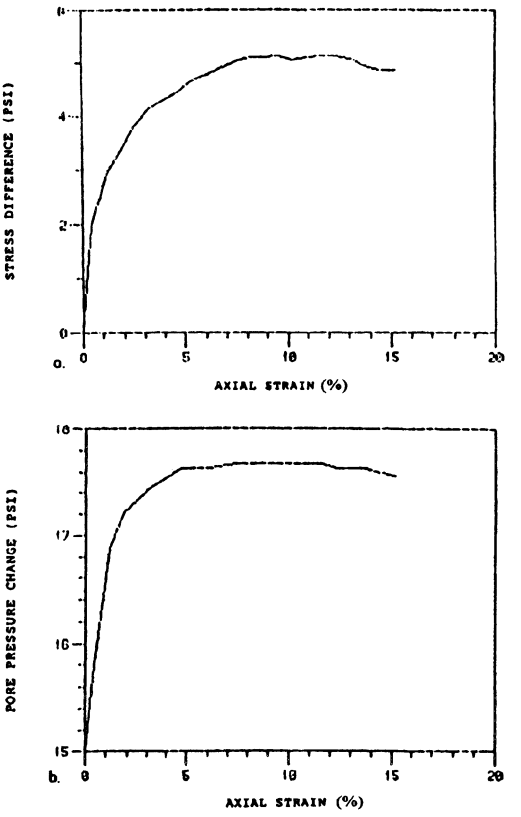

Figure 4.9. Differential stress $(\sigma_1 - \sigma_3)$ and pore pressure as a function of axial strain (e_1) for triaxial soil tests with dissociating gas-hydrates (without drainage); pore pressure is repeating external shear load due to the dilatancy effect because of small gas saturation.

In situ, the gas-hydrates can be found in soils because of the high seismic velocities (from 2 km/sec to 5 km/sec) of formations with hydrates. The difference depends on the presence of gas bubbles and on the rigidity of bonds between soil grains constructed from the gas-hydrates themselves.

The process of hydratation can be observed by the increase of wave velocities with temperature decrease. This means that the phase-transition zone is continuous and limited by two curves (liquidus and solidus), corresponding to full liquid and solid states. The temperature interval is of the order of $5° C$ and corresponds to the state of partial melting. Therefore, the Stefan frontal model must be changed into the moving continuous zone with partial saturation, $0 \leq \theta_h \leq 1$, of gas-hydrates.

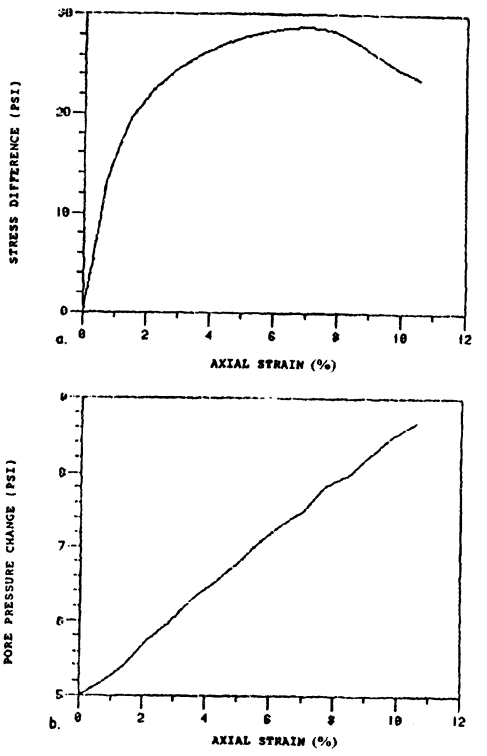

Figure 4.10. Differential stress ($\sigma_1 - \sigma_3$) and pore pressure as a function of axial strain (e_1) for triaxial soil tests with dissociating gas hydrate (without drainage); pore pressure grows proportionally to pore space decrease without the dilatancy effect if gas saturation is high.

4.2.3. GAS-HYDRATE DISSOCIATION PROCESS

The mathematical model is formulated as a gas component balance

$$m\frac{\partial}{\partial t}\left\{\theta_h g_h \rho_h + (1-\theta_h)(1-\theta_w)\rho_g\right\} + \frac{\partial}{\partial x_j}\left(\rho_g w_j^{(g)}\right) = 0 \qquad (4.49)$$

and water balance

$$m\frac{\partial}{\partial t}\{\theta_h(1-g_h)\rho_h+(1-\theta_h)\theta_w\rho_w\}+\frac{\partial}{\partial x_j}(\rho_w w_i^{(w)})=0 \tag{4.50}$$

where ρ_h, ρ_w are the densities of gas-hydrate and water, g_h is the gas concentration in gas-hydrates, $(1-g_h)$ is the water concentration and $(1-\theta_h)$ is the pore saturation by the water and gas phase with density ρ_g, the latter saturation being equal to $(1-\theta_w)$. The filter velocities are determined by the generalized Darcy law:

$$w_i^{(w)}=-\frac{k}{\mu_w}f_w(\theta_h,\theta_w)\frac{\partial p}{\partial x_i} \tag{4.51}$$

$$w_i^{(g)}=-\frac{k}{\mu_g}f_g(\theta_h,\theta_w)\frac{\partial p}{\partial x_i} \tag{4.52}$$

where θ_h plays the role of an additional parameter of the relative phase permeability (f_w for water and f_g for gas). Physically, this means porosity, m, diminishes by part θ_h.

The energy balance includes the specific discharge, g, for dissociation of the volume unit of the gas-hydrate [117]:

$$\rho C_{hT}\frac{\partial T}{\partial t}-mq\rho_h\frac{\partial\theta_h}{\partial t}-m(1-\theta_h)(1-\theta_w)\frac{\partial p}{\partial t}+$$
$$\left(\rho_w w_i^{(w)}C_w+\rho_g w_i^{(g)}C_g\right)\frac{\partial T}{\partial x_i}+w_i^{(w)}\frac{\partial p}{\partial x_i}=\frac{\partial}{\partial x_i}\lambda_e\frac{\partial T}{\partial x_i} \tag{4.53}$$

where ρC_{hT} is the effective heat capacity of the porous medium, and λ_e is its effective thermal conductivity.

The condition of thermodynamical equilibrium for the mixture has the following form:

$$T=\alpha_1 \ln p+\alpha_2 \tag{4.54}$$

which is equivalent to the chemical potential equality for hydrate and mixture free states, and α_i are constants.

At the moving boundary $X_i(x_i,t)$ of the phase transition, pore pressure and temperature are continuous, the gas-hydrate is absent behind it, and saturations θ_h and θ_w can be discontinuous.

The water mass balance must be valid at this discontinuity. It is represented here for the one-dimensional case:

$$m\left\{\rho_w \theta_w^{(-)} - \rho_w \theta_w^{(+)}\left(1-\theta_h^{(+)}\right) - \left(1-g_h^{(+)}\right)\theta_h^{(+)}\rho_h\right\}\frac{dX}{dt} = \rho_w\left(w_{(-)}^{(w)} - w_{(+)}^{(w)}\right) \qquad (4.55)$$

The gas balance

$$m\left\{\left(1-\theta_w^-\right)\rho_g - \theta_h^+\left(1-g_h^+\right)\rho_h^-\left(1-\theta_w^+\right)\left(1-\theta_h^+\right)\rho_g\right\}\frac{dX}{dt} = \rho_g\left(w_{(-)}^{(g)} - w_{(+)}^{(g)}\right) \qquad (4.56)$$

must be added to the energy balance

$$m\,\theta_w^{(+)}\rho_h q\frac{dX}{dt} = \lambda_e^{(+)}\left(\frac{\partial T}{\partial x}\right)^{(+)} - \lambda_e^{(-)}\left(\frac{\partial T}{\partial x}\right)^{(-)} \qquad (4.57)$$

Again, the one-dimensional plane problem permits a self-similar solution when all unknown variables are functions of one new variable: $\xi = x/\sqrt{t}$. Numerical examples are given in Figures 4.11 and 4.12.

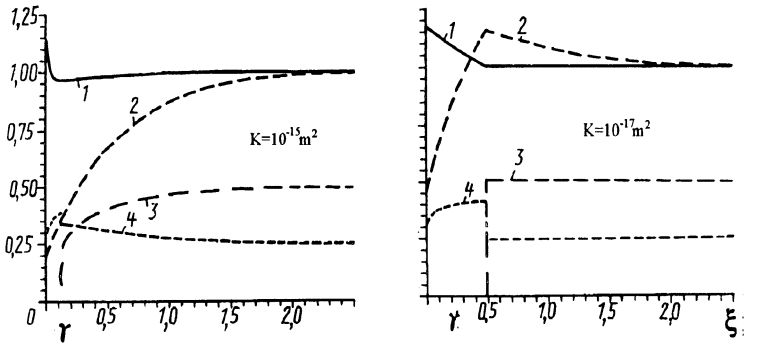

Figure 4.11. Self-similar solution of a one-dimensional plane gas-hydrate soil under dissociation (here, *1* is the temperature T/T_0 profile; *2* is pressure, p/p_0; and *3* is the gas-hydrate saturation θ_h; *4* is the water saturation θ_w) [117].

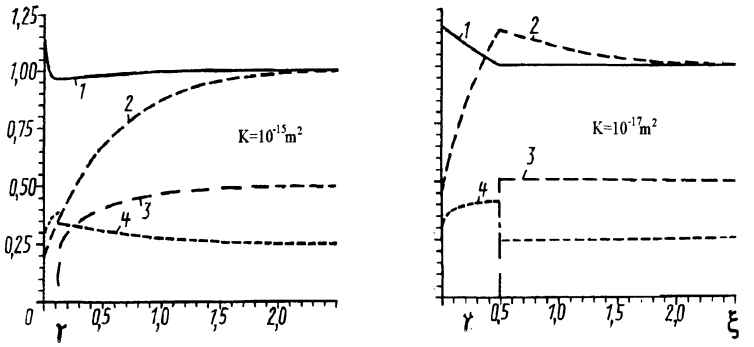

Figure 4.12. The same solution for water saturation θ_w. under drainage condition (*4*) and without drainage (*5*); the permeability values are shown as in Figure 4.11.

You can see that distributions of water saturation, θ_w, are essentially dependent on water filter flows. The effect of the permeability value is also essential. Such calculations must be accomplished by estimation of gas-hydrated soil failure, which can be a serious danger for gas wells drilled in the marine conditions.

4.2.4. FROZEN SOIL STRENGTH

In Figure 4.13, the dependency of soil strength is given for two permafrost's and a gas-hydrated soil. You can see that the first two soils show the essential dependence on strain-rate but the gas-hydrated soil has no practical creep behavior. Physically, it is explained by the existence of water films in a permafrost that permit sliding at grain contacts. The gas-hydrate case corresponds to more total solidification at the microlevel.

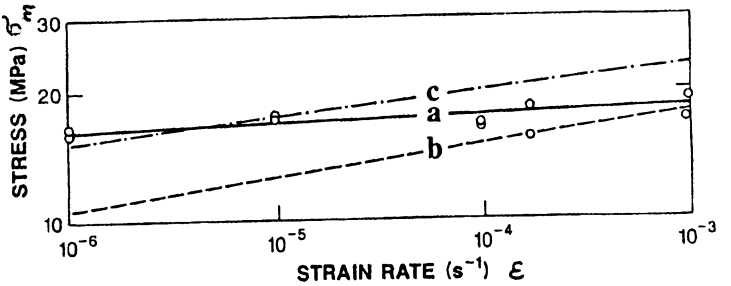

Figure 4.13. Peak strength of soil sample with gas-hydrate (a) is practically independent of strain rate; permafrost (c, b) has a creep response [38].

Although strain rate does not influence the peak strength of gas-hydrated soils, the failure process is sensitive to the strain-rate effect. In Figure 4.14, it is shown that pure brittle fracture is changed to plastic flow, or even to plastic flow with hardening, with strain-rate growth.

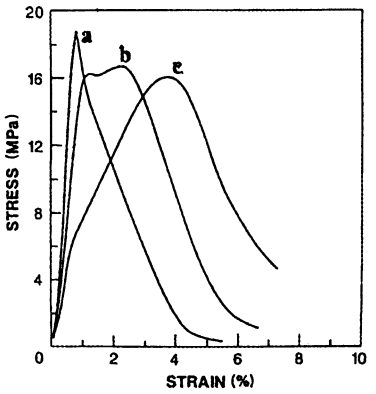

Figure 4.14. Gas-hydrate soil behavior depend on strain rate: (a) - brittle rupture, $de/dt \approx 10^{-3}\ 1/s$; (b) - plastic flow; (c) - plastic rupture with hardening, $de/dt \approx 10^{-6}\ 1/s$ [167].

All these data support the idea that frozen soils possess the usual brittle dilatancy properties.

4.2.5. ICE STRENGTH AND DILATANCY

The rheologic law for polycrystalline ice has the conventional form:

$$\dot{e}_{ij} = A\tau^{n-1}\sigma_{ij}$$

with the coefficient sensitive to a temperature. However, the temperature changes can create qualitative rheological changes.

V. Epifanov [62] has shown that polycrystalline ice also exhibits dilatant features during irreversible deformation. These data are extremely important because they provide an opportunity to study temperature effect [70]. For example, temperature decrease leads to a more plastic type of deformation, as can be seen in Figure 4.15. Moreover, it has been found that a volume strain is proportional to the modulus of shear (Figure 4.16) and is a typical dilatancy property.

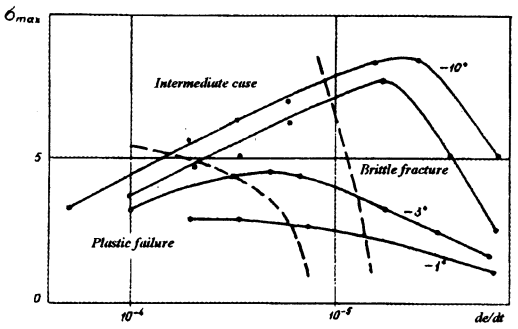

Figure 4.15. Type of ice failure as well as ice strength depends on temperature and strain rate (de/dt), according to H.C. Wu, K.J. Chang and J. Schwartz.

This rheology is typical for temperatures below $T = -30^0$ and corresponds to finite totally crashed samples. For higher temperatures the rheology is plastic because cracks are healing.

Of course, the temperature effects have to be accounted for the proper description of fracturing of ice. Strain-rates have the analogous effect as we can see in Figure 4.15.

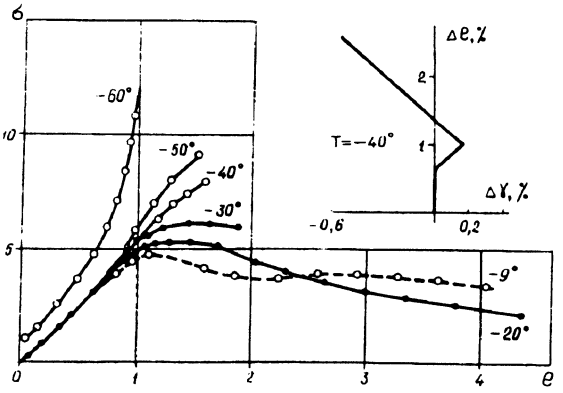

Figure 4.16. Triaxial compression of polycrystalline ice samples with measurements e_1 and e_3 under the $\sigma_3 = 0$ condition $(\sigma \equiv \sigma_1)$ [62].

4.3. Electrokinetic effects

4.3.1. DOUBLE ELECTRICAL LAYER

This effect appears in the electropotential field of a water-saturated porous medium during seismic wave propagation. The corresponding theory was developed by Ya.I.Frenkel [67] even earlier than the well-known wave theory of M.A. Biot [20].

Electrokinetic phenomena are the interactions of the electric field and phase relative motions if one phase is represented by an electrolyte.

Consider the case of a porous medium saturated by an electrolyte, for example, salt solution in water [156]. The relative electrolyte flow begins under the action of the external electric field. (Vise versa, relative electrolyte flow has to create the electrical field.) The relative flow of the electrolyte in the electrical field is termed the electroosmosis. The electric field created by electrolyte flows through a porous medium is called a flow potential.

The mechanics of an electrokinetic phenomenon is explained by the generation of a double electrical layer at the interphase boundary. Signs of solid and fluid phase charges are different and depend on their nature; however, solid phase is quite often charged negatively. The face of a double electric layer that belongs to a fluid has a diffuse structure with continuous decrease of ion concentration within a small distance from the boundary of solid material. It is connected with the interaction between electrostatic forces and molecular thermal motion inside the electrolytic solution. Ions from the adsorption layer that is in intimate contact with the solid boundary are immovable during electrokinetic phenomena because electrostatic forces are too high. Only the outer part of the diffuse layer can be displaced because of the loose packing of its ions.

Consider the electro-osmosis phenomenon. If a capillary is filled by an electrolyte and an external electric field is applied, then ions of one sign belonging to the outer part of diffuse layer begin to move to the pole of the opposite sign. So, the directional flux of ions of the diffuse layer appears. Due to viscous friction, this flux involves other parts of fluid. As the result, some pressure difference is created and can generate secondary back-fluid flow. The pressure difference will increase until the stationary state is reached (when the direct and back-fluid flows become equal to each other).

In contrast, if a pressure difference is created, laminar fluid flow begins. Then the ions of outer part of diffuse layer are displaced in the direction of the inducing flow. It is equivalent to a convective surface electric current, which creates a potential difference at the capillary ends. This potential difference creates the bulk current in the back direction. Again, some equilibrium stationary state will be reached.

4.3.2. STATIONARY ELECTROKINETICS

Consider, now, the quantitative description of electrokinetic effects, with the introduction of the electrical potential, Φ. In this case, Onsager's rule (page 13) will give the following relations for the filter velocity, w_k, and for the electric current density, i_k, for the unit cross-section of an isotropic porous medium:

$$w_k = - L_{ww} \frac{\partial p}{\partial x_k} + L_{wi} \frac{\partial \Phi}{\partial x_k} \tag{4.58}$$

$$i_k = L_{iw} \frac{\partial p}{\partial x_k} - L_{ii} \frac{\partial \Phi}{\partial x_k} \tag{4.59}$$

In addition the cross kinetic coefficients must equal each other:

$$L_{iw} = L_{wi} \tag{4.60}$$

The first term of the filter velocity expression is standard ($L_{ww} = k / \mu$), and the second term corresponds to electro-osmosis motion. For a porous medium, the electro-osmosis coefficient, C_e, can be expressed as:

$$C_e = L_{wi} = - \frac{D_e \zeta_0 m}{4 \pi \mu} \tag{4.61}$$

where D_e is a dielectric constant of the saturating fluid, ζ_0 is electrokinetic potential, and m is introduced as the porosity.

The first term of the current density, i_k, corresponds to the convective surface component created by the pore-pressure gradient. The second is the bulk current; and therefore,

$$L_{ww} = m\sigma \tag{4.62}$$

where σ is the specific electroconductivity of the fluid.

The stationary state mentioned above means that there is no flow

$$w_k = 0 \tag{4.63}$$

and it determines the equilibrium between gradients of pressure and electric potential:

$$\frac{\partial p}{\partial x_k} = - \frac{C_e \mu}{k} \frac{\partial \Phi}{\partial x_k} \tag{4.64}$$

Then at the electro-osmosis stationary state, the electric current density is determined by

$$i_k = -m\sigma\left(1 - \frac{C_e \mu}{m\sigma k}\right)\frac{\partial \Phi}{\partial x_k} \tag{4.65}$$

showing the decrease of electro-conductivity due to the electro-osmosis phenomenon.

In the same way, if the pressure gradient is given, the stationary state is determined by the condition $i_k = 0$. Therefore, the electromotive force, E, created by the pressure gradient is

$$E = -\nabla\Phi = \frac{C_e}{m\sigma}\nabla p \tag{4.66}$$

Introducing expression (4.66) into the initial flux rule (4.58), the following relation of an induced electric field with the filter velocity can be obtained:

$$E = \frac{\mu C_e}{k\sigma(1 - \Pi)}\frac{w}{m} \tag{4.67}$$

where $\Pi = \left(C_e^2 \mu / m\sigma k\right)$.

4.3.3. WAVE ELECTROKINETICS

If oscillation frequencies are such that the electric field can be treated as stationary at every instant (if they are less than 10^6 *Hz*), formulae (4.67) is valid for seismic waves in soils and rocks in the following form:

$$E_i = \frac{\mu C_e}{k\sigma(1 - \Pi)}\left(v_i^{(l)} - v_i^{(s)}\right) \tag{4.68}$$

where the matrix displacement velocity is taken into account.

It is possible to show that the wave model discussed in Sections 2.3 and 5.3 gives the following dependency for relative velocities in the first mode of P-wave:

$$v_i^{(l)} - v_i^{(s)} = -\frac{k_0 \rho_0}{\mu}\omega^2\left(1 - \frac{\rho^{(l)}}{\rho_0}\right)u_{i0}^{(s)} \tag{4.69}$$

where $u_{i0}^{(s)}$ is the displacement amplitude of the solid matrix. The combination of these two expressions shows that the electric field is also proportional to the second power of seismic frequency:

$$E = \frac{C_e \rho_0}{\sigma(1 - \Pi)} \left(1 - \frac{\rho^{(l)}}{\rho_0} \right) \omega^2 \tag{4.70}$$

For example, a sandstone with porosity $m = 10\ \%$ and permeability *10 millidarcy* saturated by distilled water possess the electric field of the mV/cm order (N.Migunov's data) under an acoustic pressure *10 kPa* with a frequency *20 kHz*. The growth of permeability leads to the exponential decrease of seismo-electric effect for sandstones [132].

Electrokinetic effect increases the dissipation of seismic waves, especially for crude oil which contains inorganic and organic electrolytes with very low electroconductivity. In this case, electric dissipation can be even higher than viscous dissipation [170], although, for salt water, it can be not more than a half the viscous dissipation. The separate motion of ions under an electric field and gradient action can be used for electromelioration of some salty soils.

It is found also that salty water can be used to flood reservoirs having a clay matrix. In such a matrix, normal water flow is determined by nonlinear deviations of Darcy's law.

The electrokinetic field can be created by the soil consolidation process, which corresponds to the more essential relative phase displacements than occur in the first P-wave, see also [26].

4.3.4. BOUNDARY CONDITIONS

Electric current, i_k, must satisfy the continuity equation

$$\partial i_k / \partial x_k = 0 \tag{4.71}$$

which, due to the kinetic relation (4.59), can be rewritten as follows:

$$\frac{\partial}{\partial x_k} \left(\sigma \frac{\partial \Phi}{\partial x_k} + \sigma C \frac{\partial p}{\partial x_k} \right) = 0 \tag{4.72}$$

The boundary condition must be formulated for the electric currents:

$$\frac{\partial \Phi}{\partial n} + C \frac{\partial p}{\partial n} = i_n \tag{4.73}$$

where n is the boundary normal. For example, at the ground surface the assumed condition is $i_n = 0$ and shows that

$$\frac{\partial \Phi}{\partial n} = -C \frac{\partial p}{\partial n} \tag{4.74}$$

In addition, the pore pressure gradient is interconnected with permeability of the layer at the surface. Other variants of (4.73) have to account for interaction with the Earth's lower ionosphere. This problem is important for earthquake prediction programs and is discussed here.

4.3.5. ELECTROMAGNETIC EMISSION

Because the dilatancy effect foreruns earthquake events (Section 7.3), induced water flows can create the electric field anomalies observed in situ.

Rock fracturing is characterized by electromagnetic radiation as well as by acoustic emission. The model of microfracturing or contact opening during irreversible deformation of rocks and soils was developed for estimation of surface events at an earthquake's epicentral zone or just before avalanche along the slip surface. Physically, it can be explained by electric dipole emission, depending on charges at the contact surfaces and the time of opening.

Consider the following estimations [76]. The emission power of the single crack is determined as

$$\mathcal{M}_0 \approx \frac{2}{3c^2}\left(\frac{d}{\tau}\right)^2 \tag{4.75}$$

where c is the light velocity, d is the electric dipole moment, and τ is the opening time. Assuming that crack number N is proportional to deformation,

$$N = \left(\frac{N_{max}}{e_{max}}\right)e \tag{4.76}$$

Then the emission of the geomaterial unit is expressed by

$$\mathcal{M} = \mathcal{M}_0\left(\frac{N_{max}}{e_{max}}\right)\dot{e}\tau \tag{4.77}$$

where $\dot{e}$ is the strain rate. The peak density of cracks is estimated by

$$N_{max} = 3l^3 \tag{4.78}$$

and the opening time is estimated as

$$\tau = l / c_l \tag{4.79}$$

where c_l is the limit crack-growth velocity ($\approx 1000\ m / sec$).

Thus [76]

$$\mathcal{M} \approx 7\left(10^{-6} - 10^{-4}\right)\frac{\dot{e}}{e_{max}} \tag{4.80}$$

and the emission frequency is

$$\omega \approx \frac{1}{\tau} \approx 10^{4} - 10^{7}\ Hz \tag{4.81}$$

If $\dot{e}/e_{max} \approx 10^{-6}\ sec^{-1}$, then $\mathcal{M} \approx 5\ (0{,}1 - 10)\ Wt$. This is in accordance with electromagnetic emission measurement for the Chilean earthquake that happened in 1960.

4.3.6. FLOWS WITH THRESHOLD PHENOMENA

Interaction of a one-phase fluid with a solid phase having an electric background can influence flows through a porous matrix. The most essential effect is created by clay components in the matrix or by special properties of asphalthenes and some other components in crude oil.

Mathematically, the deviations of Darcy's law are described by a special function, $\Phi(w)$, of the filter velocity [12]:

$$\Phi(w)\frac{w_i}{w} = -\frac{\partial H}{\partial x_i} \tag{4.82}$$

where $\Phi(0) \geq 0$, $\Phi'(0)$, $w = |w_i|$, H is the generalized head, and the external potential U can be added

$$H = \frac{k}{\mu}p + \frac{k}{\mu}U \tag{4.83}$$

Usually, stationary problems are considered when

$$\partial w_i / \partial x_i = 0 \tag{4.84}$$

In the planar case, the stream function $\psi(x, y)$ can be utilized:

$$\frac{\partial \psi}{\partial x} = -w \sin\theta \quad , \quad \frac{\partial \psi}{\partial y} = w \cos\theta \tag{4.85}$$

$$\frac{\partial H}{\partial x} = -\Phi(w)\cos\theta \quad , \quad \frac{\partial H}{\partial y} = -\Phi(w)\sin\theta \tag{4.86}$$

Using w and θ as independent variables,

$$\frac{\partial H}{\partial \theta} = -\frac{\Phi^2}{w\Phi'(w)}\frac{\partial \psi}{\partial w}, \quad \frac{\partial H}{\partial w} = \frac{\Phi}{w^2}\frac{\partial \psi}{\partial \theta} \tag{4.87}$$

$$dx = -\left(\frac{\cos\theta}{\Phi}dH + \frac{\sin\theta}{w}d\psi\right) \tag{4.88}$$

$$dy = -\frac{\sin\theta}{\Phi}dH + \frac{\cos\theta}{w}d\psi$$

and equations (4.87) can be represented for stream function

$$\frac{\partial}{\partial w}\left(\frac{\Phi^2}{w\Phi'(w)}\frac{\partial \psi}{\partial w}\right) + \frac{\Phi}{w^2}\frac{\partial^2 \psi}{\partial \theta^2} = 0 \tag{4.89}$$

and for the head

$$\frac{\partial}{\partial w}\left(\frac{w^2}{\Phi}\frac{\partial H}{\partial w}\right) + \frac{w\Phi'(w)}{\Phi^2(w)}\frac{\partial^2 H}{\partial \theta^2} = 0 \tag{4.90}$$

This is the hodograph transformation known in gas dynamics.

The viscoplastic flows are determined by the following Darcy law:

$$w_i = -\frac{k}{\mu}\left(1 - \frac{G}{|\partial H / \partial x_i|}\right)\frac{\partial H}{\partial x_i}$$

$$w_i = 0 \quad , \quad \frac{G}{|\partial H / \partial x_i|} \geq 1 \tag{4.91}$$

More details can be found in Ref. [12].

Clays themselves can have essential volumes of internally connected water with its own pore pressure corresponding to its high mobility under tectonic conditions.

4.4. Physical measurements in wells

4.4.1. ACOUSTIC NOISE OF ACTING WELLS

Gas wells often have very high production which corresponding to extremely high filter velocities in close vicinities. Sometimes, even intensive acoustic noise can be created by such a flow through a porous medium. We can use the same ideas as in turbulence theory because the sources are created by an internal microstructure which transforms the mean velocity, $v_j^{(g)}$, of the flow into its local value [142]:

$$v_i^* = L_{ij} v_j^{(g)} \tag{4.92}$$

where L_{ij} is the local tensor of the porous medium, which is a function of space coordinates and the realization parameter, χ, corresponding to the random character of pore geometry. Usually, according to Onsager's rule, the hypothesis on microstationarity of flow is accepted - in which case, L_{ij} is independent of time. This tensor was used earlier for problems of flow dispersion through porous media (Section 3.5).

In the isothermal case, the dynamic system discussed in Section 2.3 can be studied in a more simple form consisting of the mass balances

$$\frac{\partial}{\partial t}(1 - m)\rho^{(s)} + \frac{\partial}{\partial x_i}(1 - m)\rho^{(s)} v_i^{(s)} = 0 \tag{4.93}$$

$$\frac{\partial}{\partial t} m \rho^{(g)} + \frac{\partial}{\partial x_i} m \rho^{(g)} v_i^{(g)} = 0 \tag{4.94}$$

and momentum balances

$$\frac{\partial}{\partial t}(1 - m)\rho^{(s)} v_i^{(s)} + \frac{\partial}{\partial x_j}(1 - m)\left(\rho^{(s)} v_i^{(s)} v_j^{(s)} - \sigma_{ij}\right) = (1 - m)\rho^{(s)} g_i + R_i + p_{ij}\frac{\partial m}{\partial x_j} \tag{4.95}$$

$$\frac{\partial}{\partial t} m \rho^{(g)} v_i^{(g)} + \frac{\partial}{\partial x_j} m\left(\rho^{(g)} v_i^{(s)} v_j^{(s)} - p_{ij}\right) = m \rho^{(g)} g_i - R_i - p_{ij}\frac{\partial m}{\partial x_j} \tag{4.96}$$

where the pore-stress tensor also includes the Reynolds turbulent stresses generated by the local geometry tensor (4.92):

$$p_{ij} = -p\,\delta_{ij} + < \rho^{(g)} v_i^* v_j^* > \tag{4.97}$$

The expression (2.70) for bulk forces is utilized:

$$R_i = r\left(v_i^{(g)} - v_i^{(s)}\right) + rb\left|v_i^{(g)} - v_i^{(s)}\right|\left(v_i^{(g)} - v_i^{(s)}\right) \tag{4.98}$$

where $r = \left(\mu m^2/k\right)\varphi(Re)$. The coefficient of inertial losses can be expressed as:

$$b = \frac{k\,\rho^{(g)} m}{\mu} A_s \tag{4.99}$$

where A_s is the coefficient of microasperity.

The gas dynamic equations can be transformed [3] in the following way:

$$\frac{\partial^2\left(m\,\rho^{(g)}\right)}{\partial t^2} + \frac{\partial^2\left(m\,\rho^{(g)} v_i^{(g)}\right)}{\partial x_i \partial t} = 0 \tag{4.100}$$

$$\frac{\partial^2\left(m\,\rho^{(g)} v_i^{(g)}\right)}{\partial x_i\,\partial t} + \frac{\partial^2}{\partial x_i\,\partial x_j}\left(m\,\rho^{(g)} v_i^{(g)} v_j^{(g)} - p_{ij}\right) = \frac{\partial}{\partial x_i}\left(m\,\rho^{(g)} g_i - R_i - p_{ij}\frac{\partial m}{\partial x_j}\right) \tag{4.101}$$

and their difference has the form

$$\frac{\partial^2\left(m\,\rho^{(g)}\right)}{\partial t^2} = \frac{\partial^2}{\partial x_i\,\partial x_j}\left(m\,\rho^{(g)} v_i^{(g)} v_j^{(g)} - p_{ij}\right) - \frac{\partial}{\partial x_i}\left(m\,\rho^{(g)} g_i - R_i - p_{ij}\frac{\partial m}{\partial x_j}\right) \tag{4.102}$$

The subtraction of the expression

$$\partial^2\left(c_0^2\, m\,\rho^{(g)}\,\delta_{ij}\right) / \partial x_i\,\partial x_j$$

where c_0 is the linear wave velocity in the gas at rest, leads to the wave equation of the Lighthill type with acoustical sources

$$\frac{\partial^2\left(m\,\rho^{(g)}\right)}{\partial t^2} - c_0^2\frac{\partial^2\left(m\,\rho^{(g)}\right)}{\partial x_i^2} = \frac{\partial^2\left(m\,T_{ij}\right)}{\partial x_i\,\partial x_j} + \frac{\partial G_i}{\partial x_i} \tag{4.103}$$

The quadripole, mT_{ij}, and the dipole, G_i, sources are expressed as sums of the filter flow parameters:

$$\begin{aligned} T_{ij} &= \rho^{(g)} v_i^{(g)} v_j^{(g)} - p_{ij} - c_0^2\,\rho^{(g)}\delta_{ij} = \\ &\rho^{(g)} v_i^{(g)} v_j^{(g)} + \rho^{(g)} < v_i^* v_j^* > + \left(p - c_0^2\,\rho^{(g)}\right)\delta_{ij} \end{aligned} \tag{4.104}$$

$$G_i = R_i + p_{ij}(\partial m / \partial x_j) - m\rho^{(g)} g_i \tag{4.105}$$

because, practically,

$$p = c_0^2 \rho^{(g)} \tag{4.106}$$

the real quadripole sources of filter noise are connected with the dynamic head of the gas flow

$$T_{ij} = \rho_0^{(g)} \alpha_{ijkl} v_k^{(g)} v_l^{(g)} \tag{4.107}$$

where the dynamic coefficient is determined as

$$\alpha_{ijkl} = \left(\rho^{(g)} / \rho_0^{(g)}\right)(\delta_{ij}\,\delta_{kl} + < L_{ik}\, L_{jl} >) v_k^{(g)} v_l^{(g)} \tag{4.108}$$

and can be anisotropic in a general case.

4.4.2. MEASUREMENTS IN GAS FLOWS

Noise "pressure", P_n, is measured for rock samples and is shown in Figure 4.17, where the dependency on the gas flow velocity is evident for very wide intervals of core porosity. Noise dependence on Re number (gas output) is shown in Figure 4.18. Example measurements in situ are given in Figure 4.19.

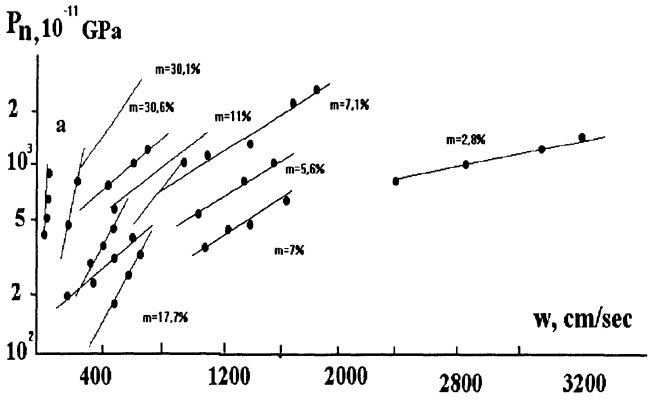

Figure 4.17. Noise pressure P_n depends on the filter velocity and porosity (**a** free gas jet) [3].

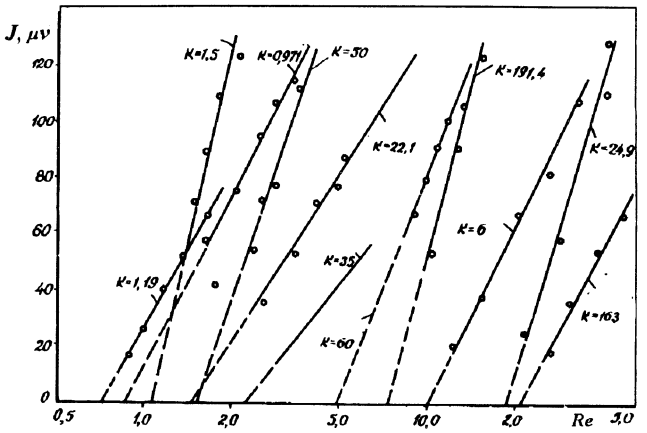

Figure 4.18. Noise relative intensity depends on the Reynolds number corresponding to inertial deviation from the Darcy law (according to Yu. P. Korotaev);
k is the sample permeability, millidarcy .

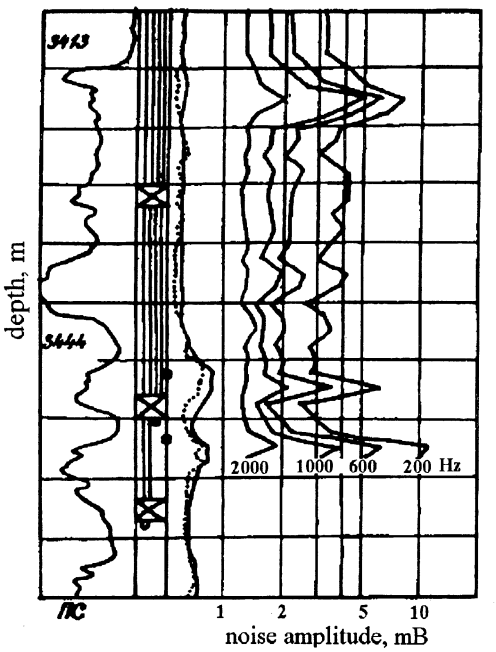

Figure 4.19. Amplitude measurements of different frequency noise in acting oil well.

4.4.3. THERMOELASTIC STATE OF SEAMS

The second problem considered is the well reaction to geodynamic changes [210]. If the wave length of the tectonic disturbance is much larger then the reservoir thickness and if the time interval is of the order of days and hours, the inertial forces in the dynamic equations for porous media are negligible and equation (2.152) for pore pressure can be represented as [159]

$$\frac{\partial p}{\partial t} + a\frac{\partial \Gamma_{kk}}{\partial t} + b\frac{\partial T}{\partial t} = \kappa \nabla^2 p \tag{4.109}$$

$$\frac{\partial T}{\partial t} - \frac{\alpha^{(f)} T_0}{C_p}\frac{\partial p}{\partial t} = \frac{D}{C_p}\nabla^2 T \tag{4.110}$$

Here Γ_{kk} is the total stress identified with the tectonic stress, $D = D^{(f)}m + D^{(s)}(1-m)$, and $\alpha^{(s)}$, $\alpha^{(f)}$ are thermal expansion coefficients, - see (2.25), (2.26):

$$\kappa = \frac{k_0}{\mu\beta} \quad , \quad \beta = m_0\beta^{(f)} + \frac{1-(1+m_0)\beta^{(s)}K}{(1-m_0)K} \quad , \quad b = \left(\alpha^{(s)} - \alpha^{(f)}\right)\frac{\kappa\mu\, m_0}{k_0}$$

$$a = \frac{1-\beta^{(s)}K}{3(1-m_0)\beta K} \quad , \quad e = \frac{\Gamma_{kk}+3p}{3(1-m_0)K} - \beta^{(s)} p$$

Let us formulate the boundary condition corresponding to the fluid level (or head), h, inside the observation well. The change of fluid volume, $\Delta V = S\Delta h$, creates the pressure change, $\Delta p = \rho^{(f)} g\Delta h$. Accounting for fluid compressibility, $\beta^{(f)}$, changes the effective cross-section, S, of the well with the volume, V, to the value

$$S_* = S + \beta^{(f)}(dp/dh)V$$

The fluid flux equalizes this volume change and gives the following boundary condition:

$$\left(d\frac{\partial p}{\partial r} + B\frac{\partial T}{\partial r}\right) = \frac{dh}{dt} \quad , \quad r = r_w \tag{4.111}$$

$$d = 2\pi r_w h_0 \frac{k_0}{S_*\mu} \quad , \quad B = 2\pi r_w h \frac{\alpha^{(f)} D}{C_p}$$

which is added to the expression for fluid pressure and temperature at the bottom hole:

$$p = \rho^{(f)} g h \quad , \qquad \alpha^{(f)} dT = \beta^{(f)}\, dp \tag{4.112}$$

4.4.4. WELL RESPONSE TO TECTONIC CHANGES

We must find the well reaction to the tectonic stress changes which are assumed:

$$\Gamma_{kk} = f(t) \tag{4.113}$$

The system - (4.109) through (4.110) - can be reduced to

$$\kappa \nabla^4 p - \left(1 + \frac{\kappa C_p}{D}\right) \frac{\partial}{\partial t} \Delta^2 p + \frac{C_p + \alpha^{\varphi} b T_0}{D} \frac{\partial^2 p}{\partial t^2} = \tag{4.114}$$

$$= a \left(\frac{\partial}{\partial t} \nabla^2 \Gamma_{kk} - \frac{C_p}{D} \frac{\partial^2}{\partial t^2} \Gamma_{kk} \right)$$

Introducing the new variable

$$\wp = p + \frac{a C_p}{C_p + \alpha^{\varphi} b T_0} f(t) \tag{4.115}$$

We can solve the equation

$$\kappa \nabla^4 \wp - \left(1 + \kappa \frac{C_p}{D}\right) \nabla^2 \frac{\partial \wp}{\partial t} + \frac{C_p + \alpha^{\varphi} b T_0}{D} \frac{\partial^2 \wp}{\partial t^2} = 0 \tag{4.116}$$

represented in the form

$$\wp = \wp_1 + \wp_2 \quad , \quad \nabla^2 \wp_i + k_i^2 \frac{\partial \wp_i}{\partial t} = 0 \tag{4.117}$$

where $s_i (i = 1,2)$ are the roots of the equation

$$\kappa s^4 + \left(1 + \kappa \frac{C_p}{D}\right) s^2 + \frac{C_p + \alpha^{\varphi} b T_0}{D} = 0$$

The boundary condition is rewritten in the form

$$\wp_i(r_w,t) = \eta_i(t); \qquad \partial\wp_i / \partial r = 0, \quad r \to \infty \tag{4.118}$$

and

$$\eta_1(t) \equiv \eta(t) = \rho g h + \frac{aC_p}{C_p + \alpha^{\wp} b T_0} f(t), \qquad \eta_2(t) = 0 \tag{4.119}$$

Then $\wp_2 \equiv 0$ and

$$\wp_1 = \int_0^t \frac{\partial U(r,t-\tau)}{\partial t} \eta(\tau) d\tau$$

$$U(r,t) = 1 + \frac{2}{\pi} \int_0^{\infty} exp\left(\frac{z^2 t}{k_1}\right) \frac{W(r,z) z dz}{J_0^2(r_w z) + Y_0^2(r_w z)} \tag{4.120}$$

$$W(r,z) = J_0(rz) Y_0(r_w z) - J_0(r_w z) Y_0(rz)$$

where J_o, Y_0 are the Bessel functions of the first and second types of the zero order.

The temperature changes are determined by the pore-pressure field, $\wp$, and tectonic stress, $f(t)$:

$$bT = -(1 + \kappa s_1^2)\wp - \frac{ab\alpha^{(f)}}{C_p + \alpha^{\wp} bT_0} f(t) \tag{4.121}$$

The introduction of (4.120) and (4.121) into the boundary condition (4.111) gives the following equation [159]

$$\frac{dh}{dt} = \frac{2}{\pi} \frac{M}{s^2} \int_0^{\infty} \frac{W(r,z)}{J_0^2(r_w z) + Y_0^2(r_w z)} \left(\int_0^{\infty} exp\left\{ -\left(\frac{z}{s}\right)^2 (t-\tau) \right\} \eta(\tau) d\tau \right) z dz$$

$$s^2 = \frac{1}{2\kappa D} \left(D + \kappa C_p - \sqrt{(\kappa C_p - D)^2 - 4\kappa b \alpha^{(f)} D T_0} \right) \tag{4.122}$$

$$M = d - \frac{B}{b}(1 + \kappa s^2)$$

The linear equation (4.122) can be solved by the Fourier method:

$$h(t) = A_0 + \Sigma(A_n \cos n\omega t + B_n \sin n\omega t)$$

If the tectonic stresses change in a harmonic way:

$$f(t) = A \cos \omega t$$

Then

$$h(t) = A_1 \cos \omega t + B_1 \sin \omega t \equiv A_m \cos(\omega t - \varphi) \tag{4.123}$$

and the well production will be

$$Q_p = -A_p \sin(\omega t - \psi) \quad , \quad A_p = SA_m\omega \tag{4.124}$$

where

$$A_m = \sqrt{A_1^2 + B_1^2} \quad , \quad \psi = arctg \frac{B_1}{A_1}$$

Because of (4.123), Q_p is more sensitive to frequency changes.

You can see that the most important role belongs to the time of reservoir relaxation

$$\Theta_R \approx \frac{\mu\beta r_w^2}{k_0}\left(1 + \frac{\alpha^{\varphi} bT}{C_p}\right) \tag{4.125}$$

and the pore-pressure changes can be from *1* to *10* bars and the temperature changes can be in the interval $(1 \div 3)^0 C$ during earthquake events. Usually the temperature fluctuation are much smaller, but they can be measured in practice.

4.5. Rupture in dilating geomaterials

4.5.1. DYNAMICS OF UNDERGROUND CAVITY

Consider the important problem of underground empty-cavity stability [235] under the action of an intensive convergent wave. The geomaterial behavior will be described by an elastoviscoplastic model that has the following system of equations valid for spherical symmetric motion

$$\frac{dv}{dt} = \frac{\partial}{\partial r}(S_r - p) + 3\frac{S_r}{r} \tag{4.126}$$

$$\frac{dS_r}{dt} = \frac{4}{3}\overline{G}\left(\frac{\partial v}{\partial r} - \frac{v}{r} - \frac{3}{2}\dot{\lambda} S_r\right) \tag{4.127}$$

$$\frac{dp}{dt} = -\overline{K}\left(\frac{\partial v}{\partial r} + 2\frac{v}{r} - 2\Lambda\dot{\lambda} J_2\right) \tag{4.128}$$

where v is the radial displacement velocity, $S_r = \sigma_r - \sigma$, σ_r is the radial stress, $\sigma = -(1/3)\sigma_{ii}$ is the pressure in solid (one-phased) geomaterial, and $\overline{G}, \overline{K}$ are normalized shear and volume moduli, respectively:

$$\overline{G} = G/(\rho c_p^2), \quad \overline{K} = K/(\rho c_p^2) \tag{4.129}$$

where ρ is the density, and c_p is the P-wave velocity,

$$\dot{\lambda} = 0 \quad , \quad \text{if } F_i \le 0 \quad ; \quad \dot{\lambda} = \mu F_i \quad , \quad \text{if } F_i > 0 \tag{4.130}$$

$F_i = \Phi_i(J, p, \chi)/J$, $J^2 = (3/4)S_r$ is the second stress invariant, Φ_i are statically determined yield surfaces for the softening process down to residual strength, χ is the softening parameter (1.86), μ is the viscous parameter, and Λ is the dilatancy rate.

The system - (4.126) through (4.130) - is written in dimensionless form based on the time of peak loading, t_m, the radial coordinate equal to $c_p t_m$, the maximum applied stress, $\sigma_{r\,max}$, and the maximum velocity, $\sigma_{r\,max}/(\rho c_p)$.

It is assumed that geomaterial cannot stand tension (compare [197]). The viscous effect simplifies calculation under unloading conditions and corresponds to the physical properties of geomaterials. Moreover, adding viscous effects permits more adequate estimation of explosion wave length. In the limit case of elastoplasticity, the parameter A has to be found from coincidence of the solution with the elastoplastic solution.

The Wilkins variant of numerical methods [235] is realized and based on finite-difference schemes.

Additionally, the following parameters were used. The first one is the geometric parameter $r_* = r_1 / r_0$, where r_0 is the underground cavity radius and r_1 is the outer boundary where the impulse load is applied. The loading intensity, $K_1 = \sigma_{r\,max} / R_c$, is determined relative to maximum strength, R_c, of the geomaterial at uniaxial compression. The ratio $R_1 = R_c^0 / R_c$ is the reduced residual strength, $R_* = R_c / (\rho c_p^2)$ is the dimensionless strength, and $R_2 = R_t / R_c$, where R_t is the strength under tension.

The rate of softening was estimated by the parameter $G_p^* = G_p^0 / (\rho c_p^2)$, where G_p^0 is the plastic modulus ($0 \le G_p^0 \le 0{,}5$) of the unloading curve for uniaxial deformation. The dilatancy rate Λ^0 for the same unloading was introduced as well as s_2 and s_3 which are exponents of the yield surface. The dependence of Λ on σ was measured by the parameter a_0. All these complicated parameter systems correspond to the rheological properties of rocks published elsewhere [96]. This representation was used in special codes for computer calculations.

Physically sensible solutions have to be independent on mesh choice. It was found that its space mesh step has to be less then $0.1\,r_*$. The diffraction parameter is $A = c_p t_m / (2r_0)$, and $R_3 = \sigma_{rs}/\sigma_{rm}$ is a measure of initial static stress, σ_{rs}, acting at the outer boundary, r_1, before impulse action.

The impulse action is assumed as the stress, σ_r, added dynamically to σ_{rs} at the radius $r_1 = 20\,r_0$ proportionally to time in the interval $0 \le t \le t_m$. The resulting stress, $\sigma_r + \sigma_{rs}$, is constant at $t > t_m$.

4.5.2. CALCULATIONS OF A CAVITY COLLAPSE

The following set of values was used for all calculations:

$$R_1 = 0.02, \quad R_2 = 0.05, \quad s_2 = 0.65, \quad s_3 = 0.85, \quad A = 2.5 \qquad (4.131)$$

and the Poisson's coefficient, ν, is equal to 0.17 where

$$\nu = \frac{1}{2}\frac{K - 2G/3}{K + G/3}$$

The results are given in Figures 4.20 through 4.25. We can see the changes of hoop stress, σ_θ, at the cavity surface as well as the radial velocity, v, which is positive if directed inside the cavity. Curve 1 corresponds to the elastic solution and curve 2 corresponds to the considered dilatancy theory ($K_1 = 1$; $R = 0.0005$, $G_p^0 = 0.5$, $\Lambda^0 = 1$, $a_0 = 1$); as do curve 4 ($a_0 = 0.2$) and curve 5 ($K_1 = 2$). Curve 3 corresponds to the

plastic associative rule with the Mises limit condition ($\sigma_\tau = const$). Curves 6 and 7 are given for larger values of viscous parameter μ and are close to elastoplastic solution 2.

Plastic deformation essentially diminishes hoop stresses and increases displacement velocities. The latter effect is larger if the loading intensity (K_1) is growing and the dilatancy decreasing with pressure growth (the parameter a_0) is diminishing. Maximum dilatancy effect means a *20 %* increase of the velocity.

The hoop stress represented by curve *2* in Figure 4.20 is in accordance with experimental data. Its drop corresponds to the cavity wall rupture. Failed geomaterial possesses a residual strength. The plastic incompressibility is in contradiction with the experiments.

The displacement velocity at the cavity wall is given in Figure 4.21. Return displacements are essential in the case of elastic solution *1*.

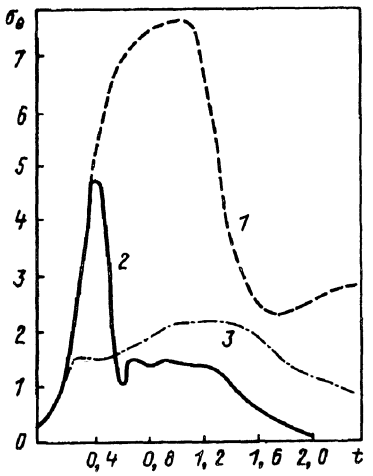

Figure 4.20. Dynamics of hoop stress at the surface of an underground cavity under strong wave action.

The wave profiles are given in Figure 4.22 by solid lines for $t = 0.5; 0.7; 1.0; 1.3; 1.5; 2.0$ when the dilatancy is accounted for. You can see the kink moving inside the geomaterial from the cavity surface; it corresponds to the rupture front. Its velocity is approximately equal to $0.13\, c_p$; therefore, the effect of limit crack velocity is negligible in this case. The kink motion is stopped at $t > 1.5$, determining the outer radius of rupture, r_r (see Table 4.1).

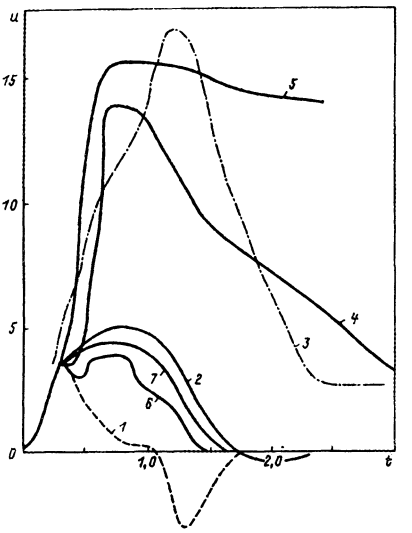

Figure 4.21. Temporal changes of displacement velocity at the surface of an underground cavity under wave action.

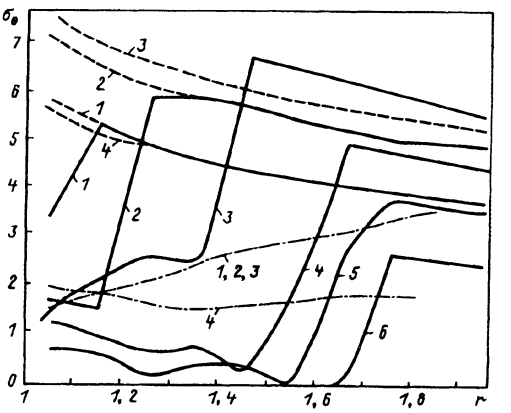

Figure 4.22. Hoop stresses around the cavity for different times; kinks correspond to the fracture front moving in toward the geomaterial.

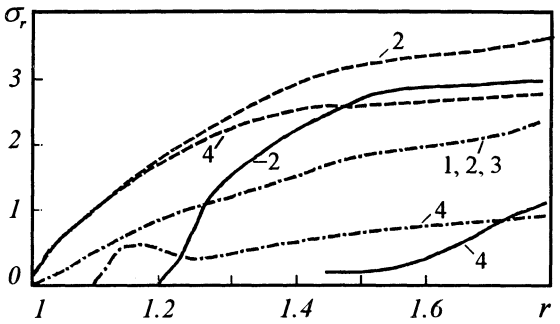

Figure 4.23. Radial stresses around the cavity for different times.

Variants *1*, *2*, *3* and *5* correspond to the dilatancy theory ($\Lambda^0 = 1$), and variant *4* corresponds to the plastic associative rule given by the broken-dot lines. It gives a rupture zone too big in comparison with experimental data, which are close to variant *5*. The parameter a_0 reflects the hardening role of dilatancy.

TABLE 4.1. Radius of rupture around an underground cavity under explosion action.

N	r_*	K_1	a_0	r_r / r_0
1	20	1	1.0	1.6
2	20	1	0.2	1.4
3	20	2	0.2	2.1
4	20	1	0.1	6.7
5	5	2	1.0	1.6

The broken lines correspond to the elastic solution with very low changes of velocity along with the radial coordinates; plastic models give nonhomogeneous velocity fields. The radial stresses have smooth wave profiles. The residual volume strains can have an extremum in the cavity vicinity and correspond to new pore space formation.

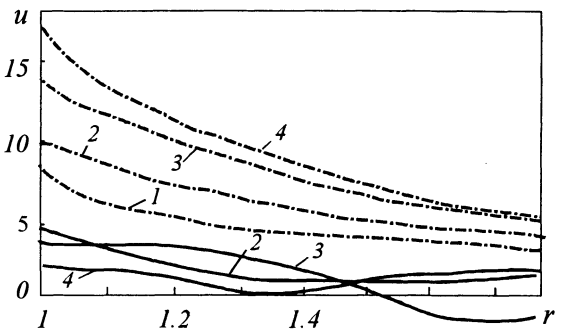

Figure 4.24. Displacement around the underground cavity for different times.

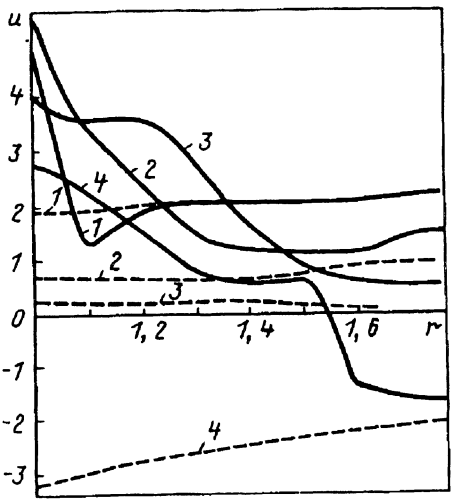

Figure 4.25. Residual volume deformation around an underground cavity
$(1 - K_1 = 2, \quad L^0 = 1; \quad a_0 = 0.2; \quad 2 - K_1 = 1)$

4.5.3. SHEAR LOCALIZATION EFFECT

Localization of rupture can take place inside continuous elasto-plastic fields during active deformation with hardening because of the principal internal instability of an elasto-plastic pressure-sensitive geomaterial. It is possible to rewrite [70], the constitutive laws given in Section 1.3, in the following form:

$$\delta e_{ij} = \Pi_{ijkl}\delta\sigma_{kl}$$

$$\Pi_{ijkl} = \left\{ -\frac{\nu}{2G(1+\nu)}\delta_{ij}\,\delta_{kl} + \frac{1}{4G}\left(\delta_{ik}\,\delta_{jl} + \delta_{kl}\,\delta_{il}\right)\right\} + \tag{4.132}$$

$$\frac{\Lambda}{G_p}\left(\frac{\sigma_{ij}}{2J_2} + \frac{1}{3}\Lambda\,\delta_{ij}\right)\left(\frac{\sigma_{kl}}{2J_2} + \frac{1}{3}\alpha\,\delta_{ij}\right)$$

where G_p is the instant plasticity modulus (Figure 4.26).

The equilibrium equations are formulated for stress increments, $\delta\sigma_{ij}$,

$$\frac{\partial}{\partial x_j}\left(\delta\sigma_{ij}\right) = 0 \tag{4.133}$$

and can be used to study the internal changes inside the plastic field without any disturbances at its boundaries:

$$\delta\left(\sigma_{ij}n_i\right) = 0 \tag{4.134}$$

The main idea [186] is to find nonunique solutions (bifurcation) inside a band determined by its normal, l_i, such that there exists a function

$$L = L(l_i x_i), \quad l_i l_i = 1 \tag{4.135}$$

that changes across the band and

$$\delta u_1 = \frac{\partial^2 L}{\partial x_1 \partial x_3} + \frac{\partial N}{\partial x_2}, \qquad \delta u_2 = \frac{\partial^2 L}{\partial x_2 \partial x_3} - \frac{\partial N}{\partial x_1}$$

$$\delta u_3 = -\frac{1}{a_{13} + G}\left(a_{11}\nabla^2 L + G\frac{\partial^4 L}{\partial x_3^4}\right) \tag{4.136}$$

if the initial state is

$$\sigma_{11}^0 = \sigma_{22}^0 = -p, \quad \sigma_{33}^0 = -q \tag{4.137}$$

Coefficients a_{ij} are determined by elastic coefficients, Λ, and by the instant plastic modulus

$$G_p = \left(-\sigma \frac{d\alpha}{d\chi} + \frac{dY}{d\chi} \right) \tag{4.138}$$

whose physical interpretation is shown in Figure 4.26.

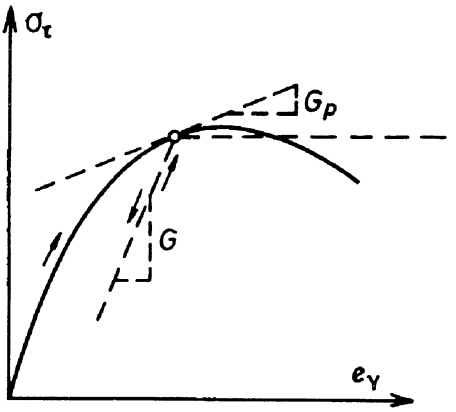

Figure 4.26 Stress-strain curve at shear with instant plastic modulus, G_p, and true elastic modulus, G, at unloading (scheme of J. R. Rice [160]).

The functions L and N have to satisfy the following equations:

$$\nabla^2 \nabla^2 L + \Im_1 \nabla^2 \left(\partial^2 L / \partial x_3^2 \right) + \Im_2 \left(\partial^4 L / \partial x_3^4 \right) = 0 \tag{4.139}$$

$$\nabla^2 N + \partial^2 N / \partial x_3^2 = 0 \quad , \quad \nabla^2 = \partial^2 / \partial x_1^2 + \partial^2 / \partial x_2^2 \tag{4.140}$$

If $N \equiv 0$ and (4.135) is valid, then equation (4.139) is transformed into the following characteristic equation:

$$\xi^4 + \frac{\Im_1}{\Im_2} \xi^2 + \frac{1}{\Im_2} = 0 \quad , \qquad \xi = \frac{l_3^2}{l_1^2 + l_2^2} \tag{4.141}$$

where $\Im_1$, $\Im_2$ are combinations of the coefficients a_{ij} [70]. Condition (4.141) indicates loss of ellipticity of equation (4.139) inside the band when the critical state is reached.

Resolving (4.141) for the parameter G_p / G determines the maximum value of instant plastic modulus [186]

$$\left(\frac{G_p}{G}\right)_{max} = -\frac{1+\nu}{6}\left\{(1-\lambda-\kappa)^2 - \frac{2}{1-\nu}(\lambda-\kappa)^2\right\} \tag{4.142}$$

which corresponds to critical state

$$\xi_{cr}^2 = \frac{(1+\nu)(1-\lambda-\kappa)}{(2-\nu)+(1+\nu)(\lambda+\kappa)} \tag{4.143}$$

$$\lambda = sign(p-q)\frac{\alpha}{\sqrt{3}}, \quad \kappa = sign(p-q)\frac{\Lambda}{3} \tag{4.144}$$

In the simple case of plane deformation, criterion (4.142) has the form

$$\left(\frac{G_p}{G}\right)_{max} = \frac{(1+\nu)^2}{18(1-\nu)}(\alpha-\Lambda)^2 \tag{4.145}$$

You can see here that the critical modulus is positive and that growth of plastic strains can take place in the band at the hardening regime. In the case of the associative flow rule ($\alpha = \Lambda$), the critical value is zero, meaning that the band appearance can take place only under softening conditions.

4.5.4. BOUDINE AND BAND SYSTEM BIFURCATION

According to I. Garagash [70], the solutions

$$L = \psi(x_1, x_2) f(x_3) \tag{4.146}$$

of equation (4.139) must satisfy the Helmholtz equation

$$\Delta^2 \psi + \zeta^2 \psi = 0 \tag{4.148}$$

where ζ is the parameter and

$$\mathfrak{I}_2 \frac{\partial^4 f}{\partial x_3^4} - \mathfrak{I}_1 \zeta^2 \frac{\partial^2 f}{\partial x_3^2} + \zeta^4 f = 0 \tag{4.148}$$

The latter equation has the following solution

$$f = C_i \exp(\zeta s_i x_3) \quad , \qquad s_i = \pm(\eta + i\beta),$$

$$\eta = \frac{1}{\sqrt{2}} \sqrt{\frac{1}{\sqrt{\mathfrak{I}_2}} + \frac{\mathfrak{I}_1}{\mathfrak{I}_2}} \quad , \qquad \beta = \frac{1}{\sqrt{2}} \sqrt{\frac{1}{\sqrt{\mathfrak{I}_2}} - \frac{\mathfrak{I}_2}{\mathfrak{I}_1}}$$

and $\eta = 0$ is necessary due to the condition of finite stresses and displacements in the material. Periodic solutions are also possible, - that is, the internal instability can also lead to hexagon cell structures (known in geology as boudine systems), - see Figure 4.27 and [21].

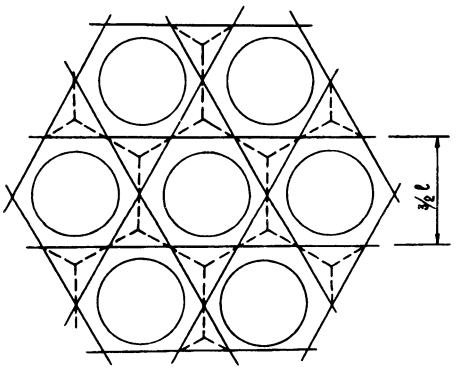

Figure 4.27 Cross-section of a geomaterial body under boudine instability with horizontal scale $l \approx \beta^{-1}$ [71].

The cells are determined by the following solution of equation (4.147):

$$\psi = \frac{1}{3}\left(2\cos\frac{2\pi}{l\sqrt{3}}x_1 \cos\frac{2\pi}{3l}x_2 + \cos\frac{4\pi}{3l}x_2\right) \tag{4.149}$$

In reality, shear bands appear inside the geomaterial as a system with definite geometrical scales. The bands are separated by zones (Figure 4.28) with thickness a_2 of elastic unloading. For pure shear,

$$a_2 = \frac{18}{\alpha^2}\frac{1-\nu}{(1+\nu)^2}a_1 \tag{4.150}$$

where a_1 is the band thickness proportional to the grain radius [70].

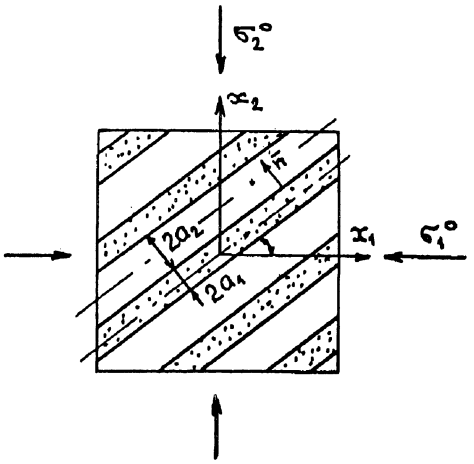

Figure 4.28. Orientation and thickness of localization bands (according to I.Garagash).

4.5.5. ANISOTROPY AND TENSION EFFECTS

The appearance of the band or fracture system gives the anisotropy features to the geomaterial. Correspondingly, the yield function

$$\Phi_\sigma(J_i, \chi_j) = 0 \tag{4.151}$$

and dilatancy condition

$$\Phi_\varepsilon(I_k, \chi_j) = 0 \tag{4.152}$$

depend on a number of stress-strain tensor invariants, J_i, I_k, including the initial stresses and plastic strains determining the anisotropy [95].

Remember that the yield surface changes if one of normal stress components is tensional, although the mean pressure, $\sigma = (1/3)\sigma_{ij}\delta_{ij}$, still corresponds to the compression [70, 197].

CHAPTER 5

EXPLOSIONS AND SEISMIC WAVES IN GEOSTRATA

5.1. Elementary theory of underground explosion

5.1.1. STATEMENT OF PROBLEM

Underground contained explosions are characterized by minimal ground surface damage. In this case only weak elastic waves can reach the ground surface due to the depth of the explosive charge disposal. From mathematical point of view the underground contained explosion is the simplest one [183] because this dynamical motion possesses the spherical symmetry. The corresponding mass and momentum balances have the following form

$$\frac{\partial \rho}{\partial t} + v\frac{\partial \rho}{\partial r} = \rho\left(\frac{\partial v}{\partial r} + \frac{2}{r}v\right) \tag{5.1}$$

$$\rho\left(\frac{\partial v}{\partial t} + v\frac{\partial v}{\partial r}\right) = \frac{\partial \sigma_r}{\partial r} + \frac{\sigma_\tau}{r} \tag{5.2}$$

where $\rho = (1 - m)\rho_0$ is the rock density, v, σ_r are the radial component of mass velocity and stress, $\sigma_\tau = \sigma_r - \sigma_\theta$ and σ_θ is the hoop stress.

These equations are valid for a rock stratum including a cavity filled by explosive gases under high pressure. Such a cavity will expand into rocks according to the law

$$p = p_0\left(\frac{a_0}{a}\right)^{3\gamma} = -\sigma_r(a) \tag{5.3}$$

with the gas adiabatic exponent γ. Here p is the cavity pressure, a is the cavity radius, p_0, a_0 are the initial values changing with the cavity volume which is proportional to a^3. The right-hand part of (5.3) means the boundary condition for the radial stress σ_r at $r = a$, which are positive in tension.

So, the expanding cavity is modeling the explosion dynamic action. The difference between nuclear and chemical explosives is accounted for by gas masses and by initial energy [183]

$$\mathcal{E} = \frac{3}{4}\pi a_0^3 \frac{p - p_L}{\gamma - 1} \tag{5.4}$$

which is proportional to the initial cavity pressure. Here p_L is the lithostatic mean pressure.

Nuclear explosions are characterized by a very high energy level and, simultaneously, by very small gas masses created only by the evaporation of the nuclear device metal and of the rock at the cavity surface. If the rock is wet, the water vapor could be added to these gases and the effective nuclear explosion energy increased essentially [32]. Chemical explosions are characterized by essential masses of detonated gases although their energy is much smaller. The different types of motion dissipation in rocks must be taken into account, and the effective seismic wave radiated by explosions depends on type of geomaterials surrounding the charge (Figure 5.1) [152].

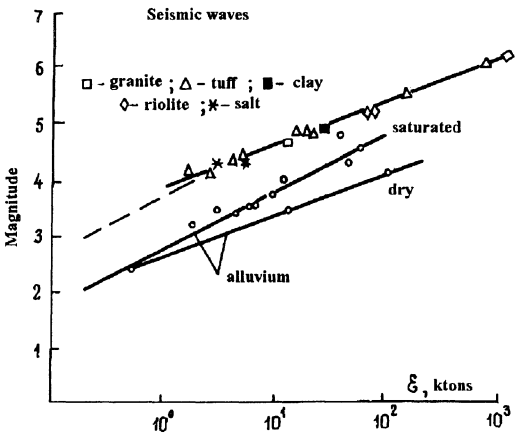

Figure 5.1. Seismic wave intensity of contained explosions is one order less in a high porous stratum than in intact rock; water saturation effect is also essential [182].

In the close vicinity (zone *I*) of a nuclear explosion cavity, the rock behavior is fluid-like because of the high pressure. The intensive plastic deformation takes place in zone *II* of the cavity vicinity, where the volume strain has a dilatant origin. The corresponding dilatancy condition (1.78) has the form of a differential equation with the radial velocity as an unknown variable:

$$\frac{\partial v}{\partial r} + 2\frac{v}{r} = \frac{2}{\sqrt{3}}\Lambda\left|\frac{\partial v}{\partial r} - \frac{v}{r}\right| \tag{5.5}$$

The dilatant equation (5.5) is valid only if the plastic limit (1.77) is also fulfilled - that is,

$$\left|\sigma_r - \sigma_\Theta\right| + \alpha(\sigma_r + 2\sigma_\theta) + \alpha H = 0 \tag{5.6}$$

So, the system - (5.1), (5.2), (5.5) and (5.6) - includes four unknown variables and permits the solution of the problem with boundary condition (5.3) added to the initial conditions of the rest:

$$v = 0, \quad t = 0, \quad r > a_0 \tag{5.7}$$

However, at infinity, the outer zone of the rest

$$v = 0, \quad r \to \infty \tag{5.8}$$

is separated from the zone of motion by the moving front with the following conditions

$$\rho\{v(R) - U\} = -\rho^0 U \tag{5.9}$$

$$\rho v(R)\{v(R) - U\} - \sigma_r = 0 \tag{5.10}$$

according to the well-known shock balances (1.33) and (1.34). Here, R is the discontinuity radius, and its velocity is determined by

$$U = dR / dt \tag{5.11}$$

5.1.2. DILATANT KINEMATIC INTEGRALS

The integration of the dilatancy condition under constant Λ, gives the first kinematic integral [143]:

$$v(r,t) = \frac{C(t)}{r^n}, \quad n = \frac{2\sqrt{3} + 2\Lambda\Theta}{\sqrt{3} - 2\Lambda\Theta} \tag{5.12}$$

where $C(t)$ is the arbitrary function, and Θ is the sign of plastic shear:

$$d\gamma / dt = (dv / dr) - (v / r) \tag{5.13}$$

Experimental explosions in sand have shown [144] that

$$n = 1.5 - 1.8 \tag{5.14}$$

The values of (5.14) indicate that sands dilate with the rate interval [143, 152]

$$\Lambda = 0.18 \div 0.09 \tag{5.15}$$

because $v / r > dv / dr$, $\Theta = -1$. The positive values (5.15) correspond to dilatant loosening of dense geomaterials. In the case of plastic incompressibility, $\Lambda = 0$ and $n = 2$, corresponding to explosions in water (or in metals).

Rock behavior is quite similar to the behavior of dense sand because of their polycrystalline nature and weak intercrystalline bonds. Only very porous rocks are characterized by the condition $\Lambda < 0$, and the explosion will compact the geomaterial in the vicinity of the cavity.

Introducing integral (5.12) into the mass balance (5.1), the second integral for density field [57, 191] can be obtained. Because of (5.12), balance (5.1) can be rewritten as [152]

$$\frac{\partial \ln \rho}{\partial t} + (n+1)\frac{\partial \ln \rho}{\partial r^{n+1}} + C(t)(2-n)\frac{\partial \ln r^{n+1}}{\partial r^{n+1}} = 0 \tag{5.16}$$

The function $C(t)$ can be determined by the displacement velocity, $v(R)$, at the moving front (5.10), giving the following form of the first kinematic integral (5.12):

$$v = v(R)\left(\frac{R}{r}\right)^n \tag{5.17}$$

The front radius, $R(t)$, can be used instead of time. Then equation (5.16) is transformed further:

$$\frac{U}{v(R)R^n}\frac{\partial \ln \rho r^{(2-n)}}{\partial R} + (n+1)\frac{\partial \ln \rho r^{(2-n)}}{\partial r^{n+1}} = 0 \tag{5.18}$$

The new variables can be used in the equation (5.18):

$$z = \ln \rho r^{(2-n)}, \quad dy = (U / v)\, dR^{n+1} \tag{5.19}$$

which now has the form:

$$\frac{\partial z}{\partial y} + \frac{\partial z}{\partial r^{n+1}} = 0 \tag{5.20}$$

The second kinematic integral is valid in the following form of a simple wave:

$$z = z\left(r^{n+1} - \int \frac{v(R)}{U} dR^{n+1}\right) \tag{5.21}$$

or, equivalently,

$$\rho = r^{n-2} f\left(r^{n+1} - \int \frac{v(R)}{U} dR^{n+1} \right) \tag{5.22}$$

The mass balance (5.9) at the front can be used:

$$\frac{v}{U} = \frac{\rho - \rho_0}{\rho} = \frac{e}{e+1}, \quad e = \frac{\rho - \rho_0}{\rho_0} \tag{5.23}$$

If volume deformation at the front is constant (that is, $e(R) = e_*$), then one has

$$\rho = R^{n-2} f(x_r) = \rho_0 (1 + e_*), \quad x_R = R^{n+1} / (1 + e_*) \tag{5.24}$$

at the front $(r = R)$, and the calculation is simplified.

The function $f(x)$ as be defined as:

$$f(x) = \rho R^{2-n} = \rho_0 (1 + e_*) \{ x(1 + e_*) \}^{\frac{2-n}{1+n}} \tag{5.25}$$

The kinematic integrals (5.17) and (5.25), together with the plastic limit (5.6) and the momentum balance at the front (5.10), allows us to transform the dynamic equation (5.2) to the ordinary differential equation which has to be integrated numerically.

5.1.3. NUMERICAL SOLUTION OF A CONTAINED EXPLOSION

Consider the variant of numerical study from the very beginning. Such an approach gives the possibility of taking into account the changes of dilatancy rates (from positive to negative values) accompanied by changes of the solid friction coefficient, α, and cohesion, $chs = \alpha H$. Moreover, there is also a possibility to account for the elastic part of strain in plastic zone *II*, together with the existence of outer elastic zone *III*.

In zone *III*, the usual Hooke law is valid, but it is necessary to use the substantional derivatives

$$\frac{d\sigma_\tau}{dt} = G\left(\frac{\partial v}{\partial r} - \frac{v}{r} \right) \qquad \frac{d\sigma}{dt} = K\left(\frac{\partial v}{\partial r} + 2\frac{v}{r} \right) \tag{5.26}$$

because the nonlinearity determined by displacement velocities is essential during an explosion motion. In plastic zone *II*, the elastic part must be eliminated before using the dilatancy condition (5.5):

$$\left(\frac{\partial v}{\partial r} + 2\frac{v}{r} \right) + \frac{1}{K}\left(\frac{\partial \sigma}{\partial t} + v\frac{\partial \sigma}{\partial r} \right) = \frac{2}{\sqrt{3}} \Lambda \left| \frac{\partial v}{\partial r} - \frac{v}{r} \right| \tag{5.27}$$

In both zones, the balance equations - (5.1) and (5.2) - are valid, but the plastic limit (5.6) is used in zone *II* instead of the first elastic constitutive laws (5.26). It is necessary to note that the same plastic condition (5.6) is valid just before the boundary, R, between zones *II* and *III* (that is, at $r = R - 0$), but, generally speaking, it includes higher values of the coefficients α and H, corresponding to the strength of the initially intact rock. As the result, the hoop stress, σ_θ, can be discontinuous here, although the shock front may not coincide with this boundary. Because the computation method includes the numerical viscosity concept, frontal discontinuities are modeled by moving zones of high-gradient variables.

In Figures 5.2 through 5.4, some typical results of calculations are given for an underground contained explosion. Here the reduced coordinate $r/\varepsilon^{1/3}$ is used, where ε is the explosion energy (TNT equivalent of a charge weight). The explosion wave profiles (Figure 5.2) are given for three moments of time, $t = 28t_0, 56t_0, 84t_0$, where $t_0 = a_0/c_p$, c_p is the velocity of the longitudinal wave. Solid lines correspond to dilatant loosening of geomaterials with $\Lambda = 0.1$. Broken lines are for $\Lambda = 0$. The specific volume, $V = 1/\rho$, is diminishing and the density is growing for the second case because of pressure increase and elastic compressibility. The level of lithospheric pressure, p_L, is also mentioned here.

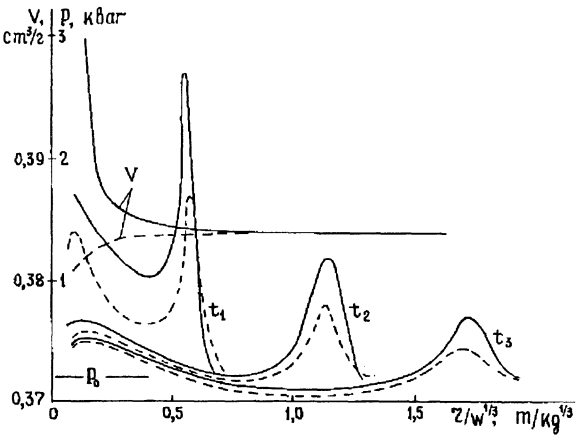

Figure 5.2. Profiles of stress waves radiated by dynamic cavity growth in dilating (solid lines) and nondilating (broken lines) strata.

In Figure 5.3, maxima of velocity, pressure and shear stresses in the stress wave are also given for two cases, $\Lambda = 0.1$ and $\Lambda = 0$. The kink at $r/\varepsilon^{1/3} \approx (0.4 \div 0.5)$ corresponds to the instant at which the shock front separates and begins to move with elastic velocity - that is, faster than the plastic boundary.

In Figure 5.4, the hodographs of the plastic boundary (curve *1*), cavity radius (*2*), pressure maximum, identified with the shock front (*3*), and the second pressure maximums, identified with residual stress (*4*), are given. You can see that the dilatancy effect intensifies the outward motion and diminishes the cavity size because of pore volume growth in the plastic dilatant zone [152].

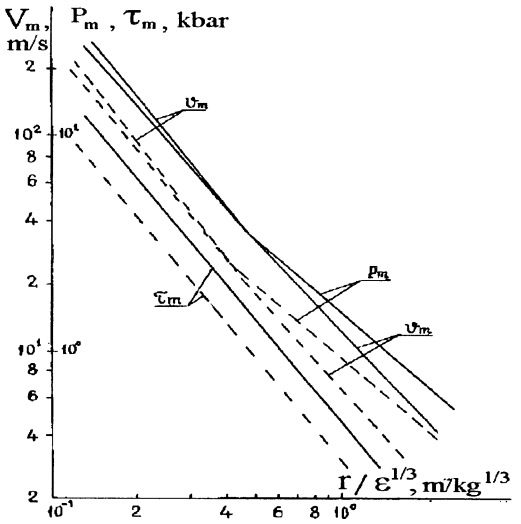

Figure 5.3. Decay of stress waves in the close vicinity of the explosion (solid lines correspond to dilatancy accounting for; $1\,m/kg^{1/3} \equiv 100\,m/kton^{1/3}$; energy is given in equivalent charge weight).

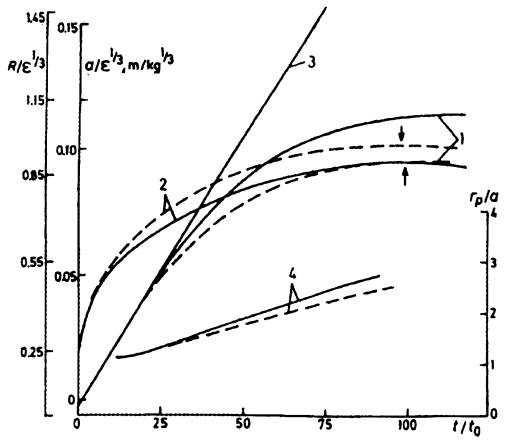

Figure 5.4. Fronts of stress waves in dilating (solid lines) and nondilating (broken lines) rocks.

The first stage of explosion motion is characterized by more essential compaction at the shock front in the case of high initial porosity and by further consolidation with negative dilatancy coefficient due to shear behind this front. The initial lithostatic pressure also influences the compaction process. In Figure 5.5, the characteristic intervals of dilatant loosening (1) and of compaction (3), together with the intermediate case (2), are shown. The initial porosity decreases the amplitude of the explosion wave, as can be seen in Figure 5.6.

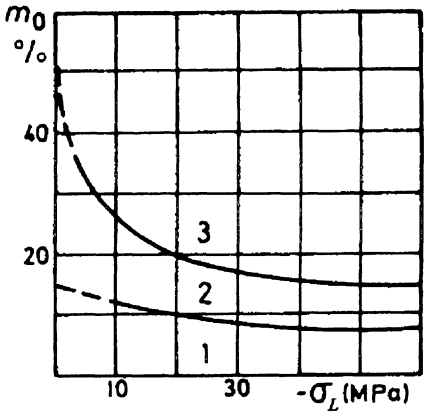

Figure 5.5. Initial porosity and lithostatic pressure control the predominant effects of underground explosions [152].

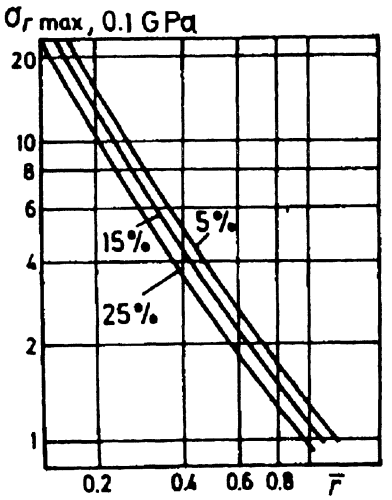

Figure 5.6. Decay of seismic waves depends on the initial porosity of the strata [152].

5.1.4. EXPLOSION EXPERIMENTS

The physical modeling of underground explosions by small charges in grouted sands gives the same picture of dynamic deformation of porous space as in the close vicinity of the explosion cavity. The results are shown for initial porosity, m_0, in Figure 5.7. You can see the residual density increase in the spherical zone around the explosion cavity, and the corresponding increase of radial P-wave velocity is mentioned. There is no change of the P-wave velocity in the hoop direction indicates the explosion residual effects of high anisotropy. Although density (and porosity) changes are nonmonotonous, the permeability decreases everywhere because of the simultaneous diminishing of sand grain size to the powder state.

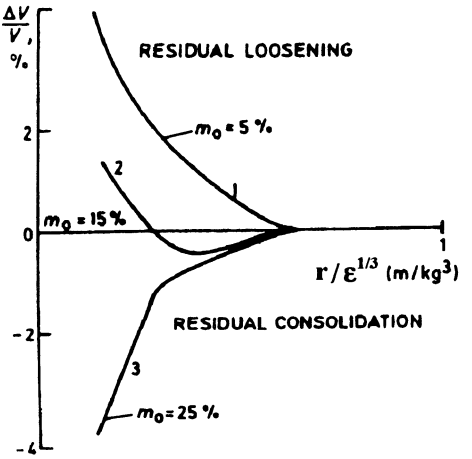

Figure 5.7. Residual density $(V = 1/\rho)$ distribution around the explosion cavity depends on initial porosity [152].

Nonmonotonous changes of permeability are not suppressed only in the case of extremely small values of initial porosity. The explosion in the rock sample with $m_0 = 10\%$ is given in Figure 5.8. However, these permeability changes are not bigger than *3* times the initial value. They are much smaller than the drastic changes (*1000* times or even more) in granites due to fracture appearance and to extremely small initial porosity (see Figure 5.9 and [198]).

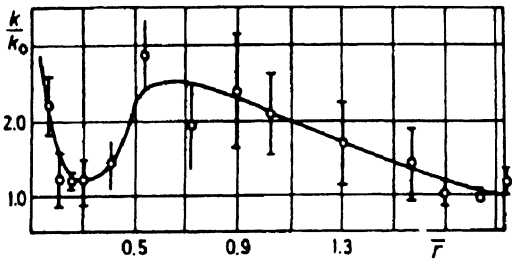

Figure 5.8. Nonmonotonous permeability field after explosion in porous grouted sand ($m_0 = 10\ \%$).

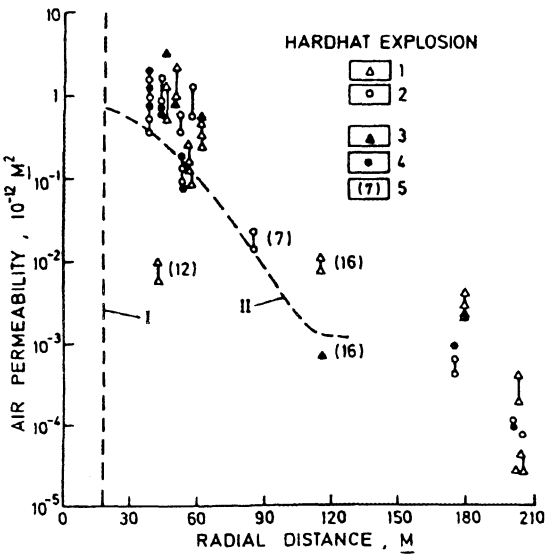

Figure 5.9. Data of well testing after nuclear explosions in granites
(I = cavity radius, II = the Hoggar explosion);
1, 2 - vertical and horizontal wells, 1964 measurements;
3, 4 - 1965 measurements; numbers in brackets correspond to wells.

According to these experiments, all residual changes are located in the zone $\bar{r} \le 0{,}47\left(m/kg^{1/3}\right)$ in porous geomaterials, compared with $\bar{r} \le 1\left(m/kg^{1/3}\right)$ for intact rocks. The pore space changes take place without fracturing the surrounding strata. Numerous rigid grains suppress development of long fractures in shock wave tails. The

experimental data are in accordance with the numerical calculations done on the basis of rock strength properties measured in static experiments.

5.1.5. DYNAMIC STRENGTH OF MATERIALS

The problem of the dynamic strength of materials has to be clarified. First, stress states propagate in materials with the elastic wave velocities, but fracturing has its own limit velocity that is essentially smaller. The limit velocity is explained by the growth of the material toughness when the velocity is close to the Rayleigh wave velocity or by the dynamic instability of cracks at high-velocity growth. The limit velocity has to be measured relative to moving material - that is, to the particle velocity, v. For example, in experiments with PMMA, it is equal to *500* m/s or the same order of *2-3* km/s as the solid sliding [29] for granites. In confined sands, this velocity is equal to *450* m/s, which is close to the Rayleigh value for sand masses [152].

This preliminary note explains the dynamic strength as the overloading phenomenon [148]. The simple elasto-brittle calculation of the plane dynamic problem of shock action with fracturing shows the distribution of stresses in the two-front wave (Figure 5.10).

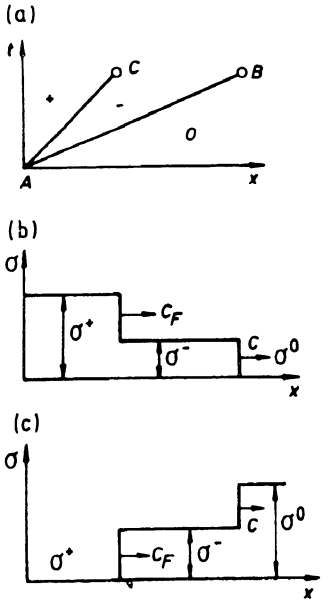

Figure 5.10. Scheme of loading (b) and unloading (c) waves taking account of the fracturing front as dynamic discontinuity.

The first front corresponds to the elastic precursor that moves along the line AB. Fracturing of the material takes place at the second front. If the rupture condition $\sigma^- = \sigma_F$ is fulfilled at the same line, AC, then the stress is calculated by discontinuity balances. The difference of intact <<->> and crushed <<+>> states is accounted for in the constitutive laws. However, if the front velocity, c_F, is equal to its real limit value, then the stress σ^- is much higher in the zone <<->> than the fracturing stress σ_F.

The value σ^- measured in experiments is sometimes interpreted as dynamic strength. However, it depends on the condition of the shock, sample geometry, etc. - that is, the dynamic strength is not a material property but the function of the dynamical process [148, 152].

In the zone <<->>, small cracks begin to grow, but, for the case in which the duration of σ^- is short, these defects disturb the internal structure of the material only and do not change its bearing capacity. Crack length is proportional to the time duration of overloading. The fineness of crashing depends on the amplitude of σ^-, because the latter determines the initial scale of cracks which begin to grow [148].

Thus, during explosive action, the fracturing process begins, as shown by static strength data. The dynamic overloading effect determines the kinetics of fracturing and microstructure changes. The large-scale calculation can be done on the basis of static strength data.

5.2. Fronts and evolution of seismic waves

5.2.1. ELASTODYNAMICS OF WAVE RADIATION

The shock front velocity decreases during underground explosive motion, but the elastic wave velocities are constants of the surrounding geostratum. There is a moment after which the shock front begins to radiate the elastic wave, sometimes called the elastic precursor. For simplicity, the seismic waves are assumed to be radiated by the outer boundary of damaged zone b.

Further calculation is based on the theory of dynamic elasticity, according to which the displacement, u, and displacement velocity, v, can be expressed with the help of the scalar elastic potential:

$$\Phi = f_1\left(t - \frac{r}{c}\right) + f_2\left(t + \frac{r}{c}\right) \tag{5.28}$$

This potential includes divergent, f_1, and a convergent, f_2, parts, satisfies the wave equation

$$\frac{\partial^2 \Phi}{\partial t^2} = c_p{}^2 \nabla^2 \Phi \tag{5.29}$$

and appears in the general expressions

$$\vec{u} = \vec{\nabla}\,\Phi + rot\ \vec{\Psi} \tag{5.30}$$

together with the vector potential, $\vec{\Psi}$, such that

$$\frac{\partial^2 \vec{\Psi}}{\partial t^1} = c_s^2 \nabla^2 \vec{\Psi} \tag{5.31}$$

Here, standard P-wave and S-wave velocities appear:

$$c_p{}^2 = \frac{1}{\rho}\left(K + \frac{4}{3}G\right) \quad , \qquad c_s{}^2 = \frac{1}{\rho}G \tag{5.32}$$

However, the potential, f_1, is sufficient for seismic wave radiation by the contained underground explosion. This potential can be found from equation (5.29), where the Laplace operator is simplified due to the spherical symmetry:

$$\nabla^2 \equiv \frac{1}{r^2}\frac{\partial}{\partial r}\left(r^2 \frac{\partial}{\partial r}\right) \tag{5.33}$$

Then [183]

$$u = \frac{\partial \Phi}{\partial r} = -\frac{1}{cr}\frac{df}{d\xi} - \frac{1}{r^2} f(\xi) \tag{5.34}$$

$$\xi = t - \frac{r}{c}, \qquad f_1 = \frac{1}{r} f \tag{5.35}$$

At the larger distances from the explosion cavity, the effective expression (5.34) is:

$$u(\xi) = \frac{u_0 b^2}{c_p r T}\left(1 - \cos\frac{2\pi\xi}{T}\right) \tag{5.36}$$

where T is the characteristic period, u_0 is the displacement at $r = b$, $0 \le \xi \le T$, and $u = 0$ out of the interval $(\xi < 0, \xi > T)$.

The displacement velocity, v, has the corresponding form [183]

$$v(\xi) = \frac{u_0 b^2}{c_p r T^2} 2\pi \sin\frac{2\pi\xi}{T} \tag{5.37}$$

5.2.2. SEISMIC RISK ESTIMATION

It is now possible to make some estimations. According to Section 5.1, the characteristic radius of damage is $b \approx 1 m/kg^{1/3}$ for explosions in intact rocks and $b \approx 0{,}5\, m/kg^{1/3}$ in porous geomaterials. Field measurements have shown [8] that velocities, v, in porous strata (tuff, for example) are much smaller than in intact rocks, but displacements, u, have the same order. This means that period $T = 2\pi u/v$ is much larger (and frequency $\omega = 2\pi/T$ is much smaller) in intact rocks than in porous ones.

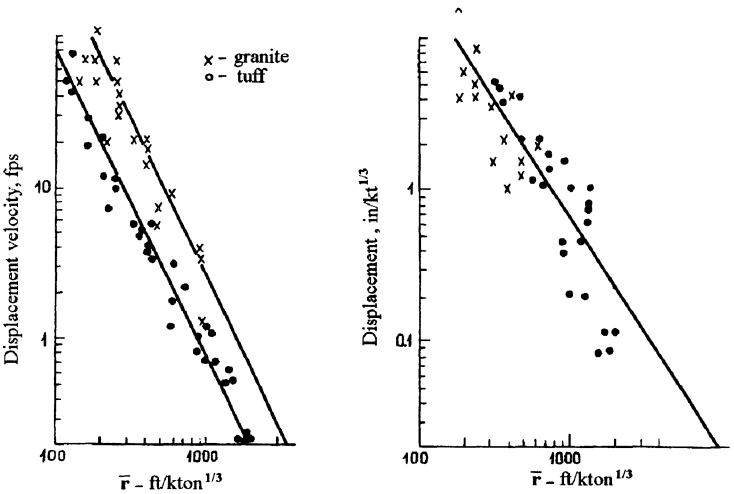

Figure 5.11. Ground motions from contained blasts in rocks [8].

The impact force, F, acting at the underground construction with plane cross-section B, is determined as

$$F = B\rho cv \tag{5.38}$$

Therefore, the first criterion of seismic risk for constructions must be formulated in terms of the maximum of the displacement velocity, v_{max}, as found by observation data [183]. The smallest level of danger is estimated as *10* cm/s, the point at which fractures can appear in old building walls. This level is larger for new buildings (*20* cm/s) and very high (*150* cm/s) for small wooden houses. The estimate (5.38) shows that seismic risk for porous rocks is less.

The second criterion is formulated in terms of frequencies, ω, because there is a possibility of resonance between ground waves and constructions. More detailed calculations must be done for this phenomenon. It has been found from field experience that there is a dominant wave frequency, ω_d, for each type of geostratum.

TABLE 5.1. Dominant geomaterial frequencies

geomaterial	gravel	sand	clay	eroded granite
ω_d, Hz	*8-10*	*25*	*40*	*100*

The dominant frequency effect was utilized to generate working frequencies by choosing explosion sites during seismic exploration [231].

5.2.3. EVOLUTION OF SEISMIC SPECTRA

Evolution of seismic spectra can be explained by the nonlinear evolution of seismic waves due to viscoelastic rheology of fragmented geomaterials. Corresponding, the rheology is given by the constitutive law - (1.69) and (1.70) - and is illustrated by Figure 1.5.

Consider this rheology together with nonlinear balances of mass and momentum:

$$\frac{\partial \rho}{\partial t} + \frac{\partial (\rho v_j)}{\partial x_j} = 0 \tag{5.38}$$

$$\frac{\partial (\rho v_i)}{\partial t} + \frac{\partial (\rho v_i v_j)}{\partial x_j} = \frac{\partial \sigma_{ij}}{\partial x_j} \tag{5.39}$$

and with the following nonlinear relation between deformation e_{ij} and velocity field:

$$\frac{D e_{ij}}{Dt} \equiv \frac{\partial e_{ij}}{\partial t} + v_k \frac{\partial e_{ij}}{\partial x_k} + e_{ik} \frac{\partial v_i}{\partial x_k} + e_{ik} \frac{\partial v_i}{\partial x_k} = \frac{1}{2} \left(\frac{\partial v_i}{\partial x_j} + \frac{\partial v_j}{\partial x_i} \right) \tag{5.40}$$

Here, as in (1.69) and (1.70), the Oldroyd time derivative is used because these two determinations of the strain rate are noncontradictory to each other only in this case.

Introducing the following expansions

$$\begin{gathered} v_i = \zeta v_i^{(1)} + \zeta^2 v_i^{(2)} + \ldots \quad , \qquad \rho = \rho_0 + \zeta \rho^{(1)} + \ldots \quad , \\ \sigma_{ij} = \sigma_{ij}^{(0)} + \zeta \sigma_{ij}^{(1)} + \zeta^2 \sigma_{ij}^{(2)} + \ldots \quad , \quad \ldots \end{gathered} \tag{5.41}$$

where ζ is a small parameter, then equations (1.69) and (5.38) through (5.40) will give the following relaxation equation for the vector potential [152]:

$$\left(\frac{\partial^2 \Psi_k}{\partial t^2} - c_{so}^2 \frac{\partial^2 \Psi_k}{\partial x_i \partial x_i} + \kappa_{so}^2 \frac{\partial^4 \Psi_k}{\partial x_i \partial x_i \partial t^2} \right) +$$

$$+ \Theta_\tau \frac{\partial}{\partial t} \left(\frac{\partial^2 \Psi_k}{\partial t^2} - c_{s\infty}^2 \frac{\partial^2 \Psi_k}{\partial x_i \partial x_i} + \kappa_{s\infty}^2 \frac{\partial^4 \Psi_k}{\partial x_i \partial x_i \partial t^2} \right) = 0 \tag{5.42}$$

If the case $n = 1,\ m = 3$ of (1.69) is considered, $c_{s\infty}, c_{s0}$ are the frozen and equilibrium shear wave velocities, $\kappa_{s\infty}, \kappa_{s0}$ are the "frozen" and "equilibrium" length scales of oscillating fragments

$$c_{s0} = \sqrt{\frac{G_{II}}{\rho_0}} \quad , \quad c_{s\infty} = \sqrt{\frac{G_I + G_{II}}{\rho_0}} \quad , \quad \kappa_{s0} = \sqrt{\frac{M_{II}}{\rho_0}} \quad , \quad \kappa_{s\infty} = \sqrt{\frac{M_I + M_{II}}{\rho_0}} \tag{5.43}$$

and Θ_τ is the relaxation time.

Equation (5.42) is the generalization of (5.31) as result of dissipation viscous effect and the fragmentary microstructure of geomaterials. The analogous equation is valid for scalar wave potential Φ but with different coefficients.

The forth-order Bussinesq operators appear in brackets in equation (5.42) meaning that we can get the Korteweg-de Vries equations [106] or its generalizations instead of (5.42) in the approximation of weak nonlinear waves . The latter corresponds to the nonlinear evolution of seismic spectra.

To get the nonlinear evolution equation, use the special coordinate system

$$\xi_m = \eta^\alpha (x_m - c_m t) \quad , \qquad \tau = \frac{1}{2}\eta^\beta t \tag{5.44}$$

where the same small parameter is used. Using (5.41) and (5.44) simultaneously for P-waves gives the following standard acoustic expressions as the first approximation

$$\begin{gathered} c = c_{p0}, \quad c_{p0} e = - v^{(1)} \\ \rho_0 v^{(1)} = \rho_1 c_{p0}, \quad \sigma = - \rho_0 c_{p0} v^{(1)} \end{gathered} \tag{5.45}$$

For S-waves, we obtain

$$\begin{gathered} c = c_{s0}, \quad c_{s0}\gamma = -\frac{1}{2} v^{(1)} \\ \rho_1 \equiv \rho_0, \quad \tau = - \rho_0 c_{s0} v^{(1)} \end{gathered} \tag{5.46}$$

where γ, τ are shear and shear stress amplitude, respectively, and $v^{(1)}$ is displacement velocity which is orthogonal to direction of wave propagation.

The second approximation gives the nonhomogenous set of equations which is in agreement with the results of (5.45) or (5.46) only if the following nonlinear evolution equation is valid for P-waves [153]:

$$\frac{\partial v}{\partial \tau} + Nv \frac{\partial v}{\partial \xi} + \sum_{p=1}^{n} \Gamma_{2p+1} \frac{\partial^{2p+1} v}{\partial \xi^{2p+1}} = \sum_{p=1}^{m} \Gamma_{2p} \frac{\partial^{2p} v}{\partial \xi^{2p}} \tag{5.47}$$

where N is the coefficient of nonlinearity, primarily dependent on the physical nonlinearity in the rheological relations and Γ_p are positive coefficients dependent on seismic wave velocities and the rheological coefficients in (1.69). Here we consider equation (5.47) with $n = 2, m = 3$ that correcponds to rheological law (1.69) illustrated in Figure 1.5.

5.2.4. DOMINANT FREQUENCY AS A RESONANCE PHENOMENON

In linear approximation, standard disturbances

$$v = v_0 \exp i(\omega\tau - \chi\xi) \tag{5.48}$$

propagate in the wave form according to the following dispersion connection:

$$\omega = \chi v_* - \Gamma_3 \chi^3 + \Gamma_5 \chi^5 + i\chi^2(\Gamma_2 - \Gamma_4 \chi^2 + \Gamma_6 \chi^4) \tag{5.49}$$

where v_* is the velocity value in whose vicinity the linearization is made.

The waves will dissipate if $Im\,\omega > 0$, but their amplitude will grow without limit in linear approximation if $Im\,\omega < 0$. The interval of this instability is between two roots, χ_1^2, χ_2^2, of the quadric equation (Figure 5.12):

$$\Gamma_6 \chi^4 - \Gamma_4 \chi^2 + \Gamma_2 = 0 \tag{5.50}$$

However, this amplitude growth can be limited by a nonlinear term which results in oscillations with higher frequencies out of the interval being created and hence dissipated. The numerical calculation has shown that the seismic signal with the "white noise" spectrum is converted to oscillations with the dominant frequency, ω_d, corresponding to the wave number, χ_d (Figure 5.13).

In accordance with this analysis, seismic wave fronts propagate with elastic wave velocities, and traditional elasticity theory is valid for calculation of their front position at every instant. Practically, however, only the fronts of different waves are utilized from numerous observation records.

The seismic spectrum changes along the path and the dominant frequency appears. Estimating [151] the characteristic parameters of the medium which correspond to ω_d from Table 5.1,

$$\omega_d \approx c\,\chi_d \approx c\sqrt{\frac{\Gamma_4}{2\Gamma_6}} \tag{5.51}$$

$$\lambda_d \approx \frac{1}{\chi_d} \approx \sqrt{\frac{2\Gamma_6}{\Gamma_4}} \approx \kappa\frac{c}{\Delta c} \tag{5.52}$$

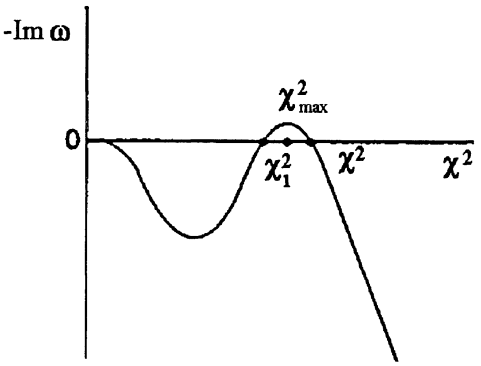

Figure 5.12. Frequency domain of (signal) amplification (of negative dissipation) [153].

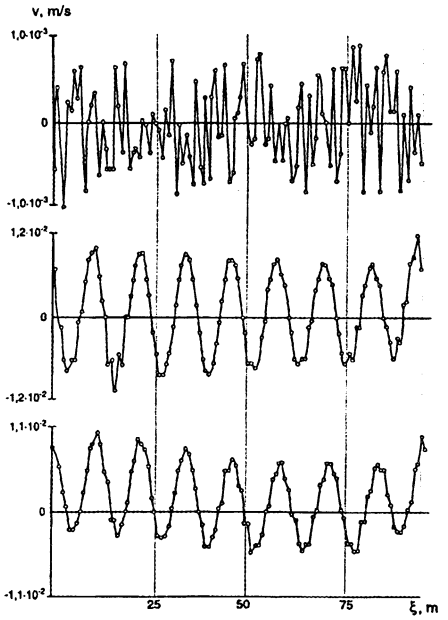

Figure 5.13. Evolution of initial white-noise disturbance (a) for time interval Δt to dominant (*12 Hz*) frequency oscillations (b) that are stable for the interval $7\ \Delta t$ (c) [19].

So, the values $\omega_d \approx 25\ Hz$, $c = 100\ m$ and particle size $d \approx \kappa \approx 0{,}4\ mm$, characteristic of sands, correspond to $\lambda_d \approx 4\ m$, and have a practically negligible wave velocity dispersion, $\Delta c \approx 0{,}1\ m / sec$.

Distant nuclear explosions are observed in the frequency interval $1 - 3\ Hz$, with $c \approx 6\ km/s$. This means that $\lambda_d \approx 6\ km$ and $\kappa \approx (\Delta c / c)\lambda_d \approx 100\ m$ if the relative wave dispersion is estimated at *1.5%*. So, *100 m* is the characteristic length scale of the Earth's crustal microstructure.

5.2.5. MACROSTRUCTURE WAVE EFFECTS

The P-wave fronts are described by equation (5.29) and the S-waves by equation (5.31). However, there are two types of S-waves, each with a different polarization. SH-waves have displacements in the horizontal plane and SV-waves in vertical direction. If the rock masses have the system of fractures, the measured shear-wave velocities are different depending on their polarization. If displacement is normal to the fracture, the effective rigidity is smaller, as well as the wave velocity. In case of displacement tangential to the fracture surface, the wave velocity is higher. This effect [45] was used to determine fracture system orientation in situ and even to determine fracture changes due to the fast tectonic movement characteristic of earthquake "preparation" (Section 7.3).

The free surface diminishes velocities of seismic waves which are connected to this plane. In such a case the solution is developed in the form of an approximation sequence ($\beta = 0,1,\ldots$) [135] - that is,

$$v_i^{(\beta)} = v_i^{(\beta)}\left(\chi_1^{(\beta)} x_1 - ct + \chi_2^{(\beta)} x_2\right) \tag{5.53}$$

Substitution of (5.53) into the approximation sequences of nonlinear dynamic equations corresponding to different orders of small parameters determines an integro-differential equation which can be solved numerically [135]. The condition of traction absence at the free surface gives the famous equation

$$\frac{c^6}{c_s^6} - 8\frac{c^4}{c_s^4} + c^2\left(\frac{24}{c_s^2} - \frac{16}{c_p^2}\right) - 16\left(1 - \frac{c_s^2}{c_p^2}\right) = 0 \tag{5.54}$$

of which one root, $c = c_R$, corresponds to the Rayleigh wave combination of SV- and P-waves. c_R approximately equals $c_R = 0{,}92\, c_{so}$, and particles displace along the elliptic paths in the plane x_1, x_2.

Analogously, the Love waves propagate along the layer at the free surface and include the SH-component. The adequate solution exists if the S-wave velocity in the layer is

smaller than in the base half-space. The stratification resonance effect will be discussed in Section 5.5.

5.2.6. WAVE DISSIPATION

Attenuation of seismic waves is the major unsolved problem of conventional mathematical theory because experiments have shown that the attenuation coefficient, b, is proportional to the first power of frequency, ω:

$$v = v_0 \exp(-bx) \exp i(x - ct) \quad , \qquad b \approx a\omega \tag{5.55}$$

or even $b \approx a_1\omega^n$, $n=0.7$, as follows from observation of seismic signals at long distances [98].

Physical explanations of these data are based on visco-elastic models with some special spectra of relaxation times or on the concept of nonlinear sublimit solid friction [152]. In the latter case, dissipation is created by relative slippage at grain contacts or at crack edges. These problems can be studied by the energetic method [161] and by the harmonic linearization method [152]. It is possible to show that seismic wave has practically no dispersion but possesses the attenuation $b \approx a\omega$ or the damping decrement Q, independent of frequency:

$$Q = \frac{\omega}{2cb} = const \tag{5.56}$$

Connection (5.56) can be verified in experiments with resonance columns where a single harmonic is used. Field observation, for example, has found that shear waves have $Q_s = 20 \div 50$ in dry sands and P-waves have $Q_p = 100 - 200$ in granite, limestone or sandstone. Usually, $Q_s/Q_p \approx 2$ for the same geomaterial. In intact minerals, $Q_p \approx 2000$, as found from ultrasound experiments. It means that main attenuation mechanism inside real geomaterials is connected with the relative motion at the microstructure level.

5.3. Seismics of oil and gas reservoirs

5.3.1. RELAXATION OF SHEAR WAVES

The mathematical model of dynamic poro-elasticity with thermal relaxation, as formulated in Section 2.3, describes two modes of P-waves and one mode of S-waves. Equation (2.96), for the S-wave, is the simplest, and it gives the dispersion equation [156]

$$\chi^2\left(c_{s\infty}^2+c_{s0}^2+i\omega\Theta_\rho c_{s\infty}^2\right)-\omega^2\left(1+i\omega\Theta_\rho\right)=0 \tag{5.57}$$

for harmonic one-dimensional waves:

$$\psi=\psi_0 \exp i(\omega t-\chi x), \quad \chi=\frac{\omega}{c_s}-i\,\delta_s \tag{5.58}$$

Correspondingly, we obtain the following expressions for shear wave velocity dispersion, c_s, and its attenuation coefficient, δ_s:

$$\frac{1}{c_s}=\frac{1}{c_{s0}\sqrt{2}}\left\{A^{1/2}+B\right\}^{1/2} \tag{5.59}$$

$$\delta_s=\frac{\omega}{c_{s0}\sqrt{2}}\left\{A^{1/2}-B\right\}^{1/2} \tag{5.60}$$

where

$$A=\frac{c_{s0}^4\left(1+\omega^2\Theta_\rho^2\right)}{c_{s0}^4+c_{s\infty}^4\omega^2\Theta_\rho^2} \tag{5.61}$$

$$B=\frac{c_{s0}^2\left(c_{s0}^2+c_{s\infty}^2\omega^2\Theta_\rho^2\right)}{c_{s0}^4+c_{s\infty}^4\omega^2\Theta_\rho^2} \tag{5.62}$$

The resulting velocity dispersion and the frequency dependence of attenuation coefficient are given in Figures 5.14 and 5.15 in dimensionless form.

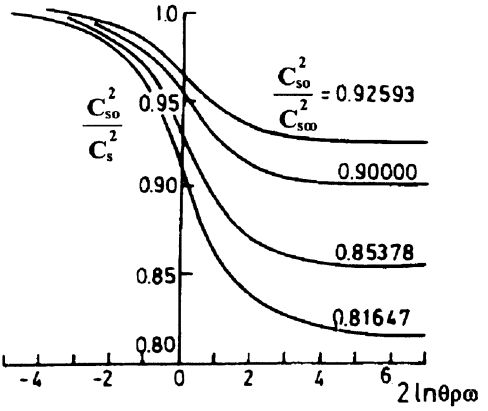

Figure 5.14. Wave velocity depends on frequency caused by inertia relaxation [156].

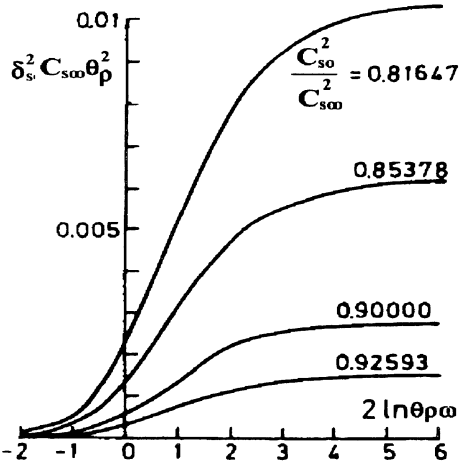

Figure 5.15. Attenuation coefficient depends on frequency caused by inertia relaxation [156].

5.3.2. TWO MODES OF P-WAVES

The system of dynamic equations, - (2.88) through (2.94), - for longitudinal waves is very complicated because it accounts for the interaction of the matrix and particle compressibilities together with thermal effect and filter-inertial relaxation, as in the S-wave case.

If the thermal effect is sufficiently small and the solid particles are much more rigid than the entire matrix, see (2.103), as in the case of water-saturated soils, then the effective system (2.104) is valid. The existence of two P-waves becomes evident because their effective dynamic equations - (2.104) and (2.111) - separate. You can see that the equation for the first P-wave mode (2.105) differs from the equation for the S-wave (2.96) only due to other "frozen" and "equilibrium" states values. So, the analogous dispersion equation

$$\chi^2\left(c_{I\infty}^2+c_{I0}^2+i\omega\Theta_\rho c_{I\infty}^2\right)-\omega^2\left(1+i\omega\Theta_\rho\right)=0 \tag{5.63}$$

is valid for pore pressure waves:

$$p = p_0 \exp i(\omega t - \chi x) \tag{5.64}$$

Therefore, Figures (5.14) and (5.15) can be used for c_p and δ_p. The first mode is characterized by the identical direction of solid and fluid particle motions. However, their motions have opposite directions in the P-wave of the second mode. It means that the fluid has to leave pores to permit full deformation of the porous matrix. This leads to very high filter dissipation, and the corresponding telegraph equation (2.112) has to be used instead of the standard wave equation.

The dispersion equation for the second P-wave is

$$\chi^2 c_*^2 \theta_\rho^2 = \omega^2 \theta_\rho^2 - i(\rho_\infty / \rho_0)^2 \tag{5.65}$$

where the corresponding wave number, χ, is used for matrix deformation:

$$e = e_0 \exp i(\omega t - \chi x) \quad , \quad \chi = \frac{\omega}{c_{II}} - i\,\delta_{II} \tag{5.66}$$

The following expressions for wave velocity, c_{II}, and attenuation coefficient, δ_{II}, are valid (Figures 5.16 and 5.17)

$$c_{II}^2 = 2c_*^2 \frac{\rho_0 \omega \theta_\rho}{\sqrt{\rho_0^2 \omega^2 \theta_\rho^2 + \rho_\infty^2} + \rho_0 \omega \theta_\rho} \tag{5.67}$$

$$\delta_{II}^2 = \frac{\omega^2}{2c_*^2} \frac{\sqrt{\rho_0^2 \omega^2 \theta_\rho^2 + \rho_\infty^2} - 1}{\rho_0 \omega \theta_\rho} \tag{5.68}$$

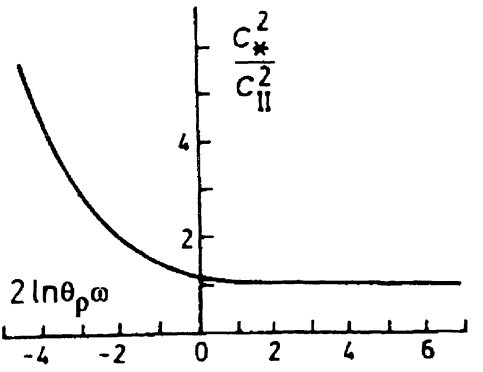

Figure 5.16. Dispersion of the second P-wave velocity [156].

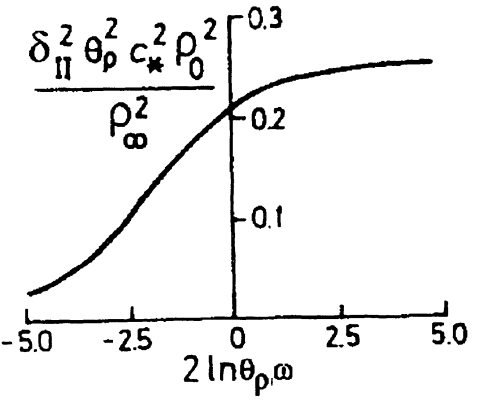

Figure 5.17. Frequency dependence of attenuation coefficient for the second P-wave [156].

Water-saturated quartz sands are characterized by the following set of parameters [151]:

$$m_0 = 0.3 \quad , \quad \rho_0^{(s)} = 2.5\, g/cm^3 \quad , \quad \rho_0^{(f)} = 1\, g/cm^3$$

$$K = 10^2\, MPa \quad , \quad K^{(s)} = 0.5 \times 10^5\, MPa \quad , \quad K^{(f)} = 0.25 \times 10^4\, MPa \tag{5.69}$$

with wave velocities

$$c_{po} = 1900\ m/s\ ,\quad c_{p\infty} = 2200\ m/s\ ,\quad c_* = 140\ m/s \tag{5.70}$$

You can see that the first-wave mode has the features of observable seismic P-waves in saturated soils and the second-wave velocity corresponds to observations of seismic waves in nonsaturated soils.

5.3.3. GAS-FLUID CONTACT IN POROUS SPACE

The poro-elasticity model provides the opportunity to interprete properly seismic data for strata saturated by water, gas and oil. First, the second P-wave mode, as well as the S-wave, mode corresponds to the deformation of the porous matrix independently of its saturation. If the geomaterial is saturated by gas and the pore pressure is very low, the second P-wave and S-wave are the only observable waves. This is the case of a gas cap in a depleted reservoir or gas underground storage in an aquifer. However, beneath the oil (or water) level, the relative motion of the fluid and matrix creates a dissipation so high that the second P-waves are practically excluded. As the result, only the first mode of P-waves becomes observable, and the velocity jump, N_P, of seismic longitudinal waves at the boundary separating gas and fluid in the same porous medium is essential:

$$N_p = \frac{c_{p0}}{c_*} = \sqrt{\frac{K + (4G/3)}{1/\beta}}\sqrt{\frac{\rho_*}{\rho_0}} \tag{5.71}$$

This follows from (2.106) and (2.113) if the relative low frequencies of real seismic waves are taken into account. Because $\rho_*/\rho_0 = O(1)$, the large value N_p is determined by the ratio of mineral grain and porous matrix compressibilites. At the same time, the velocity jump, N_s, of the seismic shear waves is much smaller; it has just the order of density ratio [152] of the gas and fluid saturated media:

$$N_s = \sqrt{\frac{(1-m_0)\rho_0^{(s)}}{(1-m_0)\rho_0^{(s)} + m_0\rho_0^{(f)}}} \tag{5.72}$$

This follows from (2.97) in the case of $\rho_0^{(f)} >> \rho_0^{(g)}$.

The second P-waves can propagate as a component of the second Rayleigh wave along the contact of gas and fluid inside the porous geomaterial or along the porous sea (or river) bottom because, in this situation, the fluid can easily leave the porous space in the lateral direction and essential deformation of the matrix becomes possible. The corresponding boundary-layer procedure was developed [65]. Such Rayleigh waves can be observed if geophones are situated exactly at the sea bottom [224].

5.3.4. GAS-SATURATION EFFECTS

The first and second modes of P-waves can coexist in the form of body waves if the porous fluid has small fraction of gas bubbles. The problem of the mechanism change of observable seismic waves from the first to second mode is nontrivial. Such a problem was studied for gas-saturated porous media for the case of growth of rigidity and initial pore pressure [156]. It was shown that in the case of low pressure of a gas-saturated porous medium, the second-wave velocity was determined by matrix rigidity and was larger than the first-wave velocity. The latter is determined by effective gas compressibility. Moreover, the distribution of loading impulse is dependent upon the boundary condition (2.42)-(2.45). If a gas wave is incident on a porous gas-saturated medium, the first P-wave, called also the "gas" or "air" wave, is generated and dissipated due to losses inside the gas-saturated, ideally rigid, porous matrix. In this case, the load applied to the solid phase is negligible, and the medium plays the role of sound absorber. However, in the case of pulse loading of the solid matrix, the stress wave spreads mainly in the second-wave form.

Sound damping in gas-saturated media is controlled by viscous resistance to gas filter flow and by thermal effect. The latter corresponds to the heating of gas under compression and to the heat irreversible flux into the solid matrix because of its high thermal capacity. It is possible to show that the total wave attenuation is the sum of viscous and thermal parts [156]; moreover, due to the estimation of porous media parameters, they are both of the same order. This is why gas-saturated media have very high damping effects.

The velocity dispersion due to filter-inertial relaxation is relatively small, and it can be suppressed by the rigid growth of the porous matrix. This is the case for water-saturated porous rocks. However, additional relaxation due to thermal damping, as in the case of oil-saturated porous geomaterials, permits more essential seismic velocity dispersion (see Table 5.2). Of course, the high thermal properties of reservoir oil are connected with the gas dissolved in it.

TABLE 5.2. Dispersion of P-waves in thermoporoelastic saturated rocks.

Quartz media	Velocity c_p, m/s			
	Saturated by Water		Saturated by Oil	
	$\omega \to 0$	$\omega \to \infty$	$\omega \to 0$	$\omega \to \infty$
$K\beta^{(s)} \gg 0.1$	2000	2160	1570	1880
$K\beta^{(s)} = 0.1$	2200	2340	1830	2100
$K\beta^{(s)} = 0.2$	2400	2500	2050	2300
$K\beta^{(s)} = 0.3$	2600	2660	2350	2520
$K\beta^{(s)} = 0.4$	2800	2830	2570	2720
$K\beta^{(s)} = 0.5$	3000	3000	2800	2920

The calculations for Table 5.2 were performed according to the dispersion equation resulting from the equations given in Section 2.3 for the general case [156].

5.3.5. MATRIX-VISCOSITY EFFECT

An additional source of wave energy dissipation is the viscosity of the geomaterial matrix accounted by the constitutive law (2.198). Using this relation instead of (2.3), the following equations valid for one-dimensional P-waves can be obtained from the system (2.4) through (2.7):

$$\frac{\partial^2}{\partial x^2}(He - C\xi) = \frac{\partial^2}{\partial t^2}\left(\rho_0 e - \rho^{(f)}\xi\right) - \left(\zeta + \frac{4}{3}\eta\right)\frac{\partial^3 e}{\partial x^2 \partial t} \tag{5.73}$$

$$\frac{\partial^2}{\partial x^2}(Ce - M\xi) = \frac{\partial^2}{\partial t^2}\left(\rho^{(f)} e - \rho^{(f)}\xi m^{-1}\right) - \frac{\mu}{k}\frac{\partial \xi}{\partial t} \tag{5.74}$$

Here, the Biot coefficients [20] and variable ξ are used:

$$\begin{gathered} H = K + \frac{4}{3}G - \left(1 - \beta^{(s)}K\right)^2 M, \quad C = \left(1 - \beta^{(s)}K\right)M, \\ M = \left(\beta - \beta^{(f)}\beta^{(s)}K\right)^{-1}, \quad \xi = m(\partial / \partial x)\left(v^{(s)} - v^{(f)}\right) \end{gathered} \tag{5.75}$$

The dispersion equation has the form

$$\left(\frac{\chi}{\omega}\right)^2 = -r + \frac{1}{2l}\sqrt{r^2 - 4lq} \tag{5.76}$$

$$r = \rho^{(f)}\frac{H}{m} - \rho_0 M - 2\rho^{(f)}C + \frac{\mu}{k}\left(\zeta + \frac{4}{3}\eta\right) - i\left\{\frac{\mu H}{k\omega} - \frac{\rho^2{}_0\,\omega}{m}\left(\zeta + \frac{4}{3}\eta\right)\right\} \tag{5.77}$$

$$l = HC + C^2 - i\omega M\left(\zeta + \frac{4}{3}\eta\right), \qquad q = \rho^{(f)}\rho^{(f)} - \frac{\rho_0 \rho^{(f)}}{m} + i\frac{\rho_0 M}{k\omega} \tag{5.78}$$

Calculations [35] performed for equation (5.76) have shown that the viscosity of a solid matrix can essentially change the attenuation coefficient, δ_p, and even the type of its frequency dependence, ω.

In Figure 5.18 typical data are given for the different fluids that can saturate geomaterials.

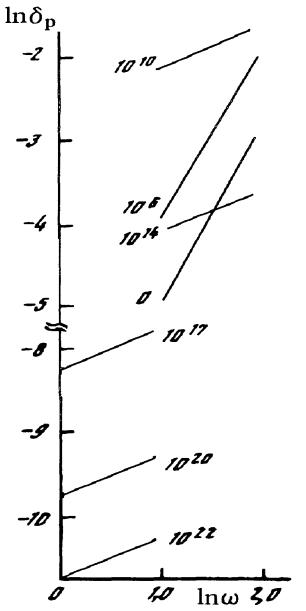

Figure 5.18. Frequency dependence of the attenuation coefficient for P-waves [35].

As can be seen, the matrix viscosity can surpress the effect of fluid differences in the interval of $\zeta, \eta \approx 10^6 - 10^{10}\,\Pi$, corresponding to sands, sandstones and limestones. Geomaterial parameters used are given in Table 5.3.

TABLE 5.3. Effect of matrix viscosity for waves.

Parameters	Sand	Sandstone	Limestone
$\rho^{(s)}$, g/cm^3	2.65	2.62	2.60
$\beta^{(s)}$, $10^{-12}\ cm^2/dyne$	2.7	2.94	1.35
η, ζ, Π	10^5	10^6	10^6
m	0.35	0.16	0.05
k, cm^2	10^{-7}	10^{-8}	10^{-10}
G, $dyne/cm^2$	4×10^9	4×10^{10}	3×10^{11}
K, $dyne/cm^2$	7×10^9	6×10^{10}	4×10^{11}
c_p $(10^2\ Hz)$, km/s	1.7	2.7	3.6
c_p $(10^4\ Hz)$, km/s	1.8	3.7	3.7

The matrix-viscosity approach accounts for the difference between the seismic wave velocity (at *100 Hz*) and the ultrasound wave velocity (at *10,000 Hz*). This difference is essential for proper interpretation of experimental laboratory data and effects wave energy transformation from seismic to ultrasound frequencies.

Another source of dissipation is explained by the wave interaction with nonhomogeneities because of the second P-wave generation at each boundary. This effect gives the following dependence in case of random distribution of inclusions in geomaterial volume [152]:

$$\delta \approx a\,\omega^{2/3} \tag{5.79}$$

If nonhomogeneities are represented by a set of cracks, the splitting of S-waves with different polarization appears to be essential. This effect is observable during earthquake preparation processes and inside porous-fractured reservoirs [45].

5.4. Microstructure transformation and wave generation

5.4.1. ONE-DIMENSIONAL MICRO-ELASTIC DYNAMICS

There is a possibility for kinematically independent motion of fragments composing a real geomaterial, if its matrix is not too rigid. For a mathematical description of the resulting effects, we can use the methods of generalized continua mentioned in Sections 1.1 and 2.2 and we shall use the balance of moment of momentum (1.13) in addition to the balances of mass and impulse to study the dynamic processes in a porous medium.

Consider, for example, the one-dimensional micro-elastic dynamics described by the following two dynamic equations [102], which are a sequence of equations (1.13) and (1.20) through (1.22) with additional nonlinear terms:

$$\frac{\partial^2 u}{\partial t^2} - c_1^2 \frac{\partial^2 u}{\partial x^2} - \nu \frac{\partial u}{\partial x}\frac{\partial^2 u}{\partial x^2} - \delta \frac{\partial^4 u}{\partial x^4} + \beta \frac{\partial \Phi^2}{\partial x} = 0 \tag{5.80}$$

$$\frac{\partial^2 \Phi}{\partial t^2} - c_2^2 \frac{\partial^2 \Phi}{\partial x^2} + a\Phi - \left(c_2^2 \frac{\partial^2 \Phi}{\partial x^2} - a\Phi \right) \frac{\partial u}{\partial x} = 0 \tag{5.81}$$

You can see that in equation (5.80), the usual wave operator is generalized by the fourth space derivative, which has the same order as the microstructure effect of fragment rotation at angle Φ [30]. This requires using the so-called gradient-consistent rheological law. The nonlinearity introduced here is the simplest way to account for density dependence on deformation

$$\rho = \rho_0 (1 + \partial u / \partial x)^{-1} \tag{5.82}$$

In the linear approximation, equations (5.80) and (5.81) are split.

The antisymmetrical part of the stress tensor is proportional to angle Φ - that is,

$$\sigma_{ij}^a = \gamma \, \varepsilon_{ijk} \, \Phi_k \tag{5.83}$$

This does not include mean distortion, because the mean motion is purely longitudinal, $\partial u_i / \partial x_j = 0, \; i \neq j$. Here, ν, δ, β, a are the material elastic constants, c_1, c_2 are the wave velocities

$$c_1^2 = \frac{E}{\rho_0}, \quad c_2^2 = \frac{A}{\rho_0 J} \tag{5.84}$$

The following rheological relations are used for stresses:

$$\sigma = E\frac{\partial u}{\partial x} + C\frac{\partial^3 u}{\partial x^3} + B\frac{\partial u}{\partial x}\frac{\partial u}{\partial x} - \beta\rho_0\Phi\Phi \tag{5.85}$$

and for couple-stresses:

$$\mathcal{M} = A\frac{\partial \Phi}{\partial x} \tag{5.86}$$

They are all in agreement with Section 2.2. Then

$$\nu = c_1^2 + 2\frac{B}{\rho_0},\quad \delta = \frac{c}{\rho_0},\quad a = \frac{\gamma}{\rho J} \tag{5.87}$$

and γ is determined by equation (5.83).

5.4.2. MODULATION OF HIGH FREQUENCIES

The traditional usage of the running coordinate ξ with change of length and time scales

$$\xi = \eta(x - c_g t),\quad \tau = \eta^2 t \tag{5.88}$$

transforms equations (5.80) and (5.81) into [102]:

$$\left(c_g^2 - c_1^2\right)\frac{\partial^2 V}{\partial \xi^2} - 2\eta c_g \frac{\partial^2 V}{\partial \tau \partial \xi} = 2\beta\eta^{2(q-1)}\frac{\partial^2 |A|^2}{\partial \xi^2} \tag{5.89}$$

$$2i\chi\frac{\partial A}{\partial \tau} - \left(c_2^2 - c_g^2\right)\frac{\partial^2 A}{\partial \xi^2} = \left(\chi^2 c_2^2 + 2\omega_0^2\right)VA \tag{5.90}$$

where new variables A and V are used

$$\Phi = Ae^{i\Theta}\quad ,\qquad V = \frac{\partial u}{\partial \xi} \tag{5.91}$$

and

$$\omega_0 = \frac{\sqrt{a}}{2}\ ,\ c_g = \frac{d\omega}{d\chi}\ ,\ \Theta = \chi\xi - \omega\tau \tag{5.92}$$

with c_g as the group velocity.

Equation (5.89) is formulated for the amplitude of seismic deformation, V. and equation (5.90) is formulated for the amplitude of the rotation angle oscillation, A. Because the parameters of equation (5.89) or (5.90) include small internal length scale,

$\sqrt{J}$, the mentioned oscillations correspond to wavelengths of the same order as the matrix grains.

If $q = 1$ in the exponent (5.89) and $\eta \to 0$, then equation (5.8) gives the nonlinear connection between V and A

$$V = 2\beta |A|^2 / \left(c_g^{\,2} - c_1^{\,2}\right) \tag{5.93}$$

and the amplitude A is described by the Shroedinger nonlinear equation which follows from (5.90):

$$2i\chi \frac{\partial A}{\partial \tau} + \left(c_2^{\,2} - c_g^{\,2}\right) \frac{\partial^2 A}{\partial \xi^2} = 2\beta \frac{\chi^2 c_2^{\,2} + 2\omega_0^{\,2}}{c_1^{\,2} - c_g^{\,2}} |A|^2 A \tag{5.94}$$

So, the envelope of high-frequency oscillations can have the soliton form because equation (5.94) has the following solution:

$$A = A_0 \sqrt{\frac{2\left(c_1^{\,2} - c_g^{\,2}\right)}{\chi^2 c_2^{\,2} - 2\omega_0^{\,2}}} \times$$

$$\exp\left\{ i \frac{B_0 \xi}{2\sqrt{c_2^{\,2} c_1^{\,2}}} - i\left(\frac{B_0^{\,2}}{4} - A_0^{\,2} \right) \right\} sech\, A_0 \left(\frac{\xi}{\sqrt{c_2^{\,2} - c_1^{\,2}}} - B_0 t \right) \tag{5.95}$$

Some experimental data for seismic noise support this mathematical result.

5.4.3. LONG-SHORT WAVE RESONANCE

Another effect is connected with energy flux from seismic waves to ultrasound oscillations in case of long-short-wave resonance when the group ultrasound velocity, c_g, is equal to the seismic wave velocity, c_1. In Figure 5.19, dispersion curves for the linear variants of equations (5.80) and (5.81) are given for seismic and ultrasound frequencies, respectively:

$$\omega_s^2 = c_1^2 \chi_s^{\,2} + \delta \chi_s^{\,4} \quad , \qquad \omega_{us}^2 = c_2^2 \chi_{us}^2 + 2\omega_0^2 \tag{5.96}$$

You can also see the resonance condition in Figure 5.19:

$$c_g = c_s \approx c_1 \tag{5.97}$$

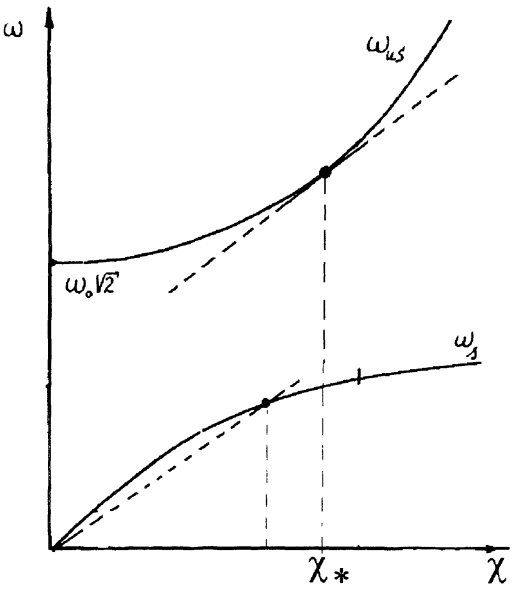

Figure 5.19. Seismic and ultrasound dispersion curves for geomaterial with microstructure (Wave number $\chi_{us} = \chi_*$ corresponds to long-short-wave resonance (LSWR)).

Then equations (5.89) and (5.90) convert into the canonical system [102]:

$$\frac{\partial L}{\partial t} = \pm \frac{\partial |S|^2}{\partial x} \tag{5.98}$$

$$2i\frac{\partial S}{\partial t} + \frac{\partial^2 S}{\partial x^2} = 2LS \tag{5.99}$$

where $\chi_* = \bar{\chi}\eta^p$, and q is such that equation (5.89) becomes simpler

$$\frac{\partial V}{\partial \tau} = \bar{\chi}\frac{-\partial |A|^2}{\partial \xi} \quad , \qquad \bar{\chi} = O(1) \tag{5.100}$$

Here, L and S are the special normalized variables V and A.

From the resonance condition (5.97), we can obtain the wavelength of the generated ultrasound, λ^*_{us}, by

$$\lambda_{us}^{*} = \frac{2\pi c_2}{\omega_0 c_1}\sqrt{c_2^2 - c_1^2} \tag{5.101}$$

This means λ_{us}^{*} does not depend upon seismic frequencies and is proportional to internal length scale because

$$\frac{1}{\omega} = \sqrt{\frac{2}{a}} = \sqrt{\frac{2\rho_0 J}{\gamma}} \tag{5.102}$$

Using approximations for long-short-wave resonance is valid if

$$\lambda_{us}^{*} / \lambda_s = O(\eta) \quad , \qquad \eta << 1 \tag{5.103}$$

where λ_s is the length of acting seismic waves and

$$\lambda_s >> \delta^{1/2} / c_1 \tag{5.104}$$

It is also suggested that $c_2 > c_1$ - that is, ultrasound velocity must be larger than the velocity of seismic wave (see Table 5.3). (This is essential for proper interpretation of laboratory velocity measurements based on ultrasound technique.)

5.4.4. SEISMIC - ULTRASOUND ENERGY FLUX

Seismic energy transfer has the following form, which is standard for wave motion

$$q_{es} = \frac{1}{2} c_1^2 \omega_s \chi_s \rho u^2 \tag{5.105}$$

and the ultrasound energy transfer is analogous

$$q_{eu} = \frac{1}{2} c_2^2 \omega_{us} \chi_{us} \rho J \Phi^2 \tag{5.106}$$

Seismic deformation (5.91) can be expressed as

$$V = \frac{du}{d\xi} = \chi_s u \tag{5.107}$$

and

$$\Phi^2 = \eta^{2q}|A|^2 \tag{5.108}$$

At the approximate resonance condition (5.97), the seismic energy flux is

$$q_{es} \approx \frac{1}{2}\eta^2 \rho c_1^3 V^2 \tag{5.109}$$

and the ultrasound energy flux is

$$q_{eu} \approx \frac{1}{2}\rho J \omega_0^2 \frac{c_1 c_2^2}{c_2^2 - c_1^2}\frac{\eta^3}{\beta}|A|^2 \tag{5.110}$$

Their ratio permits the estimate of the energy-exchange coefficient between the two wave modes.

5.4.5. SEISMIC NOISE OF ROCK CREEP

Due to the microstructure of rocks, the mechanical energy of slow rock creep can be transformed into seismic noise. For a mathematical study of this phenomenon, it is necessary to use Cosserat mechanics with the assumption that macromotion is viscous.

Let us begin by formulating the moment of momentum balance in following linear form [51]:

$$\rho_0 J \frac{\partial^2 \Phi_i}{\partial t^2} - \left(A_1 + \frac{1}{6}A_2 - \frac{1}{2}A_3\right)\frac{\partial^2 \Phi}{\partial x_k \partial x_k} -$$

$$-\frac{1}{2}(A_2 + A_3)\frac{\partial^2 \Phi_i}{\partial x_k^2} + 2B\left(2\frac{\partial \Phi_i}{\partial t} - \varepsilon_{ijk}\frac{\partial v_j}{\partial x_k}\right) + \tag{5.111}$$

$$+ \gamma\left(\Phi_i - \frac{1}{2}\varepsilon_{ijk}\frac{\partial u_k}{\partial x_j}\right) = 0$$

where the couple-stresses (1.22) are characterized by the elastic coefficients, A_i. The last two interaction terms correspond to the viscous body source (with coefficient B) and to the elastic body response (coefficient γ) of mean macromotion [41, 42].

The elastic microstructure potential must be written as

$$W = W^0 + \frac{1}{2} A_1 \frac{\partial \Phi_i}{\partial x_i} \frac{\partial \Phi_i}{\partial x_i} + \frac{1}{2} A_2 \left(\frac{\partial \Phi_i}{\partial x_j} \right)^s \left(\frac{\partial \Phi_i}{\partial x_j} \right)^s + \frac{1}{2} A_3 \left(\frac{\partial \Phi_i}{\partial x_j} \right)^a \left(\frac{\partial \Phi_i}{\partial x_j} \right)^a \quad (5.112)$$

where

$$W_0 = \frac{\gamma}{2} \Phi_i^* \Phi_i^* = \frac{1}{2} \gamma \left(\Phi_i - \frac{1}{2} \varepsilon_{ijk} \frac{\partial u_k}{\partial x_j} \right)^2 \quad (5.113)$$

is the elastic interaction potential that can deviate from the quadratic form if γ is itself a function of acting variables.

According to (5.111), even the simplest one-dimensional S-wave includes rotation effects. Assuming that

$$v_i = v(x,t)\delta_{i2}, \quad u_i = u(x,t)\delta_{i2}, \quad \Phi_i = \Phi(x,t)\delta_{i3}, \quad x = x_1 \quad (5.114)$$

the resulting equation has the form

$$\left(\frac{\partial^2 \Phi}{\partial t^2} - \frac{A}{\rho_0 J} \frac{\partial^2 \Phi}{\partial x^2} \right) + 4 \frac{B}{\rho_0 J} \frac{\partial \Phi}{\partial t} + \frac{1}{\rho_0 J} \frac{\partial W_0}{\partial \Phi} = F \quad (5.115)$$

$$A = \frac{1}{2}(A_1 + A_2) \quad , \qquad F = \frac{\gamma}{4} \varepsilon_{ijk} \frac{\partial u_k}{\partial x_j} + 2B \varepsilon_{ijk} \frac{\partial v_k}{\partial x_j} \quad (5.116)$$

This equation includes the wave operator, dissipation term and relaxing body source, F, given by mean dynamics of rocks and describes the dynamic processes in granulated and fragmented rocks.

Consider the situation [52] when mean shear rate field is stationary and

$$\frac{\partial v_2}{\partial x_1} \equiv F(x) \quad (5.117)$$

Then, equation (5.116) can be transformed to

$$\rho_0 J \frac{\partial^2 \Phi'}{\partial t^2} + 4B \frac{\partial \Phi'}{\partial t} + Shr\, \Phi' = 0 \quad (5.122)$$

for small perturbations $\Phi' = \Phi - \Phi_0(x)$. Here, $\Phi_0(x)$ is the stationary solution, the Shroedinger operator is

$$Shr = -A\frac{\partial^2}{\partial x^2} + V(x) \tag{5.123}$$

and

$$V = \left.\frac{\partial^2 W^0}{\partial \Phi^2}\right|_{\Phi_0} = \gamma \Phi'(\Phi' - \alpha)^2 \tag{5.124}$$

It is possible to show that in the vicinity of $\Phi' = \alpha/2$, the solution (5.122) is unstable [52]. The numerical procedure was developed for the following stationary field:

$$\Phi_0(x) = a(L - x)\frac{x}{4L} \tag{5.125}$$

The nonstationary Φ' solution with spectra, presented in Figure 5.19, reveals the features of the compact Hausdorf attractor for equations (5.122) through (5.124). These spectra indicate that a source of energy such as mean creep flow can generate seismic noise observable in situ. Maximum amplitude changes together with block sizes, $\sqrt{J} \approx d$, and creep flow, L.

TABLE 5.4. Data of numerical simulation of creep noise

Parameters	Dimension	Variant 1	Variant 2	Variant 3
L, creep flow scale	m	1	10	10^3
J, specific inertia moment	kg/m	10^{-10}	10^{-8}	10^{-4}
$J/(4B)$, time of relaxation	sec	10^{-4}	10^{-3}	10
A, rotation modulus	$kg/(ms^2)$	10^{-1}	10	10^9
a, angle	rad	10^{-2}	10^2	10^{-2}
$\sqrt{J}$, internal scale	m	3×10^{-7}	1.7×10^{-6}	1.7
$\sqrt{J/L^2}$, relative scale	-	3×10^{-7}	1.7×10^{-7}	1.7×10^{-3}

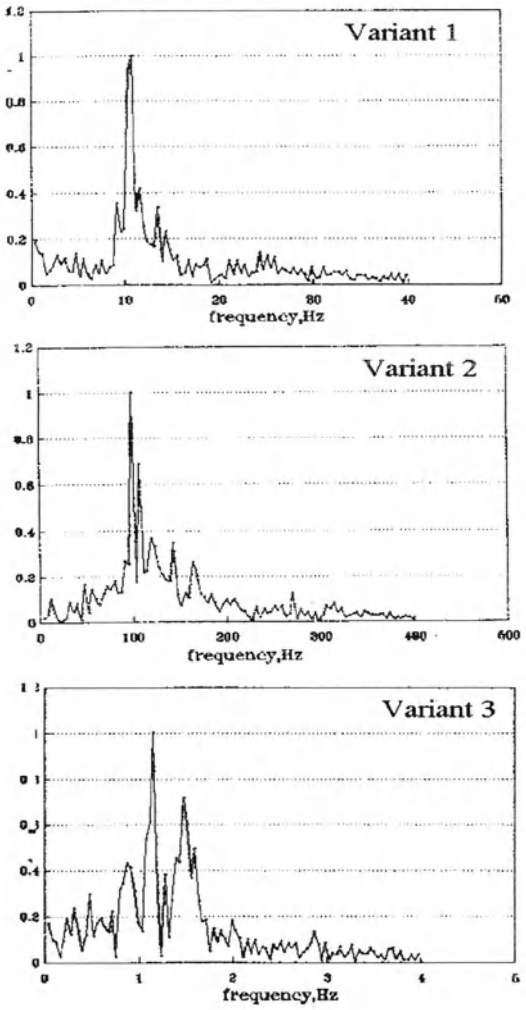

Figure 5.20. Calculated reduced spectra of seismic noise generated by creep flow due to geomaterial microstructure (Table 5.4) with $\alpha = 10^{-2}$ *rad* [52].

5.5. Vibro-action at geomasses and reservoirs

5.5.1. DOMINANT FREQUENCY EVIDENCE

Vibration of rock and soil masses can be created by heavy surface vibrators, by traffic, by explosions and by many natural sources, such as volcano, earthquakes, storms, tides, etc. Vibration can influence many processes because it leads to loss of stability (of slopes, for example), to acceleration of such dynamic processes as rock creep. Vibration can generate seismic noise, which is essential if the shear wave acts as an initial disturbance. The important feature, however, is the role of special frequencies, and it is connected, of course, with resonance effects [151].

The first source of resonance is the natural rock stratification which amplifies the frequencies:

$$\omega_r = \frac{c_s}{4H} \tag{5.126}$$

where c_s is the shear wave velocity, and H is the layer thickness. This frequency appears due to multiple reflection of the wave at the layer boundaries.

Another resonance source, according to the theory in Sections 5.3 and 5.4, is connected with the microstructure of soils and of fragmented rocks. The corresponding oscillations were studied during special experiments performed at a sandy beach of the Riga bay [224]. Marine sand was standard one, with a mean grain diameter of approximately *0.4 mm* but with different levels of water saturation.

The first experiment was done with ultrasound pulses ($\approx$ *20 kHz*) which were dampened after a distance of *10 cm* into the dry sand. For comparison, in rocks, such pulses attenuate totally after 1 m. If the medium was not fully saturated with water, the second type of P-wave appeared, which could be discriminated not only by a lower wave velocity than ultrasound but also by the typical spectrum with peak amplitude at *25 Hz*. It approximately corresponded to the acoustic emission spectrum of the same sand under any weak mechanical disturbance. The peak frequency mentioned above can be treated as a dominant one and evaluated as a ratio of displacement velocity, v,

$$\omega = v/u \tag{5.127}$$

to displacement, u, itself or by the expression

$$\omega = v/l \tag{5.128}$$

where l is a length size of the effective internal oscillator. The measurements had shown that

$$l \approx 10d \tag{5.129}$$

where d is grain or rock fragment diameter [224].

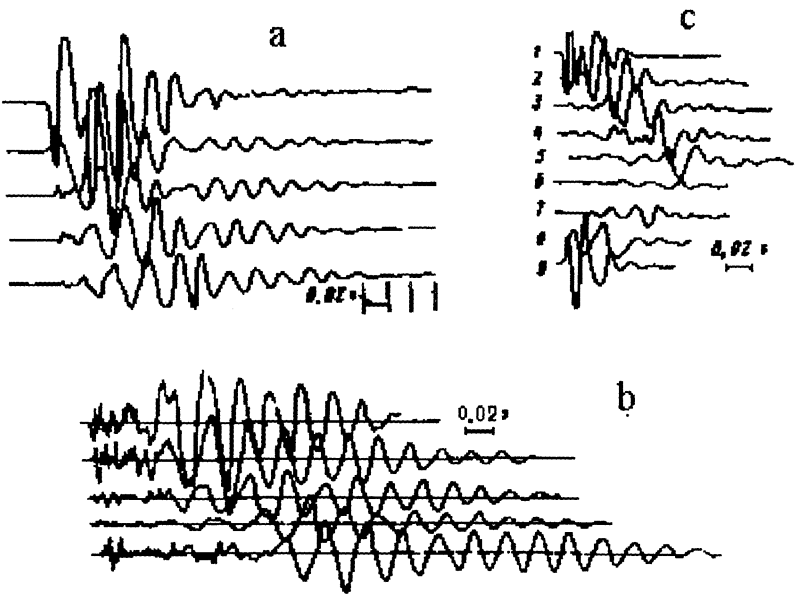

Figure 5.21. Oscillation recording: (a) -heavy body's fall from height $h = 1$ *m*; (b) - explosion, wetness 26 %, sand layer thickness $H = 2$ *m*; (c) - the same, $h = 1$ *m*, $H = 15$ *m*, wetness 20 % (The distance between gages is *2 m*.) [224].

The second experiment was performed with small charges (*20* grams of TNT explosive) with the wave field been measured by gauges situated along a radius at *4 m* intervals. For the third experiment, waves were generated by dropping a heavy body on the sand surface from the height *1* or *2 m*. As seen in Figure 5.21, the first wave always had much higher frequencies depending on the seismic source type. The second wave had much lower frequencies which changed and, after some distance, converted to the dominant value of *25 Hz*. If the thickness H = *2* m is close to resonance thickness at the same frequency, *25 Hz*, then the wave tail with these oscillations is longer.

In the near vicinity of the source, the existence of the first wave can be identified as an ultrasound effect because the grains of sand have extremely low levels of displacements due to very short duration and to the threshold role of solid friction or water-film viscosity. Therefore, both types of waves observed in wet sands can be interpreted to be the first and second modes of P-waves, respectively, with theoretical wave velocities of *460 m/s* and *210 m/s* (Sections 1.3 and 5.2). It is necessary to mention that these two

modes also create two observable types of surface waves where P-waves appear in combination with S-waves, see [65].

All spectra observed in the field had an ultrasound component even at far distances, where the main wave energy corresponds to the dominant *25 Hz* frequency. This was explained by the generation of high frequencies due to asperity at grain contacts or to relative grain motion (rotation) under long wave-short wave resonance conditions (Section 5.4).

Summarizing these experimental results, fragmented geomaterials act as nonlinear transformers of seismic waves. Changes of the seismic spectra of earthquake sources were noticed after observing, via geophones, waves crossing the fault body in the Cajon-pass well [1]. This property was also mentioned in many geophysical explorations in the form of rules for obtaining definite frequencies by the same charge (about *1 kg* of TNT) imbedded in a sand for *25 Hz*, in a clay for *40 Hz*, in gravel for *10 Hz*, and in eroded granite for *100 Hz* frequency.

5.5.2. WAVE RESPONSE OF RESERVOIRS

It was also discovered that the amplitude of seam reaction depends on the frequency of the external source and reaction maximum corresponds to some dominant frequency. Their observed values were *6, 8* or *12 Hz* for oil water-flooded seams at which the pore pressure, gas release and even water-oil production ratio had a maximum response.

Studies of earthquake influence on oil wells at distances of 70-200 km from epicenters have shown that an earthquake swarm can increase the oil-water ratio of their production if this ratio was very small initially or can diminish its value if the oil phase was in preference by volume (Figure 5.22). Of course, there are some intermediate observations, but this conclusion gives a proper idealization of the phenomenon which can also be seen during vibration tests.

Consider the vibration technology of gas-oil recovery. It was mentioned earlier that oscillations could increase gas passage in a seam. In some laboratory experiments, changes of absolute permeability were also observed at vibrations, but the effect was not essential. Displacements of oil drops in water-saturated porous media were also studied in laboratories under simultaneous gravitation and vibration action. Such studies were performed in accordance with the idea that the vibrations could accelerate oil and gas separation in deleted reservoirs at the macroscale level. It was determined that high amplitudes of vibrations are needed for this.

The criterion of oil drop mobility in other fluid flows is the ratio of capillaries forces, $\sigma \cos\theta$, to a displacing force:

$$\frac{\rho\sigma\cos\theta}{\left(\gamma\sin\alpha+\partial p/\partial x+A\rho\omega^2\right)\Delta\rho}\le M_0\approx 0.3 \tag{5.130}$$

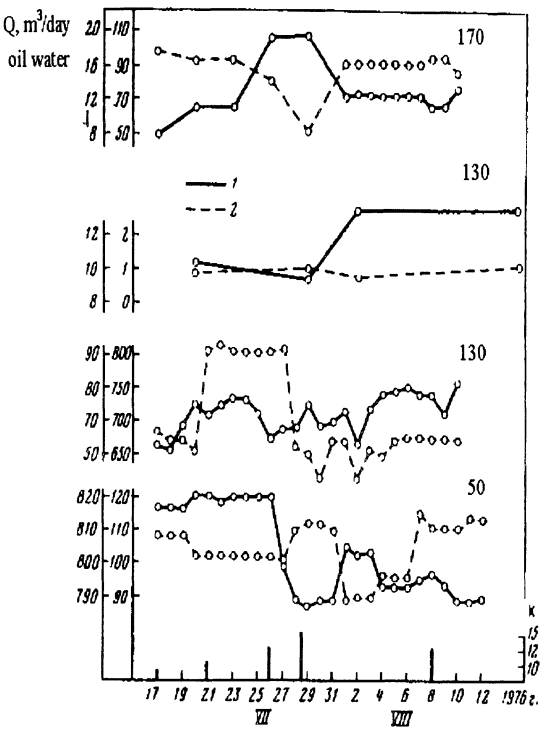

Figure 5.22. Dynamics of oil (solid lines) and water (broken lines) production during the earthquake swarm with energy class K at the Northern Caucasus (the city of Groznii); epicentral distances are given in *km* [165].

where $\Delta\rho$ is the density difference, $\gamma = \rho g$ is the specific weight; $\partial p/\partial x$ is the pressure gradient in (water) flow; A and ω are the amplitude and frequency of the wave, respectively; σ is the interface tension; and θ is the wetting angle. The critical number M_0 was found by experimental works [112].

On the other hand, the acoustic treatment of oil wells during standard logging had shown that it could increase oil production in some cases. During such an operation, the ultrasound frequencies were generated at the well bottom and the treatment evidently cleaned the neighborhood of the borehole, because the ultrasound cannot enter real soil or porous rocks further than the first meter.

Another variant of vibro-action at the oil-pay-zone of a stratum consists of putting a bell-type sound generator (which uses the energy of the fluid flow) through the well column. Of course, any mechanical or electrical generator of sound, acting at the well-bottom, is limited energetically by the well's internal volume.

5.5.3. RESIDUAL OIL VIBRORECOVERY

It is known that seismic waves created by heavy vibrators can be observed at very long distances. Therefore, vibrators moving at the ground surface above oil reservoirs were used. The results of the first field work performed at the "Abuzy" reservoir in the Krasnodar region at the North Caucasus follow. The reservoir has been developed since 1938 and was fully water-flooded when the experiments were conducted. The seismovibrator CB-20/60 was used. It had an active weight equal to *20 tons*. The depth was equal to *1400 m*, and the productive layer was represented by sandstone. Productivity of wells N 56 and N 32 equal *2* to *3* tons/day; the wells had extremely low oil/water ratios. Vibrations were continuous for *20 min* per every hour, the operation took place for *15-20* hours of each day, and total the duration field work was *37* days. The oil/water ratio increased and was stable for *17* days after operation (Table 5.5).

TABLE 5.5. Oil-water ratio changes during a field vibration test [188].

Well number	Interval of perforation, (m)	Oil-Water Ratio before vibration (%)	Oil-Water Ratio during vibration (%)	ω, (Hz)	Distance from vibrator, (m)
33	*1471-1496*	*3.2*	*6.7-8.0*	*12*	*1000*
56	*1259-1452*	*7.3*	*12.5-17.8*	*12*	*100*

It was found that the frequency of *12 Hz* was optimal for positive change of the above-mentioned ratio. This fact was also supported by measurement of rock mass microseismicity, including the reservoir (Figure 5.23). Their amplitude grows *20* minutes after vibration began.

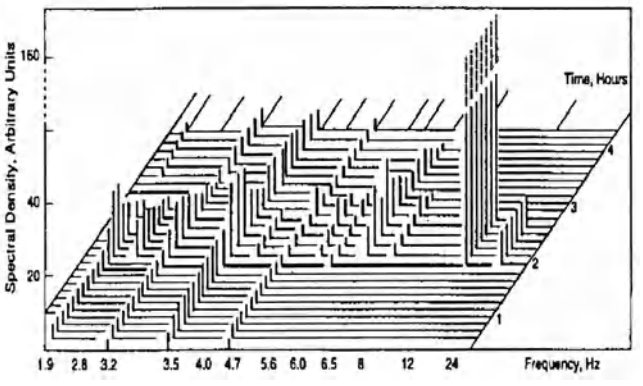

Figure 5.23. Dynamic seismicity or reservoir strata due to vibrator work at *12 Hz* frequency [19].

Even the chemical content of released hydrocarbon gases changed. Methane content definitely increased in the well annular space. Head growth was noted, but it did not exceed a meter, although its maximum increment also corresponds to the same frequency. It was mentioned that, at other reservoirs, the dominant frequency was different (*6 Hz, 18 Hz*). However, the temporal oil/water ratio diminishes in the case of the initial small percentage of water (the reservoir "Zybza") [188]. When some geophysical tools were taken out from the observation wells after vibro-operation, they were intensively covered by oil films (mentioned by V. V. Kuznetzov). This means that even the so-called "connected" oil out of the reservoir became movable under vibration.

The positive result achieved in the case of a water-flooded reservoir indicates that new technology was found to solve the residual oil problem. The most essential point of this approach is the following. The vibro-action was performed during the intense pumping of water from the reservoir. This is the pressure-gradient effect in the criterion (5.130). So, vibrations can disturb the existed water-oil flow inside formations at the microlevel.

5.5.4. PHASE PERMEABILITY OF OSCILLATING POROUS SPACE

It is well-known that two-phase filter flow is governed by the generalized Darcy law (3.78), including the relative permeability concept of the oil and water phases. If the permeability for oil is equal to zero, this part of oil is residual, and can be distributed over pore space in the form of isolated drops or films, although it can be moved slightly by intense water flow. It can be accounted for by the generalization (3.80) according to Onsager's rule [152]. Under standard quasistatic conditions for which Onsager's rule is valid, the total transfer ot this oil is so small that the residual oil flux is usually assumed to be negligible and the threshold saturation θ_* exists. That is, if oil saturation $\theta \le \theta_*$, then there is almost no oil flux and only water can reach the production wells.

However, the relative permeability curves given in Figure 3.13 are measured for stationary phase states inside porous rocks during testing. The possible deviations are connected with separate drop mobility (5.130) in other phase flows.

The above-mentioned drastic change of the oil-water production ratio means that oil drops are possibly moving in water flows under vibration conditions. This could happen only if the oil permeability at $\theta \le \theta_*$ is nonzero due to the process of drop merging into "streams" (Figure 5.24) or due to the appearance of drop sizes smaller than the pore channel radius. The latter effect transforms the oil-water mixture into a state of fine micro-emulsion [92,207].

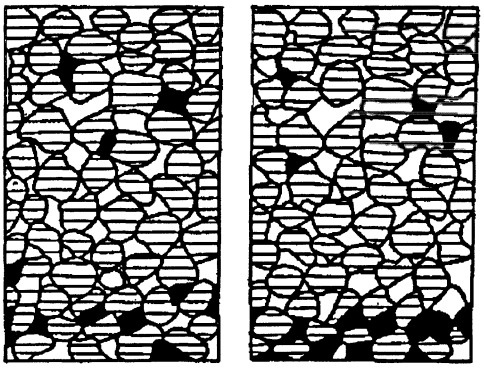

Figure 5.24. Clasterization of oil drops during vibration ($a \rightarrow b$) in water flows [151].

Another scenario is connected with gas release in the form of very small bubbles which can move with the water flow, or even faster. The corresponding hydrodynamic scheme is described in Section 3.3 and is based on the concept of a common filter flow in which saturation plays the role of volume concentration. As the formulae (3.103) shows, gas bubbles can diminish heads which are necessary for well productivity and provides an explanation for the unusual form of well's productivity curves at the moment when the dissolved gas just begins to be released from oil in the formation (Figure 3.18).

Although changes in total well productivity are not very essential, because they depend on pumping intensity that depends on conventional conditions of the field works, the gas-release effect plays a positive role. This effect can also be stimulated by simultaneous gas injection into the reservoir.

Transformation of the oil-gas mixture into the micro-emulsion state can be described by equation system, (4.34) through (4.36), if the emulgation kinetics, instead of desorption terms, are introduced.

It is necessary to underline that residual oil mobility can be realized in water-flooded reservoirs only under the action of ultrasound waves with lengths of the same order as an oil drop or a pore channel or less. According to Section 5.4 and the experiments mentioned above with marine sands, seismovibration can indeed ultrasound oscillations inside a porous stratum. The corresponding theoretical analysis is given in Section 5.4.

5.5.5. UTILIZATION OF RESONANCE EFFECTS

Heavy vibrators radiate mainly the surface seismic waves; therefore, probably less than one-tenth of the seismic energy can reach the reservoir. Because there are some optimal frequencies that can influence the well productivity more effectively, suppose that, in accordance with field experiments, the dominant frequency (Section 5.3) is created by the rock microstructure and stratification. This process is described by equation (5.47)

or by its more complicated variant. Its essential feature is that the bigger the coefficient N of nonlinearity, the quicker the transition of seismic energy to dominant frequency. Moreover, the dominant frequency must be created by the vibration itself, because the wave can leave the seam before effective dominant spectrum is reached.

The motivation of equation (5.47) is connected with possibility of matrix grains of porous or fragmented rocks having their own motion. As was shown in Section 5.2, length scales (5.43) of the geostratum structure were accounted for by equation (5.47).

It is necessary to note that at the "Abuzy" reservoir the dominant frequency generated by stratification gives a realistic value of layer thickness ($H = 30\ m$) if shear wave velocity $c_s = 1500\ m/s$ and the dominant frequency is $12\ Hz$. The value of $H = 30\ m$ is close to the formation thickness, but it needs too much wave energy for any essential effect. However, it was observed experimentally that wave oscillation takes place for a longer time if the microstructure and stratification resonance frequencies coincide (Figure 5.21). So, the problem of resonance response of stratified rock masses must be studied carefully.

Ultrasound, which is necessary for reorganization of the microstate of oil-water flow, is created continuously by seismic waves during their propagation in porous or fractured geomaterial. This was shown experimentally in sands [224], where seismic waves were accompanied by ultrasound. Really, sand deformations is impossible without the relative motion of particles in contact and every solid friction contact is radiating ultrasound.

As one can see in Figure 5.25, the relative sinking velocity of a light body in sand is higher under vibro-action at the same dominant frequency $\omega_d = 25\ Hz$. One can conclude that sand possesses a special vibroviscous rheology.

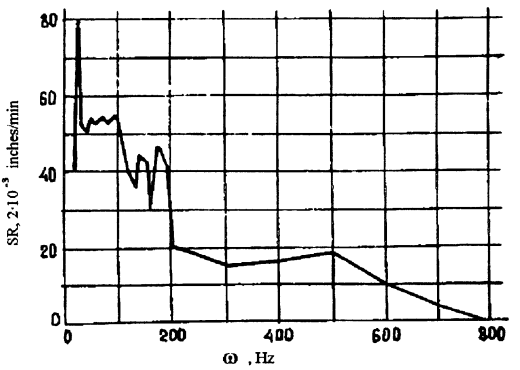

Figure 5.25. Sinking velocity of a body at the surface of marine sand at different vibration frequencies [78].

As it was shown in Section 5.4, the simplest mathematical model of this phenomenon utilizes the idea of particle rotation kinematically independent of the mean motion. Thus, we can use the model of grade-consistent micropolar continuum [30] but keep the

nonlinear terms. There are many possibilities of micromotion generation and many corresponding nonlinear effects that can be studied.

Another scenario can be imaged as a combination of rock creep under vibro-action (vibrocreep) and radiation of ultrasound by creeping masses (Section 5.4). The elastic initial energy, or filter-flow energy, created by conventional fluid production from the reservoir can be also additional energy sources for vibrations disturbing the water-oil distribution in pore space and for violation of the zero oil-permeability threshold.

In practice, the main unsolved problem is the optimal transfer of wave energy to the reservoir. However, the above mentioned technology gives a definite increase of the oil/water ratio in shallow water-flooded reservoirs where seismic energy can be transported. It gives a new chance to many old regions of the petroleum industry.

5.5.6. LABORATORY TESTING AND EVALUATION OF OIL VIBRO-WORKS

According to criterion (5.130), the oil mobility can be reached by adding of vibro-acceleration force to existing water flows in the pay zone and by increasing of the density difference.

The first step was a verification of the mobility criterion by the special two-dimensional model. The model consists of two plexiglas sheets between which one layer of glass balls was situated. Under action of longitudinal and lateral oscillations the ball packing was changing. As the result, a number of fragments with more dense hexagonal structure appeared. So, the natural state of fractured-porous geomaterials was modeled. The averaged porosity m was high and equal 0.6. The permeability k was $3.7\ (10^{-10}\ m^2)$. The cumulative acceleration was created by the vibrotable up to $16\ g$. The frequencies were selected in order to get stable oscillations with constant amplitudes and simultaneously to avoid ball displacements under vibrations. (This happened at frequencies higher than $40\ Hz$ because the vibroforce has become more than friction forces as during a liquefaction).

The oscillations had the stable amplitude $A = 0.45\ mm$ if their frequencies belonged to the interval $15 - 40\ Hz$. Some amount of water was injected into the model via special hole. So, water lenses (drops) were created in the pore space saturated by air. They have the thickness $r = (4 - 5)$ mm and lengths $l < 33$ mm. The results of experiments are given in Table 5.5 for drop recorded motion.

TABLE 5.5. Critical liquid drop sizes and frequencies.

l , mm	22	21	20	19	18	17
ω , Hz	16	18	18	19	20	22

It is known that minimal size l of water lens which begins to move under action of gravity in the glass ball packing is equal to $33\ mm$. It opens the possibility to find the constant in the consequence of criterion (5.130)

$$l\,(g + A\omega\omega) = const\ t \qquad (5.131)$$

which is valid if all other parameters are not changed. For checking of its validity the amplitude of oscillations was changed to $A = 3\ mm$. Then the lens with $l = 17\ mm$ began to move at the frequency $27\ Hz$.

There is no possibility to get so high acceleration in situ as it was reached in laboratory conditions with help of the vibrotable. Because of extremely low real amplitudes of waves, that can be generated in strata by ordinary technical sources, the effect is expectable if waves of ultrasound frequencies are used. For example, in the case of $2\ KHz$ frequency the critical amplitude of mobility of heterogeneous fluid inclusions can be deminished by $10{,}000$ times. Moreover, only if ultrasound wave length has the same order as a diameter of a solid grain of porous matrix of the pay zone or less, residual oil drop (or film) will move.

We have discussed the possibility to create ultrasound by seismic waves propagating in rocks. The energy exchange coefficient K is the ratio of energy fluxes (5.109) and (5.108) and can be estimated as 0.001 or less. Because of hierarhial structure of dissipation, the ultrasound energy is supposed to transfer further to heat - that is, to the molecular chaos. It can be accounted by introduction of ordinary viscous terms into the momentum balances.

It was found that there is a dominant frequency for any pay zone, and it could include the microstructure visco-elastic resonance as well as stratification one. This preferable working frequency exists and it has to be found in situ by observing of reservoir response to vibroloading.

This was the first important position of technology proposed by the author's certificate [*USSR No 1549301, Cl. E21 B43/00, 1986. Bull. # 36, SU 1596081 A1*] and the second one was the vibroloading simultaneously with intensive water pumping from flooded reservoir or its flooded parts. It means utilization of $grad\ p$ - effect in criterion (5. 130) for stimulation of residual oil recovery.

[Remember, that vibration at a fresh oil reservoir can generate mobility of water masses and diminish oil recovery from the very beginning].

5.5.7. ROLE OF DEEP ACOUSTIC NOISE.

The dominant frequency effect can create intense seismic noise of the pay zone or it can increase (or be accompanied by) this natural phenomenon. Special measurements were performed to study the acoustical noise level during vibroworks at water-flooded reservoirs Changyr-Tash (in Kirgizstan) and Zhirnovskoe (close to Volga-river).

Reservoir Changyr-Tash is situated Fergana valley at the depth $410\text{-}570\ m$ beneath loose sediments, gravel conglomerate ($100\ m$ thickness) and clay layer. The oil - bearing sandstone has a permeability k up to 30 millidarcy, porosity $10\ -\ 23\ \%$, total thickness $25\ m$, effective one $5.7\text{-}6.4\ m$. Oil density was $0.8769\ g/cub.cm$ at the surface

conditions, dynamical viscosity *35* centipoise. The reservoir was exploited from 1938. The work was performed at the area Tekebel, including 6 productive wells from October 5 till October 20, 1988 and in December 1988. Here the pay zone has a thickness *18-25 m* at the depth *240-448 m* with *35* degree of inclination.

Initially the well *149* had *60%* of water and total fluid production was equal to *2 - 3 ton* per day. Vibro-action was done by two electromagnetic hammers situated at *20 m* from each other and at the *200 m* distance from this well at the ground that had *25 m* altitude less. The hammers created *55* stress pulses per minute with *50 ms* duration at the piles which were embedded into the ground.. So, the working frequency was *20 Hz*. The mean well fluid production increase was equal to *36%* of its initial value and its water percentage became less by *13 %*.

It was found that the acoustic noise level was increased in the oil-bearing interval *(302 - 310 m)* due to vibrations. Its definite constancy after vibration means that there is some limit for the noise intensity.

The reservoir Zhirnovskoe is being exploited from 1949 - 1951. Its structure is an anticline fold. Seismic waves were generated in such a manner that to act at the seam B-1 represented by sands and sandstones as well as at two more seams above and beneath it.

The thickness of the layer B-1 is changing from *2.0* through *44.0 m*.The pay zone has thickness *2.0 - 39.0 m*. Its maximum corresponds to the structure center. Porosity is *18 - 35 %*. Permeability is *0.004 - 5.0 sq.micrometer* after core studies and *0.1 - 5.0* according to hydrodynamic studies in situ. Geophysical data correspond to *0.89* value of oil saturation. Gas dissolving pressure is close to the layer pore pressure and equal to *102* bars. Oil viscosity is *4.5* centipoise in the seam, that has *59.9 %* of total reserves. Its initial geological resource was *62,497 000 tons* of oil, oil recovery coefficient is estimated as *0.7*, but as *0.6* on 1.01.1992. Water flooding began in 1952.

During last years the balance of water injection and fluid production was kept sufficiently, so pore pressure was stabilized and equal to *96.6 - 98.5 bars*. Averaged water production was *92%* of total fluid production. Gas factor is diminishing and in 1991 it was *70 cub.m/ ton*.

Vibration was performed at the northern area *3.3 km* × *2.5 km* with *34* producing wells from 20 Oct. 1991 till 15 dec. 1991 through well waveguide in the well # *157*. Electromagnet hammer acted at its ground surface. Vibration changes were observed at *23* wells of the area of B-1 layer, at *3* wells of the lower layer and at *1* well of the upper one. After the first cycle of vibration high increase of oil production was observed and sharp decrease of water presence. Maximum effect was recorded in February 1992. Averaged increase of oil production at the area of testing was *54 %* with decrease of water percentage by *6.0 %*.

Acoustic noise was measured in the well # *186* at the distance *850 m* from vibrating well # *157*. Its increase was up to *30%*. Detailed information is published elsewhere [112].

CHAPTER 6

STRUCTURE AND RHEOLOGY OF THE LITHOSPHERE

6.1. Strength of geomaterials at depth

6.1.1. STANDARD TESTING OF ROCKS

The main source of rock strength data [93, 166] is triaxial tests fulfilled under high confining pressure and high temperature. The continuous measurements of loads and deformation have led to the discovery of the rheological laws of geomaterials [160]. In Section 1.3, the basic mathematical model of deformation of dilating rocks is given. The detailed description of the hardening and softening processes is necessary for an adequate computer simulation. However, competing processes (for example, sliding along faults under the same high thermodynamic condition, rock creep, etc.) must also be examined. Moreover, additional information on the microstructure of deformed or failed geomaterial is necessary because any internal change results in such hydrological or geophysical properties as permeability, electroconductivity, etc.

Figure 6.1 shows a general representation of laboratory test data for a brittle-ductile rock rupture under pressure, p, and shear stress, $\sigma_\tau = (1/2)(\sigma_1 - \sigma_3)$. Quantitative data are given here for typical variants of the real temperature distribution in the lithosphere (geotherms) and for confining pressures determining boundaries of different finite destruction states (Figure 6.2).

The strength surface (that is, the peak bearing capacity of rock samples) and the elasticity limit are also shown in the same plane. They are the boundaries of the dilatancy zone, where microcracks and pores open [226]. This zone corresponds to prefracture states [27]. All these data were obtained for strain rates $De/Dt \approx 10^{-6} sec^{-1}$. As previously mentioned, the strength depends slightly on the deformation rates if the latter are lower than explosive rates (i.e., $10^{3} sec^{-1}$), and if the temperatures are not very high. Figure 6.3 shows that this conclusion is valid for the Earth's crustal temperatures. Changes of the strain rate (De/Dt) from $10^{-6} sec^{-1}$ to $10^{-3} sec^{-1}$ do not influence deformation curves when $T \leq 600°C$.

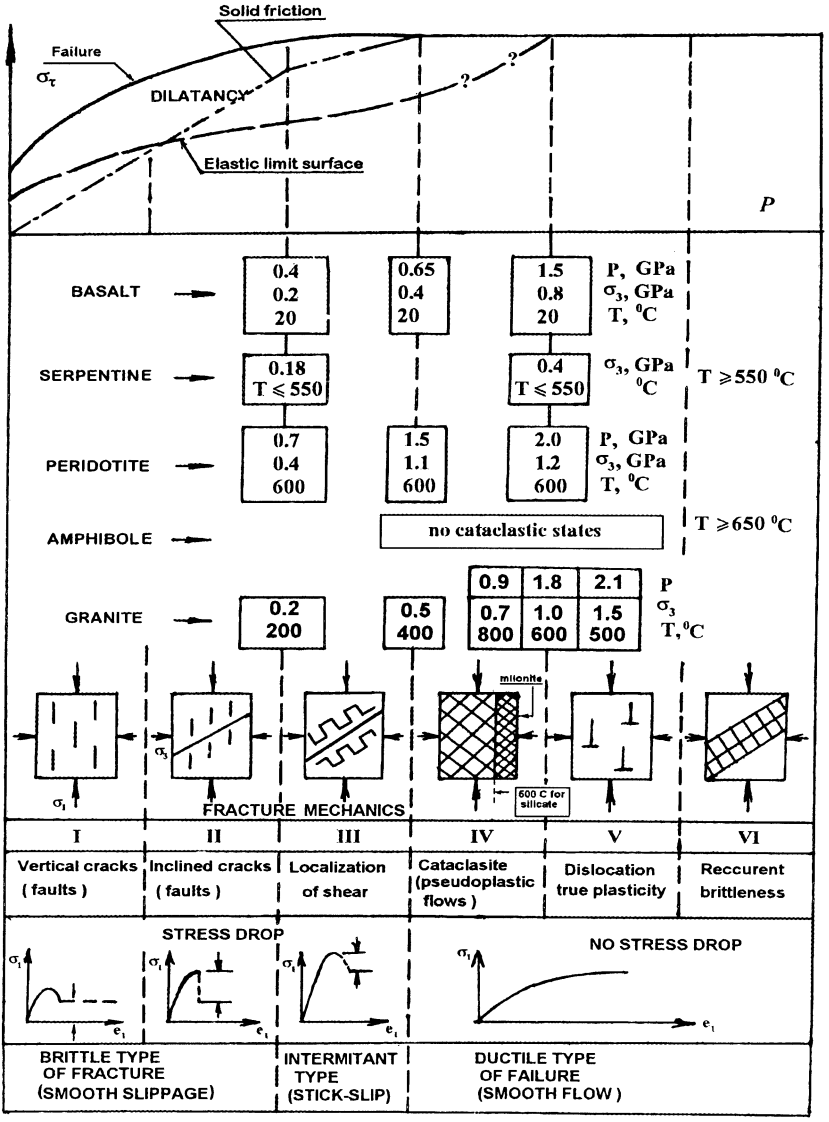

Figure 6.1. Generalized description of the brittle-ductile rupture of geomaterials at high thermodynamic conditions (further development of [152]).

6.1.2. INTERVAL CLASSIFICATION OF FINITE RUPTURE

According to [146] and to the classification given in Figure 6.1, when confining pressure, $p = -\sigma_3$ is low, the rock sample is fractured by a vertical macrocrack, and the fault in a rock stratum must be vertical (Interval *I*). This mechanism can be considered as splitting. As the confining pressure grows, the rupture macrocrack becomes inclined in the sample because the crack walls touch each other (Interval *II*) and solid friction begins to act. Due to the Coulomb law (1.77) and Section 1.3.5, the fault inclination to the main compression axis is minimal.

Solid friction forces, acting between fault edges, are determined by the Byerlee line with coefficients weakly dependent on temperature [34]:

$$\tau = 0.85p, \quad p \le 200MPa \quad ; \quad \tau = 60 \div 0.6p, \quad 200 \le p \le 1700MPa \qquad (6.1)$$

You can see that this line is broken at the transition point from sliding regime *II* to the stick-slip interval, *III*. In other words, the kink in the Byerlee line corresponds to the transformation of the macrocrack into a shear band because the solid friction is beginning to be of the same order as the strength of intact crack edges here. The cohesion ($chs \approx 60\ MPa$) is typical for asperity strength (or for edge crushing).

The competition of slippage along the fault with wall destruction determines the stick-slip phenomenon. Such an interpretation allows identification of the corresponding thermodynamic interval (*III*) with the dilatancy zone of the Earth's crust. In reality, rules of dilatant deformation for geomaterial masses are true for the case when friction resistance inside a fault and intact rock strength are of the same order. As the result, faults transform into the slip-band structure here. The effective bearing capacity of a fractured stratum is determined mainly by surface friction angle, which is lower than the internal friction angle of geomasses in initial states. That is why the residual strength of fragmented rock masses is assumed to be equal to the Byerlee evaluations (6.1).

Further growth of the confining pressure and of temperature with depth results in limiting rock strength and its independence on pressure, but fault friction resistance grows with pressure. The latter can even grow with pressure increase. Here, the rupture of a rock sample (or geomass) occurs due to the appearance of a network of small fractures, fragmenting it into many pieces (Interval *IV*). Then the residual strength equals a flow resistance of the already crashed material. In reality, it appears to be even lower due to the additional effects of particle rotation (see Section 1.4). Such a material flow is also known as being superplastic. The creep law can be found empirically for such a flow. In geology, the corresponding fragmented state is called cataclastic.

Rock cataclastic creep is intensified due to fluid migration [68], solution under pressure [187], corrosion plasticity [150], etc. Therefore, it cannot be described by the traditional rules (6.11) valid for intact rock creep; another point of view is given in [127, 173].

Within the interval of cataclastic states there is a boundary beyond which the flow of finer fragmented material corresponds to smaller shear resistance. That is why the transition from cataclasites (Subinterval IV^{*}) into milonites (Subinterval IV^{**}) occurs.

The transition from cataclastic (milonitic) states to true plasticity is represented by data obtained for granites [221]. The interval V of true plasticity corresponds to dislocation flow in crystalline lattice of minerals. Isolated cracks can appear only within some isolated mineral grains. So, rocks appear to be impermeable in this state, and we can believe that the rock masses can be permeable only where dilatant cracks exist.

6.1.3. DUCTILE (CATACLASTIC) FAILURE - SEMIBRITTLE RESPONSE

Consider, now, changes of loads admissible for fracturing rocks. For this, a testing machine can be used. At the moment of sample fracture, the machine feels a stress drop if there is no special reverse regulation system. This stress drop corresponds to the difference of peak bearing capacity and residual strength of the sample. This is the main feature of brittle type of macrorupture when there is practically no slippage resistance along the macrocrack.

On the contrary, the ductile response of a rock sample is characterized by the total absence of stress drop when failure has a form of unlimited flow. The ductile behavior has no relaxation time of its own, and it is controlled by boundary conditions only. You can see that the peak-strength state is described by the Coulomb surface up to the level of crystalline plasticity, where it becomes totally independent of pressure (Figure 6.1).

The intermittent interval of pressure and temperature which corresponds to a transition from brittle to ductile rupture, coincides with the stick-slip zone, where slippage with "flow-like" resistance and slight hardening appears instead of sudden stress drops.

According to W. Brace [25], the stick-slip zone is limited by the semi-closed boundary shown in Figure 6.2. The other plotted curve corresponds to the transition from microbrittle (cataclastic) rupture to intracrystalline plasticity [147]. Of course, these boundaries depend upon rock type. The data given in Figure 6.2 are based on granite testing. In Figure 6.1, the data for other geological materials (that is, for serpentines, basalts, amphiboles and peridotites) are given also. You can see the drastic differences between their characteristic parameters. These important geological sequences are discussed further in Sections 6.2, 6.3.

The transition from the brittle behavior of serpentines to ductile (cataclastic) behavior takes place at pressure $p \approx 0{,}2\ GPa$, independent of temperatures [165]. However, above $T^{*} = 500 - 600^{\circ}C$, these rocks are unstable and their failure again has brittle features. Serpentines, are products of the chemical reaction of water with olivines - that is, with main part of peridotites. At temperatures above T^{*}, the crystalline water becomes free, rupturing the serpentine microstructure. The same features were found

for granites at temperatures $\approx 900^{\circ}C$, where intercrystalline water also becomes free and diminishes rigidity drastically [222]. Amphiboles become unstable also at $T \geq 650^{\circ}C$, when chemically connected water is released and rock failure has definite cataclastic features [85].

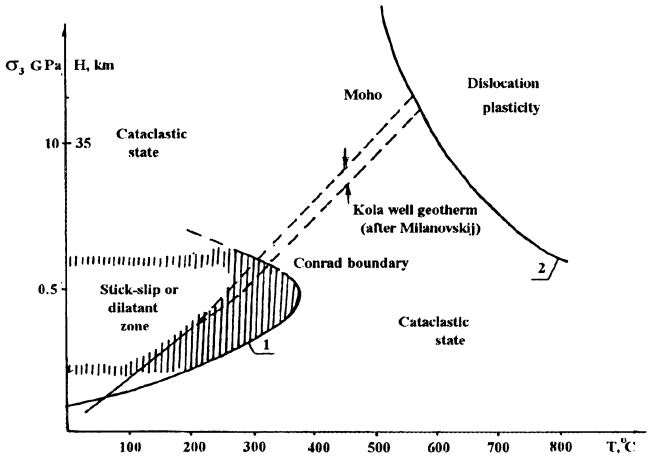

Figure 6.2. Characteristic domains of the Earth's crustal rupture under the assumption of coincidence of stick-slip and dilatancy intervals [133].

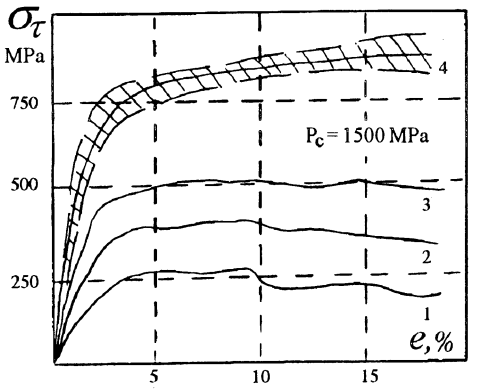

Figure 6.3. Shear strength of peridotite dependent on strain rate ($1 - de/dt = 10^{-6}\ 1/s$; $2 - 10^{-5}$; $3 - 10^{-4}$; $4 - 10^{-3}$) at $1000^{\circ}C$ but is independent at $600^{\circ}C$ (shadowed zone).

6.1.4. TEMPERATURE AND RATE EFFECTS

Peridotite strength is one-half times higher than the strength of granite; however, at temperatures $T \geq 1000^{\circ}$ (Figure 6.3), they show strain-rate features typical for creep behavior [99]. Such temperature effects must be studied carefully.

The relative measure the thermal fields is the so-called homologous temperature, T / T_m, where T_m is the melting temperature. So, the transition to true superplastic flow, where microstructure changes become connected with dislocation motion along individual mineral grain boundaries, takes place at $T / T_m \approx 0.45$. The steady creep of rocks is characteristic for $T / T_m \approx 0.6$, but it also depends on loading rate. Some typical loading times are given in Table 6.1.

TABLE 6.1. Geological loading times [98]

Cycling processes	Relaxation time	Frequencies, (*Hz*)
Acoustic emission	$\leq 10^{-3}$	$\geq 10^{3}$
Microseismisity shocks, small explosion	10^{-2} *sec*	10^{2}
Seismic waves of earthquake and intense explosion	*1 sec*	*1*
Catastrophic earthquake	*100 sec*	10^{-2}
Earth oscillation	$10^{3} \div 10^{4}$ *sec*	10^{-3}
Tides	7×10^{4} *sec*	2×10^{-5}
Geodetic observation	$0.5 - 10^{2}$ *years*	$10^{-6} - 10^{-8}$
Geomorphology	$10^{2} - 10^{6}$ *years*	—
Geology	$10^{6} - 10^{8}$ *years*	—

6.1.5 WATER-PRESENCE EFFECT

According to the Rebinder effect, brittle failure is very sensitive to water presence [190]. The Rebinder effect consists in diminishing the Griffith energy, γ, with wetness (Section 1.5). As a result, rock peak strength depends on water saturation, θ (Figure 6.4). It

means that θ plays the role of a softening parameter, in addition to the usual strain (or strain-work) parameter, χ, in the limit condition (1.77) - see (1.88):

$$\Phi_\sigma \equiv \sigma_\tau - \alpha(\chi,\theta)\sigma - Y(\chi,\theta) = 0 \tag{6.2}$$

$$d\Phi_{\sigma'} \equiv (\partial\Phi_\sigma / \partial\sigma)d\sigma + (\partial\Phi_\sigma / \partial\sigma_\tau)d\sigma_\tau + (\partial\Phi_\sigma / \partial\theta)d\theta \tag{6.3}$$

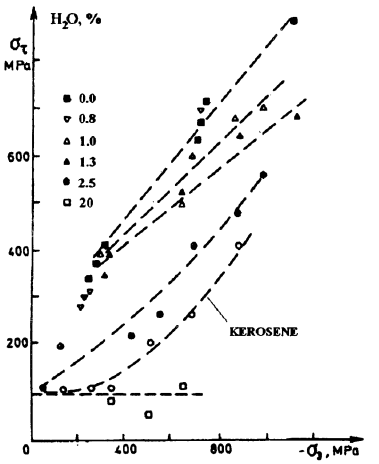

Figure 6.4. Dependence of granite shear strength on confining pressure and fluid presence; water percentage is shown (Courtesy of R.N.Schock, data recalculated).

Unloading takes place if $\Phi_\sigma < 0$. The conditions $\Phi_\sigma = 0$ and $d\Phi_\sigma = 0$ correspond to neutral loading. In both cases, the increment $d\lambda$ must be equal zero in the constitutive laws:

$$de_{ij}^p = \left(\sigma_{ij} + \frac{2}{3}\Lambda Y\,\delta_{ij} - \sigma\,\delta_{ij} - \frac{2}{3}\Lambda\alpha\sigma\,\delta_{ij}\right)d\lambda \tag{6.4}$$

The hardening process is determined by the conditions

$$\Phi_\sigma = 0, \quad d'\Phi > 0, \quad d\lambda > 0 \tag{6.5}$$

The continuous destruction of geomaterial is governed by

$$\Phi_\sigma = 0, \quad d'\Phi_\sigma < 0, \quad d\lambda > 0 \tag{6.6}$$

These constitutive equations can be interpreted on the fact of a corrosion-dilatancy model with time dependency controlled by the diffusion process [150]:

$$\frac{\partial \theta}{\partial t} + v_i \frac{\partial \theta}{\partial x_i} = \frac{\partial}{\partial x_i}\left\{ D_{ij}(\theta) \frac{\partial \theta}{\partial x_j} \right\} \tag{6.7}$$

It is possible to show that the deformation corrosion process with active moisture transfer can be unstable and, therefore, can accelerate tectonic rock-mass changes.

The moisture transfer (6.7) has its own characteristic time; hence, the entire process can be approximated by the special creep model for dilating geomaterials with the viscosity, $\mu \approx \rho D$, depending on the diffusion coefficient, D. This viscosity is much lower than the creep viscosity of intact rocks at the Earth's crustal temperatures.

6.2. Structure of the Earth's crust

6.2.1. THE EARTH'S CRUST AS A PART OF THE LITHOSPHERE

The Earth's lithosphere is a solid shell below which the asthenosphere (the weakened layer of the Earth) is situated. This has been revealed by seismic studies which showed that wave velocities in the asthenosphere are much less than the velocities above and beneath it. The lithosphere is divided into an upper part, which is the Earth's crust, and to a lower part, belonging to upper mantle (Figure 6.5). The lower mantle is in contact with the Earth's core. The boundary between the crust and upper mantle was discovered by A. Mohorovichich, who discovered that reflections of seismic waves are systematic at corresponding depths. These reflections corresponded to P-wave velocities jump in *1.5 km/s*. This boundary is explained by the transition from crustal rocks to mantle rocks, which are more rigid and dense [24].

The asthenosphere existence is explained physically by the partial melting of rocks, possible because of their polymineral composition.

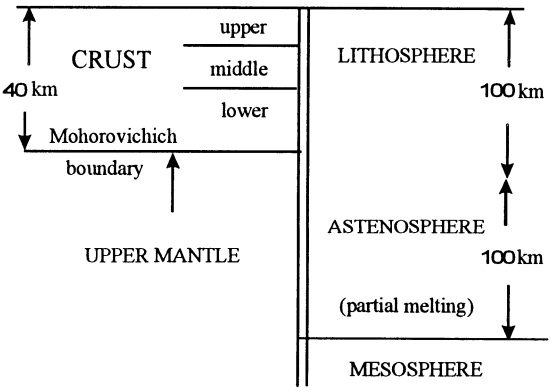

Figure 6.5. Schematic representation of the standard upper structure of the Earth's continents (see also Table 7.1).

The structure of the Earth's crust is studied by seismic-sounding methods. The Earth's crust has a very complicated structure that includes some internal boundaries with seismic velocity inversions in addition to the general tendency of velocity growth with depth.

In Figure 6.6, a seismic profile is given for P-wave velocities [24]. Conventional interpretation of the seismic stratification is based on differences in chemical composition of rocks and on measurements of ultrasound velocities for intact cores. Typical seismic

velocities are given in Table 6.2. Deep conditions are accounted for by creating corresponding temperatures and lithosphere pressures during testing, the latter being equalized to the production of the mean specific weight, γ, of rocks and the depth, H.

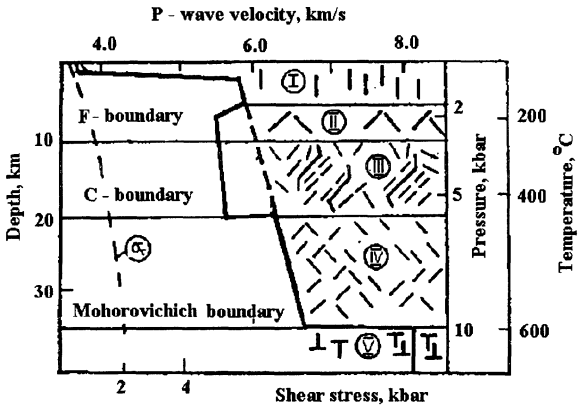

Figure 6.6. The Earth's crust according to seismic sounding with the Förtsh, Conrad and Mohorovichich boundaries (The broken line corresponds to intact rocks; the dotted line shows the tangential stresses necessary for tectonic failure of rocks.) [146].

TABLE 6.2. Typical P-wave velocities of intact rocks [24]

Geomaterial	Density, (g/cm^3)	Pressure, (*1 kbar*)	(*10 kbar*)
Granite	*2.643*	*6.13*	*6.44*
Granodiorite	*2.705*	*6.27*	*6.56*
Shale	*2.734*	*5.79*	*6.22*
Quartz diorite	*2.852*	*6.44*	*6.71*
Gabbro	*2.988*	*7.02*	*7.24*
Amphibole	*3.120*	*7.17*	*7.35*
Dunite	*3.277*	*7.87*	*8.15*
Eclogite	*3.383*	*7.52*	*7.87*

6.2.2. SEISMIC DATA OF FRACTURED CRUST

The approach based on sample testing is not sufficient because it does not take into consideration fractures larger than sample sizes which can exist in situ. Also, ultrasound

velocity is higher than seismic velocity, as was noted in Sections 5.4 and 5.5. Besides, very deep stresses can deviate from lithostatically pressured states. The typical state is that of a stress anisotropy generated by tectonic natural processes that leads to continuous dilatant creation of cracks, pores and faults. Therefore, the seismic differences introduced by pore space (represented in Figure 6.7) must be estimated. The Figure 6.7 shows that the effect of voids is much more basic in the crust than composition changes. Corresponding drastic changes in wave velocities allow us to explain seismic velocity anomalies.

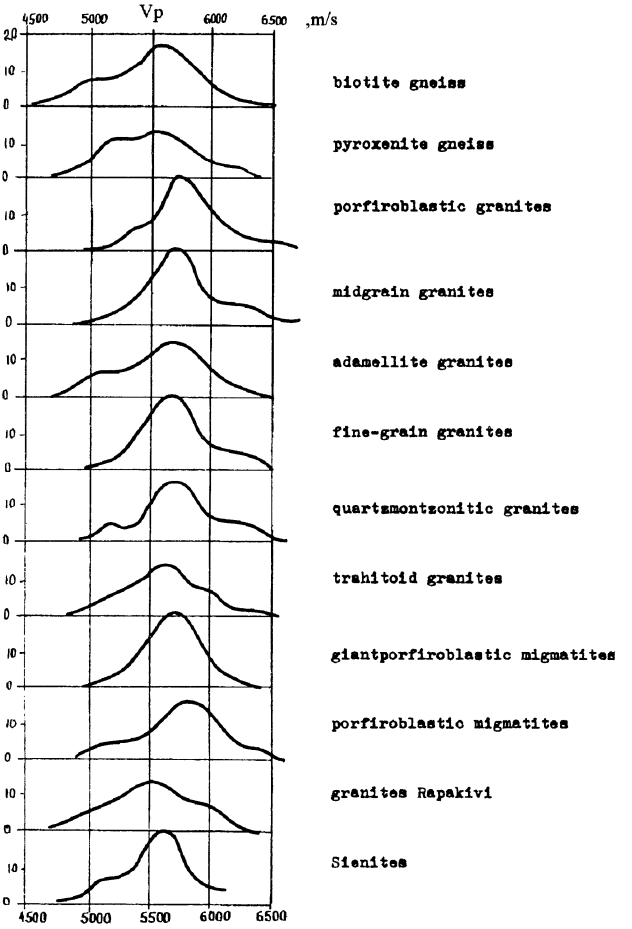

Figure 6.7. Probability density for seismic velocity due to fissures and pores (Courtesy of V.I.Sharov).

With respect to its strength characteristics, assume that granite is a typical continental crust geomaterial. In fact, the corresponding mantle geomaterials, such as peridotite (dunite) and eclogite, are *1.5* to *2* times harder than granite. A transition rock such as serpentine, typical for the Earth's oceanic crust, is one order weaker (Figure 6.1). Comparing Figures 6.1 and 6.6 gives the following results.

First, the transition from the brittle state to true crystalline plasticity in the granite crust will be at $p = 1\,GPa$ and $T = 600°C$. However, the thermodynamic conditions correspond exactly to the Mohorovichich boundary (the Moho) of the normal continental lithosphere if the confining pressure, $p_c = -\sigma_3$, coincides with the lithosphere (vertical) pressure, $\sigma_V = \gamma H = 1\,GPa$. Because a true plastic state means the annihilation of permeability, there is a plastic impermeable seal at the Moho which excludes water (vapor) transfer between the Earth's crust and the upper mantle. The latter appears to be "dry", and the mantle phase transformation and chemical reaction are different than in the crust [142].

Under high tectonic activity, if sufficiently intense tangential stresses exist, the Earth's entire crust can be transformed by fluids - first of all by meteor water. The mechanism of moisture penetration into the crust is connected with the origin of vacuumed fresh dilatant-crack voids, which act as tectonic-dilatant pumps.

You can see in Figure 6.6 that the Earth's crustal structure successively repeats the whole table of Figure 6.1. Then, if the sedimentary cover is small, the upper layer of the crystalline basement will contain vertical (*I*) and inclined (*II*) faults in accordance with the following thermodynamic conditions:

$$p \le 0.2\,GPa\,, \qquad T \le 200°C \tag{6.8}$$

Fault widening occurs at the level of the anomalous, low-seismic velocities that play a waveguide role. Thus, the Earth's crust waveguides are explained by the accumulation of dilatant-opened cracks, as was prescribed by the conditions of Interval *III*;

$$0.2\,GPa \le p \le 0.5\,GPa\,, \qquad 200°C \le T \le 400°C \tag{6.9}$$

Interval *IV* corresponds to cataclastic states in the lower crust:

$$0.5\,GPa \le p \le 1\,GPa\,, \qquad 400°C \le T \le 600°C \tag{6.10}$$

Interval *V* is the plastic sealing at the Mohorovichich boundary:

$$p = 1\,GPa\,, \qquad T = 600°C \tag{6.11}$$

The peak rock strength is given in Figure 6.6 by the $\sigma_\tau(p)$ curve, which accounts for the temperature-weakening effect. So, $\sigma_\tau \approx 0.2\,GPa$ is needed for creation of a true plastic rock state at the Moho. This value was observed in nature [129].

6.2.3. THE CRUST FAULTS

The true spatial position of faults can be found via a network of orthogonal seismic profiles. The faults occur quasivertically in the neighborhood of the free surface (Figure 6.8). Within the interval from *3* to *10* km, faults have an almost constant inclination ($\approx 60^o$) but become continuously horizontal at *18 km* depth approximately . Because the fault constitutes a smaller angle, $\theta = (\pi / 4) - (\varphi / 2)$, with the main compression axis (Section 1.3), this means that vertical compression prevails in the upper part of the crust (under its own rock weight), but the main compression at the level of the low velocity layer coincides with the horizon. So, fault inclination permits us to locate the main stress axis in the lithosphere. Therefore, the listric faults are typical under horizontal compression of the middle crust. Their dilatantly-expanding "roots" constitute local zones of low velocities in the Earth's crust.

Geomaterial's state depends on stress and temperature inside a fault also [203].

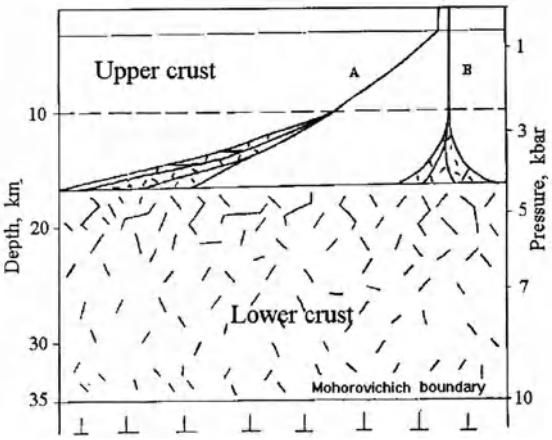

Figure 6.8. Listric faults appear due to reorientation of main compression from the vertical axis to the horizontal with depth growth (A = listric faults, B = vertical faults).

Sometimes displacements of the hanging block of a listric fault present arguments for crust extension. However, this extension should be connected with the secondary tectonic movement. In the case of lithosphere extension, the vertical faults are generated; at the depth of middle crust, they also have dilatant widening. The position of the fault roots can also be proved by the orientation of nodal planes of an earthquake

mechanism in the middle crust (Section 7.2). Their horizontal orientation is usual for many regions.

The reason for the reorientation of main stresses with depth inside the Earth's crust could be the detachment motion [109] of the hard upper part of the Earth's crust relative to the hard upper part of mantle along the lower crust, which corresponds to the cataclastic rupture of granite rocks. Note that here the horizontal compression at the Moho has been accounted for.

6.2.4. WAVEGUIDES OF THE CRUST

The correspondence of low-velocity crustal zones to the localization zones of dilatant cracks and pores was confirmed by the superdeep drilling of the Kola well (in Russia) and the KTB well (in Germany), among others.

Superdeep drilling has shown that there are seismic boundaries in the Earth's crust that are connected with the fracture of rocks, but not with changes of the rock composition. So, at the depth $H = 6$ *km* of the Kola well, where the seismic reflector intersects the lithological stratification of rocks, the inversion of seismic velocities occurs.

Low-velocity layers (waveguides) are revealed at the Russian platform at the depths from *10* to *25 km* - that is, between boundaries K_1 and K_2, at the Ukrainian Shield, within the interval from *8* to *15 km* [168].

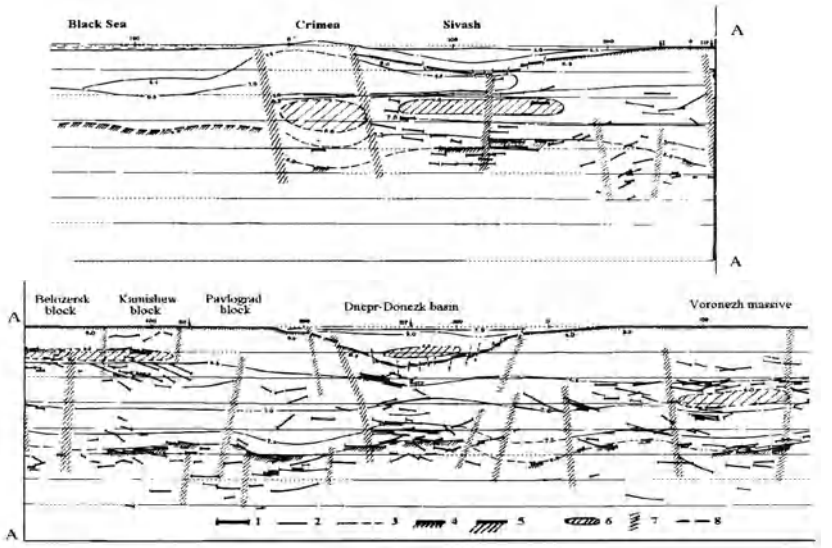

Figure 6.9. Low-velocity zones in the crust of the Ukraine Shield (Courtesy of N. I. Pavlenkova): (1) - seismic reflectors, (2) - isovelocity lines, (3) - extrapolation, (4) - sedimentary basin lower boundary, (5) - Mohorovichich boundary, (6) - low velocity zone (LVZ), (7) - block boundaries.

These variations can be explained by the various intersections of geotherms with the boundaries of the intense dilatancy zones [i.e., stick-slip zones (Figure 6.2)] and also by the competing process of crack healing due to metamorphism and dislocation rock creep. Laterally stretched low-velocity zones (layers) can be represented by the dense system of listric faults and can even include the vertical faults that appear during extension of the lithosphere. The widening of vertical faults at depth is confirmed by the study of rift-zones data [79], including magnetotelluric (electric current) methods. Low-velocity zones were noticed even beneath the ocean at the same depths (about *12 km*).

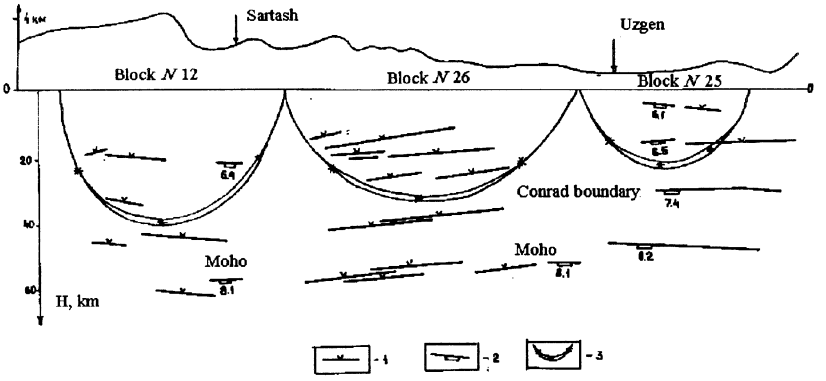

Figure 6.10. Listric faults and the Conrad boundary for one region of Central Asia (Courtesy of V. I. Sharov): (1) - seismic reflectors, (2) - typical seismic velocities, (3) - fault according to the earthquake hypocenters.

The low-velocity zone is bounded below by the Conrad boundary (C or K_2). Previously, the Conrad boundary was considered as the transition boundary from granite to gabbro-basalt strata. The superdeep Kola well has shown that this boundary corresponds not to the change of rock composition but to the change in state of the same rock. Thus, the lower crust (beneath C) differs from the upper crust by the mechano-chemical treatment of crustal geomaterial. In addition, the lower crust can include mantle material because of its intrusion. For example, the Swedish deep well (Gravberg I) discovered a seismic reflector in the deep granite strata that was in reality a horizontal fault with diorite dikes inside.

6.2.5. THE LOWER CATACLASTIC CRUST

According to Figure 6.1, the transition to the cataclastic type of rupture occurs approximately at the boundary C. The well-known discrete character of the boundary C can be explained by the space distribution of the fault system. The roots of these faults determine the observed discreteness of a seismic wave reflection.

A cross-section of the Earth's crust (shown in Figure 6.11) is in accordance with the plane view of a fault ring system that is a sequence of the bifurcation phenomenon for the tectonic plate on the viscous lower-crust layer under action of lithostatic compression or tension [71]; see also Section 4.5.

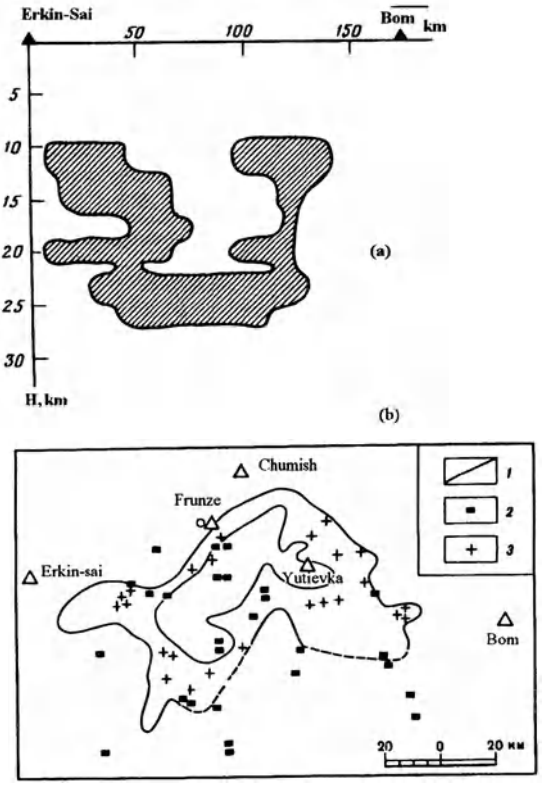

Figure 6.11. Vertical cross-section (a) of the crust in Kirgizstan mountains (b): (1) - seismic inhomogeneities observed in the years 1968-1973, (2,3) - in the years 1974-1979 (2 - c_p = 5,7 km/s; 3 - c_p = 6,30-6,38 km/s) [82].

The uplift of geomaterial should be expected near exits of large-scale faults at the upper boundary of the crystalline basement due to dilatant appearance of voids and

porous space at fault roots, see [126]. That is accomplished by the way of the horst generation, and it can be proved by experiments with sand. Analogous disturbances will also appear at the Moho, although they are usually interpreted as the interaction traces of giant vertical faults penetrating throughout the lithosphere.

The thermodynamic intervals of stick-slip zones and waveguides coincide. This means that strong crustal earthquakes (with magnitude $\mathcal{M} \approx 5.5$), which can occur in the middle crust, correspond to the generation of waveguides themselves (that is, to the transition of large volumes of deep rocks into a cataclastic state) [203]. As a rule, there are no sources of earthquakes between boundaries C (or K_2) and Moho.

However, the localization of shear into bands (Section 1.4) can take place in the case of intensive cataclastic flow inside the lower crust due to relative motion of the upper crust and upper mantle. The existence of such a motion is supported by comparison of large geological structures of the upper crust and the upper mantle or even of kimberlite tubes which can be interrupted inside the lower crust.

Recall that kimberlite tubes are filled traces of fast fracturing during magma intrusion into very rigid lithosphere from the depth of some hundred km, and they have to cross the partly melted asthenosphere in a brittle way. The sign of such brittleness could be extremely high seismic velocities (up to 9 km/sec) discovered [212] beneath the Moho in the vicinity of kimberlite tubes. The latter are famous because the geomaterials filling the tube carry diamonds from the Earth's asthenosphere directly to the ground surface.

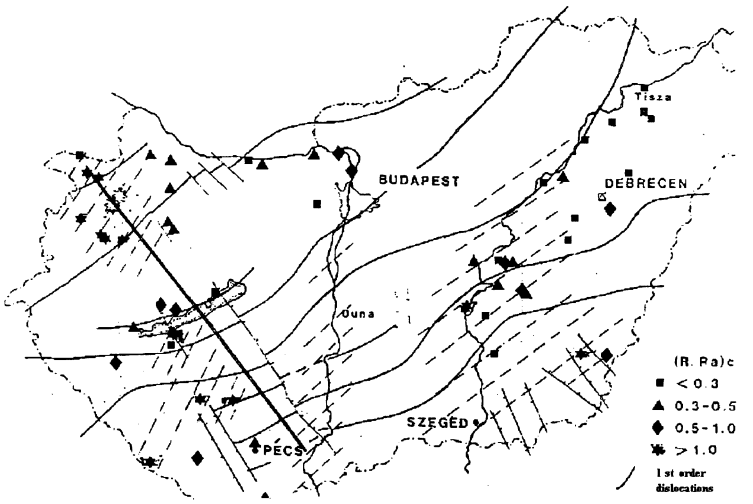

Figure 6.12. Helium isotope ratio $R/Ra \geq 1$ as an indicator of mantle gas fluxes: Ra is its atmospheric value [122]. (Broken lines correspond to sedimentary basins; the double line is the deep seismic sounding profile revealed in faults in the lower crust.)

However, beneath sedimentary basins the lower crust has many seismic reflectors, and earthquake sources sometimes exist here. The physical reason could be the thermal isolation of the lower crust due to a sedimentary upper cover or due to the double thickness of radiogenic granites created by tectonic overlapping. Overheating cataclastic geomaterial leads to the ceramisation of the lower crust. As the result, the elasto-brittle response of the lower crust is recreated and changed directly to intracrystalline plasticity at the Mohorovichich boundary. Crustal faults can be prolonged in the upper mantle only in such a case. The mantle geomaterial can enter through such faults, which are paths for intense fluids and gas migration. Also, such faults, along with dikes of solidified mantle geomaterials, become the most effective reflectors of seismic waves in the crust.

Another scenario is connected with the amphibole (Section 6.3) that is thermally unstable at $T \geq 650^{o}C$ (Figure 6.1), by which cataclastic failure can be recreated by heating the lower crust. In the amphibole masses fault structure consist of a true plastic at lower temperatures and in quartzites. This means that even impermeable faults are possible in nature. The physical explanation for this resides in the extreme rigid matrix bonds that are higher even than the strength of mineral grains.

The helium mantle is the best indicator of fluid penetration into the crust from the Earth's mantle because of its different isotope ratio ($R = He_3/He_4$) content. In Figure 6.12, the mantle helium distribution is given for the Pannonia basin [122]. You can see that the maximum numbers correspond not to the mountain regions, where deep faults cross the free surface, but to deep sedimentary valleys. The explanation of such a map consists of two parts. The first one is that faults cannot continuously cross the entire crust down to the mantle; the second is that only widely developed water-layer systems in the sedimentary cover can gather mantle helium percolated through mantle faults in the lower crust overheated beneath a sedimentary pillow.

6.3. The Mohorovichich boundary as impermeable sealing

6.3.1. THE CRUST-MANTLE PETROLOGIC TRANSITION

The annihilation of crustal rock permeability at the Mohorovichich boundary indicates the appearance of the isolator that excludes water percolation both down and up [146]. This is in accordance with the experimental data that upper mantle rocks such as peridotites and eclogites do not include any essential amount of water [181].

Consider the phase transition from continental crustal rocks characteristic for the lower crust (gabbro, basalt, amphibole) to eclogites via garnet granulites. The corresponding fields of thermodynamic stability are found experimentally (Figure 6.13) for "dry" conditions. This phase transition can explain the seismic velocity discontinuity at the Moho because the above-mentioned crustal rocks have roughly the same mechanical properties as granites ($c_p \approx 6\text{-}7\ km/s$ at $p = 1\ GPa$ $\gamma \approx 2.6 - 3\ g/cm^3$), but eclogites and peridotites are very different ($c_p \approx 8\ km/s$, $\gamma > 3\ g/cm^3$). Amphiboles are intermediate rocks ($c_p \approx 7.3\ km/s$, $\gamma \approx 3.12\ g/cm^3$) and include a basic amount of water.

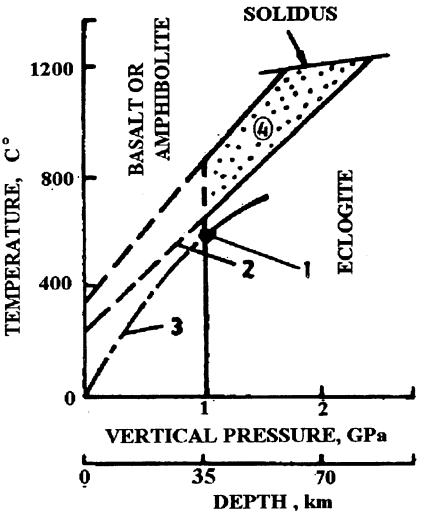

Figure 6.13. Thermodynamic stability fields of crustal (basalt, amphibole) and mantle (eclogite) rocks: (1) - state at the Moho, (2) - transition boundaries for "dry "conditions, (3)- geotherm, (4) - intermediate phase of granulites [147].

You can see that the boundaries between crustal rocks and eclogites intersect the axis of temperatures at the point $T = 400^{\circ}C,\ p = 0$. If this were so, the Earth's surface (with $p \approx 0,\ T \approx 20^{\circ}C$) would be represented by mantle (not crustal) rocks, but water action inside the crust makes the part of thermodynamic estimations shown in Figure 6.13 meaningless (as is shown by broken lines).

The zone of real eclogite stability and its transition to basalt-gabbro strata are determined by the positions of the geotherm curves in the *PT*- plane. The phase transformation of eclogites under diminishing of pressure and temperature creates amphiboles if the crust is wet. More detailed plane representation of metamorphic rock changes [133] account for "dry" as well as "wet" states and transformations and may also explain the detailed stratification of the lower crust.

According to the satellite measurements, the thermodynamic conditions at point $T \approx 400^{\circ}C,\ p \approx 0$ may correspond to the free surface of the planet Venus. Because of the absence of water, it could correspond to the basalt stability and, indeed, the basalt plato was observed there by Russian cosmic stations.

6.3.2. GEOTHERMAL AND WATER EFFECTS

The path of a geotherm plays a decisive role in rock-phase transformation.

If point *1* of the thermodynamic state at the Moho is displaced from the boundary of the eclogite stability upward into the area of stability of the garnet granulite, then the intensity of the seismic wave jump at the Moho decreases. In reality, "the sharpness" of the Moho transition can be different in nature. The thickness of the Earth's crust as a whole diminishes if the geotherm is moved closer to the temperature axis because of the high crustal thermoconductivity connected with massive water circulation from the ground surface down to the lower crust, as in the case of the Pannonia basin. There, the crust thickness is equal to *25 - 27* km.

The same phase transition (when the temperature increases quickly in dry lower crust) is shown in Figure 6.14. In this case, true plastic states of granitoids exist in the crust (Figure 6.15), and the depth of the Moho is from *50* down to *70* km, (depending on path *4* or *5* of geotherm *3* in the lower crust).

The seismic profile of Figure 6.15 corresponds to the Central Alps, where the lower crust is “dry”. It is easy to see that geotherm "inclination" determines the thickness of the "wet" part of crust *1*, the lower floor of the crust *7* being composed of garnet granulites. Thus, it becomes clear that the Mohorovichich boundary cannot be identified with any isotherm in the lithosphere.

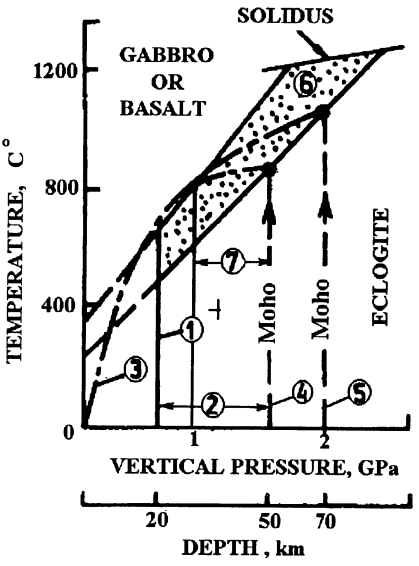

Figure 6.14. Thermodynamic stability fields and high geotherms for a nonstandard continental crust:(1) water penetration limit, (2) "dry" lower crust, (3) geotherm, (4,5) two variants of the Moho states, (6) granulite phase, (7) granulate part of the crust [147].

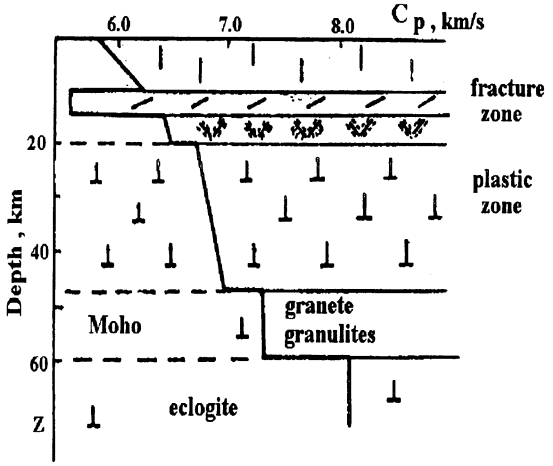

Figure 6.15. Dry (plastic) lower crust of Central Alps that can be seen in the intrusive body Ivrea [147].

Unfortunately, up until now, the data on the eclogite hardness tests are not known well enough, and only some data on eclogite plasticity (for $T = 600^{\circ}C$ and $p \approx 1.5\ MPa$) are available. These experiments have shown that mantle rocks are *1.5* times harder than crustal rocks.

6.3.3. WHY OCEANIC CRUST IS THINNER?

The oceanic crust is much thinner than the continental crust. This can be explained by another role that water plays at the oceanic Moho. Ocean water migrates through cracks of the basaltic crust downward, reaching mantle peridotites. When the water meets the peridotites, the Hess chemical reaction ("water + peridotite ↔ serpentine") takes place. Apparently, serpentine is transferred into the plastic state (Figure 6.16) when the confining pressure is equal *0.2 GPa* within a wide interval of temperatures (from 0° up to $550^{\circ}C$). The volume of serpentine inside faults grows, and the faults become impermeable.

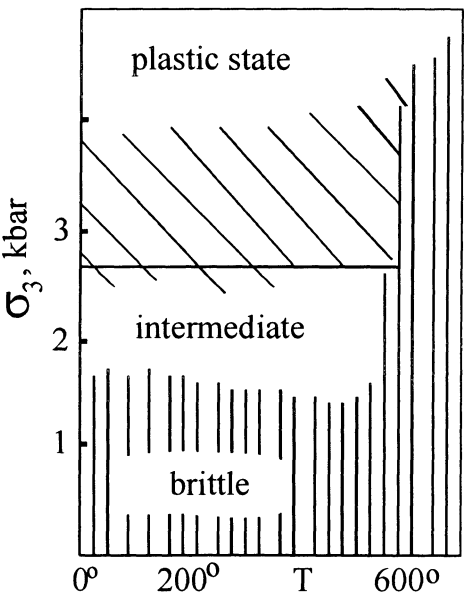

Figure 6.16. Fields of serpentine stability.

That is why the Moho under oceans corresponds to the isobar of *0.2 GPa* or, in other words, to the depths of *7-11 km*, taking into account the weight of ocean water. It has also been supposed that serpentinization of the oceanic crust occurs only along faults, as is indicated by the study of ancient crustal pieces [97]. This means that such water migration paths as faults are isolated.

Thus, the Earth's crust as a whole is the zone of active impact of water and water vapor. The most intensive meteor water circulation is shown in Figure 6.17. The serpentine lower oceanic crust itself is movable and serves as a water transport agent.

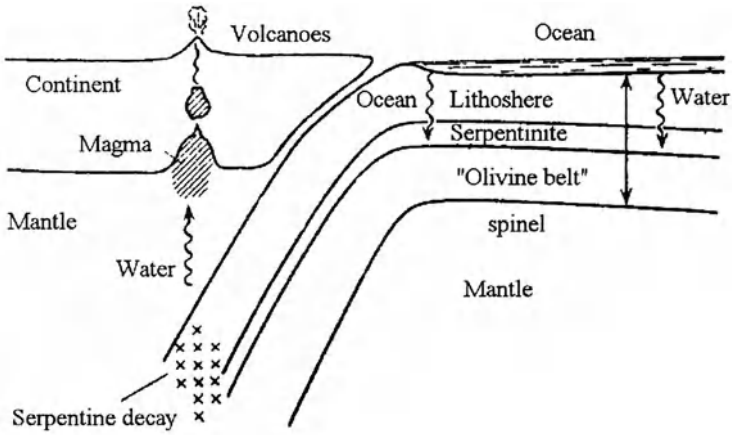

Figure 6.17. Global circulation of the Earth's meteoritic waters.

6.3.4. UPPER MANTLE FRACTURING

Upper mantle rocks are *1.5* to *2* times harder than crustal geomaterials. That is why under real mantle thermodynamic conditions they can be failured in a brittle way and faults and waveguides can appear beneath the crust. This is the only way of understanding the origin of mantle waveguide (at the depth of *50-80 km* in Tornkwist-Teysseiry zone in Sweden or in the Siberian upper mantle [206]). The waveguide system exists independently of the asthenosphere (Figure 6.18).

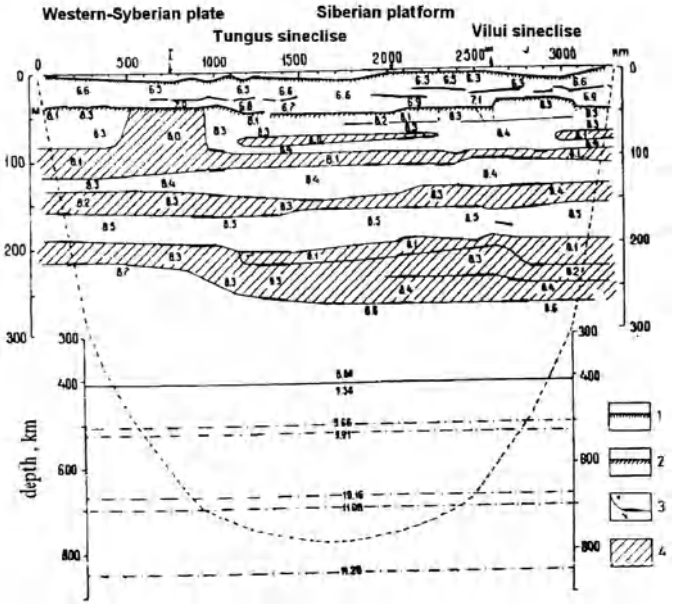

Figure 6.18. Deep seismic sounding by nuclear explosions in Siberia: (1) foundation boundary, (2) Mohorovichich boundary, (3) reflectors, (4) low velocity zone; numbers correspond to P-wave velocities, *km/s*.

When analyzing the structure and possible brittle destruction of the upper mantle, it should borne in mind that at $T \approx 1000^{\circ}$, the pyroxenite strength (Figure 6.3) depends on the deformation rate. It means that under standard geodynamic conditions ($De/Dt \approx 10^{-16}\ 1/sec$), the upper-mantle rock cannot accumulate the energy sufficient for earthquake in situ. Therefore, the earthquake energy accumulate in the upper part of the lithosphere. However, when the "fast" earthquake occurs, the whole lithosphere is elasto-brittle, and the earthquake fault expands instantly from the crust into the upper mantle. ("Slow" earthquakes are observed also and correspond to creep fracturing, see Section 1.5.3.)

6.3.5. THERMOVISCOUS SOFTENING

The temperature increase lowers the effective nonlinear viscosity, μ, according to the law [87]:

$$\mu = \frac{1}{2A}\sigma_{\tau}^{1-n} exp\left(\frac{Q_*}{RT}\right) \tag{6.11}$$

This is typical for olivines and other rocks in a continuous state. Corresponding data were used often to explain of the detachment phenomena [109, 127], although they do not take into account further viscosity decrease due to the cataclastic states of the lower crust. Vice versa, solidification can take place after strain heating and thermal-softening effects [31], which are connected with the exponential decrease of rock viscosity with temperature, according to the rheological rule (1.64). If we use the Frank-Kamenetzky approximation for viscosity (6.11):

$$\frac{2B_0}{T} exp\left(-\frac{Q^*}{RT}\right) \approx exp\, a(T - T_0) \tag{6.12}$$

then the one-dimensional heat balance (1.43), together with Onsager's rule (1.61) across the band of shear localization

$$c\frac{\partial T}{\partial t} = \kappa\frac{\partial^2 T}{\partial y^2} + \sigma_{xy}\frac{\partial v_x}{\partial y} \tag{6.13}$$

would be:

$$\frac{\partial \theta}{\partial \tau} = \frac{\partial^2 \theta}{\partial \xi^2} - \beta exp\,\theta \tag{6.14}$$

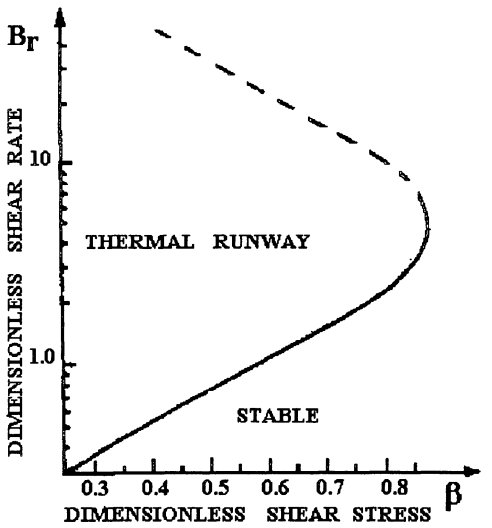

Figure 6.19. Stationary solution of (6.14), in the form $Br = a\mu_0 v_x^2/\kappa$ as the function of β, shows stable heating and loss of stability if $\beta > 0.88$.

Here, $\theta = a(T - T_0)$, $\xi = y / h$, $\tau = \kappa t / ch^2$, $\beta = (ah^2 / \kappa)\sigma_{xy}^{n+1}$, $\dot{e} = \partial v_x / \partial y$. The second term at the right-hand side of (6.13) is the dissipation rate of mechanical energy per unit volume inside the band with thickness h. It has been shown numerically that, depending on value β, thermal stationary distributions in a shear band can be unstable (as in the case of explosive detonations [232], where the same equation controls the transition from combustion to explosion). The main conclusion is that at very high differential stresses ($\approx$*1 kbar*) or for wide bands (more than *1 km*), the thermal runaway instability (Figure 6.19) and the resulting melting and dike creation are quite possible.

The differential stresses $(\sigma_1 - \sigma_3)$ have the necessary order in the Earth's crust, as was shown by paleopiezometry methods based on the recrystallization process, which depends on acting shear stresses. The measurements have shown that crustal shear stresses are possible up to the level of *2 kbars*. This is exactly the order of shear strength of intact rocks if one accounts for their thermal weakening at depth (Figure 6.6).

6.3.6. STRUCTURE OF THE ASTHENOSPHERE

The transition to the asthenosphere occurs also due to partial melting, which takes place easier when small portions of water are added. (Water dissolves in rock melt.) This process is important for the magma-generation process. That is why active volcanoes appear in regions where serpentines become unstable and release crystalline water inside the mantle (Figure 6.17). Light mantle material can percolate through the permeable asthenosphere matrix in a form of "fluxons" [179].

Due to melting, the astenospheric viscosity is three orders lower ($10^{17} - 10^{20} P$) than the lithospheric viscosity ($10^{22} P$). You can see that the melting effect is very essential. The combination of this "tectonic" viscosity and elasticity, corresponding to seismic velocities, in the elasto-viscosity form of a porous matrix provides an explanation for the attenuation of seismic waves in the asthenosphere. The calculations were made on the basis of the rheological model (2.198) for effective stresses [35].

It has also been found that there is a "jump" of the P-wave velocity at the lower boundary of asthenosphere, but the analogous "jump" for the S-wave is practically absent. According to Section 5.3, this can be explained by the gas-like phase state inside the porous space above these boundaries (Figure 6.20) and fluid-like phase beneath them. The porous space of the asthenosphere is created by partial melting, and "gas-fluid" separation can happened due to the gravity effect, see also [179].

The mantle waveguides discovered by Deep Sounding Profiling (Figure 6.18) cross the asthenosphere boundaries assumed on the base of thermal calculations (N. I. Pavlenkova, private communication). This can be explained by gravitational separation of geomaterials inside a real asthenosphere.

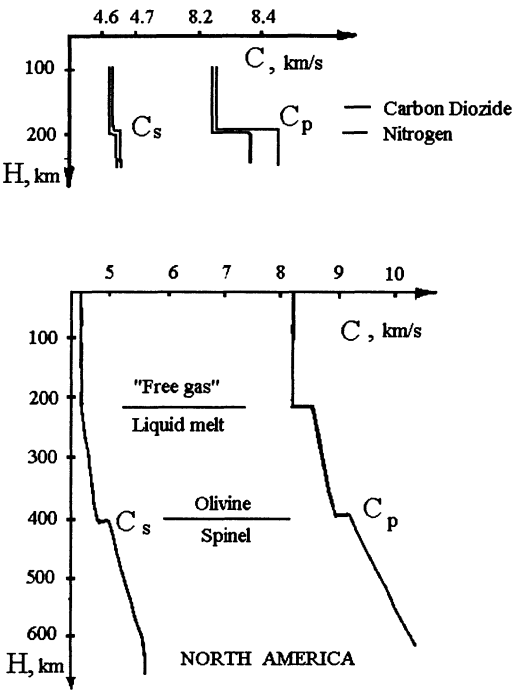

Figure 6.20. Asthenosphere seismic profiles and transition from gas-type saturation of a porous space to a more dense liquid saturation (calculated and observed) [36].

The next seismic boundary takes place at a depth equal to *400 km* and corresponds to solidification of the melt in pores due to the olivine-spinel phase transition.

The presence of gases in the upper part of the asthenosphere is essential for many processes. Under high pressures, these gases can quickly penetrate into the lithosphere during such magmatic events as volcano eruptions or slowly through systems of permeable faults. Because masses of methane can exist in the asthenosphere, their upward flux can be important for formation of rich oil/gas reservoirs and coal deposits [40, 73, 74].

6.4. Fluid dynamics of the crust

6.4.1. DILATANT LOOSENING AND FLUID ACCUMULATION

For analysis of the problem of fluid migration, it is essential that free circulation is possible in the Earth's crust, that there are deep layers of "open" porosity and dilatant cracks, and that there is a plastic impermeable barrier at the Moho [146, 147].

Remember that typical sedimentary rocks are five times weaker than granite. Thus, the limiting depths for "open" porosity in a sedimentary basin are close to *7-10 km*. However, metamorphism of the lower layers of sedimentary rocks makes them more rigid, and their dilatant destruction becomes possible at depths larger than *7 km*. Figure 6.21 shows the typical profile [83] of the Deep Seismic Profiling across the Southern part of the Caspian Sea. High velocity layers are shown by a shadow that can be explained by plastic compaction and possible metamorphism. A wide interval of dilatant loosening exists below and has contacts with a deep fault, intersecting the Moho boundary. The transformation of hydrocarbon masses which come down, together with sedimentary rocks, or percolated up in gas form from the asthenosphere, can take place just in this interval of loosening.

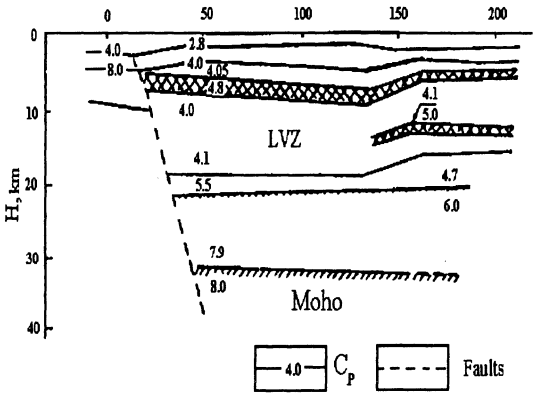

Figure 6.21. Intermediate zone of possible hydrocarbon accumulation in the crustal low-velocity zones with high-velocity sealing.

An intermediate stage of hydrocarbon accumulation in porous layers revealed beneath the Caspian Sea and at Sakhalin island (Figures 6.21, 6.22) is necessary for the nonorganic theory of petroleum origin [40].

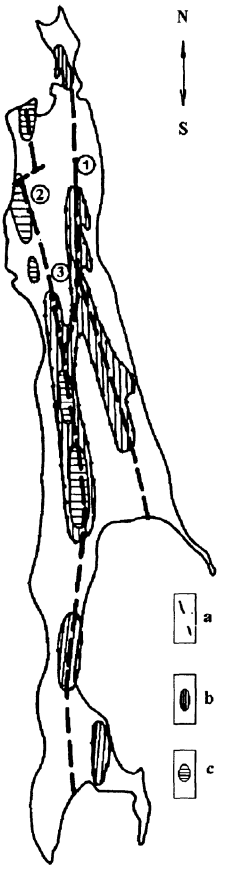

Figure 6.22. Sakhalin faults (a) and low electroresistance deep zones [5] (b), (c) at 15 km depths: (1) oil reservoirs with high initial pore pressures, (2) oil-gas reservoirs, (3) gas reservoirs with low initial pore pressures.

It should be noted that plastic barriers in the lithosphere result in the generation of anomalously high fluid pore pressure in underlying rocks. Generally speaking, this pressure can even reach values of lithostatic pressures. It provides, for example, hydrocarbon and water breakthrough and the appearance of gas-mud diapers. Of course, such processes are realistic in the softer sedimentary basins. Diffusion of hydrocarbon gases causes the fluidity of clays and plays the role analogous to heat conduction during magmatic diaperism [179]. The latter is connected with the high mobility of liquid magma below the Mohorovichich boundary, where fluid pressure can also be anomalously high. The breakthrough of a asthenosphere light fluids in the form of magmas into the Earth's crust can also be treated as hydrofracturing process.

The reservoirs of nonorganic methane were found in the vicinities of volcano in Japan. The superdeep Swedish well Gravberg-I, drilled in the Silian meteor crater, gave evidence of the presence of nonorganic methane in quasihorizontal faults in granite strata. Large masses of helium and even free hydrogen have been found with methane. However, all of them are of crustal (not mantle) origin.

6.4.2. MANTLE FLUIDS AND SEDIMENTARY BASINS

Upward flows of mantle fluids can be found in the Earth's crust where faults cross the Moho [123]. Such fault channels exist through the cataclastic lower crust beneath sedimentary basins (Figure 6.23).

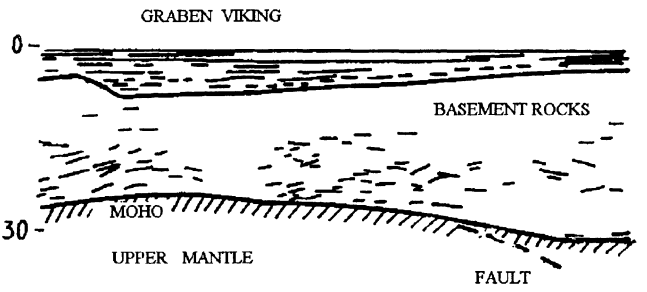

Figure 6.23. Mantle fault crossing of the Mohorovichich boundary beneath sedimentary basins (Courtesy of D. H. Matthews).

Here, therefore, only nonorganic hydrocarbons could pass through the lower crust and enter the technically accessible depths of sedimentary basins. First, they accumulate in porous and fractured layers, revealed by such seismic methods as waveguides, and by magnetotelluric profiling of zones with anomalously low electroresistivity [225].

In reality, the zones of saturated porous rocks have often extremely low electroresistance (*10 Ω/m* instead of *1000 Ω/m* for intact rocks). The reason for this is connected with the melting properties for the asthenosphere in the presence of thin solid films of grafite created by filter flows of gas mixtures and chemical reactions under deficit oxygen. Another explanation, supported by many direct observations, is that it is caused by presence of brines (salt waters) or hydrocarbon fluids (gas-condensates) as water emulsions in the lithosphere. Such a layer exists on the Sakhalin island at depths of *10-15 km*, in the form of isolated spots that probably correspond to a discrete system of fault roots (Figure 6.22) [5].

Hydrocarbons can be thermodynamically stable only in gas-condensate form at such depths of their accumulations. In the upper strata, hydrocarbon mixtures are separated into gas and oil groups.

Under tectonic stress changes and seismic waves, the fault system undergoes pulse deformations with typical dilatant increments of geomaterial pore volume inside fault bodies. In addition to the usual gravity, there are zones of temporal decrease and increase of pore pressure that cause the fluid migration in the crust. Undoubtedly seismo-tectonic deformations mechanochemically accelerate the transformation of migrating hydrocarbon masses within the faults. Hydrocarbon transformation can also be created by bacterial activity at these depths because bacteria are simply tissue shells filled with water. (Bacteria are killed if water is boiling but the temperature of boiling is dependent on pressure. That is why they can be alive up to $374^{\circ}C$.)

6.4.3. WATER MOBILIZATION OF TECTONICS

Water effects are very essential for the lower crust for two main reasons. The first is the high physicochemical activity of water, due to high temperatures, when it dissolves and transfers quartz (SiO_2) masses upward together with gold, and other metals. The paths of quartz transfer and further sedimentation inside the faults in the Earth's upper crust show where to find gold deposits, for example. Hot gases such methane play the same role. They also diminish the critical thermodynamically conditions (at $374^{\circ}C$) of water, but the salt present acts in the opposite direction.

The second reason is the dynamic high mobility of water-saturated layers due to the lessening of solid friction coefficients as well as to the appearance of effective lithostatic pressure [68]

$$\sigma^{ef} = \sigma - p \tag{6.15}$$

in the Coulomb limit condition (1.77) instead of the usual lithostatic stresses, σ. Here, p is the pore pressure, which can be high in undrained conditions [163], σ is the total lithostatic pressure.

The catastrophic Neftegorsk earthquake (1995) happens (Figure 6.22) because of the fault (*1*) sudden motion that could be a result of global tectonic events at the Japanese isles (Kobe earthquake) together with deep water redistribution stimulated by oil production.

6.4.4. STRESSED LITHOSPHERE AND MINERAL TRANSFER

If the ceramization of cataclastic rocks takes place beneath a sedimentary basin, the lower crust becomes very rigid as a whole, and brittle fracturing leads to inclined faults (in accordance with Figure 6.1). The same situation occurs in the case of amphibole brittleness. Hydrocarbons from asthenosphere migrate through the fault system upward and are accumulated in the form of reservoirs if clay or salt sediments play the role of their sealing. Of course, this isolation is not absolutely full; therefore, the strata above

contains hydrocarbon gas traces which can be revealed by geochemical exploration. The geostructures themselves are searched by seismic methods.

The pores and dilatant cracks are opened for gas and fluid migration if the level of lithostatic pressure, σ, is low. This gives the key for finding gas-oil reservoirs through maps of lithosphere stress distribution.

In Figure 6.24, the corresponding maps are given for the Southern California and Kirgizstan. These maps were constructed numerically by solving the plane-stress problem for a lithosphere rectangular block if tectonic forces were given at its boundaries [72]. Stress inhomogeneities are created by the presence of the fault which is accounted for by lessening the averaged elastic modules in proportion to fault concentration. You can see that hydrocarbon reservoirs coincide with zones of anomalous low lithostatic pressure.

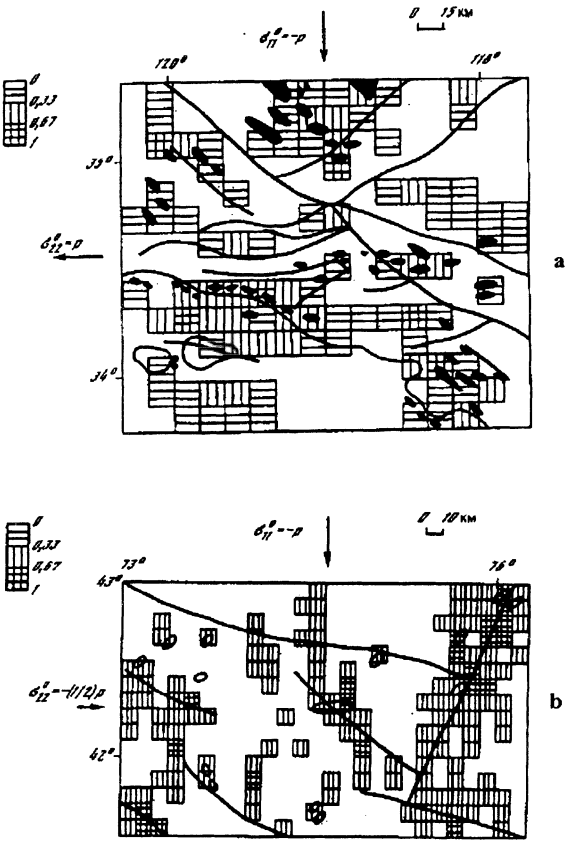

Figure 6.24. Zones of low lithostatic pressure are correlated with oil reservoirs in Southern California (a) and with polymetallic ore deposits in the Northern Tyan-Shan (b) (Degree of pressure decrease is shown from 0 to 1.).

Moreover, ore deposits are also situated in such zones. This can be explained by metal transportation, with hot hydrocarbon gases or with deep waters, and by metal sedimentation in the vicinity of the ground surface, where temperature becomes low. It is similar to the case of "black smokers" in the ocean, where hot gases or waters saturated with hydrocarbon gases penetrate into the cold ocean and ore concretions appear.

The analogous calculations were performed for plane cross-sections of the Earth's crust beneath several giant hydrocarbon reservoir of the Northern Caspian Basin as Tengiz. It is situated below saltstone masses, its productive interval is more than *1.5 km*, and it consists of limestones, dolomites, etc. It was found that the pore pressure is much higher here than the hydrostatic value, which means that the reservoir is isolated from the surrounding water basin. However, it can have deep fracture roots because the low lithostatic pressure zone down to *18 km* was found by calculations. This means that crack system is open down to the middle crust (Figure 6.25). The analogous Karachaganah gas-condensate reservoir, also in the Northern Caspian Basin, is known to have extremely rich metals in a colloidal state. This could be result of a hydroconnection with the Earth's lower crust.

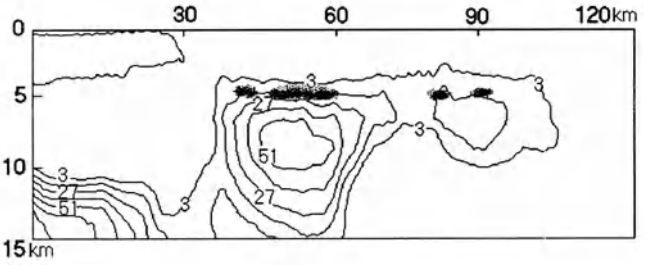

Figure 6.25. Low lithostatic pressures beneath the Tengiz oil reservoir found by calculations on the basis of seismic and gravitational fields [73]. (Numbers correspond to pressure deficit (bars); the oil reservoir is shown by the spots.)

6.4.5. RADON INDICATOR OF WATER FLOWS

Very sensitive measurements of fast tectonic changes can be made by observing radon gas concentrations. Because this gas is radioactive, its concentration may be measured by counting number N of tracks of α, β, γ - particles inside the sensitive films.

The radon measurements [218] at the ground surface show the contour of the oil reservoir at the depth (Figure 6.25). This means that radon can migrate (with other

gases or water) upward through the system of small cracks and pores. Displacements of α- and γ-contours can be connected with water flows in the strata.

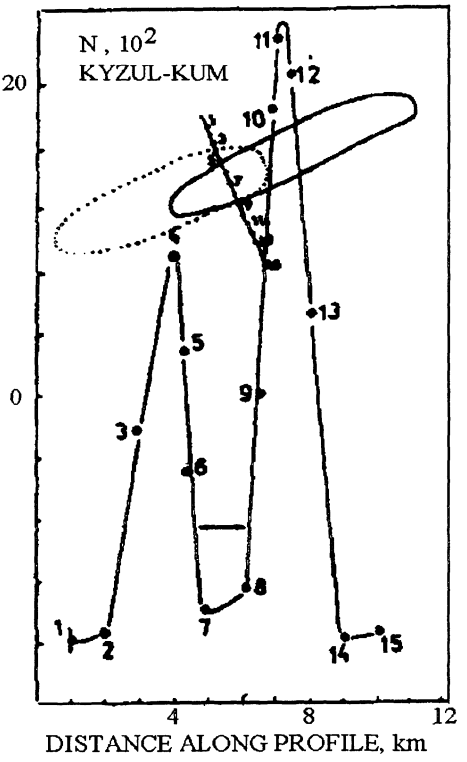

Figure 6.26. The ground radon anomalies along the shown profile due to α-particles corresponds to the contacts of the oil reservoir with water outside the zone (The dotted line corresponds to an anomaly of γ - particles.) [218].

Deep water sources are of extreme importance for many regions of the Earth where conventional water flows are absent. Therefore, the fault system in basement rocks should be studied as a water-migration path as well as to find out juvenile (mantle) waters, or even waters connected with deep free hydrogen sources, that are discovered in some superdeep wells (Gravberg 1 at Sylian Lake, Sweden).

6.5. Superdeep drilling and well stability

6.5.1. DEEP WELLS FOR THE CRUST OBSERVATION

Superdeep drilling can be extremely useful for studying such cases as the deep strata beneath the Tengiz reservoir. Currently, some deep wells are being drilled in Tatarstan and in other places in a search for oil and gas inside crystalline basement (Figure 6.27).

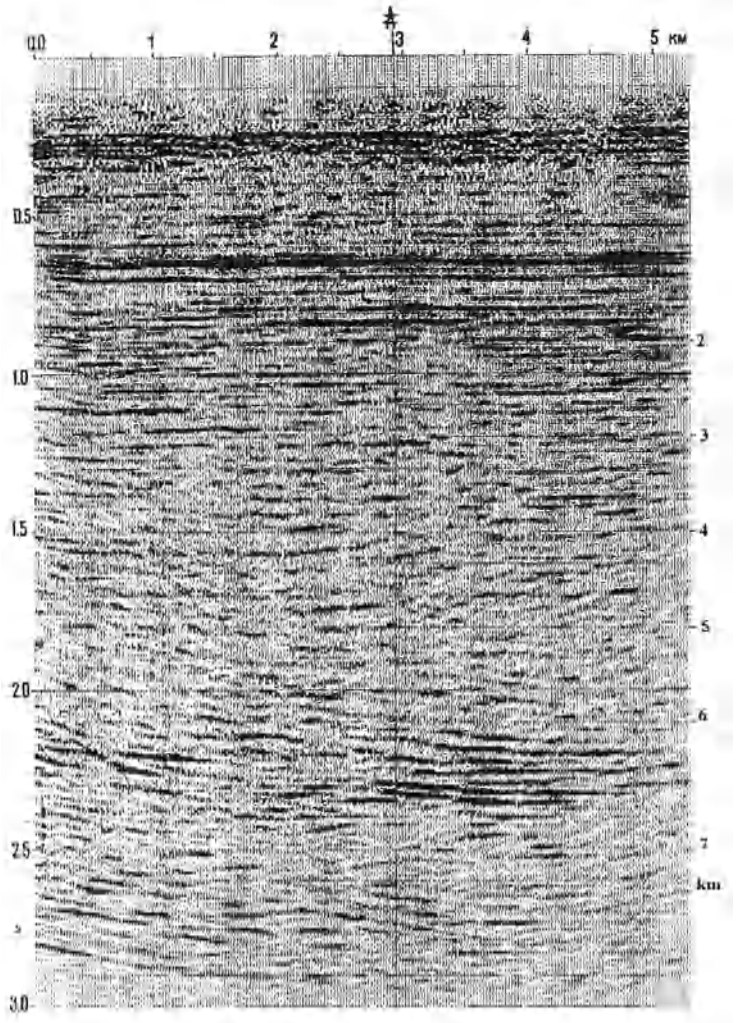

Figure 6.27. The Tatarstan deep well is being drilled to deep reflectors beneath the Bavly oil reservoir (Double time - of wave travel down and back - is also given [219].).

The rheological properties of rocks at depth, as well as specific tectonic-stress distribution, can create serious problems for superdeep drilling. As a result, many superdeep wells cannot reach their projected targets because of rock breakout and loss of borehole direction. You may think that there is some depth limit for drilling, but it actually depends on regional conditions. So, the famous Kola hole was drilled down to *12.6 km* instead of *15 km*. The Swedish well (Gravberg-1) had a *6.5 km* depth instead of *8 km*, and the KTB well that will have a *14 km* depth met with many problems *8 km* down.

The first well was drilled to the Conrad boundary and the granite-basalt transition had to be found at a depth of *7-10 km*. It was found, however, that, in reality, the corresponding seismic reflection was generated by a listric fault of an essential thickness saturated by water and gas. Two other superdeep wells were drilled to intensive but very localized seismic reflections. It was thought that these reflections corresponded to the high porous space of fractured rocks filled by fluid or gases.

These works were stopped by the growth of the tectonic stress level and its anisotropy. So, according to observed listric fault form, one of the horizontal components of tectonic stress grows quicker than vertical stress, because a fault has a tendency to be closer to the axis of main compression (see Figure 6.8). The same result was obtained later by interpretation of deep well damage; it was also determined that the vertical stress is higher than both horizontal components above the depth of *2 km* [238], but deeper the horizontal stress becomes the main compressive one. The difference of the two horizontal stress components also grows with depth. It creates the conditions for shear dilatant failure of rocks in the vicinity of a borehole.

6.5.2. BOREHOLE STABILITY

The mathematical simulation of the corresponding rock state follows. The drilling process is modeled by the instant appearance of a cylindrical void hole in nonequally stressed rocks. Under stress, rock material is displaced in the direction of the hole axis, but it is stopped by solid friction growth because of convergence and pore closure in the ring zone surrounding the appearing well.

For computer calculation [236, 237] of the stress-strain distribution in a well's vicinity, the numerical method was used according in which the dynamic forces were conserved in the momentum balance even for quasistatic problems:

$$\rho \frac{\partial v_i}{\partial t} = -\frac{\partial S_{ij}}{\partial x_j} - \frac{\partial \sigma}{\partial x_i} + \rho g_i \tag{6.16}$$

where $S_{ij} = \sigma_{ij} + \sigma\delta_{ij}$ is the stress tensor-deviator, and $\sigma = -\sigma_{ij}\delta_{ij} / 3$ is the lithostatic pressure. They are connected with strains by elastoplastic constitutive laws (Section 1.3) that can be written as

$$\frac{\partial S_{ij}}{\partial t} + v_j \frac{\partial S_{ij}}{\partial x_j} = 2G\left(\varepsilon_{ij} - \frac{1}{3}\varepsilon_{ij}\delta_{ij} - S_{ij}\frac{d\lambda}{dt}\right) \tag{6.17}$$

$$\frac{\partial \sigma}{\partial t} + v_j \frac{\partial \sigma}{\partial x_j} = K\left(\varepsilon - 2\Lambda\sigma_\tau \frac{d\lambda}{dt}\right) \tag{6.18}$$

where strain rates are determined as usual:

$$\frac{\partial \rho}{\partial t} + v_j \frac{\partial \rho}{\partial x_j} = \rho\varepsilon \tag{6.19}$$

$$\varepsilon_{ij} = \frac{1}{2}\left(\frac{\partial v_i}{\partial x_j} + \frac{\partial v_j}{\partial x_i}\right) \tag{6.20}$$

The additional unknown function $(d\lambda / dt) \geq 0$ if shear stresses, σ_τ, are equalized by the pressure, σ, according to Coulomb's law (1.77):

$$\sigma \equiv \left(3S_{ij}S_{ij} / 8\right)^{1/2} = Y + \alpha\sigma \tag{6.21}$$

Active loading is then taking place.

The dilatancy rate, Λ, internal friction, α, and cohesion, Y, are functions of the strain parameter, x, which is different for hardening and softening regimes. There functions were determined experimentally and used in computer code elsewhere [96, 235]. The latter includes mathematical viscosity to smooth discontinuities.

First, the plane-stress distribution corresponding to the cross-section of an infinitely long well is shown in Figure 6.28 for the nonequal horizontal stresses, σ_H and σ_h, when vertical pressure, $\sigma_V = \rho g H$, is intermediate; $\sigma_H > \sigma_V > \sigma_h$. In this case, nonelastic strains (that is, dilatant damage) appear below the depth $H = 600\ m$ for limestones and below $H = 1000\ m$ for sandstones and diabases.

You can see that the elastoplastic solution determines a larger scale of damage zone than the estimation of its boundary according to the pure elastic stress-strain solution (Figure 6.29).

Moreover, the nonmonotonous stress distribution inside the damage (plastic) zone explains the appearance of subzones of unstability that are potentially dangerous for the drilling process and the well's existence. According to Figure 6.28, the ring zone of high

hoop stresses, σ_θ, exists inside the damage zone due to closure of pores and increasing internal friction. Between mentioned peak stress line and the borehole wall, the damaged geomaterial is practically under zero compression. The rocks fragments from this subzone of instability drop into the borehole during drilling or hang at the wall ready to fall down, stopping the drilling process if their size is of the order of the well radius.

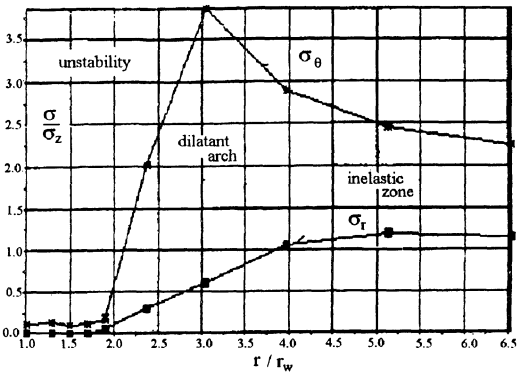

Figure 6.28. Stress profiles along the minimal horizontal compression axis, σ_h; r_w is the initial well radius [236].

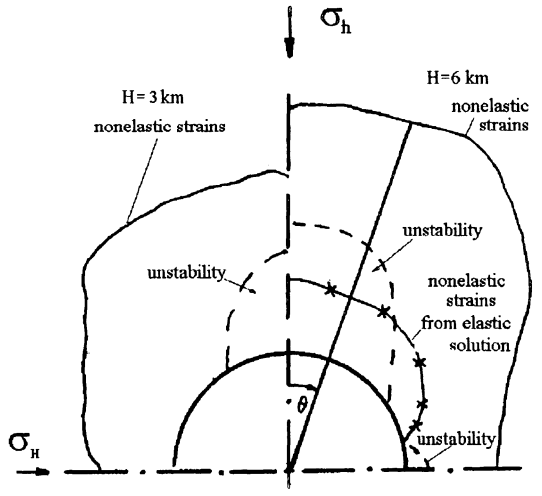

Figure 6.29. Zones of the nonelastic strain-field (damage) around a well in the anisotropic lithostatic stresses [236].

A cross-section of the resulting damage zone has roughly an elliptic form with a long axis along the minimal horizontal compression, but the subzones of instability form narrow corridors confined by the geomaterial in a dense state. This means that these subzones can exist in a semistable state and are a source of breakouts. This phenomenon is quite analogous to a rockburst in a mine, and the necessary condition of having higher wave velocities in the surrounding rocks than in the dangerous zone of fragmented geomaterial is fulfilled.

The damage zone is bigger in initially weaker rocks, and the arch of hardening is higher relative to the reference state than in the case of intact rocks. So, in weak rocks, the cavities are bigger but more stable than in intact rocks, where a smaller caliper of cavity and more frequent rock breakouts are typical.

The outer boundary of instability zone shows the optimal cross-section of the borehole. The technological problem consists in removing crushed geomaterial from the subzone of instability.

6.5.3. DRILLING AND TECTONICAL ANISOTROPY

During the drilling process, the borehole can occasionally become curved. The stress-strain distribution in the vicinity of curvilinear wells can be explained by the subproblem of plane-curved channel (a fault with internal and external radii with respect to the curvature center).

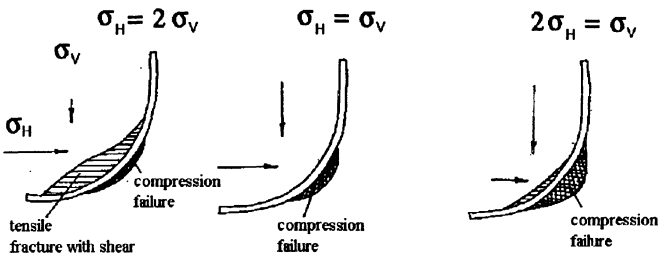

Figure 6.30. Types of failure due to a curvilinear well profile and a stress anisotropy [237].

It was found that failure zones are not symmetrical with respect to well axis [237]; they are spread more in the direction of minimal compression. The interval of curvature effect is equal to *4* lengths of the curved part of the borehole.

The main conclusion concerns the dependence of failure on the ratio of vertical, σ_V, and horizontal, σ_H, maximum compression. If the horizontal stress, $\sigma_H = \sigma_h$, is bigger than the vertical stress, $\sigma_H > \sigma_V$, then wall failure at the internal radius is larger (Figure 6.30). In this situation, the drilling tool will move into the direction of the initial deviation, the well curvature will increase, and drilling direction can be lost. In the opposite case, when $\sigma_V > \sigma_H$, the failure zone will be larger at the external radius, the drilling tool will have a tendency to return to the proper vertical direction, and the drilling process will be self-stabilizing. So, the inclination of the boreholes tends to have the same form as the faults in the rock masses, depending on the tectonic stress anisotropy. In the case of the equality, $\sigma_V = \sigma_H = \sigma_h$, the stress distribution is neutral with respect to the drilling process.

So, superdeep drilling has more perspectives in the crust under tension - that is, in the rift zones.

It was noted also that maximum stress concentration takes place at the contact of weak and hard rock layers.

These problems are essential also for deep mining technology [49, 93].

CHAPTER 7

GEODYNAMICAL PROCESSES

7.1. Global tectonic dynamics

7.1.1. THE EARTH'S STRUCTURE

The Earth is a rotating stratified solid ball surrounded by gasous movable shells - that is, by the atmosphere and ionosphere. The upper solid layer is called the lithosphere. It is more cold and rigid than the others beneath it. Temperature and pressure grow with the depth inside the Earth, and the result is a partial melting of polycrystalline rocks at a depth of *100* to *200 km*. The corresponding layer of the Earth is known as the astenosphere, which is practically porous (with porosity $m \approx 10\%$). Its porous space is saturated by melts that are more light. The melting temperature is very sensitive to the presence of water, changing the pT-boundaries of the start (solidus) and finish (liquidus) of the melting. The astenosphere itself was found by seismic studies because of its diminished wave velocities and the high dissipation in accordance with its visco-elastic properties.

Beneath the asthenosphere there is the much more dense geomaterial of the Earth's mesosphere, which can move convectively at a geological timescale but which is elastic for seismic waves or for the Earth's oscillation. The characteristic thickness, H, of these layer can be found in Table 7.1 for two variants of stratification.

TABLE 7.1. The Earth's global stratification

Stratification	H, (*km*)	Stratification	Interval, (*km*)
Lithosphere	0-100	Crust	0-35
Asthenosphere	100-200	Upper mantle	35-400
Mesosphere	200-2900		
Liquid core	2900-4980	Intermediate mantle	400-1000
Porous core	4980-5120	Deep mantle	1000-2900
Solid core	5120-6370	Earth core	2900-6370

There is also another type of stratification that is connected with the petrophysical content of rocks - that is, with their physic and chemical properties. It was found that the crust's density is of the order of $2.7\ g/cm^3$, but the mantle rocks have a density close to $3.3\ g/cm^3$ at the Earth-surface pT-conditions. Corresponding seismic velocities change instantly from *6-7 km/s* in the Earth's crust to *8-9 km/s* in the mantle. This transition takes place at the Mohorovichich boundary, discussed earlier. The crustal geomaterial is more rich in SiO_2, the mantle more rich in *CaO, MgO*. Corresponding depths are also given in Table 7.1.

The center of the Earth is represented by a metallic core that consists of liquid and solid parts. Between them there is a porous zone of metal freezing in accordance with PT-conditions. Here, part of the metal is a liquid, saturating the porous space. The outer liquid core, where the liquidus PT-condition is reached, is characterized by intense fluido-metallic flows and plays the role of an Earth dynamo-machine, generating the internal geomagnetic field. The Earth's core is extremely dense ($\approx 9\ g/cm^3$) and movable because of the liquid state of its outer layer. Therefore, the core can influence the Earth's planetary dynamics, changing, for example, its axis position. As a result, the instant rotation axis is wobbling around the Earth's geographic poles. According to this Chandler's wobbling, the lithosphere is moving relative to the mesosphere with characteristic periodicity (*6* years, *12* years, etc.) sliding at the viscous asthenospherical layer.

This oscillation takes place at the background of the global relative motion of separate pieces of lithosphere known as tectonic plates. The global motion is known as continental drift [229] and is induced by large-scale thermogravitational convection [208] in the Earth's mantle and by the density difference of lithospheric and mantle geomaterials.

7.1.2. PLATE-TECTONIC CONCEPTS

The global convection of the Earth's mantle is separated into flows in the deep mantle and smaller cell-type convection in the upper mantle, which leads to asthenospheric flows beneath every tectonic plate and creates their collision. There are a number of tectonic plates (Figure 7.1) representing the Earth's continents and oceans. They are discriminated by the earthquake epicenter map, because their main part is distributed along boundaries of colliding tectonic plates [107]. The plate displacements were estimated by geological data as well as by direct observation from satellites. It was found that their velocities are no more than *5-10 cm/year*.

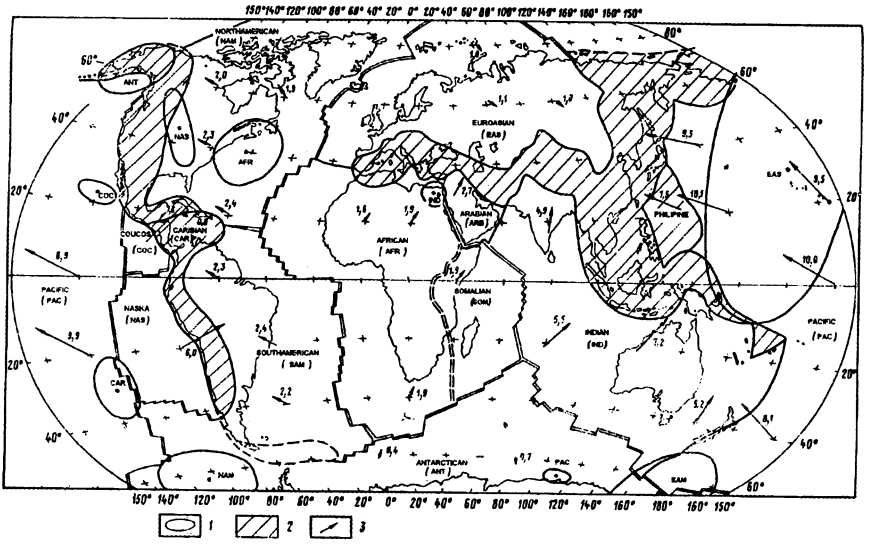

Figure 7.1. Global kinematic representation of absolute motion of lithospheric plates: (1) pole position of instant rotation, (2) Circum-Pacific and Alp-Himalaian belts of planetar compression of lithosphere, (3) displacement velocity (cm/year) [107].

The main features of plate tectonics were found from seismic studies. Along the meridians in the center of Pacific and Atlantic oceans, rift zones exist where the mesospheric material goes upward in the form of basalt intrusion and creates a new oceanic lithosphere. After cooling, this basalt has magnetic properties corresponding to the Earth's recent magnetic field. Because the magnetic Earth poles change position periodically ($T \approx 10^6$ *years*), the basalt strips, with differently oriented magnetization, are distributed at the ocean bottom. Their periodical dependence on distance from the rifts permits estimation of the rate of oceanic lithosphere spread [107]. This coincides with measurements made by satellites.

Appearance of additional lithospheric geomaterial creates tectonic relative motion, but its superfluous part is subducted along the line of collision of the oceanic continental plates (Figure 7.2). So, the main geomaterial and fluid exchange between the lithosphere and the mantle happens in rift and subduction zones [109].

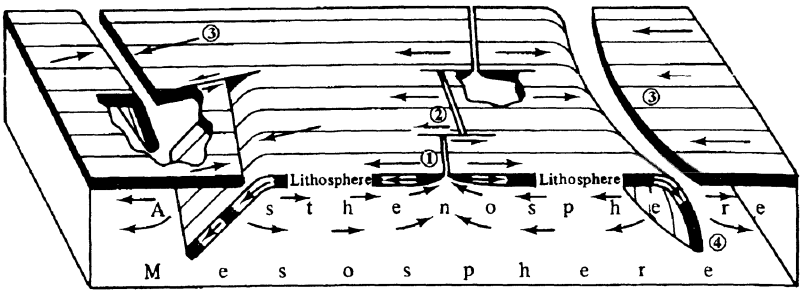

Figure 7.2. Block diagram illustrating global mass circulations, including generation of the lithosphere at rift lines, the role of transforming faults, collision and the subduction of tectonic plates [98].

The drag force was estimated [208] on the basis of a viscous model of the asthenospheric flow; it was found that it is in the tens of bars. In these calculations, the viscosity was taken as 6×10^{19} *poise* for the asthenosphere, 3×10^{21} *poise* for the deep mantle and 2×10^{20} *poise* for the whole mantle.

As seen from seismic-velocity distribution and mantle earthquake-hypocenter maps the subducting slabs go down into the mantle to *600* to *700 km*. Because all mantle earthquakes take place inside the slabs, it appears as an earthquake type of rupture is connected only with crustal geomaterial (in its normal horizontal position or inside the slab sinking into the mantle). The difference is that during a crustal earthquake, the brittle rupture of rocks occurs due to stress concentration; under inadequate mantle PT-conditions, instant brittle states and rupture occurs possibly due to the phase transition of the crustal geomaterial.

The subducting slabs differ by the angle of their inclination and tectonic fields. The corresponding mechanical models are discussed in the literature [98]. They are based on physical or computer modelling. The Pacific Ocean is bounded by a giant subduction ring along which excess geomaterials are removed upward creating mountain systems. The subducting material has a lot of water connected in a crystalline lattice of serpentine. According to Figure 6.1, at temperature level $T \approx 600^{\circ}C$, serpentines become unstable, water is released and penetrates the surrounding mantle material. The latter converts into a state of movable magma and begins its upward flow. So, a volcano system is essentially created by ocean water action on the Earth's mantle.

More deep mantle roots belong to plumes, which correspond to so-called "hot spots" at the Earth's surface. It is understood now that these spots are fixed in the Earth's space and moving plates get irreversible traces there [137].

The subduction process can take place also along the collision line of tectonic plates belonging to different continents [120]. One of the colliding plates subducts and the

other creates mountains. Such a situation is typical for the Pamir-Hindu-Kush and Tian-Shan regions, for the Hymalaian mountains and for the Alpien region, where the mantle material is situated very close to the surface and creates the Ivrea intrusion body. A surprising observation was made at the Tibet plato, where two tectonic plates composed the unique horizontal double lithosphere.

7.1.3. ENDOGENEOUS PROCESSES

In addition to tectonic processes with horizontal plane basic kinematics [229], there are many geodynamic processes that develop along the vertical axis. They are connected with erosion, sedimentation and gravitational effects [18]. It is necessary to emphasize that water plays an essential role as rupture and transport factors at the ground level as well as inside the entire Earth's crust. Displacements of large geomaterial masses creates additional loading of the lithospheric plates (for example, at river mouths). In such a place, the plate bends accelerate the sedimentation process further. Also, sedimentation takes place in the rift zone, where horizontal tension prevails [79]. Sedimentary geomaterials go downward generating characteristical strata under action of metamorphic processes, including hydrometamorphism. Sometimes waveguides are created at depths of typical dilatant rupture as you can see in Figure 6.9 in the case of Dnepr-Donetz basin [168].

Usually, the lower crust is represented by cataclastically ruptured geomaterials and has characteristic superplastic features. That is, the lower crust is mobile and therefore plays the role of the intracrust asthenosphere [109]. As a result, the upper elasto-brittle crust can be removed locally relative to the upper mantle. The system of listric faults of the upper crust mentioned above transforms the horizontal motion beneath the Moho into a vertical block uplift. High temperatures of the lower crust can be generated by radiogenic middle crust strata overlapped along listric faults that duplicates their thickness above the lower crust.

More intensive vertical geodynamic process is created by the sedimentation. The sedimentary basins begins to grow under action of lithosphere tension when vertical faults (Section 6.2.5) appear in the crust and below the Moho [79]. Then basalt magma from astenosphere enters upwards into the lithosphere. Due to data, given in Figure 6.13, the phase transition of basalt into eclogite can take place at the Moho under its P,T-conditions (in the water absence). Heavy eclogites will force the lithosphere to sink into the mantle [9, 110]. This creates the next stages of the sedimentary basin development. Rivers and wind erosion of the edges of the basin will remove masses of sediments upon its bottom.

The sinking has to be "geologically fast" (for example, *1 km per 1 million years*) for creation of hydrocarbon organic potential reserves because for more slow process [9] the organic hydrocarbons (kerogen) will be oxidized before the burial in pore space of sediments. The temperature interval for an petroleum origin from the kerogen are

determined by chemical transformation rates [112] and it corresponds to the depth of 4-5 *km* in the sedimentary rocks for usual geotherms in these regions. Hydrocarbon gases and fluids circulate inside fault system according to the global fluidodynamics of the lithosphere.

The alternative non-organic theory of petroleum origin is based on the assumption that methane, CH_4, is created by reaction between hydrogen and carbon oxide gas in the magnetite presence and by further polymerization under high thermodynamic conditions [40], corresponding to the Earth mantle. Methane can percolate into the crust beneath sedimentary basins through the fault system, discussed above, and enrich petroleum reservoirs and coal deposits. Practically, the main problem of mineral resources is the sealing of pore space and fracture voids that is necessary for petroleum and gas trapping. The competition of theories of a petroleum origin is basic for a choice of targets of deep drilling. Plate tectonic has to be taken into account also [64].

7.1.4. ISOSTASY PRINCIPLE

The gravimeter measurements have shown that the rock masses are more light beneath mountains and have the same specific weight as mountains themselves. Vice versa, valleys are based by heavier geomasses. This means that the Earth's strata are non-uniform in vertical cross-sections and their nonhomogeneity is compensated isostatically at a deep level. The surface geostructures as mountains have more deep "roots" represented by the same geomaterials but the crust is thinner beneath basins or oceans.

It seems to be in accordance with Figures 6.13 - 6.15 where the same property is explained by measured geotherm gradients and by phase or chemical transitions to more dense rocks at the Moho. That is, the difference of specific weights of rocks inside the Earth crust is not basic for the isostatical compensation. The difference between the crustal and mantle rocks plays the major role.

There are two approaches to the isostasy principle. The first belongs to J.H. Pratt (1855) and means the equality

$$\rho(h + D) = const \tag{7.1}$$

where D is the compensation depth and h is the topographical height (Figure 7.3). The calculation shows that D is equal to 113,7 km [24] and corresponds to the upper astenospheric boundary. This means that ρ is the averaged density for the considered cross-section of the lithosphere and pressure (7.1) is compensated by hydrodynamic flows inside the astenosphere in the geological time scale.

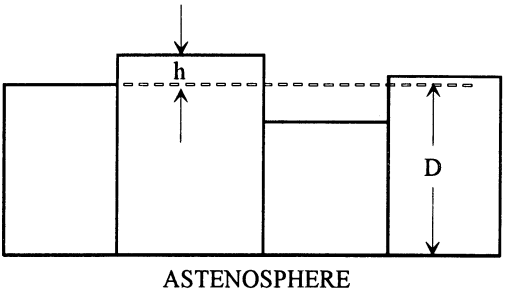

Figure 7.3 Isostatic block hydraulic compensation by the astenosphere creep

The second approach was suggested by G.B. Airy (1855) as follows

$$(\rho_s - \rho_c)r = \rho_c h \tag{7.2}$$

where r is the root depth, ρ_c is the averaged crust density, ρ_s is the density of the substrata. The main part T of the geostructure is assumed to be self-compensated (Figure 7.4). That is, hydrodynamic compensation (7.2) corresponds to creep flows in the upper mantle but above the astenosphere. Because the rock viscosity is much higher there than the viscosity of the astenosphere, compensation (7.1) will be established "geologically quicker" than (7.2).

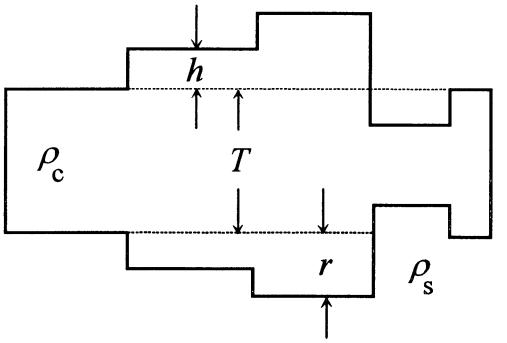

Figure 7.4 Isostatic hydraulic compensation by upper mantle creep.

7.1.5. FLEXURE OF LAYERS AND LITHOSPHERE

The flexure effect is basic for solid layers inside the Earth if strata above and beneath them are less rigid and playing just the roles of the load or the support. Sometimes such a layer is named "competent" and upper and lower strata as "noncompetent" ones [18]. The lithosphere is flexible in comparison with the "soft" astenosphere. In this case, topographycal deviations from the averaged surface level as mountains and islands can be treated as a load. The flexure of the lithosphere leads to redistribution of the loading pressure over wider zones of the astenosphere and the isostasy principle has to be changed to some nonlocal form.

Consider the elastic layer [18, 223], flexing under effective vertical load q(x) when the tangential traction Q(x) is acting in a cross-section of the layer. The equilibrium means that:

$$Q - (Q + dQ) + qdx = 0 \tag{7.3}$$

and the first momentum balance takes a form of the differential equation:

$$dQ / dx = - q(x) \tag{7.4}$$

According to Figure 7.5, the rotation effect of the tangential force Q(x) acting at cross-sections, as well as the normal force P(x), have to be compensated by moment of forces $\mathcal{N}(x)$:

$$(\mathcal{N} + d\mathcal{N}) - \mathcal{N} = Qdx + Pdz \tag{7.5}$$

where $z(x)$ is the vertical displacement of the layer considered. So, the balance of moment of momentum for a flexing layer follows

$$d\mathcal{N} / dx = Q + P\,(dz / dx) \tag{7.6}$$

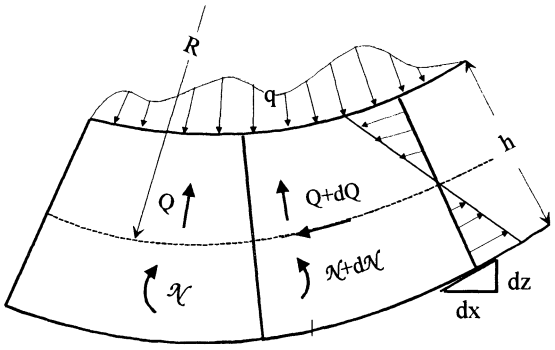

Figure 7.5 Sinclinal bending of the layer under distributed load q(x)

Now we have to relate of $\mathcal{N}(x)$ with the normal stress σ_{xx}, acting in sublayers, as shown in Figure 7.5

$$\mathcal{N} = \int_{-h/2}^{h/2} \sigma_{xx} y dy \tag{7.7}$$

where h is the layer thickness. The normal stress is proportional to the strain component e_{xx} according to the Hooke law (1.23), that is,

$$\sigma_{xx} = \frac{E}{(1-\nu^2)} e_{xx} \tag{7.8}$$

where E is the Young modulus, ν is the Poisson coefficient

$$E = \frac{2KG}{3K+G}, \quad \nu = \frac{3K-2G}{6K+2G} z \tag{7.9}$$

and the condition of zero vertical deformation

$$e_{yy} = \frac{1}{E}(\sigma_{yy} - \nu\sigma_{xx}) = 0 \tag{7.10}$$

is used inside the flexing layer. Further, the sublayer strain is proportional to the vertical distance y from the neutral plane and inverse proportional to the curvature radius R of the flexure:

$$R = - d/dx(dz/dx) \tag{7.11}$$

Correspondingly, the flexing moment $\mathcal{N}(x)$ is the following

$$\mathcal{N} = -\frac{E}{1-\nu^2}\frac{d^2z}{dx^2}\int_{-h/2}^{h/2} y^2 dy = -\frac{D}{R} = -D\frac{d^2z}{dx^2} \tag{7.12}$$

where the flexure rigidity D is introduced:

$$D = \frac{Eh^3}{12(1-\nu^2)} \tag{7.13}$$

Now we can represent the moment of momentum balance (7.6) in the resulting form

$$D\frac{d^4z}{dx^4} = q(x) - P\frac{d^2z}{dx^2} \tag{7.14}$$

where $q(x)$ and P are supposed to be given for particular problems. For example, the crust, flowing on the mantle, is under action of the following disributed load

$$q = q_t + (\rho_c - \rho_s)gz \tag{7.15}$$

and q_t is the topographycal load, ρ_c, ρ_s are the densities of the crust and of the strata below (mantle). If one considers the lithosphere as an entire object, these densities correspond to the lithosphere and astenosphere. The horizontal tectonic force P is accounted for in the problems of the lithosphere forms and stability beneath islands and of the folding process in sedimentary basins, etc.

According to Figure 7.5 the layer extension and corresponding pore appearance takes place in their upper part in the anticline case and it is basic for oil and gas accumulation.

7.2. Basic concepts of earthquake mechanics

7.2.1. SOURCE MODELS

At the large scale an earthquake source acts as a system of instant point forces at an external elastic medium. Two simple models are well-known (Figure 7.6) [147].

Figure 7.6. Schemes of acting forces in the earthquake hypocenter: (a) dipole, (b) double force couple.

The first is a dipole (a couple of forces) with an unbalanced moment of momentum that corresponds to a simultaneous rotation of blocks or plates. The second is a double-force couple, which accounts for the moment of momentum balance. Such models can be created on the basis of frontal characteristics of seismic waves. First, it is possible to discriminate waves radiated by explosions and by earthquakes by seismic monitoring by station nets. Explosion waves correspond to a simple expanding sphere (Section 5.1) and displacements have the same sign at all prints of observation although they are changing in time. Earthquake waves (see Figure 7.7) have quadrants of compression and extension.

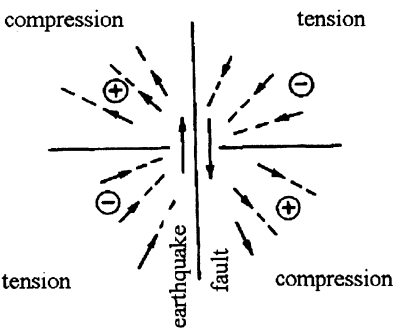

Figure 7.7. Earthquake hypocenter with two nodal planes (earthquake fault and orthogonal plane).

Historically, the first quantitative model was Reid's. It was one of elastic rebound, according to which there is a system of rock bended layers crossed by an earthquake fault in the section of maximum distortion (Figure 7.8).

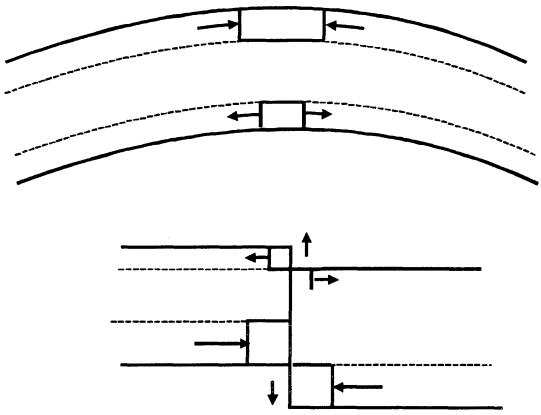

Figure 7.8. Earthquake fault and seismic wave radiation in stratified bonded media.

Main elastic energy is then instantly radiated in the form of shear waves. Associated P-waves with different front-displacements signs are generated by compression of some layers and by extension of others before rupture.

Shear waves are observed also at underground explosions. Sometimes it is explained by tectonic energy release. Laboratory explosions in initially stressed blocks support this point of view. In addition, it was found that underground explosions initiate the growth and creation of cracks belonging to initially existing tectonic faults [141].

Earthquake elastic energy releases an initially stressed volume that can be identified with the aftershocks zone. The preparation of rock volume to rupture can be observed by seismic exploration or other methods. However, solids usually fail along an individual macrocrack and sometimes in a form of a new fault appearing at the ground surface after an earthquakes.

A growing fracture in the elastic strata was suggested for modeling an earthquake source [98, 204]. The elastic waves generated by displacements along the earthquake fault can be found by summation of the pulses radiated with a delay - that is, determined by rupture velocity. The latter is limited by the Rayleigh wave velocity but can be even less because of branching effects. Slippage along an existing fault has the same limitation. In experiments with dunite, the slip velocity in the interval from *1 km/s* up to the shear wave velocity *4.6 km/s*, was measured.

Proper calculations show that the bulk wave spectrum has the typical form, with kink and characteristic corner frequency. However, the spectrum can be changed during wave

propagation because of nonlinear effects (as one can see in Figure 7.9, for example), where data were measured before and after crossing the fault body, represented by cataclastically ruptured geomaterial.

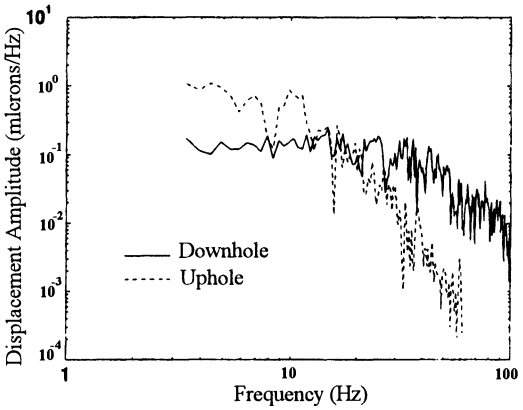

Figure 7.9. Earthquake wave spectra measured at the ground surface and inside a deep well crossed the fault [1]

The displacement formulae

$$u(t) = \frac{\sigma}{G} c_s \Theta\left(1 - e^{-t/\Theta}\right) \tag{7.16}$$

was suggested J. Brune (see [98]) for the earthquake source and is in agreement principally with curves in Figure 7.9. Here, σ is the pre-existing stress and Θ is the characteristic time of the source, estimated as the effective fault length divided by shear wave velocity. For strong earthquakes, $50\ s < \Theta < 300\ s$.

At the moment of branching (turning), the crack can be arrested and smaller cracks appear ahead of it with the radiation of weak acoustical impulses. This fact can be observed also by optical techniques. The corresponding parts of seismic signals of earthquakes are known as "stopping" phases. Some features of earthquake seismic signals also support the idea of crack arrests or crack turning. So, typical oscillating displacements are explained by the resistance of barriers converting a crack motion into chain of discrete jumps. The different signs of frontal displacements are interpreted sometimes as a result of crack turning. Much laboratory data show the appearance of a small crack cloud ahead of a growing main fracture.

7.2.2. ESTIMATION OF EARTHQUAKE ENERGY

The dynamic characteristic of an earthquake source is the seismic moment [4]

$$\mathcal{N}_0 = GUA \tag{7.17}$$

where A is the fault area, U is the displacement amplitude (dislocation), and G is the usual rigidity. The source energy is estimated by the expression

$$\mathcal{E} = \frac{1}{2}\sigma UA \tag{7.18}$$

Therefore,

$$\frac{\mathcal{E}}{\mathcal{N}_0} = \frac{\sigma}{2G} \tag{7.19}$$

where σ is the stress drop in the source volume.

In practice, the data on seismic signal are used for energy estimations of the earthquake source process. The main source parameter is seismic energy, $\mathcal{E}_s$, found outside the hypocentral earthquake zone (at the distance of *100 km* from the source), where rupture effects become negligible. The value $\mathcal{E}_s$ is connected with earthquake magnitude, M - that is, with special earthquake yield measure, by the Gutenberg-Richter formula [22, 178]:

$$aM = lg(\mathcal{E}_s / \mathcal{E}_0) \quad , \quad a = 1{,}5 \quad , \quad \mathcal{E}_0 = 2{,}5 \times 10^{11}\ erg \tag{7.20}$$

In accordance with the traditional view and on the basis of the elasto-brittle model of earthquake sources, energy $\mathcal{E}_s$ is equal to the full energy, $\mathcal{E}_s$, released from some initially stressed domain because the Griffith energy for creating a new fault surface is negligible. It is possible to estimate a linear scale, R_u, of an unloading domain under the assumption that the rock was initially loaded up to the shear strength, $\sigma_s = const$:

$$R_u = \left(\mathcal{E}_s G / \sigma_s^2\right)^{1/3} \tag{7.21}$$

The typical values $\sigma_s = 1\ kbar = 10^9\ dyne/cm^2$, $G = 0.4 \times 10^3\ kbar = 0.4 \times 10^{12}$ $dyne/cm^2$. If $\mathcal{E}_s = 2 \times 10^{20}\ erg$, it is equivalent to the explosion energy of *5 kt* of TNT or to earthquake energy of magnitude $M = 6$. Then, $R_u = 400\ m$. The contained underground explosion with a *5 kt TNT* yield (for example, in the salt masses) gives the same order of crushed zone: $R_c \approx 200\ m$ [144]. This means that the part of unloading rock may be ruptured and a significant part of the full energy, $\mathcal{E}$, is discharged for this process. Therefore, $\mathcal{E}_s = \eta\mathcal{E}$, and η is the coefficient of earthquake efficiency.

If the individual crack is used as a source model, the dissipation is accounted for by the introduction of solid friction between the faces of the crack. Anyhow, the following estimations are valid even in this case. The stress drop is evaluated by the expression

$$\Delta\sigma = (GK_c / \pi l_o)^{1/2} = const / l_0^{1/2} \tag{7.22}$$

under the assumption that rock toughness, K_c, is approximately constant and that rock strength is determined by internal crack size. The crack size inside the intact sample is of the same order as a grain ($l \approx 0.1\,cm$); in the field, however, $l_0 \approx 0.1 - 100\,km = 10^4 - 10^7\,cm$. Therefore, the following estimation can be used:

$$\Delta\sigma = \sigma_s (l_* / l_o)^{1/2} \approx 1000\,bar \times 10^{-3} = 1\,bar \tag{7.23}$$

where σ_s is the bearing capacity (strength) of the intact sample.

However, this estimation is arbitrary because of the too-wide interval of l_0 of the earthquake source. Recall that the size l_0 must correspond to the initial crack - that is, to only *1%* of the real fault size, l, created by the earthquake. Therefore, a more reasonable approach is connected with the seismic moment concept (7.2). The corresponding calculation gives the order of *1 bar* as the lower boundary. The stress drop grows up to *100 bars* with the depth of the source:

$$\Delta\sigma \approx 1 \div 100\,bar \tag{7.24}$$

Because the seismic moment is calculated on the basis of a seismic-wave amplitude, this stress-drop value corresponds to wave amplitudes in the outer elastic zone.

However, measurements of unloading waves during brittle fracturing of solid bodies showed that their amplitudes have the order of the initial strength, σ_s, of a failed body [101]. Taking into account the residual strength, σ_r, of the rock mass, the amplitude of radiating waves must be proportional to the difference, $\sigma_s - \sigma_r$. Because the energy of elastic waves is proportional to square of their amplitude, the following estimation holds if $\Delta\sigma \approx 1 - 100\,bars$ and $\sigma_s - \sigma_r \approx 100 - 1000\,bars$ [147]:

$$\eta = \frac{\mathcal{E}_s}{\mathcal{E}} \sim \left(\frac{\Delta\sigma}{\sigma_s - \sigma_r}\right)^2 \approx 10^{-6} \div 10^{-2} \tag{7.25}$$

According to rock-burst data [124], the seismic efficiency coefficient has an even smaller order, $\eta = 10^{-4}$. Estimations of the work, $\mathcal{E}_g$, done on the gravitational forces (the mass uplift which is measured by geodetic methods) also gives the energy, $\mathcal{E}_g \approx (10^2 \div 10^3)\mathcal{E}_s$ which is much more than the seismic energy. Energy $\mathcal{E}_g$ as a measure of the elastic energy storage before the earthquake, is again in agreement with estimate (7.25).

Let us suppose that the efficiency coefficient η has the same order as the coefficient of mechanical efficiency of an underground contained explosion - that is, $\eta \approx 0.01$. Then the usage of $\mathcal{E} = 100\mathcal{E}_s$ in the expression (7.21) allows determination of the true scale R_{tr} of the elastic energy-release domain.

The typical values are given in Table 7.2 for some earthquake magnitudes and energies. The linear scales of the aftershock zone A and the precursor duration Θ are given here also. From Table 7.2, you can see that the maximum earthquake energy corresponds to the linear scale A_m, equal to *100 km*, the mean distance between the giant vertical faults at the crust surface for seismic region. Therefore, intervals between such faults and maximum earthquake energies are interconnected.

TABLE 7.2. Earthquake source parameters [147]

Earthquake	Moderate	Strong	Catastrophic
Magnitude [M]	*5*	*7*	*9*
$\mathcal{E}_g$ [erg]	10^{19}	10^{22}	10^{25}
$\mathcal{E}_g$ [TNT]	*1 kt*	*1 Mt*	10^3 *Mt*
R_u [km]	*0.1*	*1*	*10*
$\mathcal{E}_g$ [erg]	10^{21}	10^{24}	10^{27}
$\mathcal{E}_g$ [TNT]	*100 kt*	*100 Mt*	10^5 *Mt*
R_{tr} [km]	*1*	*10*	*100*
A [km]	*10*	*30*	*100*
Θ [days]	*100*	*1000*	-

The scale of *100 km* also corresponds to the concept that the unloading of an entire lithosphere block takes place during extremely strong earthquakes.

Because crustal materials have the same order of strength, there is a universal law of proportionality between earthquake magnitude and the rock volume unloading which releases earthquake energy. It was found that while earthquake sources take place near faults, they occur more often in more rigid block (with higher seismic velocities) that can accumulate an elastic energy. So, the elastic energy distribution is not uniform in crustal masses.

7.2.3. LITHOSPHERE FAULT SYSTEMS

Figure 7.10 presents generalized correlations for magnitudes, M, maximum fault length, l, and scale, L, of intervals between various faults (1, 2 - Central Asia, 3 - California and Nevada, 4 - San Andreas region) in terms of the above-mentioned values.

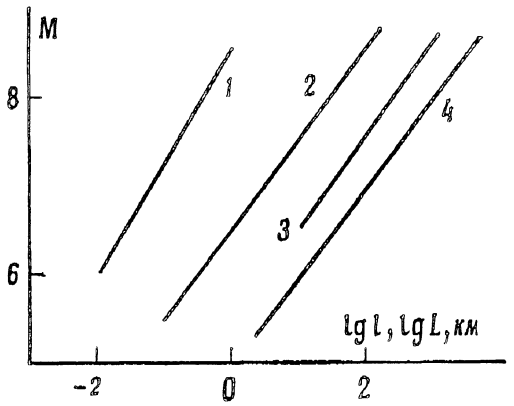

Figure 7.10. Earthquake magnitude correlated with fault geometry in the lithospheric plane (Courtesy of A. A. Nikonov).

Estimation (7.21) uses the idea that stress concentrations up to the strength σ_s can exist in rock masses. Calculations of continental plate motion show that the boundary stresses, acting from the asthenosphere, only have the order of *10 bars* due to relatively small viscous forces at observed velocities, but stresses increase up to several kbars at plate contacts. The crust differential stresses of *1-3 kbars* are supported by the mineral twinning data, by the dislocation density, and by other typical microfeatures of rocks such as recrystallization (paleopiezometric) data. It is necessary to recall that the tectonic stress level (*100 bars* or *1000 bars*) has fundamental importance to geodynamics because the rheological models necessary for calculations of many geological processes are selected on the basis of these values.

Increasing the full earthquake energy by factor of 10^2 in comparison with the seismic energy introduced by the elastic estimation (7.21), corresponds to the dissipation of mechanical energy (as in underground explosions) caused mainly by the solid friction between fragments in the rupture zone. Local rupture zones appear ahead of a main fault because of the stress concentration before the dynamic growth of earthquake faults as well as in the moment of its arrest. This dilatant zone may move with the fault tip at the steady-growth stages and followed by a trace of crushed material. Under the action of tectonic stresses, this trace will be compressed into a narrow band along the fault edges. For the given stationary set of observation stations, this results in the apparent disappearance of the dilatant zone.

Near the fault in deep mines, there are a set of subparallel shear bands, including crushed geomaterial and a set of branching cracks. Almost all the released energy is spent to create the zone of crushed rock along the fault (the so-called gouge zone). Well-

developed fault breccia can be saturated by groundwater, as it occurred after the Kita-Itzu earthquake (1930) in Japan, where the fault crossed the tunnel. Dynamically, this process corresponds to the stick-slip phenomenon.

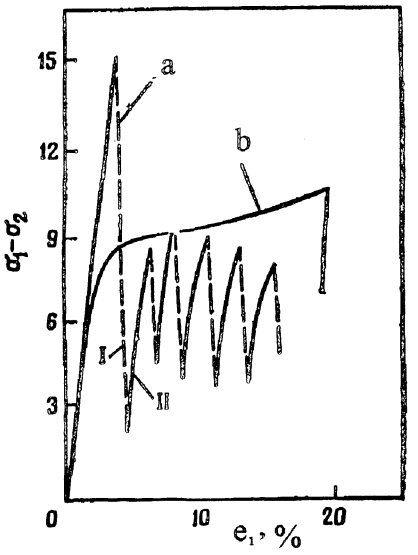

Figure 7.11. Stick-slip phenomena for dunite (a) and dunite with 3% of plastic serpentine (b) that prevents edges from crushing [25].

It is clear that the stick-slip is explained simply by the alteration of quick stable sliding and its arrest following the crushing of joint edges (Figure 7.11). Really, the PT-interval for a stick-slip coincides with the interval of deformation localization into shear bands and corresponds to the interval in which the solid friction force has the order of rock strength. So, the stick-slip along initial faults also generates volumes of dilatant rupture. The plastification (serpentinite additions) preserves the stick-slip phenomena.

The rock rheology data (Figure 6.1) show wide intervals of pressure and temperature, for which the volume rupture has a dilatant feature. It is clear that in different regions of the Earth, the corresponding thermodynamic conditions are achieved at different depths. This also depends on the tectonic situation [203]. The previous earthquake parameter estimations support the idea that dilatancy effects take place in the Earth's crust. The elasto-plastic model of dilatant deformation (Section 1.3) is valid for many earthquake situations as well as for underground explosion calculations. Stick-slip phenomena also corresponds to generation of the shear band set, having the characteristic linear interval

between them, observed in laboratory experiments with granulated materials and the shear bands investigated in situ.

There are three main types of crustal earthquakes:

(i) with a main fault without microcrack precursors - that is, without foreshocks (This can happen at a low levels of pressure and temperature.);

(ii) with microcracks (foreshocks) followed by the main fault (the intermediate case);

(iii) with a microcrack cloud in which a main event cannot be discriminated (this can happen at high levels of pressure and temperature) - that is, an earthquake swarm.

The intermediate case corresponds to localizations of deformation (that is, of dilatant cracks) into rupture bands. These concepts are in accordance with the rupture diagram given in Figure 6.1.

Volcanic earthquakes have a form of the earthquake swarm in accordance with the cataclastic flow model of rock masses at high temperatures. Vice versa, a separate macrofault can reach the ground surface and is usually correlated with the magnitude of a main earthquake event. Its orientation correlates with internal friction angle, dilatancy rate and stress components.

Let us discuss the experimental data on a linear scale between faults. A quasistatic modelling experiment was performed with faults in the cement-dust layer after shear has taken place in the basement plane [129]. It was found that the interval, L, between the faults is proportional to the layer thickness, H_*, that is, $l \approx 0.25H_* + 0.3\,(cm)$. The faults appear at some critical shear that depends moderately on H_*, and they grow from the upper surface toward the basement. Later, the set of secondary faults appears that are orthogonal to the primary. For the lithospheric plate scale, this means that the horizontal length scale of giant fault distribution is in correlation with depth or with the depth of the effective shear plane (that is, this scale has an order of the lithospheric thickness). The same result was obtained for a ring (hexagonal) crack system in the theory of bifurcation [71].

According to S. I. Sherman, the depth of the fault, H_*, which is estimated as the depth of seismic activity, is connected with its length, l, by the law $H_* = 1.04\,l - 0.7\,(km)$, with interval $L = 0.29\,l + 1.24\,(km)$ between faults of Baikal ridge. From these two correlations, we can find that $L = 0.28\,H_* + 3.70\,(km)$. This has the same coefficient of proportionality as the laboratory experimental data mentioned above.

The largest continental faults are separated by the *100 km* interval, but this is equal to only *10-15 km* for oceanic crust. The comparison of the continental lithospheric thickness (*100 km*) and the thickness of the ocean crust (*11 km*) underlines the general conclusion that the block scale, and subsequently the earthquake energy, are determined by the thickness of moving lithospheric layer. So, during the largest events, the continental lithosphere moves as a whole above the soft asthenosphere, but the ocean crust can be removed above the basement, represented by plastic serpentine when its fault are created.

7.2.4. EARTHQUAKE ACTION

Earthquake waves spread from its hypocenter creating the most essential damage at the epicenter of the earthquake, that is, at the point of the first wave arrival to a ground surface.

There are two scales of measurements of the earthquake action [22]. The first one utilizes the *magnitude M* concept which is determined by the formula [84, 177]:

$$M = \lg A, \quad [A] = 10^{-6}\ m, \quad (distance = 100\ km) \tag{7.26}$$

where A is the amplitude of displacements observed by seismographs at 100 km from the earthquake epicenter. The largest earthquake had $M = 8,9$.

Sometimes the formulae (7.26) is changed, see, for example, Section 7.3.5, to account for oscillation periods, real distances, types of waves, local conditions, but the main essence is conserved.

The second scale corresponds to earthquake *intensity* which is determined by the damage level and depended more on local conditions at the observation point. According to the Modified Mercalli (MM) scale, there are XII levels. So, the earthquake of level III is felt inside buildings; it is difficult to stand on legs (level VII); fractures appear at the slopes and in wetted soils (level VIII); sand and clay soils are flowing (level X); rails are bended and underground tubes are ruptured (level XI); the total rupture and surface ground waves are visible (level XII).

As for explosion action (see Section 5.2.2), the seismic risk is estimated by the mass velocity criterion and by frequency content of earthquake waves. Because soils and rocks have their own dominant frequencies, the constructions have to have other resonance frequencies.

Zones of equal earthquake damage are limited by isoseist lines. The maximum rupture happens inside a placetoseist zone.

The typical oscillations in lakes are named as seiches. Giant solitary ocean waves known as tsunami can be created in the case of some special action of earthquake waves at ocean bottom.

Water-saturated soil masses can be liquified. Fast oscillations can diminish solid friction and viscous resistance. Slow inertial wave connected with earth block rotations can exist. The latter can be the most dangerous for constructions.

7.3. Dilatancy and earthquake precursors

7.3.1. SEISMIC WAVE CHANGES

The previously mentioned correlation (Section 6.1) of seismic boundaries and geomaterial rupture types inside the Earth's crust is supported by the qualitative accordance of seismic velocities in situ and of sound velocity in fractured samples (Figure 7.12 and 7.13). In general, wave velocities are smaller in seismo-active rupture zones than in seismic gaps. Cracks and pores really influence the seismic velocities in rocks as well as other physical parameters [226]. The natural growth of internal crack sets in dilating rocks decreases sound velocities. So, the closing of initial voids leads to the growth of shear wave velocity, c_s; however, due to the internal fracture, the velocity decreases in granite (Figure 7.12).

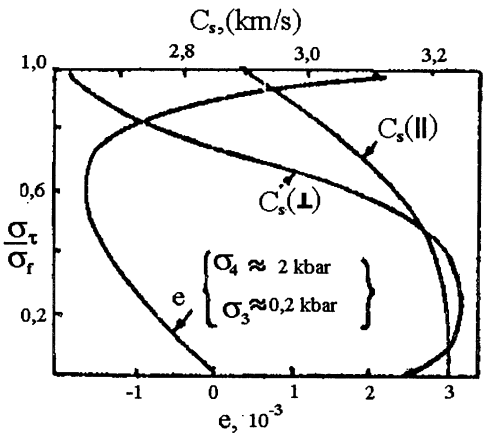

Figure 7.12. Shear wave velocity measured by ultrasound pulses in granite samples parallel or orthogonal to main compression (σ_f= shear strength) (Courtesy of B. P. Bonner).

Travel time data for the compression pulse through dilating sample show the same effects (Figure 7.13). Holography methods have shown that zones of maximum nonelastic strain and velocity decrease migrate through dilating samples during deformation [206].

Geomaterial states in the upper mantle can be also considered but it is necessary to use data for the rupture mechanics of eclogites and peridotites at high pressures and temperatures (in accordance with Figure 6.1). Decrease of seismic velocities observed in some regions below the Moho can be explained by the change of rock composition or by appearance of cracks in mantle rocks. This rupture may be interpreted as a response to the crustal earthquake because the mantle cannot accumulate elastic energy itself due to high-temperature creep effects (Figure 6.3). The appearance of cracks near the phase

transition boundaries can lead also to unstable situations in subducting slabs which, in the case of high rates of phase transition and volume changes, can generate earthquakes.

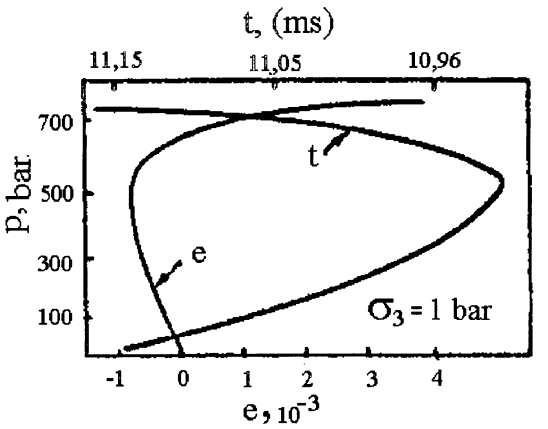

Figure 7.13. Arrival time of ultrasound P-wave in granite sample and its dilatant deformation (Courtesy of B. P. Bonner).

7.3.2. DILATANT LOOSENING AT EARTHQUAKE FAULTS

Seismic wave observation shows that the wave velocity ratio, c_p/c_s, decreases in the earthquake focal zone some months before the event. This reaches a minimum but the anomaly disappears just before the main shock [201]. This anomaly is based on the dilatancy phenomenon, and laboratory experimental data agree with geomaterial changes inside earthquake focal zones. Of course, this also means that tractions and real stress drops in situ have to have the order of several kbars [147]. The dilatancy of rock masses take place in reality only at such levels of stress (but not *1-100 bar*, estimated on the base of seismic energy measurements).

It has been shown experimentally that rock dilatancy is connected with the nonelastic changes of internal crack system [25]. The crack is a defect, characterized by a tangential displacement discontinuity as well as by a normal one (Figure 1.7). Crack voidness increases and seismic velocities decreases. The laws of changes, c_p and c_s, are somewhat different because of crack-system anisotropy. As a consequence, the ratio, c_p/c_s becomes a sensible indicator of a future earthquake (Figure 7.14).

The build-up of this seismic anomaly before the main shock can be explained by the influx of water into the focal crack zone and the growth of c_p-velocity. The corresponding motivation is called a diffusion-dilatant model. Water diminishes effective stresses; in addition, rock strength decreases because of the wetting effect. Besides, the

dilatant loosening can be changed to compaction just before rupture even without water. Crack acceleration results and generates an earthquake.

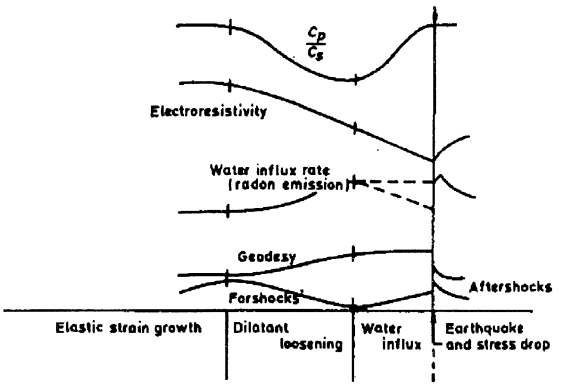

Figure 7.14. General scheme of earthquake precursors [199].

In which way does the dilating volume appear in the earthquake focal zone? The upper part of lithosphere consists of brittle-elastic blocks, and the lower part is represented by geomaterials in the superplastic (cataclastic) state. Therefore, the continental drift creates kinematic discordance in a rheologically stratified crust that can be resolved by earthquakes. Real stress concentration near existing faults reaches the elastic limit, and the dilatant plastic localized zone appears. These zones can be observed as a seismic anomaly. The dilatant zone moves simultaneously with the crack (fault) tip; for immovable observers, this means that local seismic anomaly changes with time. So, the "wandering" of earthquake source can be recorded. Earthquake events correspond to unstable mechanical situations in which deformations of dilatant zones grow while stresses decrease.

The microcrack cloud was observed ahead of main faults. This cloud is a dilating zone. Special laboratory tests with some model materials show that this cloud can be observed by ultrasound waves; real dilatant zones are observed by seismic waves in situ.

It is discovered that during rebuilding of c_p, c_s-values, the crack voids are reorganizing into thin bands inclined to the main compression axis, that is, the localization process takes place before the earthquake although thin bands can be invisible in the seismic field. It is another possible scenario of dilatant anomaly disappearence (in addition to water influx).

Cracks in the cloud are 10 times smaller than the main fault and even the linear scale of cloud itself is smaller than the elastic unloading zone. That is why a dilating zone scale does not correlate with earthquake energy [147].

7.3.3. EARTHQUAKE PRECURSORS

Earthquake precursors [136, 180, 204] includes a seismic velocity anomaly, geodetic data of surface uplift, release of radon and helium from rock strata, foreshocks, etc. The duration, Θ, of precursors and scale, A, of an aftershock zone (that is, of unloading zone) and earthquake magnitude, M, are connected (Figure 7.15). All objective precursors of earthquakes have physically understandable links with dilatancy effect inside the earthquake's focal zone.

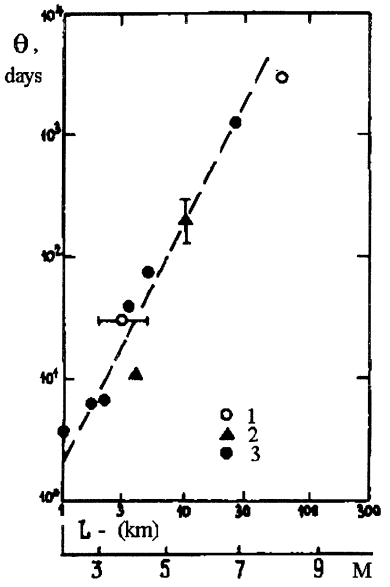

Figure 7.15. Precursor duration and earthquake scale:
1 - crust displacements, 2 - radon, 3 - c_p/c_s ratio [2].

The increase of radon content in groundwater near the earthquake source is proportional to the surface area of fresh cracks in the rocks. Adsorbed water can also migrate along the dilatant crack system.

Creation of the crack system changes the electroresistivity of the rocks, and the water influx again has an essential effect. A sharp decrease of electroresistivity of dilating granite after saturating with water or its vapour was observed; however, electroresistivity of dry dilating rocks grew.

Dilatancy also changes the magnetic fields. Electromagnetic impulses are observed during internal fracturing. A very detailed laboratory study of the electric phenomena at rocks and ceramic ruptures shows the correlation between the seismic radiation,

modelled by acoustic emission, and electro-ionic radiation, generated by surface currents at crack edges.

Water effects ion migration, which gives additional electropulses after rupture. This emission is observed as lights (of earthquakes) in dark laboratory. The latter (and ultrasound) may explain the unusual frightening of animals in dark earthen cavities before an earthquake.

The sources of foreshocks and aftershocks are explained by nonsteady cracks whose scales are much smaller than the earthquake fault. So, the foreshocks and aftershocks are signals of dilatant-crack creation in the zone of stress concentration. Aftershocks of the Parkfield earthquake were generated in a narrow zone along the fault but the aftershock zone at the Tango earthquake was very wide. The difference of the radiation zone of foreshocks and aftershocks can be interpreted in the following way. The initial dilatancy zone coincides with the foreshock zone. Due to the localization of deformation, the number of foreshocks diminishes. The main earthquake event leads to unloading of the ambient rocks, where new cracks are generated, and radiates aftershocks.

The exponential growth of acoustical emission coincides with the dilatancy onset, additional signals are correlated with dilatancy stages. To check the correlation of earthquake swarms and cataclastic flow, it is necessary to study acoustical emission at high temperatures. Acoustical emission, which is treated as seismic radiation on a small scale, begin when the stress reaches the maximum prestress level. This is the so-called Kaiser effect. However, in the dilatant zone, the Kaiser effect becomes invalid [104].

7.3.4. SPREADING OF DISTURBED ZONES

The velocity of aftershock zone propagation was measured. Values of *30* to *100 km/day* were found. After the underground contained nuclear explosion of Benham, the aftershock zone spreaded with a velocity equal to *2* to *3 km/day*. This motion might be connected with a pore-water wave in a crack set.

A good argument for the model of pore-pressure diffusion is the dependence of duration, Θ, of the earthquake precursors on the scale, A, of the aftershock zone (Table 7.2). As can be seen, $\kappa\Theta = A^2$ if piezoconductivity $\kappa = 6 \times 10^4\ cm^2/s$. However, for the diffusion process, continuous changes are characteristic and beginning of a rupture is not determined if diffusion is linear.

The hypocenter migration of the Mazusiro earthquake swarm was definitely connected with water uplift [164]. However, pore-space deformation is induced by the tectonic process, and water penetration happens under other conditions than lithostatic pressure constancy valid in the case of piezoconductivity process (Section 3.1). Precursor duration Θ and the scale, A, of the aftershock focal zone are dependent on earthquake magnitude, but seismic-anomaly amplitude has the same order for very different magnitudes. This means that magnitude increase leads to the volume growth

under preparation for a rupture, but orders of dilatancy and strength parameters of geomaterials are invariable for the crust geomaterial.

Geodetic methods show that the ground (ocean) surface uplifts at the earthquake hypocenter. Such an uplift agrees with dilatant changes of geomaterial volume. The reverse settlement of the ground surface after the earthquake has the velocity that coincides with the consolidation theory of saturated media (if $\kappa \approx 10^4\ cm^2/s$).

There is one more typical diffusion-type process. It is connected with the transfer of tectonic loading. The tectonic forces may propagate along the boundary between the lithosphere and asthenosphere according to the Elsasser theory [60] of stress migration (Section 7.4). Estimations for the Kuril earthquakes give the characteristic value of $\kappa_E = H_1 H_2 E/\mu \approx 10^6\ cm^2/s$ - that is, 100 times higher than the pressure-diffusion coefficient [147]. Here, H_1, H_2 are the lithospheric and asthenospheric thicknesses ($\approx 100\ km$ each), respectively. E is the Young modulus of the lithosphere ($10^{11}\ dyne\ /\ cm^2$), and μ is the viscosity ($10^{19}\ poise$).

However, sometimes tectonic changes definitely evolve from the diffusion scheme. The aftershock activity velocity can have the order of *100 km/day* (the Tockhachi-Oki earthquake of 1968) [136]. Such a velocity is much less than seismic velocities and may be connected with the front of some nonlinear wave or with a single crack growth with stop-phases before every next event. In other words, aftershock activity can be analogous to a stick-slip phenomenon distributed in space. The aftershock activity is usual for shallow earthquakes and decays with distance according to logarithmic law. In the case of mantle earthquakes (sources deeper than *100 km*), aftershocks are rare and in accordance with the concept of true plastic rheology of geomaterials surrounding subducting slabs at such depths.

The number of shocks, N, is connected with magnitude, M, by the simple law:

$$\ln N = a - b M \tag{7.27}$$

which is apparently connected with crack distribution. The longer a crack, the larger is M, but the bigger volume is unloaded by this crack appearance and, therefore, the number of cracks diminishes. Such a speculation utilizes *de facto* the concept of uniform energy flux rate into the Earth's crust and of an approximate constancy of crustal geomaterial strength [147].

Tectonic forces act in large crustal volumes. As a result of the wide distribution of dilatant cracks, earthquake "precursors" are observed long away from future earthquake sources. For example, the hydraulic sensor can show (see Section 7.5.1) the decrease and following increase [213] of ambient rock stress (that is, the unloading and subsequent reloading processes that take place at big distances from focal zones). Such a void change, which decays with epicentral distance, sometimes leads to groundwater disturbances.

It is necessary to note that the groundwater level follows also the Earth's tides, which can be definitely observed if disturbances connected with atmospheric pressure variations

are excluded. In regions of seismic activity, it is possible to measure changes of heads and well productivity corresponding to preparation of rock masses to earthquakes as well as to tides [192]. The aquifiers themselves work as hydraulic sensors (see Section 4.4.2). These changes can have different signs that depend on orientation to the earthquake fault.

Changes of fluidoregime of seismic activity or water intrusion into a gas reservoir (as in the case of Gazli in Central Asia) can lead to earthquakes [141]. Seismic emission was mentioned in Denver, where waste waters were injected into rock masses [89]. Correspondingly, the idea of possible earthquake control by pore-pressure adjustment was formulated. Intensive gas and oil production can change tectonic stresses in ambient strata and generate earthquakes even without water-mass redistribution [81].

Dilatant zones can appear not only at fault tip but also at the faces of faults during stick-slip phenomena. This concept is similar to that of cutting asperities as a reason for stick-slip phenomena.

It was shown that increasing pore pressure can avoid stick-slip. The stick-slip is associated with the acoustic emission, with stop-intervals increase (during crashing of intact material) and with constant acoustic intensivity during stable slip (when asperities have been cut). Rock saturation with water makes acoustic emission weaker.

7.3.5. EARTHQUAKE MONITORING

The seismic attenuation coefficient, b, can also be used as a possible earthquake precursor in dilatant zones. This idea was utilized by comparison of the earthquake energy, $\mathcal{E}_s$, values measured at the different seismic stations in seismoactive regions [121].

The Russian earthquake classification is based on the value K (instead of magnitude M) such that

$$K \approx B_\varepsilon \, lg\mathcal{E}_s \approx B_A \, lgA \tag{7.28}$$

where A is the wave-displacement amplitude. Approximately,

$$A_i \approx A_0 \exp\{- b_i (x_i - x_0)\} \tag{7.29}$$

where A_0 is the initial value of A, b_i is the attenuation coefficient and $x_i - x_0$ is the distance travelled by the wave along the seismic ray from the earthquake hypocenter to the i - th seismic station.

Now, it is evident that the difference of K-values

$$\Delta_{ij} K = K_i - K_j \approx D_j - D_i \tag{7.30}$$

can show the change of cumulative dissipation of seismic energy along the i - th and j - th seismic rays:

$$D_i = b_i(x_i - x_0) \tag{7.31}$$

Correspondingly, the acting net of seismic observatories can be used to determine the energetic measure, K (or M), for every station. The next step is to determinate differences (7.30) for all pairs of the observatories. The anomalies (three times the deviation from the mean-square level) can be found at the temporal graphs of the K-differences. This gives us another possibility for predicting future earthquakes.

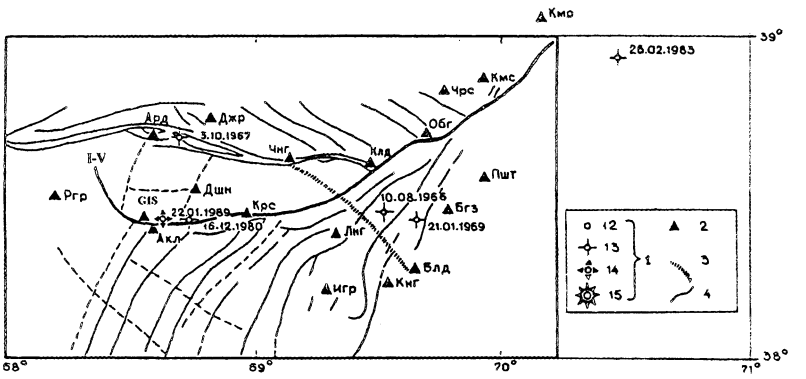

Figure 7.16. The Dushanbe-Vahsh region: (1) earthquake epicenters with K ≥ 12 and data, (2) seismic stations with their symbols, (3) Faizabad-Muminabad lineament, (4) other faults (I - V Ilyak-Vahsh fault) [121].

For example, for the Dushanbe-Vahsh region (Figure 7.16), the following formulae is used:

$$K = 1.8\ lg(A_p + A_s) + 2.1\ lg\ t_{s-p} + 0.7 \tag{7.32}$$

So, the difference (7.14) can be expressed as

$$\Delta_{ij}K = 1.8\ lg\frac{(A_p + A_s)_i}{(A_p + A_s)_j} - 2.1\ lg\frac{(t_{s-p})_j}{(t_{s-p})_i} \tag{7.33}$$

where A_p, A_s are the P and S-wave amplitudes, and t_{s-p} is the difference of arrival times of the same waves (at the stations i and j).

Let us note that (7.33) can be both positive and negative because $(A_p + A_s)$ diminishes but t_{s-p} increases with the travel distances.

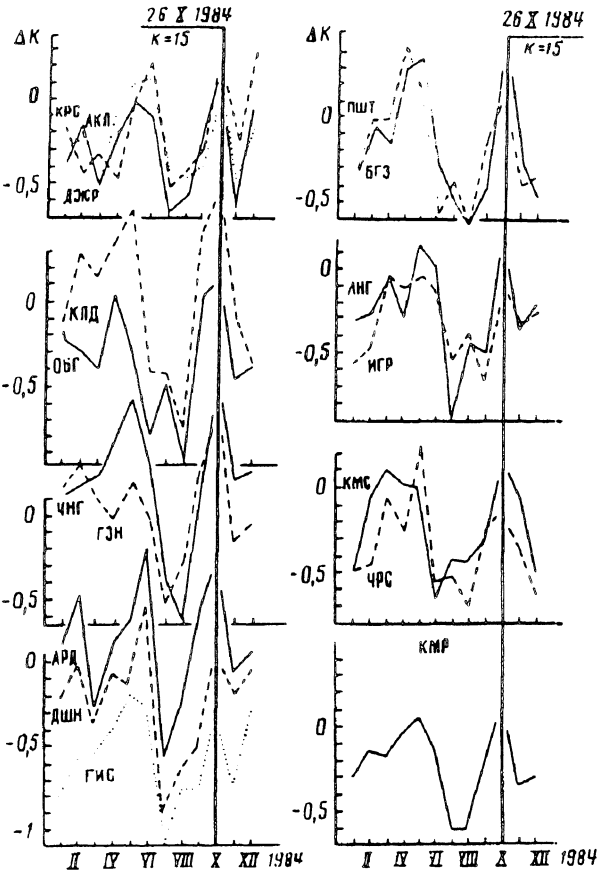

Figure 7.17. The K-difference for the base station, KMP, and others before the Djirgatal earthquake [121]. (The last graph is averaged over all stations; the vertical line corresponds to the earthquake.)

7.3.6. EARTHQUAKE PREDICTION IN THE PAMIR REGION

The net of 22 seismic stations in the Dushanbe-Vahsh region is given in Figure 7.16. It is convenient to fix one "basic" station and to calculate the K-difference for all others on that one. Further data are averaged in one-month intervals. If the "basic" station is close to the future earthquake, the anomaly is evident.

In Figure 7.17, the data for $\Delta_{ij}K$ are given for the base KMP station. The seismograms for events with $K \geq 7.6$ were used. You can see the anomaly (minimum) 2 to 3 months before the Djirgatal earthquake (October 26, 1984). The last part of Figure

7.17 presents the data averaged over previous K-differences for all stations compared with the KMP base.

Using the KMC-station as the base (for events with $K \geq 7.6$) gives the same results (but not for any other station as basic one). This means that the zone of dilatant preparation was near the KMP station. The event of October, 26, 1984 took place in the same sector of the region $(71{,}2^0$ E, $39{,}2^0$ N). The same results were obtained for events before the Garm earthquake (26.02.1984, $K = 13.6$) in the same sector (Figure 7.17). The Faizabad-Muminabad flexure-fault lineament, shown in Figure 7.16, was revealed from satellite pictures. The stations gave more stable K-data here, maybe because the crust was hardened by previous tectonic activity along the lineament.

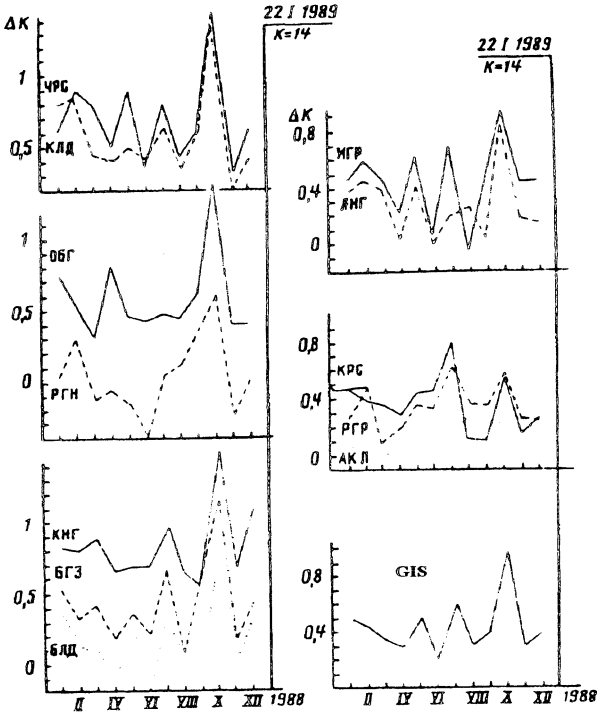

Figure 7.18. The K-difference for the base station, GIS, and others before the Gissar earthquake. The last graph is averaged one over all station [121].

The results (Figure 7.18) of the Gissar earthquake (January, 22, 1989) also shows the K-difference anomaly but of op posite sign (maximum before event).

It is necessary to note here that crustal events were used as sources for seismic sounding, but it is possible to use earthquakes with hypocenters in the Hindu-Kush mantle. It is also quite possible to use explosions as the source of seismic waves.

7.4. Large-scale tectonic waves

7.4.1. TECTONIC STRESS DIFFUSION

Long-term observations for stable seismovelocity anomalies have shown that they can be periodically changed in the zones adjoining to giant lithospheric faults, although this periodicity is not always connected with earthquakes. It was found that seismovelocity anomalies can propagate as a wave. For example, in the Garm region (Pamir - Hindu-Kush) such a wave has as a velocity equal to *7 - 33 km/year* and the period $T \approx 3$ *years*, and this agrees with a number of earthquake events [113]. These waves play the role of a trigger for faults which are "ready" for further growth.

The Elsasser theory of tectonic stress diffusion, mentioned above, is in good agreement with the spread of the aftershock zone but cannot be identified with periodic phenomena. The Elsasser tectonic changes correspond to momentum balances of the lithosphere-asthenosphere interaction [60]. Cross-sectional averaging of lithospheric stresses gives the balance for the plane one-dimensional case:

$$\frac{\partial \sigma_{xx}}{\partial x} = \frac{1}{H_1} \sigma_{xz}(H_1, t) \tag{7.34}$$

where H_1 is the lithospheric thickness, and σ_{xz} is the tangential force acting at the lithosphere's lower boundary.

Lithospheric displacement $u(x,t)$ is determined by the average Young's modulus, E, and the mean lateral stress

$$\sigma_{xx} = E \frac{\partial u}{\partial x} \tag{7.35}$$

which is also equal to the boundary value of the displacement velocity due to creep flow in the asthenosphere:

$$\sigma_{xz} = \frac{\mu}{H_2} \frac{\partial u}{\partial t} \tag{7.36}$$

Here, μ is the asthenospheric viscosity, and H_2 is the asthenospheric thickness, beneath the lower boundary of which geomaterials are immovable.

The combination of equations (7.34) through (7.36) gives the resulting stress-diffusion equation

$$\frac{\partial u}{\partial t} = \kappa_E \frac{\partial^2 u}{\partial x^2} \quad ; \quad \kappa_E = \frac{E}{\mu} H_1 H_2 \tag{7.37}$$

where $\mu / E = \theta$ is the time of relaxation, equal approximately to *3 years*, and $H_1 \approx H_2 \approx 100$ *km* - that is, $\kappa_E \approx 3000$ *km*^{2}*/year*.

7.4.2. TECTONIC SOLITARY WAVES

Consider [150] viscous asthenosphere flow, which is assumed to be incompressible - that is,

$$\frac{\partial v}{\partial x} + \frac{\partial w}{\partial z} = 0 \tag{7.38}$$

Here, $v = \partial u / \partial t$ is the plane velocity, and w is the vertical velocity that is nonzero if $\partial v / \partial x \neq 0$. So, the vertical displacement, η, at the contact ($z = H_1$) between the asthenosphere and the lithosphere will be essential:

$$w(x, H_1, t) = \frac{\partial \eta}{\partial t}, \quad \eta = \eta(x,t) \tag{7.39}$$

Therefore, bending of lithosphere must be introduced to the Elsasser theory. Let us represent a velocity field of the asthenosphere in the following form (Figure 7.19):

$$v = \left(v_0 + \frac{\partial u}{\partial t}\right)\frac{z}{H_2} + \left(B_0 + \frac{\partial \Phi}{\partial t}\right)\left(\frac{z}{H_2}\right)^2 - \left(\frac{\partial \Phi}{\partial t}\right)\left(\frac{z}{H_2}\right) \tag{7.40}$$

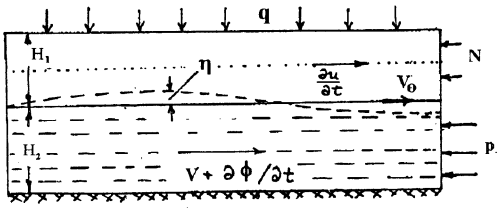

Figure 7.19. Scheme of contact interaction of a bending lithospheric plate and viscous asthenospheric flow.

The incompressibility equation (7.38) can be integrated across the asthenosphere, the bottom of which is assumed to be rigid and impermeable. Thus:

$$\frac{\partial \eta}{\partial t} + \frac{H_2}{2}\frac{\partial^2 u}{\partial x \partial t} - \frac{H_2}{6}\frac{\partial^2 \Phi}{\partial x \partial t} = 0 \tag{7.41}$$

The momentum equation of such a flow

$$\frac{\partial p}{\partial x} = 2\mu \frac{\partial^2 v}{\partial z^2} \tag{7.42}$$

allows determination of the mean pressure $< p >$ at the cross-section:

$$H_2 \frac{\partial < p >}{\partial x} = \frac{2\mu}{H_2}\left(B_0 + \frac{\partial \Phi}{\partial t}\right) \tag{7.43}$$

The lithosphere can be treated as a thin plate under the action of compressive force

$$N = \frac{EH_1}{1 - \nu^2}\frac{\partial u}{\partial x} \tag{7.44}$$

of bending moment (see Section 7.1.5)

$$\mathcal{M} = \frac{EH_1^3}{12(1 - \nu^2)}\frac{\partial^2 \eta}{\partial x^2} \tag{7.45}$$

of its own weight, $q = \gamma(H + \eta)$, shear force, $\tau(h)$, and normal pressure, $p(h) \approx < p >$, from the asthenosphere. Here, ν is the Poisson's ratio. The balance of all bending moments means that

$$< p > = q + \frac{EH_1^3}{12(1 - \nu^2)}\frac{\partial^4 \eta}{\partial x^4} + \frac{\partial}{\partial x}\left(N\frac{\partial \eta}{\partial x}\right) \tag{7.46}$$

These equations give the vertical displacement of the lithosphere:

$$\frac{\gamma}{E}\frac{\partial \eta}{\partial x} + \frac{H_1^3}{12(1 - \nu^2)}\frac{\partial^5 \eta}{\partial x^5} + \frac{\partial^2}{\partial x^2}\left(\frac{N}{E}\frac{\partial \eta}{\partial x}\right) = \frac{2\theta}{H_2}\left(\frac{\partial \Phi}{\partial t} + B_0\right) \tag{7.47}$$

where $\theta = \mu / E$ is the relaxation time of the system composed of the lithosphere plus the asthenosphere. The equation for plane displacements of the lithosphere

$$\frac{1}{1 - \nu^2}\frac{\partial^2 u}{\partial x^2} = \frac{\theta}{H_1 H_2}\left(\frac{\partial u}{\partial t} + \frac{\partial \Phi}{\partial t}\right) + \frac{\theta}{H_1}\frac{\partial^2 \eta}{\partial x \partial t} - \frac{\theta}{H_1 H_2}(v_0 + B_0) \tag{7.48}$$

appears to be a generalization of the Elsasser equation (7.21) due to the vertical displacement ($\eta \neq 0$) and the associated asthenospheric flow ($\Phi \neq 0$). The last term corresponds to the action of continuous continental drift.

The Young modulus, E, of the granitic lithosphere changes from the value of $5 \times 10^{10}\,Pa$ to $5 \times 10^{9}\,Pa$ if it is measured in quasi-static conditions, accounting for dilatant crack growth. That is why it is *10 times* smaller than its value as estimated by P-wave velocity. The range of asthenospheric viscosity is $10^{11} \leq \mu \leq 10^{12}\,(Pa.year)$, and

$2 \le \theta \le 200$ *(years)*. Let us discuss a motion for which $u \approx \Phi \approx 0.1$ *(m)*, $v_0 \approx B_0 \approx 0.1$ *(m/year)*, and $H_1 \approx H_2 \approx 10^5\,(m)$. The gravitational effect is negligible. According to M. Smoluchovsky, the nonlinear buckling term (third one on the left-hand side) of equation (7.31) can be neglected.

Tectonic waves can propagate because of the energy supply from stationary asthenospheric flows. Excluding the variable Φ, the following two equations ($\nu^2 << 1$) in the moving coordinate system can be obtained:

$$\frac{d^2u}{d\xi^2} + \frac{\beta}{H_1}\frac{du}{d\xi} = \frac{\beta(v_0 + B_0)}{4UH_1} - \frac{\beta H_2}{4H_1}\frac{d^2\eta}{d\xi^2} - \frac{6(\eta - \eta_0)}{4H_1H_2} \equiv F(\xi) \tag{7.49}$$

$$\frac{H_1^3}{12}\frac{d^5\eta}{d\xi^5} + \frac{\beta}{2}\left(\frac{3}{H_2}\frac{du}{d\xi} + \frac{6(\eta - \eta_0)}{H_2}\right) = \frac{\beta}{2H_2}\frac{B_0}{U} \tag{7.50}$$

where $\xi = x - Ut$, $\beta = 4\theta U/H_2$. Equation (7.49) can be transformed to

$$\frac{du}{d\xi} = exp\left(-\beta\frac{\xi}{H_1}\right)\int_0^{\xi} F(\xi)\,exp\left(\beta\frac{\xi}{H_1}\right)d\xi + \left(\frac{du}{d\xi}\right)_0 exp\left(-\beta\frac{\xi}{H_1}\right) \tag{7.51}$$

and the choice of the tectonic wave velocity as

$$U = \frac{H_2}{\eta_0}(3v_0 - B_0) \tag{7.52}$$

allows the transformation of equation (7.50). The latter determines the solitary wave form:

$$\left(\beta + \frac{d}{d\xi}\right)\left(\frac{1}{12}\frac{d^5\eta}{d\xi^5} + 3\beta\frac{H_1^2}{H_2^2}\eta\right) = \frac{3}{2}\beta\frac{H_1}{H_2}\left(\frac{\beta}{4}\frac{H_2}{H_1}\frac{d^2\eta}{d\xi^2} + \frac{3}{2}\beta\frac{H_1}{H_2}\eta\right) \tag{7.53}$$

Reference displacement $\eta_0 \approx 0.1$ *m* can be used for estimations. Then the tectonic wave velocity has the order of *300* km/year, or less if $B_0 \neq 0$. The reference deformation $(du/d\xi)_0$ has the order of $10^{-5} \div 10^{-6}$ and the tectonic wave length

$$\lambda \approx U\theta \approx 300\ km$$

diminishes together with the asthenospheric viscosity. However, the buckling effect for such waves could be important, indicating that the resulting equation (7.53) includes the nonlinear term corresponding to potential solitary waves.

7.4.3. GLOBAL GEOPHYSICAL OSCILLATIONS

The direct evidence of tectonic solitary waves was found through the seismic monitoring of nuclear explosions in USA and USSR from 1964 to 1984. It was discovered that the arrival time of P- and S-waves from the Nevada and Semipalatinsk Test Sites to all seismic observatories had periodic components, $\delta\tau$, equal to 3, 6 and 11 years. Moreover, the wave amplitude (Figure 7.20) - or better, the ratio of the wave amplitudes of the same explosion - is independent of the explosion yield but has the same temporal changes [69]. The explanation for this is connected with the response of pores and cracks in the lithosphere and asthenosphere to tectonic stresses migrating in the form of slow waves. Seismic velocities increase under compression, but changes of P- and S-wave dissipation are nonequal. Therefore, temporal changes of the amplitude ratio are observed.

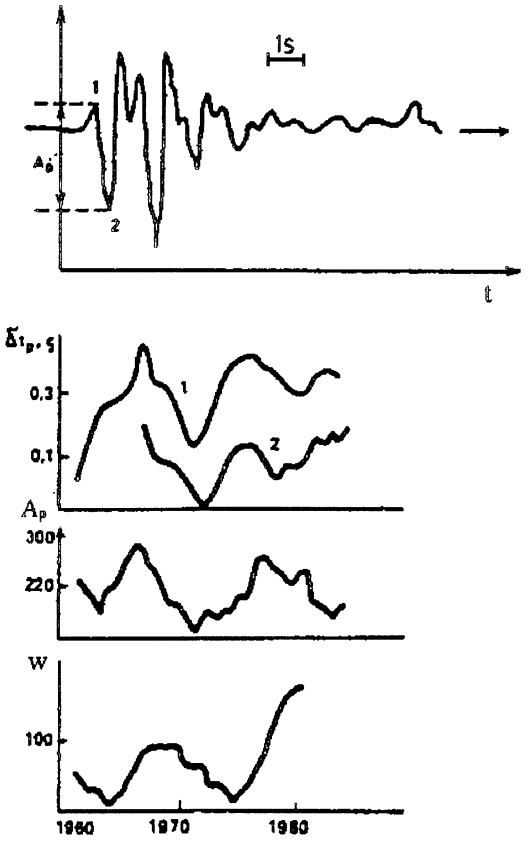

Figure 7.20. Seismogram of P-waves from the nuclear explosion at Nevada Test Site recorded in Borovoe (Kazahstan). Time deviation from the mean value, as well as the amplitude, agrees with the Wolf numbers of solar activity [6].

The independence of these phenomena on the distance of propagation means that the corresponding tectonic migration has wave character. The absence of dissipation of such tectonic waves is explained by the energy supply from continental drift motion - that is, from the stationary asthenospheric flow. E. Luquet et al. [115] have studied all available data of nuclear underground explosions observed by monitoring in the Northern Hemisphere. They found the sequence of the fronts of the tectonic compression wave with the period $T \approx 6$ *years*, moving to North-Western direction with the Northern velocity component $v_N \approx 300$ *km/year* (Figure 7.21). This means that these waves have lengths definitely bigger than the lithospheric thickness.

Moreover, the satellite SEASAT has discovered a set of co-planar lineaments of gravitational anomalies in the Southern Pacific (Haxby W. F., Weissel J. K., 1986) that had the normal oriented also to *North - West*. These are believed to be traces of the tectonic waves which are immovable at the time scale of the satellite measurements. However, the question about generation of these wave must be answered. What is the cause of forced oscillations of the lithosphere?

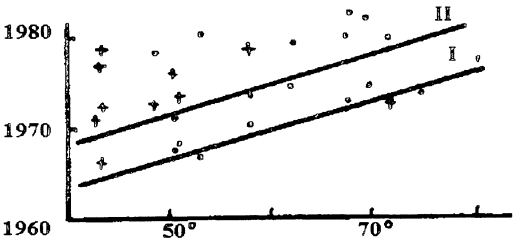

Figure 7.21. Sequence of two fronts of tectonic waves revealed by maximal travel time and amplitudes of seismic waves radiated by nuclear explosion [115].

Let us recall that the geographic coordinate system is rigidly connected with the lithosphere itself, but that the axis of the Earth's spin corresponds to its main masses - that is, to mesosphere. It was found that the spin axis wobbles around the Earth's pole for 439 days (the Chandler wobbling). The path of wobbles is quite strange, but the axis returns to the same point every *6 years*. This could be generated by force interaction of the system "Sun + Earth + Moon" [10]. The traditional explanation is based on the Earth's nutation, which can be influenced by independent Earth-core motions.

As a result, the lithosphere will follow the Chandler wobbles, and the tectonic compression waves are generated due to interaction with asthenosphere. The reverse effect of tectonic earthquakes on the Chandler wobbling is also known. The *6-year* periodicity can be found as a modulator of carefully measured gravitation field oscillations [227].

A periodicity of *10-12 years* was also found in all temporal records of seismic waves which had passed the distance of *90 degrees* from the Nevada Test Site to the seismic station Borovoe, as well as at the distance of *6 degrees* from Semipalatinsk Test Site [6].

It is necessary to note that *11-* and *22-year* periods of solid Earth oscillations cannot be generated by direct action of the solar rays because the atmosphere (which is their receiptor on the Earth) does not have sufficient mass to disturb the solid Earth, although such amplificators as monsoons also have *11-* and *22-year* periods and changes of ice masses at the South Pole must be considered. The correlation between solar activity and all geophysical fields was found for the Tyan-Shan region [114], the mud volcano action at the Caucasus [215], for groundwater levels [55] and for geomagnetic fields.

7.4.4. CYCLING SUBDUCTION SEISMICITY

The wide interval of earthquake depths in subducting plates also provides an opportunity to determine the periodicities in the hypocenter distribution in space and time [120]. Such a construction had provided the extremely surprising conclusion of the reality of some periodic processes, "turning on" earthquakes.

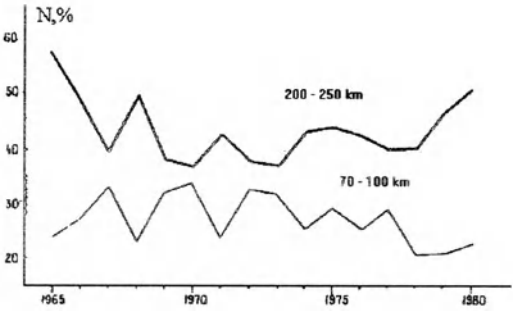

Figure 7.22. Relative seismicity (numbers of events) in two "floors" beneath Hindu-Kush.

Look [120] at the Hindu-Kush region where intercontinental subduction takes place due to a collision of Eurasian and Indian plates. There are two separate "seismic floors" (at *70* to *100* and *200* to *250 km* depths), and the relative seismic activities at these floors are in counterphase (Figure 7.22). This means that in the interval of *135 km* between the floors $(2n+1)$ halfwaves could be placed, given that tectonic waves trigger earthquakes. The observed period is equal to *3 years*. Then the wavelength of *90 km* corresponds to the velocity of *30 km/year*. This is just the value of dilatant state wave mentioned in Garm district in Pamir [113], which means that the Hindu Kush seismoactivity counterphase may be generated by the same tectonic wave but it migrates down, along the subducting slab, compare [136].

This counterphase is also characteristic for crustal earthquakes, separated by a depth interval of *10 km* in Dushanbe-Vahsh region. This means that the tectonic wave has

different signs in lithospheric cross-section, corresponding to the bending of the lithosphere.

The idea that this situation is governed by tectonic stresses is supported by well-known periodic changing of seismic wave velocities and attenuations which can correspond to the Earth solid tides. Moreover, seismic waves in deeper strata are more changed, indicating that the pulsating components of tectonic stresses grow with the depth in the lithosphere or that the crustal waveguides play the role of a damper.

Statistically meanful periodicities were found for earthquakes by many authors, but the deterministic periodical process is evident in the Hindu-Kush case. The distribution of earthquake hypocenters (with energy index $K \geq 12$) inside the Hindu-Kush subducting slab shows an aseismic band with a width of *30 km*. The data scatter has the order of *10 km*. The aseismic band lays under the waveguide. The most important observation is that this seismic gap oscillates in depth with the period of *10-12 years* and with the amplitude of *30 km* (Figure 7.23). Simultaneously, the number, N (per year), of all mantle events with energy index $K \geq 10$ shows the same oscillations. Moreover, the uplift of the aseismic band corresponds to the minimum of the Sun activity and indicates that additional subducting force appearance.(The lower position of the aseismic band corresponds to the maximum lithostatic weight.)

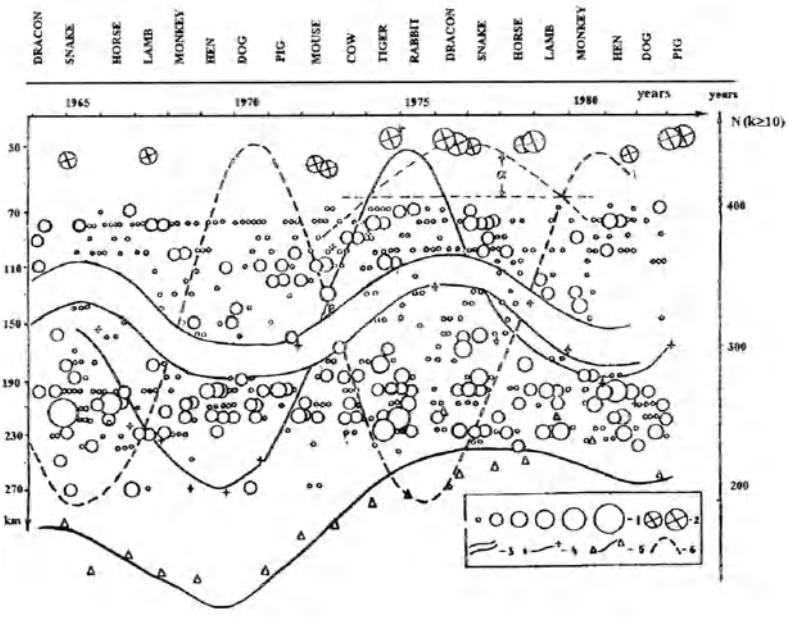

Figure 7.23. Aseismic band in the mantle beneath Hindu Kush (1 = earthquake magnitude, 2 = crustal earthquake, 3 = seismic gap, 4 = mantle earthquakes number, 5 = crust earthquake number, 6 = solar activity) [120, 154].

This situation is not accidental. At another edge of the Indian plate under the Kermadec island arc, the distribution of mantle earthquake hypocenters with magnitude $M \geq 4.6$ also shows the aseismic band but wider and at the depth of *400 km*. We have seen the same *11-year* period and the counterphase shift relative to Hindu Kush oscillations (Figure 7.24). Only the disturbance of the regular periodicity can be seen in 1973, perhaps due to the well-known change of the sign of acceleration of the Earth's own rotation in the same year.

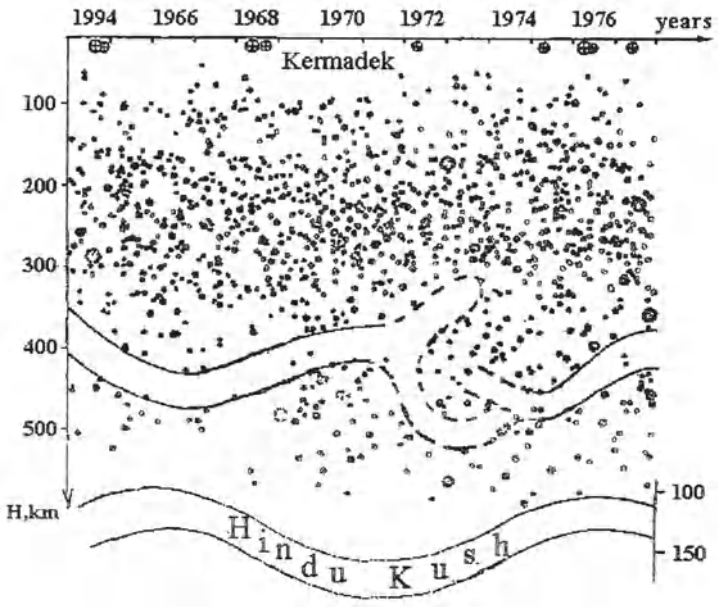

Figure 7.24. Earthquake hypocenters beneath Tongo-Kermadek archipelago and the aseismic band of Hindu-Kush [120].

Such gaps are found also in the Vranch and Pamir areas but the number of events are much less in those regions. The *11-* to *12-year* cycle can be explained by oscillation of the whole Solar System because Jupiter's period of orbital motion, equal to *11.7 years*.

If the *11-year* periodicity is connected with the tectonic stress wave with the amplitude of pressure, Δp, the latter can be estimated with the help of the amplitude, ΔH, of aseismic window wandering inside the subducting slab.

Suppose that this aseismicity is explained by the loss of brittleness due to transition to a plastic state or by some phase transition. The corresponding boundary depends on pressure and temperature and can be defined by intercrossing of transition curve

$$p_* = A_* + B_*(T - T_0) \tag{7.54}$$

and the geotherm

$$p_g = A_g + B_g(T - T_o) \tag{7.55}$$

The analysis [120] gives the equation

$$\Delta H = -\frac{B_g}{B_g - B^*}\frac{\Delta p}{(\rho_l - \rho_a)g} \tag{7.56}$$

and the values $\Delta p \approx 0.1$ *GPa* or *0.01 GPa*, usual for the modern geodynamics, follow. Here ρ_l, ρ_a are lithospheric and surrounding asthenospheric densities, and g is the gravity acceleration.

Examine the Figure 7.23 carefully. The increase of the subducting force (at Solar activity minima) corresponds to the uplift of the seismic gap, to tectonic compression, to the lessening of pore space inside the faults and to the uplift of groundwater.

Comparison with the well-known animalistic calendar shows [154] that this occurs exactly in the Dragoon and Snake years. Conversely, maxima of Solar activity corresponds to droughts, finishing by the Mouse year. So, the calendar, invented in Central Asia (probably in Tyan Shan mountains - the ancient land of Japanese people), has a definite physical motivation.

In the case of hydrological data, it is difficult to separate atmospheric and tectonic effects. However, sometimes the correlations are obvious. For example, there is a pulsating lake, Chany, in the Novosibirsk region. For two centuries, its water have definitely exhibited the Solar period, but deficit was found in water balances. This deficit (shown by d in Figure 7.23) has the same period, although evaporation and all other surface effects are accounted for. So, the deficit could be connected with deep geostratum periodical sources. The water rhythms can be also found on special hydrological maps [55].

The water chemical contents in wells are monitored, as well as radon-gas release, because they can be used to predict earthquakes. Their changes are modulated by the *6-year* periodicity (see Figure 7.25) as well as by microgravitational data (Figure 7.26).

As follows from the work of Tchijevskij [217], the Solar cycle can influence human biology, and it can be definitely found in statistical data on diseases and deaths before the achievements modern medicine.

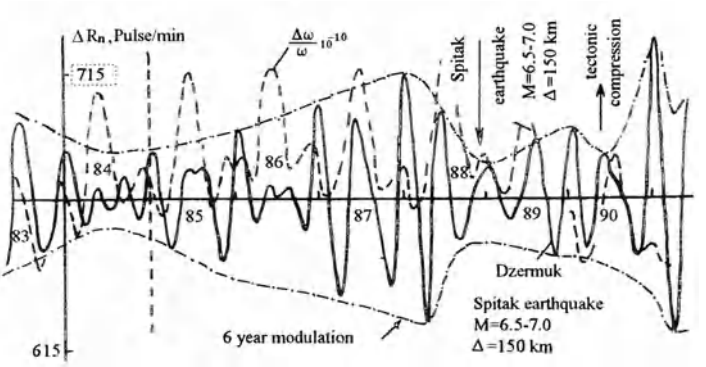

Figure 7.25. Long-term radon monitoring and Earth's rotational spin for Caucasis region (Courtesy of V. P. Rudakov).

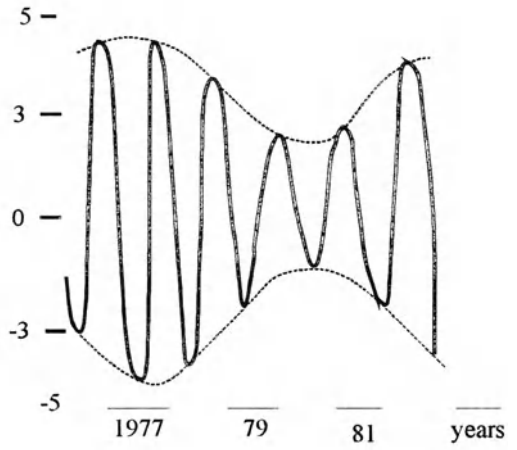

Figure 7.26. Microgravitational changes (μgal) [227] and their *6-year* modulation due to the Chandler wobbling

7.5. Fast tectonic changes and induced seismicity

7.5.1. RADON EMISSION AND TECTONICS

The method of radon measurements in situ is very sensitive to temporal tectonic changes. Radon is a radioactive gas released from a crystalline lattice of rocks that can be accumulated at the adsorption films at air-water or water-oil contacts. The results of radon measurement along the profile above a gas-oil reservoir can be seen in Figure 6.26. The radon data show a stable increase of α-particle radioactivity exactly at the reservoir's outer boundary. Because the half-decay period of radon is small (*3-4 days*), the diffusion is too slow to explain the phenomenon [53].

This idea can be used also to interpret the temporal behavior of subsoil radon content assuming that emission sources are situated at the groundwater level. Really, it can only give a reasonable explanation for the radon response to barometrical changes. Subtraction of these barometric changes permits getting data which are in very good agreement with deep tectonic events.

In Figure 7.27, worldwide data are presented for groundwater radon anomalies before earthquakes of different magnitudes M. You see that these anomalies have much bigger territory than zones of elastic energy release. As was mentioned, amplitudes of the anomaly do not depend on epicentral distances and are assumed to correspond to tectonic strains $\approx 10^{-8}$ [88]. Another important feature is the time dependency of radon precursors on magnitudes. According to [88], for the time interval, *0.1* to *7 days*,

$$\lg\theta = M - 2.16 \tag{7.57}$$

and after *7* days,

$$\lg\theta = 0.62M - 1 \tag{7.58}$$

if magnitude is less than *3*. Correlation are not found for more intense earthquakes.

In any case, radon changes, at the ground surface are an instant reaction to deep earthquake preparation. Of course, diffusion with water through stratificated crustal geomaterial cannot give such high velocity transfer as have radon gases. It can be concluded that only strain changes of saturated geomaterial, filling a fault system, are responsible for such a fast surface radon reaction to deep tectonic events.

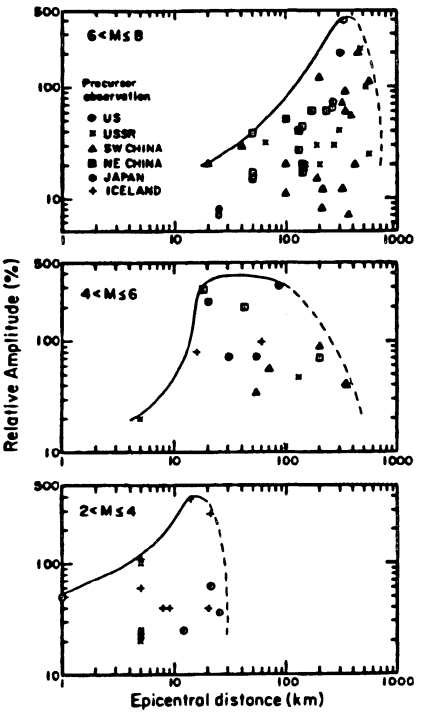

Figure 7.27. Amplitude of groundwater radon anomalies relative to background level as function of epicentral distance for a worldwide data set [88].

7.5.2. WAVES OF FAST PRECURSORS

So, if measuring device is fixed in situ, it can show temporal changes due to vertical movement of a groundwater level generated by compression of fault bodies. On the basis of Central Asia data, V. Rudakov has evaluated that radon-precursor velocity is equal to *7 km/day* (Figure 7.28) [185]. This can only be explained by the interaction of the pore pressure field and tectonic waves.

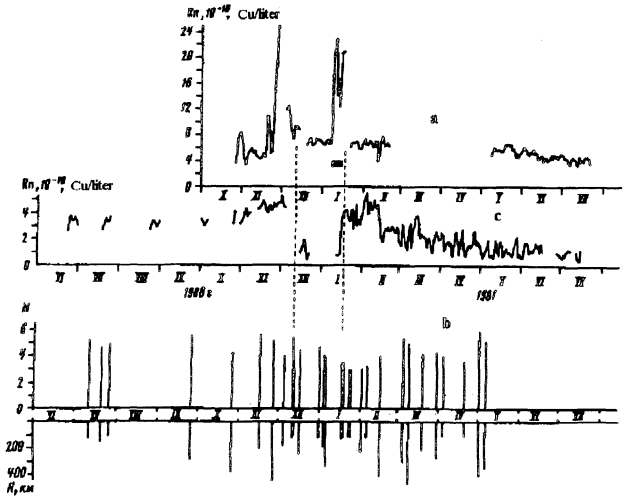

Figure 7.28. Groundwater radon variations at Ganchi (a) and Kata-Airy (c) stations spaced at *50 km* in comparison with the earthquake magnitude, M, and the epicentral distances, R, from Kata-Airy (b) [185].

Other radon data have shown that the tectonic extension period estimated by the lessening of seismic velocities corresponds to radon emission growth; in the case of tectonic compression, however, the radon emission is less. The dynamics of radon level correlates with the changes in Earth's spin (Figure 7.25), with solid-body tides and microgravitation fields (Figure 7.26).

Radon emission of two volcanoes at Kamchatka (Figure 7.29) has shown obvious correlation with tides and volcano trembling. The vibration itself can release radon; moreover, its intensivity depends on frequencies. For example, radon release had a maximum at *18 Hz* vibration and a minimum at *16 Hz* vibration during the experimental work in Byelorussia [141]. Again, the effect of dominant frequency was revealed.

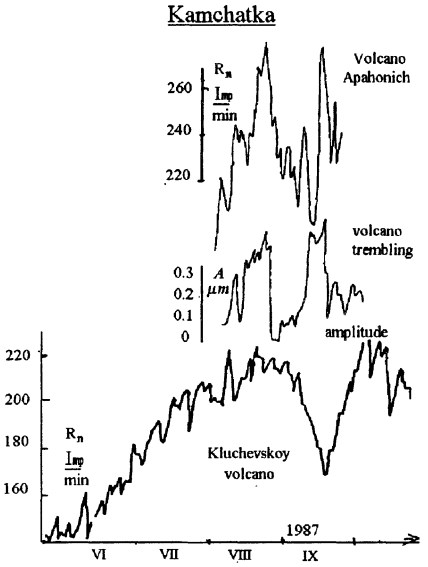

Figure 7.29. Volcano trembling and radon emission (according to V. Rudakov and E. Zhdanova).

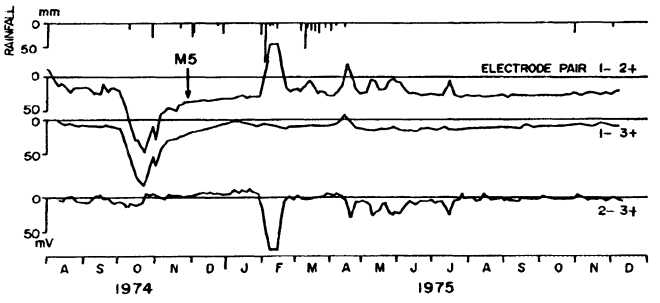

Figure 7.30. Electrokinetic pulses measured by electrode pairs with rainfall and earthquake events [43].

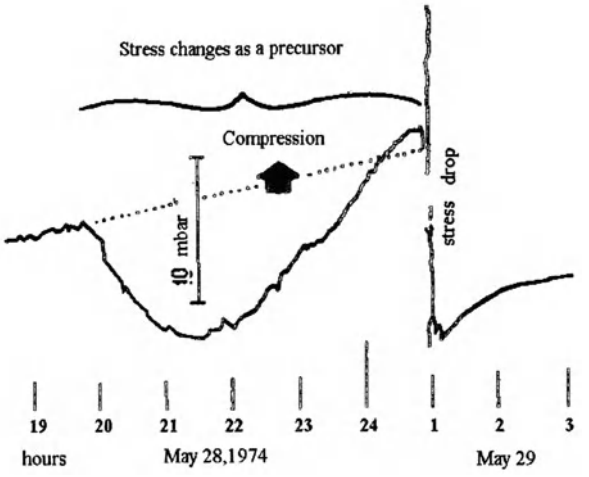

Figure 7.31. Stresses measured hydraulically [213] due to crack compression before earthquake (Courtesy of H.S.Swolfs).

The main conclusion of this discussion is that the electrokinetic pulses, described in Section 4.4 and given in Figure 7.30, strain ([213]; see Figure 7.31) and radon measurements, as well as fluctuations of other geophysical fields which appear before any tectonic event (including earthquakes) have the common origin. The signals have different forms of individual jumps or solitary deformation waves with the velocities from *10* to *100 km/day*. Such a wave velocity is much smaller than the usual P- and S-wave velocities but much higher than wave velocities discussed in Section 7.4. It has to be explained.

7.5.3. ROTATIONAL WAVES IN FRAGMENTARY ROCKS

Let us try to utilize further the generalized continuum model developed in Section 5.4, which includes mean-displacement dynamics together with microstructure dynamics. In the two-dimensional case, the latter has the following forms if it mean motion is negligible [155]

$$\frac{\partial^2 \Phi}{\partial t^2} = c_1^2 \frac{\partial^2 \Phi}{\partial x_1^2} + c_2^2 \frac{\partial^2 \Phi}{\partial x_1^2} - \mathcal{N}(\Phi) \tag{7.59}$$

$$\mathcal{N}(\Phi) = \frac{fR}{\rho_0 J} sin\left(\frac{\pi}{2}\frac{\Phi}{\Phi_m}\right) \tag{7.60}$$

where f is the restoring force multiplied vectorally by the rotation radius ($R \approx \sqrt{J}$). The vector product (7.60) determines the bulk moment of momentum.

Recall that, in practice, the monitoring recorder is attached to a sufficiently large rock block and that the relative displacements, $du \approx bd\Phi$, are measured. Here, b is the base of measurements.

Remember, for interpretation, that if the base, b, of the measurement is less than the scale, R, of blocks, then the displacement is $u \approx b\Phi$; if $b > R$, then relative displacements will be $b(\partial u/\partial x) \approx b^2\, \partial\Phi/\partial x$.

If the block is not separated by cracks from ambient media, then these data can be evaluated by the continuous deformation field, and the conventional wave dynamics are valid. Commonly, however, the block is an element of fragmented masses, and its rotation corresponds to microstructural dynamics (5.111). In such a medium, the wave velocity

$$c_i = \sqrt{\frac{A_i}{\rho_0 J}} = \frac{d_1}{d_2}\sqrt{\frac{G_i}{\rho}} = \sqrt{\frac{G_*}{\rho_*}} \tag{7.61}$$

includes two internal linear scales, d_1, d_2, the ratio of which allows the introduction of effective rigidity, G_*, and density, ρ_*, of fragmented rocks (instead of G_i , ρ for intact rocks) [52].

This value corresponds to real wave velocities in fragmented rock media. It is much larger than deformation wave changes discussed here.

However, a stationary wave is possible, running, for example, along the $x_1 = x$ axis with wave velocity $U \neq c = c_1$:

$$\zeta = x - Ut \tag{7.62}$$

Then equation (7.59) has the form

$$\frac{d^2\Phi}{d\zeta^2} = \frac{\sin\Phi}{1 - c_r^2} \quad , \qquad c_r = \frac{U}{c} \quad , \qquad U = \sqrt{\frac{\pi f R}{2\Phi_m \rho_0 J}} \tag{7.63}$$

where U is a free parameter of the "kink" solution:

$$\Phi = 4\ arctg\left(exp \pm \frac{x - Ut}{\sqrt{1 - U^2/c^2}}\right) \tag{7.64}$$

The velocity, U, is dependent on wave energy [66] and has to be smaller than c. This is the principal result.

Geodetic devices and observations of water levels in wells have showed the step-like changes (Figure 7.32) corresponding to "kink"-wave solution (7.46). The velocity could have the order of *10 km/day*, as in radon measurements, or *1600-11000 km/year* of the trigger migration for great earthquakes [131, 136].

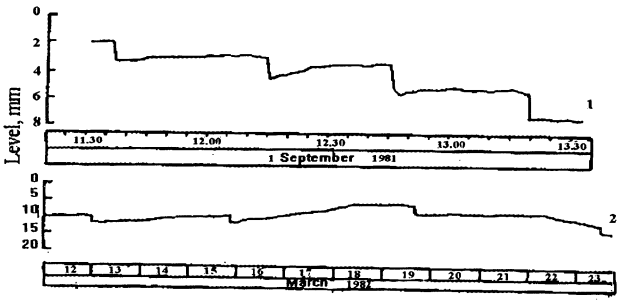

Figure 7.32. Kink-line oscillations of water-well level (1 - well Kim, 2 - well Asht) near Ashgabat (Courtesy of V. Barabanov).

The case of $c_r > 1$ corresponds to an oscillating trail

$$\Phi = 2\,arcsin\left\{sech\left(\frac{x - Ut}{\sqrt{c_r^2 - 1}}\right)\right\} \tag{7.65}$$

and the parameter U has the order of a seismic wave velocity.

If a self-similar solution [106]

$$\eta = \xi\tau, \quad \xi = \frac{x}{\sqrt{c}} + t\sqrt{c}, \quad \tau = \frac{x}{\sqrt{c}} - t\sqrt{c} \tag{7.66}$$

is valid, equation (7.59), transforms to the ordinary differential equation

$$\eta\frac{d^2\Phi}{d\eta^2} + \frac{d\Phi}{d\eta} - sin\,\Phi = 0 \tag{7.67}$$

Numerical calculations give the graphs shown in Figure 7.33 in comparison with modulation envelopes of wave oscillations in the mine after an underground explosion. The main nonlinear feature of the solution is that different phases have different velocities - that is,

$$\frac{dx_i}{dt} = \frac{tc^2}{\sqrt{\eta_i + c^2t^2}} \tag{7.68}$$

So, the wave tail is moving slowly than the front and the wave is spreading. Only the limit velocity $(t \to \infty)$ coincides with the wave velocity $c=const$ when the wave becomes linear seismic. Such a wave was observed by S. Daragan and E. Luquet (1972-1973) as low frequency parts of waves generated by TNT explosions in the fissured zone of previous nuclear explosion in saltrock masses. The first extremum had the wave velocity equal *1100 m/s* and the second *5000 m/s*, and it is unusual for a linear seismology.

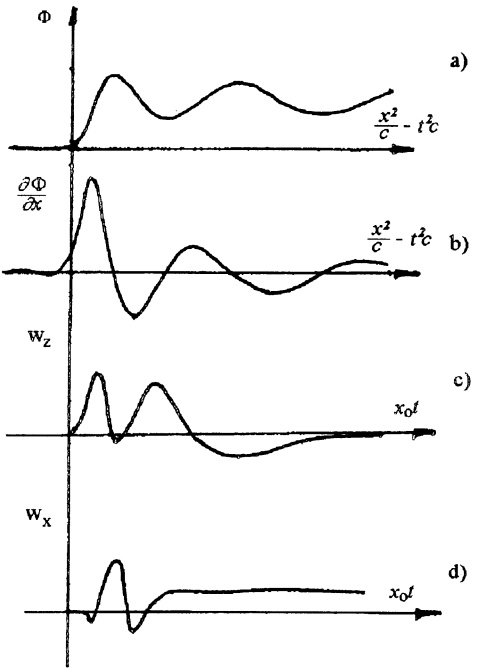

Figure 7.33. Run of a slow deformation wave (a, b) and modulation of seismic blast waves in deep mine (c, d).

So, underground explosions can create intensive slow waves that could play the main triggering role for other seismic events, known as aftershocks, just as the above-mentioned large-scale tectonic waves of many year periodicity.

It was also observed that the vibrator worked with changing frequency (in the interval *15-25 Hz*) could generate a deformation-wave process with a period *25-30 min* [141].

7.5.4. INDUCED DEFORMATION AND SEISMICITY

In many cases the deformation pulses are important for induced seismicity. The latter one is explained by recreation of fault mobility. It was shown that seismic waves could not play such a role at depths because of the stopping effect of solid friction. However, slower redistribution of tectonic forces can create a dangerous situation.

The case of the Lacq gas field [81] in France is wellknown because intensive seismic swarms (more than *800* tremors before 1990) took place due to a large amount of gas production. Initially, the seismicity was diffuse at greater depths. It corresponded to the lessening of pore gas pressure by 500 bars. In following years, seismicity was definitely connected with activization of are-existing tectonic faults.

Other event involve the three Gazly earthquakes (1976 and 1984, with M=*7.0; 7.3; 7.2*) where [141] tectonic faults were active in the Buhara region. Before these events, the intensive uplift of gas-water contacts was mentioned. One more interesting feature can be seen in Figure 7.34, where a number of small seismic shocks are correlated with the stabilization of pore pressure level after initial intensive deleting.

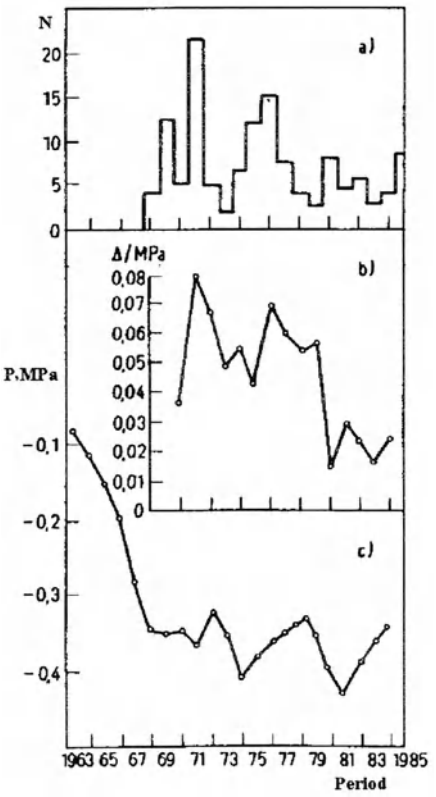

Figure 7.34. Number of earthquakes, N, difference, Δ, between the seam pressure and the operation pressure of the gas well, and variation of seam pressure drop, p, versus time period (according to L.M.Plotnikova et al. [141]).

This indicates that the Gazli gas reservoir was in a regime of water flooding (or even pore closing) in 1967-1984 due to action of the surrounding water head (or tectonic forces). The corresponding mass redistribution was a main triggering reason of the Central Asia giant fault system whose motion was recreated in the form of the Gazli earthquakes.

Remobilization of faults was observed in deep mines where explosions of 200 tons of TNT generated the fault displacements in the form of an earthquake with $M = 4.8 - 5$. The earthquake released seismic waves with an energy of $\mathcal{E}_s = 10^{12} Jouls$. The fault maximum displacement was *6-8 cm* at shear forces 10-30 MPa [214].

BIBLIOGRAPHY

[1] Abercrombie R.E., Leary P. (1993) *Source parameters of small earthquakes recorded at 2,5 km depth, Cajon Pass, Southern California; implications for earthquake scaling.* Geophys. Letts, Res. v. 20, 1511-1514.

[2] Aggarwal Y.P., Sykes L.R., Ambruster J., Sbar M.S. (1973) *Premonitory changes in seismic velocities and prediction of earthquakes.* Nature, No 241, 101-104.

[3] Afanasiev E.F., Grdzelova K.L., Plushchov D.V. (1987) *On sources of sound generation in saturated porous media.* Proc. USSR Acad. Sci. (DAN), v. 293, No 3, 554-557.

[4] Aki K. (1972) *Generation and propagation of G-waves from Niigata earthquake of June 16, 1964.* Part 1,2. Bull. Earth. Res. Inst., Tokyo University, v. 44, 23 - 88.

[5] Alperovich I.M., Nikiforov V.M., Kharakhinov V.V. (1979) *Anomalies of electroconductivity in the Earth crust of Sakhalin island.* Proc USSR Acad. Sci. (DAN), v. 244, No 5, 1194-1198 (in Russian).

[6] An V.A., Luquet E.I., Pasechnik I.P. (1985) *Variants of seismic wave parameters during sounding of the Earth at distances of* 90°. Proc. USSR Acad.Sci (DAN), v.285, No 4, 836-840 (in Russian).

[7] Anderson O.L., Grew P.S. (1977) *Stress corrosion theory of crack propagation with application to geophysics.* Revs. Geophys. Space Phys., v. 15, 77-104.

[8] ARPA *Seismic Coupling Conference* (1972) ARPA-T10-71-13-1, Columbus (Ohio), BATTELLE, 259 pp.

[9] Artyushkov E.V. (1993) *Physical Tectonics.* Moscow: Nauka, 455 pp. (in Russian).

[10] Avsjuk Yu.N. (1980) *Possible explanation of process of latitude changing (of Chandler pole wobble).* Proc. USSR Acad. Sci (DAN), v. 254, No 4, 834-838 (in Russian).

[11] Babkin V.A., Levin V.M., Nikolaevskiy V.N. (1992) *Flows of fluid and gas in porous media under induced anisotropy.* Fluid Mechanics (Izvestia), No 3, 96-103.

[12] Barenblatt G.I., Entov V.M., Ryzhik V.M. (1984) *Flows of Fluids and Gases in Natural Layers.* Moscow: Nedra, 207 pp. (in Russian).

[13] Barmin A.A., Garagash D.I. (1994) *On flow of mixture through a porous medium with adsorption at a matrix.* Fluid Mechanics (Izvestia), No 4, 97-110.

[14] Basniev K.S., Kochina I.N., Maximov V.M. (1993) *Underground Hydrodynamics.* Moscow: Nedra, 416 pp. (in Russian).

[15] Bear J. (1972) *Dynamics of Fluids in Porous Media.* New York: American Elsevier, 764 pp.

[16] Beavers G.S., Joseph D.D. (1967) *Boundary condition at a naturally permeable wall.* J. Fluid Mech., v. 30 (1), 197-207.

[17] Bedrikovetsky P. (1993) *Mathematical Theory of Oil and Gas Recovery.* Dordrecht: Kluwer Acad. Publ., 575 pp.

[18] Belousov V.V. (1986) *Structural Geology.* Moscow Univ. Press, 243 pp. (in Russian).

[19] Beresnev I.A., Nikolaevskiy V.N. (1993) *A model for nonlinear seismic waves in a medium with instability.* Physica D, v. 66, 1-6.

[20] Biot M.A. (1956) *Theory of propagation of elastic waves in a fluid-saturated porous solids.* J. Acoustic. Soc. Amer., v. 28, 168-186.

[21] Biot M.A. (1965) *Mechanics of Incremental Deformations.* New York: Wiley, 504 pp.

[22] Bolt B.A. (1978) *Earthquakes.* San Francisco: W.H.Freeman & Co.

[23] Bondarev E.A., Nikolaevskiy V.N. (1962) *Convective diffusion in porous media with account of adsorption*. J. Appl. Mech. Techn. Phys., No 5, `128-134 (in Russian).

[24] Bott M.H.P. (1971) *The Interior of the Earth*. London: E.Arnold.

[25] Brace W.F. (1972) *Laboratory studies of stick-slip and their application to earthquakes*. Tectonophysics, v. 14, No 3-4, 189-200.

[26] Brace W.F., Orange A.S. (1966) *Electrical resistivity changes in saturated rocks under stress*. Science, v. 153, 1525-1526.

[27] Brace W.F., Paulding B.W., Scholz C.H. (1966) *Dilatancy in the fracture of crystalline rocks*. J. Geophys. Res., v. 71, 3939-3953.

[28] Brenner H. (1962) *The diffusion model of longitudinal mixing in beds of finite length. Numerical values*. Chem. Engng Sci., v. 1, No 1, 229 - 243.

[29] Broberg K.B. (1978) *On transient sliding motion*. Geophys. J. Roy. Astr. Soc., v. 58, 397-432.

[30] Brulin O., Hjalmars S. (1981) *Linear grade-consistent micropolar theory*. Int. J. Engng Sci., 1731-1738.

[31] Brun J.P., Cabbold P.R. (1980) *Strain heating and thermal softening in continental shear zones: a review*. J. Structural Geology, v. 2, No 1/2, 149-158.

[32] Butkovich T.R. (1971) *Influence of water in rocks on effects of underground nuclear explosions*. J. Geophys. Res., v. 76, No 8, 1993-2011.

[33] Buzinov S.N., Peshkin M.A. (1977) *Zone of mixing of filtering gases in different porous media*. Trans. USSR Acad. Sci. (Izvestia), No 1, 142 - 145.

[34] Byerlee J.D. (1968) *Brittle-ductile transition in rocks*. J. Geophys. Res., v. 73, 4741-4750.

[35] Bykov V.G., Nikolaevskiy V.N. (1992) *Seismic waves in saturated porous geomaterials with viscoelastic matrix*. Proc. Russ. Acad. Sci. (DAN), v. 323, No 3, 446-451.

[36] Bykov V.G., Nikolaevskiy V.N. (1992) *Free gases of asthenosphere according to seismic data*. Trans. Russ. Acad. Sci. (DAN), v. 323, No 2, 253-257.

[37] Bykov V.G., Nikolaevskiy V.N. (1993) *Nonlinear waves in porous saturated media*. Proc. Russian Acad. Sci. (DAN), v. 328, 35-38.

[38] Cameron I., Baker T.H.W., Handa Y.P. (1989) *Compressive strength and creep behavior of hydrate consolidated sand*. Canad. Geotechnology J., v. 28, 235-242.

[39] Carter N.L. Horseman S.T., Russel J.E., Handlin S. (1993) *Rheology of rocksalt*. J. Structural Geology, v. 15, No 9/10, 1257-1271.

[40] Chekalyuk E.B. (1986) *Towards the petroleum synthesis problem at super depths*. J. All-Union Mendeleev Soc., v. 31, No 5, 556-562.

[41] Christensen R.J., Swanson S.R., Brown W.S. (1972) *Split-Hopkinson-bar tests on rock under confining pressure*. Exp. Mech., v. 12, No 11, 508-513.

[42] Christianovich S.A. (1941) *On flows of gas-dissolved fluid in porous rocks*. J. Appl. Mech. (PMM), v. 5, No 2, 277-282.

[43] Corwin R.F., Morrison H.F. (1977) *Self-potential variations preceding earthquakes in Central California*. Geophys. Res. Lett., v. 4, 171-174.

[44] Coulomb C.A. (1977) *Essai sur une application des regles des maximus et minimus a quelques problems de statique relatifs a architecture*. Mem. Acad. Roy. Pres. Divers. Savants, v. 7.

[45] Crampin S. (1978) *Seismic wave propagation through a cracked solid: polarization as a possible dilatancy diagnostic*. Geoph. J. R. Astron. Soc., v. 53, 467-496.

[46] Davis E.H. (1968) *Theories of plasticity and the failure of soil masses.* In: Soil Mechanics. Selected Topics (Lee I.K., ed.), London: Butterworths, 341-380.

[47] De Boer R., Ehlers W. (1990) *The development of the concept of effective stresses.* Acta Mechanica, 77-92.

[48] Desroches J., Detournay E., Lenoach B., Papanastasiou P., Pearson J.R.A., Thiercelin M., Cheng A. (1994) *The crack tip region in hydraulic fracturing.* Proc. R. Soc. Lond. A 447, 39-48.

[49] Detournay E., Fairhurst C. (1987) *Two-dimensional elastoplastic analysis of a long, cylindrical cavity under nonhydrostatic loading.* Int. J. Rock Mech. Min. Sci. and Geomech. Abstr., v. 24, No 4, 197-211.

[50] Dinariev O.Yu. (1992) *Flows of fluids and gases through porous media with fractal geometry.* Fluid Mech. (Izvestia), No 5, 101-109.

[51] Dinariev O.Yu., Nikolaevskiy V.N. (1993) *The unsteady microrotational regime.* J. Appl. Maths Mechs, v. 57, No 5, 935-940.

[52] Dinariev O.Yu., Nikolaevskiy V.N. (1993) *Rock creep as a source of seismic noise.* Trans. Russ. Acad. Sci. (DAN), v. 331, 739-741.

[53] Dongarrd G., Martinelli G. (1995) *Migration processes of radon towards the Earth surface: implications for the prediction of seismic and volcanic events.* Proc. Scientific Meeting on the Seismic Protection. Spagna V., Schiavon E., eds. Regione del Veneto, Dept. Geol., 141-147.

[54] Drescher A., Josselin de Jong G. (1972) *Photoelastic verification of a mechanical model for the flow of a granular material.* J. Mech. Phys. Solids, v. 20, 337-351.

[55] Drozdov O.A., Grigorieva A.S. (1971) *Many Years Cyclic Changes of Precipitation at the USSR Territory.* Leningrad: Gidrometeoizdat, 158 pp. (in Russian).

[56] Drucker D., Prager W. (1952) *Soil mechanics and plastic analysis or limit design.* Quart. Appl. Math., v. 10, No 2, 157-165.

[57] Dunin S.Z., Sirotkin V.K. (1977) *The expanding of a cavity in a brittle rock with dilatancy account.* J. Appl. Mech Techn. Phys., No 4, 106-109.

[58] Economides M., Hill A.D., Ehlig-Economides Ch. (1994) *Petroleum Production Systems.* Englewood Cliffs, PTR Prentice Hall, 611 pp.

[59] Economides M.J., Nolte K.G., eds. (1987) *Reservoir Stimulation.* Houston: Schlumberger.

[60] Elsasser W.H. (1969) *Convection and stress propagation in the upper mantle.* In: Application of Modern Physics to Earth & Planet. Interior, NY, Wiley, 223-246.

[61] Entov V.M., Zazovsky A.F. (1989) *Hydrodynamics of Oil Recovery Stimulation.* Moscow: Nedra, 233 pp. (in Russian).

[62] Epifanov V.P. (1984) *Mechanics of fracture of ice depending on temperature and strain rate.* Trans. USSR Acad. Sci. (Izvestia), Mech. Solids, No 2, 188-196.

[63] Ericksen J.L. (1966) *A thermo-kinetic view of elastic stability theory.* Internat. J. Solids Structures, v. 2, No 4, 573-580.

[64] Fischer A.G., Judson Sh., eds. (1975) *Petroleum and Global Tectonics.* Princeton University Press.

[65] Foda M.F., Mei C.C. (1983) *A boundary layer theory for Rayleigh waves in porous fluid-filled half space.* Int. J. Soil Dynamics and Earthquake Engng, v. 2, No 2, 62-65.

[66] Frenkel Ya.I., Kontorova T.A. (1938) *Towards theory of plastic deformation and twinning.* J. Expt. Theor. Phys ,v. 8, 89-95, 1340-1359.

[67] Frenkel Ya.I. (1944) *On the theory of seismic and seismically electric phenomena in wetted soils.* Trans. USSR Acad. Sci. (Izvestia), Ser. Geophys. Geograph., No 8, 134-149.

[68] Fyfe W.S., Price N.J., Thompson A.B. (1978) *Fluids in the Earth Crust.* Amsterdam: Elsevier.

[69] Gamburzeva N.G., Luquet E.I., Nikolaevskiy V.N., Oreshin S.I., Pasechnik I.P (1984) *Seismic waves from large explosions reveal periodical deformations at lithosphere depths.* Earth Planet. Sci. Letters, v. 71, 279-289.

[70] Garagash I.A., Nikolaevskiy V.N. (1989) *Nonassociative flow rules and localization of plastic deformation.* Advances in Mechanics (Warszawa), v. 12, No 1, 131-183 (in Russian).

[71] Garagash I.A., Nikolaevskiy V.N. (1990) *Mechanics of ring and block structure appearance in the Earth crust.* Proc. USSR Acad. Sci.. (DAN), v. 315, No 1, 62-65 (in Russain).

[72] Garagash I.A., Nikolaevskiy V.N. (1994) *Conditions of limit equilibrium of fragmented rock masses in micro- and macroscale.* Proc. Acad. Sci. (DAN), v. 338, No 5, 675-679.

[73] Garagash I.A., Nikolaevskiy V.N., Shatzilov V.I. (1994) *Deep anomalies of crust stresses in the zone of hydrocarbon reservoirs beneath salt in the Northern Caspian.* Proc. Acad. Sci. (DAN), v. 338, No 3, 383-386.

[74] Garagash I.A., Nikolaevskiy V.N., Stepanova G.S. (1992) *Migration and criteria of hydrocarbon accumulation in tectonic fault system*, Proc. Acad. Sci. (DAN), v. 324, No 6, 1169-1174.

[75] Garg S.K., Nayfeh A.N., Geod A.J. (1974) *Compressional waves in fluid-saturated elastic porous media.* J. Appl. Phys., v. 45, No 5, 1968-1974.

[76] Gershenson N.I., Gokberg M.B., Morgunov V.A., Nikolaevskiy V.N. (1987) *On sources of electromagnetic radiation, precursuring of seismic events.* Solid Earth Physics (Izvestia), No 2, 41-49 (in Russian).

[77] Glansdorff P., Prigogine I. (1971) *Thermodynamic Theory of Structure, Stability and Fluctuation.* London: Wiley, 306 pp.

[78] Gomes L., Graves L. (1962) *Stabilization of beach sand by vibrations.* Highway Research Board, Washington D. C., Bull. No 325, 44-54.

[79] Grachev A.F. (1987) *Rift Zones of the Earth.* Moscow: Nedra, 285 pp. (in Russian).

[80] Grafutko S.B., Dmitriev N.M., Nikolaevskiy V.N. (1993) *Effect of induced anisotropy in the vicinity of producing well.* Fluid mechanics (Izvestia), No 6, 67-72.

[81] Grasso J.R., Wittlinger G. (1990) *Ten years of seismic monitoring over a gas field.* Bull. Seism. Soc. America, v. 80, No 2, 450-473.

[82] Gubin I.E., ed. *Lithosphere of Tyan Shan.* Moscow: Nauka, 157 pp. (in Russian).

[83] Guliev I.S., Pavlenkova N.I., Radzhabov M.M. (1988) *Zone of regional dilatancy in Sedimentary basin of Southern Caspian Sea.* Lithology and Mineral Resources, No 5, 130-136 (in Russian).

[84] Gutenberg B. (1959). *Physics of the Earth Interior.* New York: Academic Press.

[85] Hacker B.R., Christie J.M. (1990) *Brittle/ductile and plastic/cataclastic transitions in experimentally deformed and metamorphosed amphibolite.* In: The Brittle-Ductile Transition in Rocks, Wash. D.C.: Amer. Geoph. Union, 127-147.

[86] Hall C.D., Harrisberger W.H.(1970) *Stability of sand arches: a key to sand control.* J. Petrol. Technol., v. 22, July, 821-829.

[87] Handin J., Carter N. (1980) *Rheological properties of rocks at high temperatures.* In: Proc. 4th Int. Congr. Rock. Mech, Montreux-1979, v. 3, Rotterdam, Balkema Publ. 97-106.

[88] Hauksson E. (1981) *Radon content of groundwater as an earthquake precursor: evaluation of worldwide data and physical basis.* J. Geophys. Res., v. 86, 9397-9410.

[89] Healy J.H., Rubey W.W., Griggs D.T., Rayleigh C.B. (1968) *The Denver earthquakes.* Science, v. 161, p. 1301.

[90] Hyndman R.D., Vanyan L.L. Marquis G., Law L.K. (1993) *The origin of electrically conductive lower continental crust: saline water or grafite?* Physics of the Earth and Planetary Interiors, v. 81, 325-344.

[91] Istomin V.A., Iakushev V.S. (1992) *Gas-hydrates in Nature*. Moscow: Nedra, 236 pp.

[92] Islam M.R., Farouq Ali S.M. (1994) *Numerical simulation of emulsion flow through porous media*. J. Canad. Petrol. Techn., v. 33, No 3, 59-63.

[93] Jaeger J.C., Cook N.G.W. (1976) *Fundamentals of Rock Mechanics*. London: Chapman & Hall, 585 pp.

[94] Kachanov L.M. (1974) *Fundamentals of Fracturing*. Moscow: Nauka, 311 pp. (in Russian).

[95] Kapustyanskii S.M., (1985) *Elastoplastic dilatant model of anisotropic media*. Trans. USSR Acad. Sci. (Izvestia), Solid Earth Physics, No 8, 50-59.

[96] Kapustyanskii S.M., Nikolaevskii V.N. (1985) *Parameters of elastoplastic dilatant model for geomaterials*. J. Appl. Mech. Techn. (PMTF), No 6, 145-150 (in Russian).

[97] Karakin A.V., Lobkovskii L.I., Nikolaevskii V.N. (1982) *Generation of serpentinite layer of ocean crust and some geologic-geophysical phenomena*. Proc. USSR Acad. Sci. (DAN), v. 265, No 3, 572-576 (in Russian)

[98] Kasahara K. (1981) *Earthquake Mechanics*. Cambridge University Press, 248 pp.

[99] Kirby S.H., Kronenberg A.K. (1984) *Deformation of clinopyroxenite: evidence for a transition in flow mechanics and semibrittle behavior*. J. Geophys. Res., v. 89, No B5, 3177-3192.

[100] Knauss W.G., Ravi-Chandar (1985) *Some basic problems in stress wave dominant fracture*. Int. J. Fracture, v. 27, 127-143.

[101] Kolsky H. (1973) *The stress pulses propagated as a result of the rapid growth of brittle fracture*. Engng Fracture Mech., v. 5, 513-522.

[102] Krylov A.P., Borisov Yu.P., Nikolaevskiy N.M., eds. (1962) *Design of Recovery of Oil Reservoirs*. Moscow: Gostoptechizdat, 430 pp.

[103] Krylov A.L., Mazur N.G., Nikolaevskiy V.N., El G.A. (1993) *Gradient-consistent nonlinear model of the generation of ultrasound in the propagation of seismic waves*. J. Appl. Math Mechs, v. 57, No 6, 1057-1066.

[104] Kurtia K., Fujii N. (1979) *Stress memory of crystalline rocks in acoustic emission*. Geophys. Res. Lett., v. 6, No 1, 9 - 12.

[105] Lake L.W. (1989) *Enhanced Oil Recovery*. Englewood Cliffs NY; Prentice Hall, 550 pp.

[106] Lamb G.L.Jr. (1980) *Elements of Soliton Theory*. New-York-Shichester-Brisbane-Toronto: John Wiley & Sons.

[107] Le Pishon X., Francheteau J., Bonnin J. (1973) *Plate Tectonics*. Amsterdam: Elsevier Co.

[108] Leverett N.C. (1941) *Capillary behavior in porous solids*. Trans. AIME, v. 142, 152.

[109] Lobkovsky L.I. (1988) *Geodynamics of Spreading, Subduction Zones and Two-Flow Plate Tectonics*. Moscow: Nauka, 252 pp.

[110] Lobkovsky L.I., Ismail-Zade A.T., Naimark B.M., Nikishin A.M., Kluting C. (1993) *Mechanics of the Earth crust sinking and sedimentary basin creation*. Proc. Acad. Sci. (DAN), v. 330, No 2, 256-260.

[111] Lopatin N.V. (1971). *Temperature and geologic time as carbonization factors*. Trans. USSR Acad. Sci. (Izvestia), Ser. Geology, No 3, 95-106.

[112] Lopukhov G.P., Nikolaevskiy V.N. (1995) *The role of acoustic emission at vibroseismic stimulation of waterflooded oil reservoirs*. Improved Oil Recovery, Proc. 8th Symp., v. 2, Vienna.

[113] Lukk A.A., Nersesov I.L. (1982) *Temporal variations of some parameters of seismotectonic process*. Trans. USSR Acad. Sci. (Izvestia), No 3, 10-27 (in Russian).

[114] Luquet E.I., Nikolaevskii V.N., Pasechnik I.P. (1985) *Existence of fast tectonic cycles in Tien Shan*. Proc. USSR Acad. Sci. (DAN), v. 284, No 3, 575-579 (in Russian).

[115] Luquet E.I., An V.A., Pasechnik I.P. (1988) *Revealing of tectonic global front by seismic sounding of the Earth*. Proc. USSR Acad. Sci. (DAN), v. 301, No 3, 569-573.

[116] Makogon Yu.F. *Hydrates of Natural Gas*. Tulsa: Pernn Well C°, 237 pp.

[117] Maksimov A.M. (1992) *A mathematical model of bulk dissociation of gas-hydrates in porous media: account of water phase mobility*. Eng.-Phys. J., No 1, 76-81 (in Russian).

[118] Maksimov A.M., Tsipkin G.G. (1991) *A mathematical model of a two-phase region in thawing soil*. Int. Ser. Numer. Math., v. 99, 251-258.

[119] Maksimov A., Radkevich E., Edelman I. (1993) *On modulated waves in porous media*. Siberian J. Diff. Equations (NY, Nova Sci. Publ.), v. 2, No 4, 35-80.

[120] Malamud A.S., Nikolaevskiy V.N. (1989) *Earthquake Cycles and Tectonic Waves*. Dushanbe: Donish, 140 pp (in Russian)

[121] Malamud A.S., Nikolaevskiy V.N. (1992) *Usage of seismomonitoring data for earthquake prediction*. Solid Earth Physics (Izvestia), No 8, 83-92.

[122] Martel D.J., Deek S., Dovenyi P., Horwath F., O'Nions R.K., Oxburg E.R., Stegena L., Stute M. (1989) *Leakage of helium from Pannonia basin*. Nature, v. 342, 908-912.

[123] Mathews D.H. (1984) *Profiles of vertical reflected waves around the British Islands*. Reports of the 27th Internat. Geol. Congress, Section C.08, v. 8, Moscow: Nauka. 3 - 9.

[124] McGarr A., Spottiswoode S.M., Gay N.C. (1979) *Observations relevant to seismic driving stress, stress drop and efficiency*. J. Geophysic. Res., v. 84, No B5, 2251-2261.

[125] McNamee G., Gibson R.E. (1960) *Displacement functions and linear transforms applied to diffusion through porous elastic media*. Quart. J. Mech. Appl. Math., v. 13, 98-111.

[126] Mead W.J. (1925) *The geologic role of dilatancy*. J.Geol., v. 33, 685-678.

[127] Meissner R. (1986) *The continental crust: A geophysical approach*. Orlando: Academic Press, 426 pp.

[128] Melosh J. (1977) *Shear stress on the base of a lithosphere plate*. Pure and Applied Geophysics, v. 115, No 1-2, 429-439.

[129] Mercier J.C.C. (1980) *Magnitude of the continental lithospheric stresses inferred from rheomorthic petrology*. J. Geophys. Res., v. 85, No B11, 6293 - 6303.

[130] Merzer A.M., Freund R. (1976) *Equal spacing of strike-slip faults*. Geophys. J. Roy. Astr. Soc., v. 45, 177-188.

[131] Meyer K., Olsson R., Kulhanek O. (1984/85) *High-velocity migration of large earthquakes along the Azores-Iran plate boundary segment*. Pure and Appl. Geophys., v. 122, 831-847.

[132] Migunov N.I. (1984) *On usage of seismoelectrical effects for study of stress state of saturated rocks*. Trans. USSR Acad. Sci. (Izvestia), Physics of Solid Earth, No 9, 20-28 (in Russian).

[133] Milanovskij S.Yu., Nikolaevskiy V.N. (1989) *Thermomechanical analysis of the Earth crust structure (along Barentz Sea-Eastern Alps geotravers)*. Trans. USSR Acad. Sci. (Izvestia), Solid Earth Physics, No 1, 83-91.

[134] Mitlin V.S. (1990) *Two-phase multicomponent filtration: instabilities, autowaves and retrograde phenomena*. J. Fluid Mech., v. 220, 369-395.

[135] Mitlin V.S., Nikolaevskiy V.N. (1990) *Nonlinear surface waves in media with complex rheology.* Fluid Mechanics (Izvestia), No 5, 95-103 (in Russian).

[136] Mogi K. (1985) *Earthquake Prediction.* Tokyo: Academic Press.

[137] Morgan W.J. (1972) *Convection plumes and plate motions.* Bull. Amer. Assoc. Petrol. Geol., v. 56, 203-213.

[138] Muskat M. (1937) *The Flow of Homogeneous Fluids Through Porous Media.* New York: McGraw-Hill, 763 pp.

[139] Muskat M. (1949) *Physical Principles of Oil Production.* New-York: McGraw-Hill , 922 pp.

[140] Nadai A.(1963) *Theory of Flow and Fracture of Solids.* v. 2, New-York: McGraw-Hill Co.

[141] Nikolaev A.V., Galkin I.N., eds. (1994) *Induced Seismicity.* Moscow, Nauka, 220pp.

[142] Nikolaevskii V.N. (1959) *Convective diffusion in porous media.* Appl. Math. Mech. (PMM), v. 23, No 6, 1042-1050 (in Russian).

[143] Nikolaevskii V.N. (1967) *On interconnection of volume and shear strains and on shock waves in soft soils.* Proc. USSR Acad. Sci. (DAN), v. 177, No 3, 542-545 (in Russian).

[144] Nikolaevskii V.N. (1971) *Governing equations of plastic deformation of a granular medium.* J. Appl. Math. Mech. (PMM), v. 35, No 6, 1017-1029.

[145] Nikolaevskii V.N. (1979) *Thermodynamics of crack growth. Fracture of elastic, quasi-elastic and viscous bodies.* Trans. USSR Acad. Sci. (Izvestia), Mech. Solids, No 4, 95-106 (in Russian).

[146] Nikolaevskii V.N. (1979) *The Mohorovichich boundary as a limit depth of brittle-dilatant state of rocks.* Proc. USSR Acad. Sci (DAN), v. 249, No 4, 817-821.

[147] Nikolaevskii V.N. (1980) *Dilatancy and theory of earthquake source.* Advances in Mechanics (Warszawa), v. 3, No 1, 71 - 101. (in Russian).

[148] Nikolaevskii V.N. (1981) *Limit velocity of fracture front and dynamic strength of brittle solids.* Int. J. Engng Sci., v. 19, 41-56 (Preprint in Russian: Inst. Problem of Mechanics, No 123, 1979, USSR Acad. Sci., Moscow).

[149] Nikolaevskii V.N. (1982) *Fracture criterion for inelastic solids.* Int. J. Engng Sci., v. 20, No 2, 311-318.

[150] Nikolaevskii V.N. (1985) *Mechanics of fluid-saturated geomaterials: Discusser's report.* Mechanics of Geomaterials. (Bazant Z., ed.), New-York: J.Wiley & Sons, 379-401.

[151] Nikolaevskii V.N. (1989) *Mechanism and dominant frequencies of vibrational enhancement of yield of oil pools.* Trans. USSR Acad. Sci. (DAN), v. 307, 570-575 (Engl. transl.: Scripta).

[152] Nikolaevskiy V.N. (1990) *Mechanics of Porous and Fractured Media.* Singapore: World Scientific, 472 pp.

[153] Nikolaevskiy V.N. (1992) *Rock vibration and finite oil recovery.* Fluid Mechanics, No 5, 110 - 120, (English transl: Plenum -1993, 689-695).

[154] Nikolaevskiy V.N. (1993) *Extraterrestrial induced multi-years cycles in geophysical, geochemical and biological parameters.* In: Radon Monitoring in Radioprotection, Environmental and Earth Sciences (Furlan G. and Tommasino L., eds.). Singapore, World Scientific, 401-417.

[155] Nikolaevskiy V.N. (1995) *Mathematical simulation of solitary deformation and seismic waves.* Proc Acad. Sci. (DAN), v. 341, No 3, 403-405.

[156] Nikolaevskii V.N., Basniev K.S., Gorbunov A.T., Zotov G.A. (1970) *Mechanics of Saturated Porous Media.* Moscow: Nedra, 339 pp (in Russian).

[157] Nikolaevskii V.N., Bondarev E.A., Mirkin M.I., Stepanova G.S., Terzi V.P. (1968) *Motion of Hydrocarbon Mixtures in a Porous Medium.* Moscow: Nedra, 192 pp. (in Russian).

[158] Nikolaevskiy V.N., Kuznetzov A.S., Bellendir E.N. (1991) *Mathematical dilatancy theory and conditions at strong discontinuities.* Int. J. Engng Sci., v. 29, No 11, 1375-1389.

[159] Nikolaevskiy V.N., Ramazanov T.K. (1984) *Calculation of an aquifer as hydraulical seismographs.* Soviet Fluid Mechanics, No 4, 81-86.

[160] Nikolaevskii V.N., Rice J.R. (1979) *Current topics in non-elastic deformation of geological materials.* In: High-Pressure Science And Technology, New-York: Premium Publ. Corp., v. 2, 455-464.

[161] Nikolaevskii V.N., Rotenburg L.B. (1970) *On nonlinear feature of attenuation of seismic waves.* In: Problems of Mechanics of Solid Deformable Body. Leningrad: Sudostroenie, 281-286 (in Russian).

[162] Nikolaevskii V.N., Somov B.E. (1978) *Heterogeneous flows of multi-component mixtures in porous media - Review.* Int. J. Multiphase Flow, v. 4, 203-217

[163] Nur A. (1974) *Tectonophysics: the study of relations between deformation and forces in the Earth.* Adv. Rock Mech., v. 1, Part A, Wash. D.C.

[164] Nur A. (1974) Matsushiro, Japan, *Earthquake swarm: confirmation of the dilatancy- fluid diffusion model.* Geology, May, 217-221.

[165] Osika D.G. (1981) *Fluid Regime Of Seismically Active Regions.* Moscow: Nauka, 203 pp. (in Russian)

[166] Paterson M.S. (1978) *Experimental Rock Deformation - Brittle Field.* Berlin-Heidelberg-New-York: Springer, 254 pp.

[167] Parameswaran V.R., Paradis M., Handa Y.P (1989) *Strength of frozen sand containing tetrahydrofuran hydrate.* Can. Geotech. J., 479-483.

[168] Pavlenkova N.I. (1988) *The nature of seismic boundaries in the continental lithosphere.* Tectonophysics, v. 154, 211-225.

[169] Polubarinova-Kochina P.Ya. (1962) *Theory of Ground Water Movement.* Princeton University Press (English translation).

[170] Pride S.R., Morgan F.D. (1991) *Electrokinetic dissipation induced by seismic waves.* Geophysics, 914-925.

[171] Pucknell J.K., Behrmann L.A. (1991) *An investigation of the damaged zone created by perforating.* SPE 22811, Dallas: Soc. Petr. Eng. 66th Annual Conf., 511-522.

[172] Raghavan R. (1993) *Well Test Analysis.* Englewood Cliffs, NS Prentice Hall, 558pp.

[173] Ranalli G. (1986) *Rheology of The Earth.* Boston: Allen and Unwin, 366 pp.

[174] Rau G., Chaney R.C. (1988) *Triaxial testing of marine sediments with high gas contents.* ASTM STP 977, Philadelphia, 338-352.

[175] Reiner M. (1969) *Deformation, Strain and Flow.* London: H.K. Lewis & Co.

[176] Reynolds O. (1885) *The dilating of media composed of rigid particles in contact.* Phil. Magazine. v. 20, No 127, 469-481.

[177] Rice J.R. (1978) *Thermodynamics of quasi-static growth of Griffith crack.* J. Mech. Phys. Solids, v. 26, No 2, 61 - 78.

[178] Richter Ch.F. (1958) *Elementary Seismology.* San Francisco: W.H.Freeman & Co.

[179] Richter F.M., McKenzie Dan, (1984) *Dynamical models for melt segregation from a deformable matrix.* J. Geology, v. 92, 729-740.

[180] Rikitake T. (1976) *Earthquake Prediction.* Elsevier, Amsterdam.

[181] Ringwood A.E. (1975) *Composition and Petrology of the Earth.* Mantle, New York: McGraw Hill.

[182] Rodean H.C. (1971) *Nuclear-Explosion Seismology.* University of California Lawrence Livermore Labs, Dir. Techn. Eng.

[183] Rodionov V.N., Adushkin V.V., Kostyuchenko V.N., Nikolaevskii V.N., Romashov A.N., Tsvetkov V.M. (1971) *Mechanical Effect of an Underground Explosion.* Moscow: Nedra, 221 pp. (English translation - 1972, US Atomic Energy Commision, Tech. Inf. Center, UCRL-Trans-10676).

[184] Rowe M.M., Gettrust J.F. (1993) *Fine structure of methane hydrate-bearing sediments on the Blake Outer Ridge as determinated from deep-tow multichannel seismic data.* J. Geophys. Res., v. 98, No B1, 463-473.

[185] Rudakov V.P. (1988) *Space-time features of ground radon field dynamics in Western-Fergana region before and after Tashkent earthquakes 1980-1981.* Proc. USSR Acad. Sci. (DAN), v. 302, No 5, 1183-1186.

[186] Rudnicki J.W., Rice J.R. (1975) *Condition for localization of deformation in pressure sensitive dilatant materials.* J. Mech. Phys. Solids, v.23, No 6, 371-394.

[187] Rutter E.H. (1983) *Pressure solution in nature, theory and experiment.* J. Geol. Soc. London, v.140, 725-740.

[188] Sadovskiy M.A., Nikolaev A.V., eds (1993) *Seismic Vibration at Oil Reservoir.* Inst. Earth Physics, Rus. Acad. Sci., Moscow, 239 p.

[189] Sahimi M. (1993) *Fractal and superdiffusive transport and hydrodynamic dispersion in heterogeneous porous media.* Transport in Porous Media, v. 13, 3-40.

[190] Salnikov D. I., Traskin V. Yu. (1987) *Fundamentals of physical-chemical geomechanics.* In: Study of Tectonic Deformation, Moscow: Nauka, 33-83.

[191] Samarov E.L. (1983) *Expanding of explosion cavity in dilatant plastic soils.* Trans. USSR Acad. Sci. (Izvestia), Physics of the Earth, No 2, 68-76 (in Russian)

[192] Saprygin S.M. (1980) *Mechanism of creation of hydrogeodynamical precursors of earthquakes.* Volcanology And Seismology, No 2.,122-124.

[193] Statake M. (1968) *Some considerations on the mechanics of granular materials.* Mechanics of Generalized Continua. Berlin: Springer, 156-159.

[194] Scheidegger A.E. (1964) *Statistical hydrodynamics in porous media.* Advances Hydroscience, v.1, New-York, London: Acad.Press, 161-181.

[195] Scheidegger A.E. (1974) The Physics of Flow Through Porous Media. University of Toronto Press, 3d ed., 353 pp.

[196] Schelkachev V.N. (1948) Elastic Regime of Formation Waterhead Systems. Moscow: Gostoptechizdat, 144 pp. (in Russian).

[197] Schock R.N., Louis H. (1982) *Strain behavior of a granite and a graywacke sandstone in tension.* J. Geophys. Res., v.87, No B9, 7817-7823.

[198] Schock R.N., Hanson M.E., Swift R.P., Walton O.R. (1980) *In situ fracture related to energy and resource recovery.* In "High-pressure Sci.Techn." (Vodar B., Marteau Ph., eds.), Pergamon, 902-912.

[199] Scholz C.H., Sykes L.E., Aggarwal Y.P. (1973) *Earthquake prediction: a physical basis.* Science, v.181, No 4102, 803-810.

[200] Selby R.J., Farouq Ali S.M. (1988) *Mechanics of sand production and flow of fines in porous media.* J. Canad. Petroleum Technology, v.27, No 3, 55-63.

[201] Semenov A.N. (1969) *Variation of travel times ratio of P and S waves before strong earthquakes.* Trans. Acad. Sci. USSR (Izvestia), Earth Physics, No 12,72-77.

[202] Shield B.T. (1953) *Mixed boundary value problems in soil mechanics.* Quart. Appl. Math., v. 11, No 1, 61-75.

[203] Sibson R.H. (1982) *Fault zone models, heat flow and the depth distribution of earthquakes in the continental crust of the United States.* Bull. Seism. Soc. America , v.72, No 1, 151-164.

[204] Sobolev G.A. (1993) Foundation of Earthquake Prediction. Moscow: Nauka, 313 pp. (in Russian).

[205] Sokolovski V.V. (1960) Statics of Soil Media. (Transl. from 2nd Russian edition, 1954), London: Butterworths, 237 pp.

[206] Solodilov L.N. (1994) *Center "GEON"-25 years of deep seismic researches.* Exploration and Guard of Resources. No 10, 2-8.

[207] Soo H., Radke C. J. (1984) *The flow mechanism of dilute, stable emulsion in porous media.* Ind. Eng. Chem. Fundam., v.23, 342-347.

[208] Sorohtin O. G. (1974) Global Evolution of the Earth, Moscow: Nauka, 184pp.(in Russian)

[209] Stavrogin A. N., Protosenya A. G. (1979) Plasticity of Rocks. Moscow: Nedra, 301 pp (in Russian).

[210] Sterling A., Smets E. (1971) *Study of earth tides, earthquakes and terrestrial spectroscopy by analysis of the level fluctuations in a borehole at Heinbaart, Belgium*, Geophys. J. Roy. Soc. Astr. Soc., v.23, 225 - 242.

[211] Streltsova T. D. (1988). Well Testing in Heterogeneous Formations. NewYork: Wiley & Sons, 413 pp.

[212] Suvorov V. D., Sharapov E. V. (1990) *Seismic pecularities of the mantle surface in the southern part of Yakutian kimberlite province.* Geology and Geophysics, No 7, 93-101 (in Russian).

[213] Swolfs H. S., Walsh J. B. (1990) *The theory and prototype development of a stress-monitoring system.* Bull. Seism. Soc. Amer., v. 80, No 1, 197-208.

[214] Syrnikov N. M. , Tryapizin V. M. (1990) *On mechanism of technogenous earthquake in Khibin mountains.* Proc. USSR Acad. Sci. (DAN), v. 314, No 4, 830 - 833.

[215] Tamarsyan G. P. (1963) *Space-temporal connection of volcanous activity as one of characteristics of existence of a deep fault and some questions of its periodicity.* Izvestia VUS, Geology and Exploration, No 2, 3-19 (in Russian).

[216] Terzaghi K. (1943) Theoretical Soil Mechanics. Wiley.

[217] Tchizhevskiy A.L. (1976) Earth Echo of Sun Storms, Moscow: Mysl.

[218] Tretyakova S. P., Ishankuliev J., Pazylov M., Feisyllaev A. A., Gyliev I. S., Chirkov A. M. (1993). *The investigations of subsoil radon fields in USSR.* In: Radon Monitoring in Radioprotection, Environmental and Earth Sciences. (Furlan G., Tommasino L., eds.) Singapore: World Scientific, 328 - 350.

[219] Trofimov V.A. (1991) *Evaluation of prediction possibility of loose zones inside rock basement according to seismic data.* In: Geological and Geophysical Simulation of Oil and Gas Exploration. (Krylov N. A, ed.), Moscow,: IGIRGI, 126-133 (in Russian).

[220] Truesdell C., Toupin R. (1960) *The classical field theories.* In: Heidbuch der Physik, v.III/1, Berlin: Springer-Verlag.

[221] Tullis J., Yund R. A. (1977) *Experimental deformation of dry Westerly granite.* J. Geophys. Res., v. 82, No 36, 5705 - 5718.

[222] Tullis J., Yund R. A. (1980) *Hydrolitic weakening of experimentally deformed Westerly granite and Hale albite rock.* J. Struct. Geology, v. 2, No 4, 439 - 451.

[223] Turcotte D. L., Schulbert G. (1982) Geodynamics. Application of Continuum Physics to Geological Problems. NewYork: Wiley.

[224] Vilchinskaya N. A., Nikolaevskii V. N. (1984) *Acoustical emission and spectrum of seismic signals.* Trans. USSR Acad. Sci. (Izvestia), Physics of the Solid Earth, No 5, 91 - 100 (in Russian).

[225] Vanyan L. L., Shilovskiy P. P (1983) *Deep Electroconductivity of Oceans and Continents.* Moscow: Nauka, 86 pp. (in Russian).

[226] Walsh J. B. (1965) *The effect of cracks on uniaxial compression of rocks.* J. Geophys. Res., v. 70, No 2, 399-411.

[227] Wahr J. M. (1985) *Deformation induced by polar motion.* J. Geophys. Res.,v.90,No B1, 9363-9368.

[228] Warren J. E., Root P. J. (1963) *The behavior of naturally fractured reservoirs.* J. Soc. Petrol. Engrs., v. 3, No 3.

[229] Wegener A. (1929) *Die Entstehung der Kontinenete und Oseane.* Branschweig: F.Vieweg und Sohn (4 Auflage).

[230] Wilkins M. A. (1964) *Calculation of elasto-plastic flow.* In: Methods of Computational Hydrodynamics. (Alder B., ed.), New York: Academic Press, 211 pp.

[231] Zayakin V. N. (1981) *Study of Seismic Action of Short Delay of Blasts.* Erevan: Armenian Acad. Sci. Press, 82 pp.

[232] Zeldovich Ya. B., Raizer Yu. P. (1966) *Physics of Shock Waves and High Temperature Phenomena.* Moscow: Nauka, 686 pp.

[233] Zheltov Yu. P. (1975) *Mechanics of Oil-Gas Saturated Formation.* Moscow: Nedra, 216 pp. (in Russian).

[234] Zheltov Yu.P., Zolotarev P.F. (1962) *On percolation of gas through fractured rocks.* J. Appl. Mech. Techn. Phys.(PMTF), No 5, 135-139.

[235] Zhilenkov A.G., Kapustyanskiy S.M., Nikolaevskiy V.N.(1989) *Action of intensive wave on spherical cavity in dilating material.* In: Math. Simulation of Problems of Continuum Mechanics (Kudryashov N.A., ed.). Moscow: Energoatomizdat, 17 - 24 (in Russian).

[236] Zhilenkov A.G., Kapustyanskiy S.M., Nikolaevskiy V.N. (1994) *Deformation of wells in the field of fracturing horizontal stresses.* Physics of the Solid Earth, No 7/8, 142 - 147 (in Russian)

[237] Zhilenkov A.G., Kapustyanskiy S.M., Nikolaevsskiy V.N. (1995) *Failure of a deep well due to curvature of its borehole.* Proc. Acad. Sci. (DAN), v. 341, No 2, 255 - 258.

[238] Zoback M.D., Healy J.H. (1992) *In situ stress measurements to 3.5 km depth in the Cajon-Pass scientific research borehole: implication for the mechanics of crustal faulting.* J. Geophys. Res., v. 97, No B4, 5039-5057.

INDEX

Theory and Applications of Transport in Porous Media

Series Editor:
Jacob Bear, Technion – Israel Institute of Technology, Haifa, Israel

1. H.I. Ene and D. Poliševski: *Thermal Flow in Porous Media.* 1987 ISBN 90-277-2225-0
2. J. Bear and A. Verruijt: *Modeling Groundwater Flow and Pollution.* With Computer Programs for Sample Cases. 1987 ISBN 1-55608-014-X; Pb 1-55608-015-8
3. G.I. Barenblatt, V.M. Entov and V.M. Ryzhik: *Theory of Fluid Flows Through Natural Rocks.* 1990 ISBN 0-7923-0167-6
4. J. Bear and Y. Bachmat: *Introduction to Modeling of Transport Phenomena in Porous Media.* 1990 ISBN 0-7923-0557-4; Pb (1991) 0-7923-1106-X
5. J. Bear and J-M. Buchlin (eds.): *Modelling and Applications of Transport Phenomena in Porous Media.* 1991 ISBN 0-7923-1443-3
6. Ne-Zheng Sun: *Inverse Problems in Groundwater Modeling.* 1994 ISBN 0-7923-2987-2
7. A. Verruijt: *Computational Geomechanics.* 1995 ISBN 0-7923-3407-8
8. V.N. Nikolaevskiy: *Geomechanics and Fluidodynamics.* With Applications to Reservoir Engineering. 1996 ISBN 0-7923-3793-X

Kluwer Academic Publishers – Dordrecht / Boston / London